UNIVERSITY OF SOUTHAMPTON

Faculty of Environmental and Life Sciences
School of Ocean and Earth Science

Climate Change in Space: The Impact on Space Debris

DOI: TBC

by

Matthew Kenneth Brown
MPhys
ORCiD: 0000-0002-5043-1330

A thesis for the degree of
Doctor of Philosophy

January 2023

University of Southampton

Abstract

Faculty of Environmental and Life Sciences
School of Ocean and Earth Science

Doctor of Philosophy

Climate Change in Space: The Impact on Space Debris

by Matthew Kenneth Brown

Rising carbon dioxide concentrations are causing cooling and contraction of the thermosphere, reducing the neutral density and therefore the atmospheric drag experienced by space debris. Simulations of the thermosphere under increasing carbon dioxide concentrations have been performed with the Whole Atmosphere Community Climate Model - extended (WACCM-X). These have been used to create a density scaling factor for thermospheric density, which is dependent upon altitude, ground-level carbon dioxide (CO_2) concentration, and solar activity. Results show there has already been a 21% decrease in thermospheric density at 400 km altitude since the year 2000. If global temperatures increase by 1.5°C at ground level, WACCM-X predicts there will be a 15 - 32% decrease in density at 400 km compared to the year 2000, dependent upon solar activity. Moreover, the reduction in thermospheric density is predicted to continue at faster rates with further increases in the CO_2 concentration. The debris environment has been modelled with the new Binned Representative Atmospheric Decay (BRAD) debris model under the four Representative Concentration Pathways (RCPs) for CO_2 concentration. Compared against a control scenario with no density reductions, it is shown that the number of trackable objects by the year 2100 is 40% larger under the low-emissions RCP2.6 scenario and 214% larger in the high-emissions RCP8.5 scenario.

Contents

List of Figures

List of Tables

Declaration of Authorship

I declare that this thesis and the work presented in it is my own and has been generated by me as the result of my own original research.

I confirm that:

1. This work was done wholly or mainly while in candidature for a research degree at this University;
2. Where any part of this thesis has previously been submitted for a degree or any other qualification at this University or any other institution, this has been clearly stated;
3. Where I have consulted the published work of others, this is always clearly attributed;
4. Where I have quoted from the work of others, the source is always given. With the exception of such quotations, this thesis is entirely my own work;
5. I have acknowledged all main sources of help;
6. Where the thesis is based on work done by myself jointly with others, I have made clear exactly what was done by others and what I have contributed myself;
7. Parts of this work have been published as:
   M. K. Brown, H. G. Lewis, A. J. Kavanagh, and I. Cnossen. Future decreases in thermospheric neutral density in low Earth orbit due to carbon dioxide emissions. *Journal of Geophysical Research: Atmospheres*, 126(8):1–11, 2021. URL https://doi.org/10.1029/2021JD034589

Signed:..... Date:.....

Acknowledgements

I would like to thank my supervisory team. To Professor Hugh Lewis for being an inspiration to pursue the PhD, and always being available and knowledgeable to help make the project as smooth and enjoyable as possible. To Dr Andrew Kavanagh for being a friendly face, welcoming me at the British Antarctic Survey and being supportive throughout. To Dr Ingrid Cnossen for her knowledge and support in atmospheric modelling, her willingness to support me during busy times, and her help in troubleshooting WACCM-X during the early stages of the project. Together they have been a genuinely fantastic team, creating an amazing environment in which I could develop my skills and chase interesting questions and opportunities. Thank you for supporting me throughout.

Thank you to the school teachers who cumulatively built my love for learning. To Miss Offerdal for sowing a seed of a future interest by setting a project on ”Space”. To Mr. McKnight for opening paths which I would never have considered. To Mr. Elsden for providing unique opportunities throughout secondary school. And to the physics department, in particular Mr. Ridler, Mr. Saran and Mr. Rockett, for making physics fun and inspiring me to pursue it at university.

Thank you also to my family. To my Mom and Dad for being a fixed point throughout my life, happy to help in any way, and talk at a moment’s notice. To my brothers, Stewart and Russell, for keeping me grounded and inspired. And to my Grandparents for always being proud of me, and Nan for phoning each and every day in the early stages of the pandemic. They have all been incredibly supportive throughout my journey and I am grateful to them all.

And thank you to my friends who have supported me. They have kept me happy and motivated. In particular I am grateful to Connor for giving me an external perspective, always being excited about my project, and putting up with constant messages and memes. And thank you to my housemates for inspiring me, providing memorable experiences and creating a homely environment. Most of all, thank you to Anna and Hannah for being a constant throughout the PhD, and putting up with me during the bad moments while always being supportive and motivating me. Considering we met by chance, they have made the last four years what they were and I cannot imagine that time without them.

List of Supplementary Materials

The WACCM-X data created for this project has been made openly available at:

Brown, M. (2020): Thermospheric cooling under RCP8.5 due to carbon dioxide increases only, select years from 1975-2095. Centre for Environmental Data Analysis, 03 April 2020. https://doi.org/10.5285/0bb41477e0a5416190459433cb5ab907

Brown, M. (2022): Thermospheric cooling under RCP8.5 and high solar activity due to carbon dioxide increases only, select years from 1975-2095. NERC EDS Centre for Environmental Data Analysis, 12 January 2022. https://doi.org/10.5285/09198c58032d4b8197fd7c6748b92785

Thank you to all the scientists, software engineers, and administrators who contributed to the development of CESM and WACCM-X. And thank you to the Iridis High Performance Computing Facility, and associated support services at the University of Southampton.

The density scaling tables created from this data and used in the debris model are available at:

https://doi.org/10.5258/SOTON/D2114

Nomenclature

Acronym	
ACE-FTS	Atmosphere Chemistry Experiment Fourier Transform Spectrometer
ADR	Active Debris Removal
AR5	IPCC's Fifth Assessment Report
BRAD	Binned Representative Atmospheric Decay debris model
CAM	Community Atmosphere Model
CESM	Community Earth System Model
CHAMP	Challenging Minisatellite Payload
CIRA	COSPAR International Reference Models
CMAT2	Coupled Middle Atmosphere and Thermosphere model version 2
CONOPS	Concept of Operations
COPUOS	United Nation's Committee on the Peaceful Uses of Outer Space
COSPAR	Committee on Space Research
DAMAGE	Debris Analysis and Monitoring Architecture to the Geosynchronous Environment
DELTA	Debris Environment Long Term Analysis model
DISCOS	Database and Information System Characterising Objects in Space
DOY	Day of Year
DTM	Drag Temperature Model
ESA	European Space Agency
EUV	Extreme Ultraviolet radiation
GAMDM	Global Average Mass Density Model

GCM	General Circulation Model
GEO	Geostationary Earth Orbit
GITM	Global Ionosphere Thermosphere Model
GOES	Geostationary Operational Environmental Satellite
GRACE	Gravity Recovery and Climate Experiment
HEO	Highly Eccentric Orbits
HPC	High Performance Computing
IADC	Inter-Agency Space Debris Coordination Committee
ICP	Intrinsic Collision Probability
IGRF	International Geomagnetic Reference Field
IPCC	Intergovernmental Panel on Climate Change
IR	Infrared radiation
ISN	International Sunspot Number
ISS	International Space Station
J77	Jacchia atmospheric model, released in 1977 (similar for J60, J65, J70 and J71)
JB2008	Jacchia-Bowman 2008 thermospheric model
JSpOC	Joint Space Operations Center
LEGEND	LEO to GEO Environment Debris Model
LEO	Low Earth Orbit
MASTER	ESA's Meteoroid and Space Debris Terrestrial Environment Reference
MEDEE	Modelling the Evolution of Debris in the Earth's Environment debris model
MET-99	NASA Marshall Engineering Thermosphere 1999 model (similarly for MET-88 and MET-2007)
MLT	Mesosphere & Lower Thermosphere
MSIS	Mass Spectrometer and Incoherent Scatter radar atmospheric models
NASA	National Aeronautics and Space Administration

NCAR	National Center for Atmospheric Research
NDC	Nationally Determined Contributions
NOAA	National Oceanic and Atmospheric Administration
NORAD	North American Aerospace Defense Command
NRL	Naval Research Laboratory
NRLMSISE-00	Naval Research Laboratory's Mass Spectrometer and Incoherent Scatter Radar atmospheric model Extension to ground level, released in the year 2000.
ODPO	NASA'S Orbital Debris Programme Office
ODQN	Orbital Debris Quarterly News
PIB	Particles-in-a-Box debris model
PMD	Post Mission Disposal
ppm	Parts per million
RCP	Representative Concentration Pathway
SABER	Sounding of the Atmosphere using Broadband Emission Radiometry
SBM	NASA's Standard Breakup Model
SBUV	Solar Backscatter Ultraviolet spectrometer
SDM	Space Debris Mitigation
SEM	Solar Extreme-ultraviolet Monitor
sfu	Solar flux units
SGP4	Simplified General Perturbations propagator
SOHO	Solar and Heliospheric Observatory satellite
SSP	Shared Socioeconomic Pathway
STAT	Stochastic Analog Tool debris model
TGCM	Thermospheric General Circulation Model
TI-GCM	Thermosphere-Ionosphere General Circulation Model
TIE-GCM	Thermosphere-Ionosphere-Electrodynamic General Circulation Model
TIME-GCM	Thermosphere-Ionosphere-Mesosphere-Electrodynamic General Circulation Model

TIMED	Thermosphere Ionosphere Mesosphere Energetics Dynamics satellite
TLE	Two Line Element sets
UN	United Nations
UNCOPUOS	United Nations Committee on the Peaceful Uses of Outer Space
UV	Ultraviolet radiation
WACCM	Whole Atmosphere Community Climate Model
WACCM-X	Whole Atmosphere Community Climate Model eXtended
XRS	X-Ray Spectrometer

Symbol

$\bar{a}_{drag}$	Acceleration vector due to atmospheric drag
$\bar{v}$	Velocity vector
μ	Standard gravitational parameter
Ω	Right ascension of ascending node
ω	Argument of perigee
ρ	Atmospheric neutral mass density
θ	True anomaly
A	Cross-sectional area
a	Semi-major axis
A_p	Daily average geomagnetic activity index
a_p	3-hourly geomagnetic activity index
C_D	Coefficient of drag
E	Eccentric anomaly
e	Eccentricity
G	Gravitational constant
H	Atmospheric scale height
h	Altitude (geopotential in density section, alt in Saunders
i	Inclination

K_p	3-hourly geomagnetic activity index
k_q	CO_2-O quenching rate (collisional deactivation rate)
L_c	Characteristic length (in SBM model)
M	Mean anomaly
m	Mass of object
n_M	Mean motion
P	Atmospheric Pressure
R	Universal gas constant
r_E	Earth radius
T	Temperature
T_P	Orbital Period
z	Geometric altitude
F10.7	Solar flux at a wavelength of 10.7 cm
r	Radius of satellite (assuming circular cross-section)

Chapter 1

Introduction

Carbon dioxide emissions are causing significant changes to the Earth system[1], with global warming and climate change being well known manifestations. The atmosphere plays a key role in the Earth system. The lowest parts of the atmosphere directly impact humanity as well as ground-level Earth systems such as vegetation and oceans. As a result, the majority of atmospheric research has focused on this lower region. However, the atmosphere extends thousands of kilometres above this, decreasing in density with altitude until it fades into the vacuum of outer space.

Satellites orbiting Earth travel through this thin upper atmosphere. As they do, they experience atmospheric drag which slowly reduces their altitude until they burn up in the thicker, lower atmosphere. Over the last few decades, technological advancements and interest in the unique opportunities satellites provide have also seen an increasing number of launches into space, with the number of satellites increasing. Alongside this, the leftovers from missions such as rocket bodies, dead satellites, and the fragments from collisions have also built up over time. Known as space debris, these present a risk to active satellites.

Previous simulations and observations have focused on the historical upper atmospheric density changes. Emmert (2015a) reviewed these studies and found each study reported decreasing trends in upper atmospheric densities as carbon dioxide concentrations increased. Further studies published since have agreed with these results. However, little research has been performed looking at predicting how densities could decrease in the future. This thesis will quantify by how much carbon dioxide emissions can reduce the density of the upper atmosphere over the next century, and how the reductions are dependent upon altitude and the Sun's activity.

The decreasing atmospheric density will result in less atmospheric drag on orbiting objects, including space debris. Atmospheric drag is a critical mechanism for

[1]The Earth system is the interaction between the physical, chemical and biological processes across all regions of the Earth's surface and atmosphere.

removing objects from orbit, so the reduction in density is already having a quantifiable effect by increasing orbital lifetimes. To investigate the impact on the space debris environment, the results from the atmospheric modelling will be incorporated into a new debris model. Four scenarios commonly used in climate change modelling, namely the Representative Concentration Pathways (RCPs), will be used to define four possible future carbon dioxide emissions. The thesis will then explore how the debris environment evolves within each of these scenarios.

Chapter 2

Theory

As the thesis crosses two disciplines, this chapter will give the background theory from which the current literature can be explored from either research area. The structure also flows from this, first exploring the atmosphere and the models used to simulate it. Further background reading on atmospheric physics is provided by Rees (1989). Finally, an introduction to space debris and orbital mechanics is presented, with further background provided by Klinkrad (2006) and Montenbruck and Gill (2005).

2.1 The Atmosphere

2.1.1 Atmospheric Layers

The atmosphere can be separated into five different regions, with the boundaries between the lowest four defined by the local maxima and minima in the vertical temperature profile, with this shown in Figure 2.1. Atmospheric density also decreases with altitude, and this is shown in Figure 2.2. Atmospheric scale height, H, is a measurement of the altitude over which the atmospheric density reduces by a factor of $1/e$, and is given by

$$H = \frac{kT}{mg} \tag{2.1}$$

where k is the Boltzmann constant, T is temperature, m is the mean mass of a molecule, and g is acceleration due to gravity. In the upper atmosphere, the atmospheric scale height increases with altitude as the temperature increases and the mean molecular mass decreases. As a result, density continues to decrease with increasing altitude, but at a slowing rate of change.

The majority of research on atmospheric climate change has focused on the troposphere, the densest and lowest section of the atmosphere. Ground-based

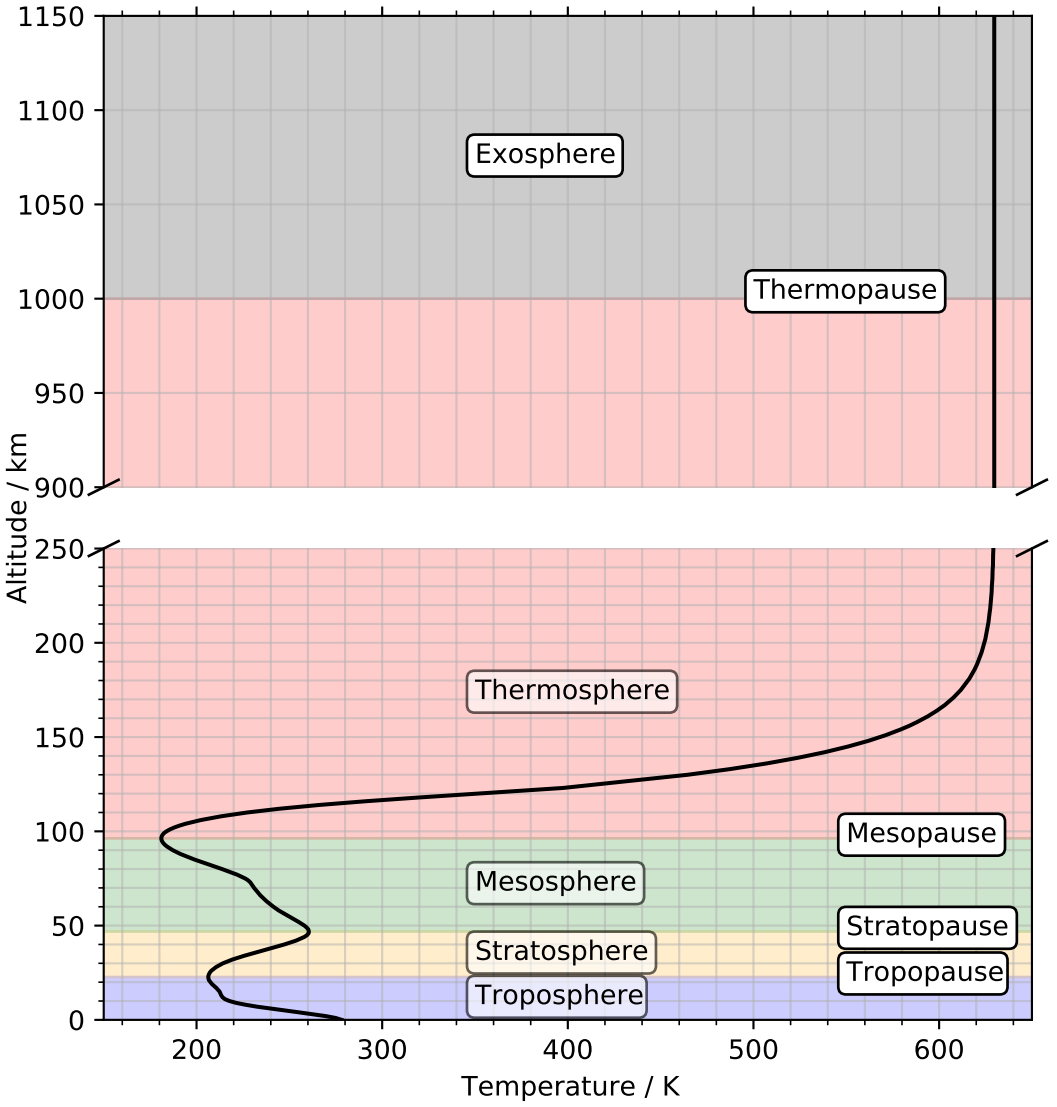

FIGURE 2.1: Temperature profile of Earth's atmosphere with increasing altitude, with the layers of the atmosphere and boundaries between named. Exact altitudes of boundaries vary with input energy. Created with NRLMSISE-00 for midnight on 1st January 2000 at 50.9° latitude and -1.4° longitude (Southampton, UK) with historic F10.7 and Ap values.

greenhouse gas emissions immediately enter the troposphere upon release, and the oceans and forest at its base act as sinks and sources for heat and carbon dioxide. The majority of heating is caused by visible light from the Sun. This in turn heats the atmosphere near the ground, slightly reducing its density and causing convection within the troposphere.

The stratosphere sits above the troposphere, with the embedded ozone layer playing a key role in the chemistry of the region. Oxygen (0_2) molecules from the troposphere can be broken down into atomic oxygen by ultraviolet (UV) radiation in a process known as photodissociation. The atomic oxygen (O) can then bond with molecular

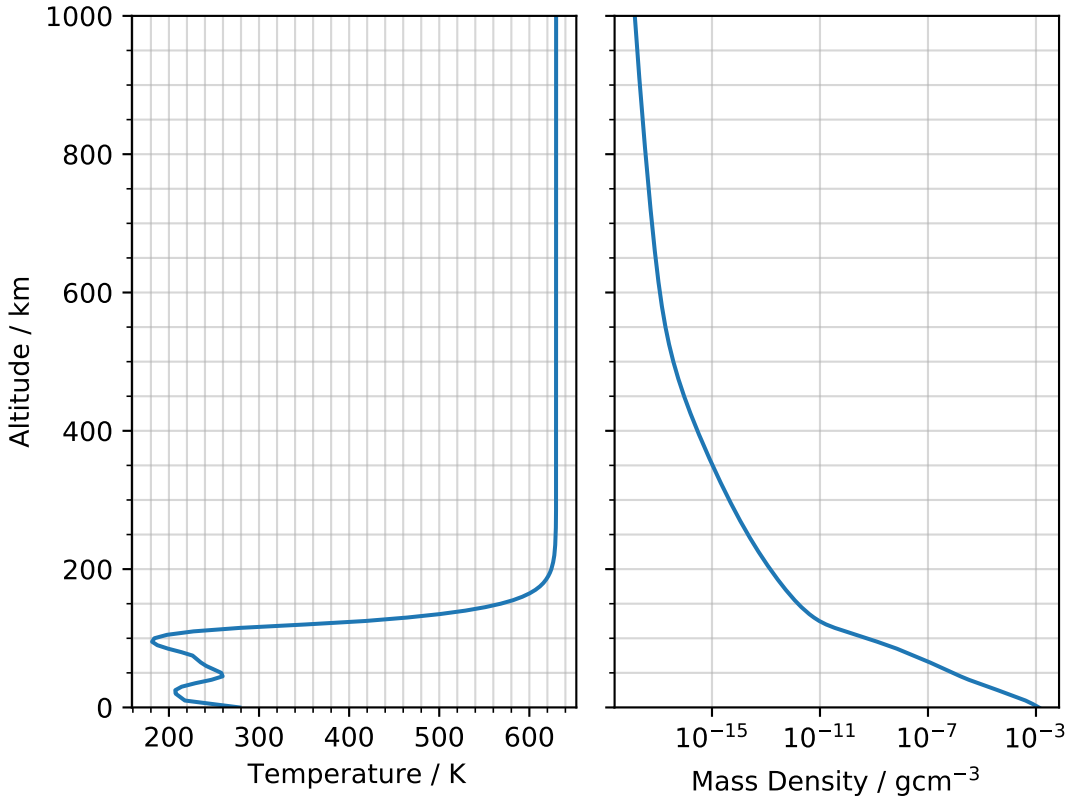

FIGURE 2.2: Atmospheric mass density and temperature profiles from the NRLMSISE-00 atmospheric model, with this model described in Section 2.2.2.3. This example is for midnight on 1st January 2000 at 50.9° latitude and -1.4° longitude (Southampton, UK) with historic F10.7 and Ap values.

oxygen to form ozone (O_3). Above the ozone layer, atomic oxygen is more common than its molecular counterpart. The mesosphere is the third atmospheric layer and the beginning of the upper atmosphere, where the thin atmospheric densities allow the Sun's UV and Extreme UV (EUV) radiation to penetrate the atmosphere, causing ionization and dissociation, releasing energy and radiatively heating this region and those above.

The troposphere, stratosphere and mesosphere approximately coincide with the homosphere. Turbulent mixing within the homosphere keeps the concentration of each chemical constituent relatively uniform with altitude until the homopause is reached at around 90-120 km, with the altitude varying with constituent species and local dynamical conditions. In the upper part of the atmosphere, beginning in the thermosphere, vertical diffusion takes over and the chemical constituents separate out via gravity, with each constituent following its own concentration profile. These profiles are dependent upon energy input from the Sun, and also molecular mass of the constituent as heavier chemicals sink towards the homopause. Temperatures in

the thermosphere increase with altitude towards an asymptotic limit, commonly known as the exospheric temperature.

The exosphere is the highest part of the atmosphere. Its lower boundary, the thermopause, marks the point at which the mean free path of an atom is equal to the atmospheric scale height (Akmaev (2011)). As the lightest constituents escape the Earth's gravitational influence, the atmospheric density decreases further with altitude, reducing to the near-vacuum of space where it is hard to distinguish the rarefied hydrogen and helium from the Earth's atmosphere from the same elements released by the Sun in solar wind.

Alongside the five neutral regions of the atmosphere is the charged region. The ionosphere is made up of the ionized atoms within the atmosphere, and is embedded within the mesosphere, thermosphere and exosphere. Charged particles interact with the Earth's magnetic field, trapping them within the atmosphere as they travel back and forth along magnetic field lines. The low atmospheric density allows ions to travel for relatively long periods of time before encountering and reacting with other species. The ionosphere is constantly replenished by photo-ionization and the solar wind.

2.1.2 Carbon Dioxide in the Upper Atmosphere

Turbulent mixing in the homosphere ensures a relatively constant concentration of carbon dioxide (CO_2) from ground level to the homopause (as seen in Figure 2.3). The ground level concentration sees small periodic variations on the order of a year due to the carbon cycle, as sources and sinks such as the oceans and organic biomass vary with the seasons (Friedlingstein et al. (2020)). Smaller variation is seen with increasing altitude within the homosphere due to the turbulent-mixing and the time taken for the carbon dioxide to propagate upwards. Above the homopause, where molecular diffusion dominates, the concentration drops rapidly with altitude in the first 70 km, and then tends towards 0 ppm above this. This is due to both carbon dioxide being a relatively heavy constituent in the upper atmosphere, as well as the increased levels of EUV radiation at higher altitudes leading to increased rates of photodissociation, breaking down the carbon dioxide into carbon monoxide and atomic oxygen (Kaufmann et al. (2002)). Carbon Dioxide concentrations within the mesosphere and lower thermosphere have been measured with both the Atmosphere Chemistry Experiment Fourier Transform Spectrometer (ACE-FTS) and Sounding of the Atmosphere using Broadband Emission Radiometry (SABER) instruments on board Science Satellite 1 (SCISAT-1) and the Thermosphere Ionosphere Mesosphere Energetics Dynamics (TIMED) satellites respectively. Qian et al. (2017) shows both instruments measured increasing CO_2 concentrations in these regions from the year 2002 to 2016.

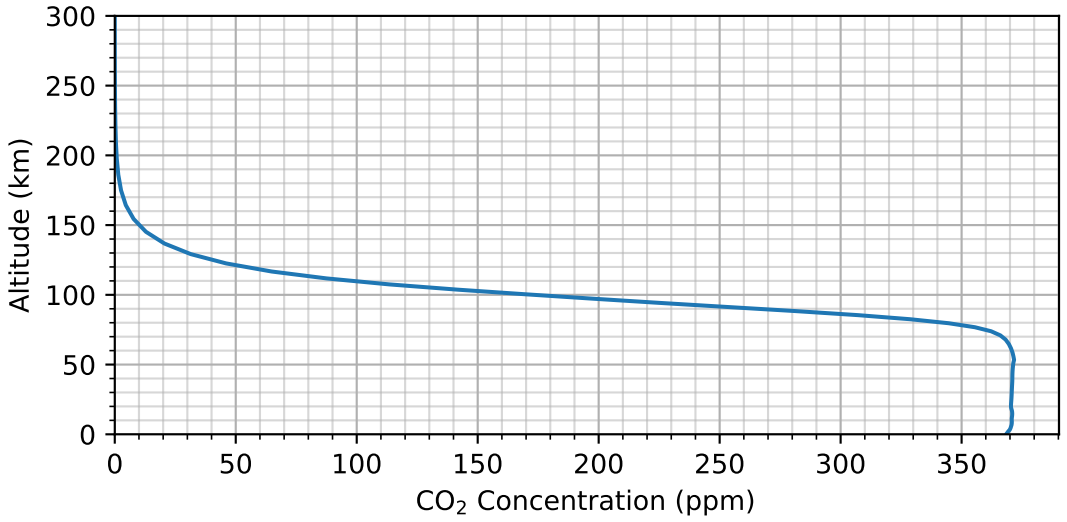

FIGURE 2.3: Example altitude profile of carbon dioxide concentration for the year 2000. Global average of the default WACCM-X initial files for the year 2000.

Anthropogenic carbon dioxide emissions at ground level have caused an observable increase in the carbon dioxide concentration in the troposphere, with the ground-level concentration plotted for the last millennium in Figure 2.4. This also leads to CO_2 concentrations above the homopause increasing over time.

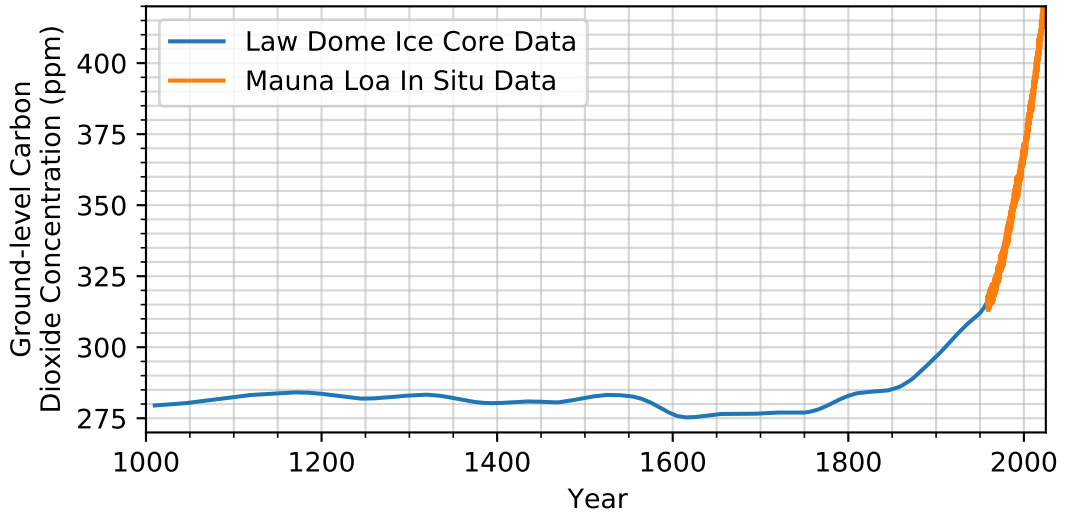

FIGURE 2.4: Ground-level carbon dioxide mixing ratio over the last millennium, with 75-year smoothed data from ice cores via Etheridge et al. (1998) and weekly in-situ measurements at Mauna Loa from Keeling et al. (2005)

The greenhouse effect causes global warming in the lower atmosphere below around 15 km in altitude. CO_2 molecules gain energy by collisional excitation or by absorption of infrared (IR) radiation, and lose energy via molecular collisions or emitting IR radiation at 15 μm (Sharma and Roble (2002)). In the lower atmosphere,

the emitted IR radiation is quickly reabsorbed by other atmospheric constituents, which along with the frequent collisions, traps the energy and heat in the locality. In the upper atmosphere, the same mechanisms occur, but the thinner atmosphere causes global cooling instead (Akmaev and Fomichev (1998), Roble and Dickinson (1989)). This is due to collisions being much less frequent, making IR emission much more likely to occur. The mean free path of this radiation is much larger through the less dense atmosphere, allowing the energy and heat to escape to the lower atmosphere or space. As the upper atmosphere cools, it contracts to maintain hydrostatic equilibrium[1]. As a result, the atmospheric density drops at a fixed altitude.

2.1.3 The Solar Cycle

The Sun and its solar cycle play a fundamental role in the heating of the upper atmosphere. The solar cycle has a mean period of 11 years with solar activity reaching a cycle-varying maximum before returning to a minimum. Increased solar activity sees the Sun emit more EUV and X-ray radiation, heating the upper atmosphere and resulting in an order of magnitude change in density, as shown in Figure 2.5.

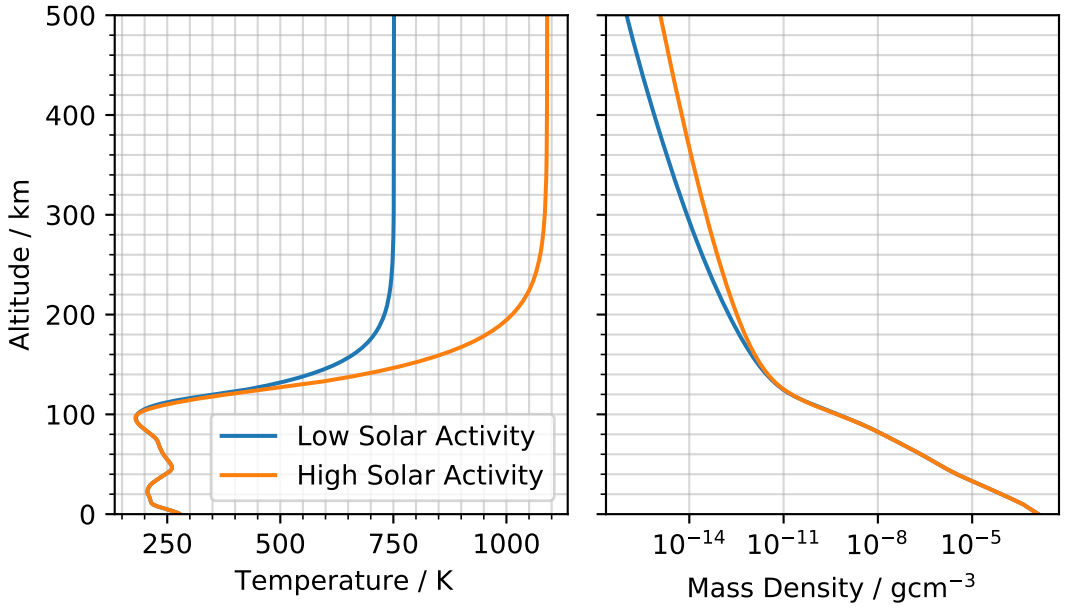

FIGURE 2.5: Similar to Figure 2.2, created with NRLMSISE-00 for Southampton at midnight on 1st January 2000, but with the blue line showing low solar activity (F10.7 = 70 sfu) and orange showing high solar activity (F10.7 = 200 sfu).

The number of sunspots on the Sun's surface, known as the International Sunspot Number (ISN), acts as a proxy for solar EUV emission. Its long historical archive

[1]Hydrostatic equilibrium exists at a given altitude when the weight of the atmosphere above that altitude is equal to the upwards force of pressure from the atmosphere below.

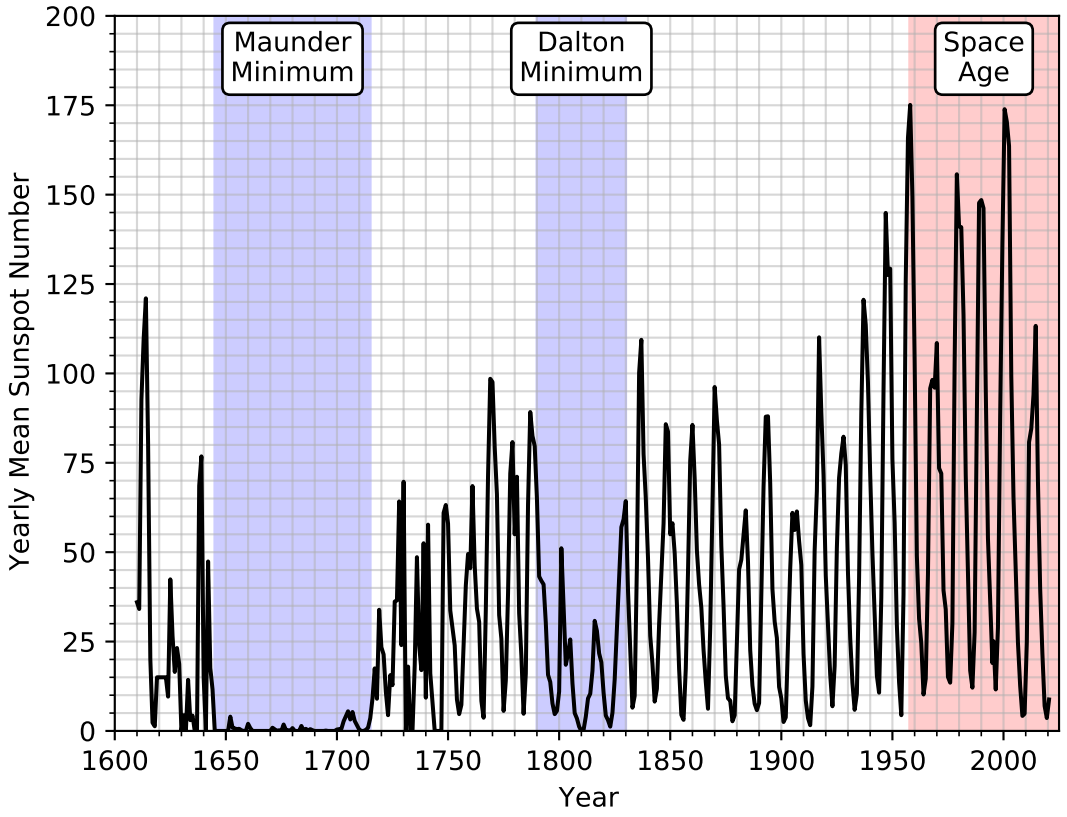

FIGURE 2.6: Yearly mean International Sunspot Numbers with periods of interest highlighted. Data obtained from SILSO World Data Center (2021).

dating from 1610 is shown in Figure 2.6 and allows for study of many solar cycles. The record reveals an extended period of low solar activity from 1645 to 1715, named the Maunder minimum. The long-term variability in the peak activity at solar maxima is also evident, with two successive low peaks during the early 19th century (the Dalton minimum), and a series of relatively high peaks during the late 20th century. The variability in solar cycle length is also evident, for example in the extended cycles of the Dalton minimum.

2.2 Atmospheric Models

Objects orbiting within Low Earth Orbit (LEO) have altitudes below around 1200 km and experience a significant atmospheric drag force[2]. The neutral atmospheric density determines the magnitude of this force, and is explored in greater detail in Section 2.5.3. Atmospheric modelling is a key part of orbital propagation in the LEO

[2]The altitude of LEO varies depending upon the context or author. For example, ESA Space Debris Office (2020) labels the highest altitude as 2000 km. However spacecraft at these altitudes experience significantly lower neutral densities, and forces causing orbital perturbations other than atmospheric drag are orders of magnitude greater

environment, both to know an object's position in the short-term for collision avoidance, but also in the long-term for environment modelling. While basic orbital propagation requires only neutral density, different models can provide other output variables useful for space applications, for example, atomic oxygen concentrations to calculate material ablation rates, or charged particle fluxes to estimate the impact on electronic circuitry. This section will briefly cover the key, common inputs to atmospheric models, along with descriptions of the atmospheric models used within this thesis and referred to within the Literature Review.

2.2.1 Common Inputs

All of the atmospheric models described in this section take input parameters, primarily to describe the location of interest and how much heat is currently in and being absorbed by the upper atmosphere. While different models can take a wide variety of inputs, the common variables will be discussed in this section. Due to intra-annual variations in the upper atmosphere, the day of the year (sometimes shortened to DOY) is often used, while the time of day is used to account for daily variations in solar heating. The position of interest is also key, and is defined by the latitude, longitude and altitude. Alongside these common inputs, there are the solar activity index, F10.7 cm radio flux, and the geomagnetic activity indices, Ap and Kp, which will be discussed in this section.

2.2.1.1 Solar Activity (F10.7)

F10.7 is a measurement of the disc-integrated flux from the Sun at a wavelength of 10.7 cm, with units often given in solar flux unit (sfu), where 1 sfu is equivalent to 10^{-22} $\mathrm{Wm^{-2}Hz^{-1}}$ (Tapping (2013)). The 10.7 cm wavelength is in the radio spectrum, but acts as a reliable and easily measurable proxy for solar EUV radiation, with observational records dating back to 1947. It provides a robust index which covers the entire space age, providing models an uninterrupted proxy with which to quantify energy input into the upper atmosphere.

The daily F10.7 data for the last five solar cycles is plotted in Figure 2.7, which highlights the daily variability in the magnitude of the Sun's EUV activity, especially during solar maxima. To better capture longer-term heating and ionospheric variations, atmospheric models also use averages multiple days in length and centred on the day of interest. The most common are 27 and 81 day averages (Girazian and Withers (2015)). The Sun takes an average of 27 days to complete one rotation around its axis, leading to the 27 day average, while the 81 day average provides longer term smoothing over three rotations.

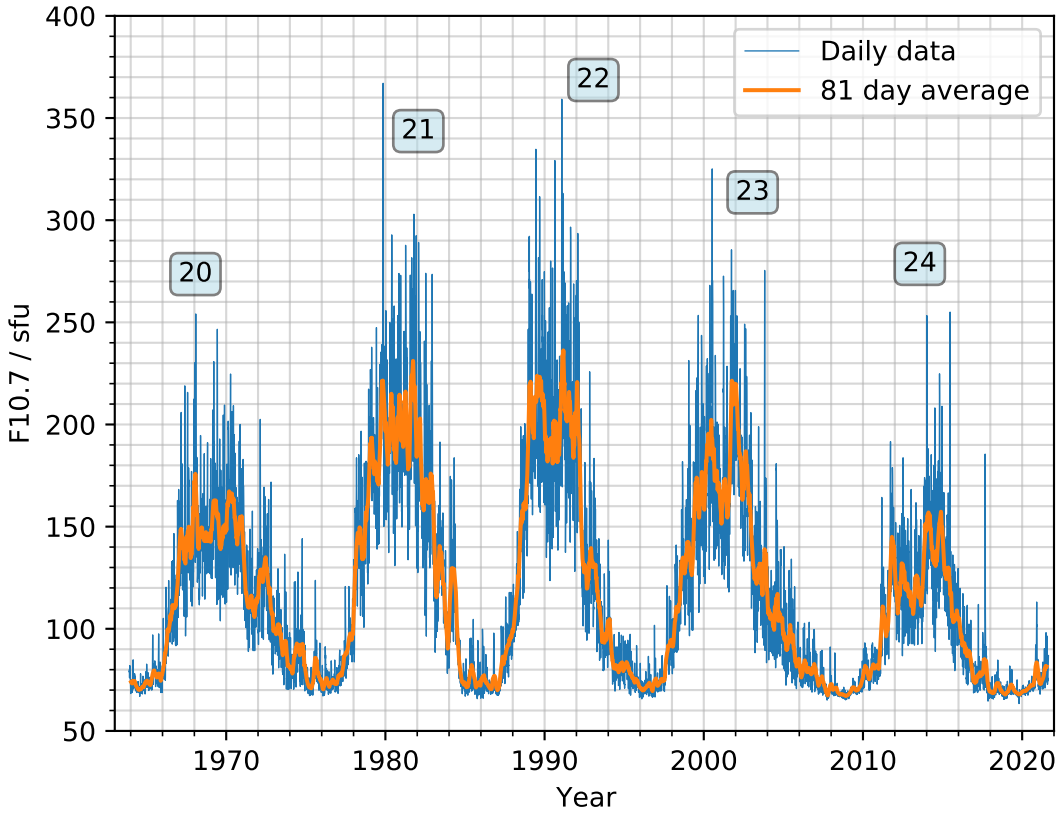

FIGURE 2.7: Daily and 81 day centred averaged F10.7 data available from Goddard Space Flight Center (2021). Cycle numbers are included near the associated cycle's peak.

The International Sunspot Number was presented in Section 2.1.3 and shown in Figure 2.6. It is a less objective measure of solar EUV emission than F10.7 due in part to the earliest data relying on rudimentary telescopes and astronomers counting sunspots by eye. However, the magnitude and periodicity of its peaks is highly correlated with F10.7, with this shown over the last five solar cycles in Figure 2.8. The long historical archive dating back to 1610 highlights some possible scenarios for F10.7 in the future, in particular the extended period of low solar activity known as the Maunder minimum. The Space Age occurred during a period of relatively high solar activity.

2.2.1.2 Geomagnetic Activity (Ap and Kp)

Earth's magnetic field is primarily created from sources within the Earth's core. Charged particles moving within the ionosphere superimpose small fluctuations upon this magnetic field. As the Sun becomes more active, increased electromagnetic radiation ionizes more atoms, and more ions are added to the ionosphere via the solar wind. This increases the size of the magnetic fluctuations, and so measuring

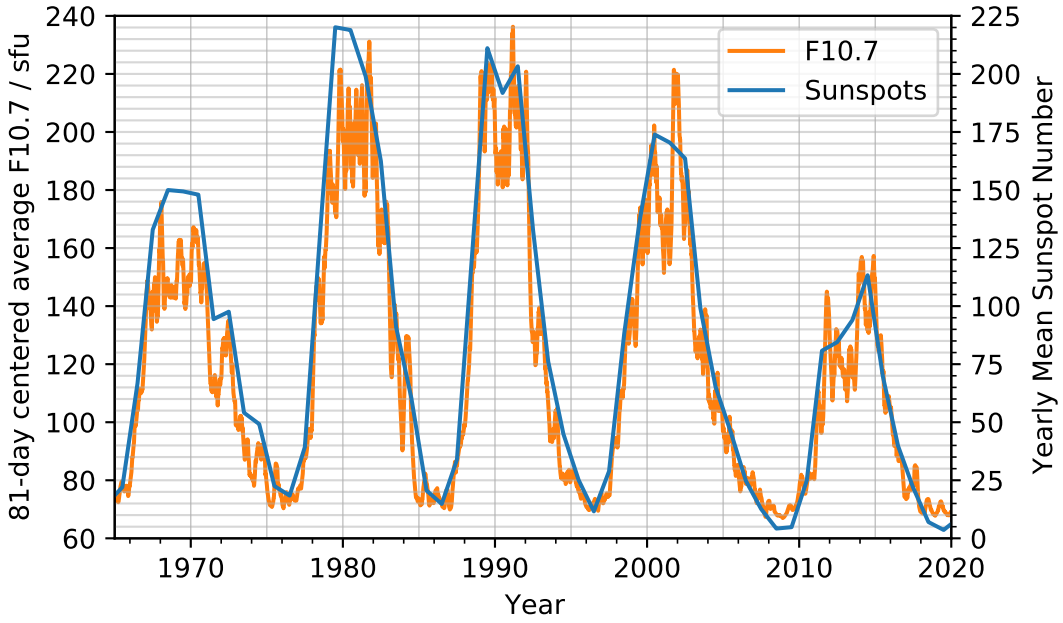

FIGURE 2.8: Yearly mean sunspot numbers and 81-day centered averaged F10.7 of the last five solar cycles plotted against each other.

geomagnetic activity can act as a proxy for solar activity, with this covered in more detail by Dieminger et al. (1996).

Ap and Kp are two related geomagnetic indices measuring magnetic activity within the ionosphere, and can be used to describe the state of the magnetosphere. Kp is a 3-hourly index ranging from 0 (low) to 9 (high) and is the mean standardized K-index measured in 13 mid-latitude locations (Bartels et al. (1939); Bartels and Veldkamp (1949)). A slightly finer scale of thirds is often denoted through use of the symbols -, o, and +, such that 1- is 2/3, 1o is 1, and 1+ is 4/3. Kp decimal values are often used within models rather than the symbol notation.

Ap is the daily average geomagnetic activity and uses a linear scale, from 0 (low) to 400 (high). A 3-hourly variation can be obtained, named ap, by converting Kp to the new scale, as shown in Table 2.1.

2.2.2 Empirical Atmospheric Models

The empirical atmospheric models are based on parametric equations which have been fitted to observational data, taking inputs such as solar activity, latitude, longitude, altitude, time of year, and at their most basic, outputting the neutral density and temperature. They have extremely fast execution times, making them the ideal solution for obtaining densities when fast execution is important.

TABLE 2.1: Kp, Kp decimal and ap conversion table.

Kp	Kp (decimal)	ap
0o	0.00	0
0+	0.33	2
1-	0.67	3
1o	1.00	4
1+	1.33	5
2-	1.67	6
2o	2.00	7
2+	2.33	9
3-	2.66	12
3o	3.00	15
3+	3.33	18
4-	3.67	22
4o	4.00	27
4+	4.33	32
5-	4.66	39
5o	5.00	48
5+	5.33	56
6-	5.67	67
6o	6.00	80
6+	6.33	94
7-	6.66	111
7o	7.00	132
7+	7.33	154
8-	7.67	179
8o	8.00	207
8+	8.33	236
9-	8.67	300
9o	9.00	400

2.2.2.1 Jacchia Models

Jacchia (1960) laid the groundwork for many of the later upper atmospheric models with the first empirical model of neutral densities and scale heights in the thermosphere. It was based on the drag-derived density data obtained from some of the earliest satellites that were launched, and the method for deriving these densities will be explored further in Section 3.1.2. The model was revised by Jacchia (1965), which sets out equations defining the temperature and density profiles for each major atmospheric constituent at a given exospheric temperature, as well as deviations from the given profile due to geomagnetic, seasonal and latitudinal effects. Formulae to calculate the exospheric temperature from F10.7 are also included within the model. Lower boundary conditions were set at the model base of 120 km altitude, and upper boundary conditions at 2500 km. Jacchia (1970) lowered the model base to 90 km altitude, as well as increasing the atomic oxygen to molecular oxygen number density ratio, ($n(O)/n(O_2)$), compared to the previous model. Jacchia (1971) increased the

number density ratio further. Finally in the Jacchia series of models, Jacchia (1977) addressed and reproduced the in-situ measurements of Nitrogen (N_2) and Atomic Oxygen (O) concentrations from the Orbiting Geophysical Observatory 6 (OGO 6) satellite. The name of each Jacchia model is commonly shortened to J60, J65, J70, J71 and J77 respectively.

The Jacchia-Bowman models, JB2006 and JB2008, are described fully by Bowman et al. (2007, 2008) and are empirical models based on Jacchia's diffusion equations (Jacchia (1971)). Both models uniquely use additional solar indices to the common F10.7, in an effort to better characterize the energy being input into the atmosphere by the Sun. Tobiska et al. (2008) details how 15 potential indices and proxies were narrowed down to the three used in JB2006. These are F10.7 (see section 2.2.1.1), $S_{10.7}$, an index of the EUV output measured at 26-34 nm by the Solar Extreme-ultraviolet Monitor (SEM) onboard the Solar and Heliospheric Observatory (SOHO), and $M_{10.7}$, an index of the photospheric continuum and chromopsheric MgII h and k line emissions at 279.56 and 280.27 nm respectively, as measured by the Solar Backscatter Ultraviolet (SBUV) spectrometer onboard National Oceanic and Atmospheric Administration (NOAA) satellites, namely NOAA-16 and NOAA-17. Additionally, JB2008 uses $Y_{10.7}$, an index created from measurements of X-ray emission at 0.1-0.8 nm in the corona, as made by the X-ray Spectrometer (XRS) onboard the Geostationary Operational Environmental Satellite (GOES). Each of the new indices is normalised to F10.7, hence the 10.7 subscripts. While the use of these indices intends to better capture solar irradience, Dudok de Wit and Bruinsma (2011) identified that there was no improvement from using multiple indices compared to just using the EUV flux in the 26-34 nm band from SEM onboard SOHO alone. The future use of the proxies, and potentially the model without refitting, is also intrinsically tied to the lifetime of the SOHO, GOES, and NOAA satellites, and/or the calibration and continuation of their instruments on newly launched satellites.

The Marshall Engineering Thermosphere 1988 (MET-88) model, as detailed by Hickey (1988a), is NASA's implementation of the equations within the J70 and J71 models. However, MET-88 had an unreliable integration algorithm, detailed by Hickey (1988b). An updated version correcting the integration issue was created, namely MET-99 of Owens et al. (2000). Further development has taken place, specifically with the release of the MET Version 2.0 (MET-V 2.0) of Owens and Vaughan (2003), and the MET-2007 model of Suggs and Suggs (2017), both adding further variations originally detailed in J71.

2.2.2.2 Drag Temperature Models (DTM)

The Drag Temperature Models (DTM) are a series of thermospheric models created within the French space agency, Centre National d'Études Spatiales (CNES), and are

described in full detail by Barlier et al. (1978); Berger et al. (1998); Bruinsma et al. (2003, 2012); Bruinsma (2015); Bruinsma and Boniface (2021). They are empirical models fitted primarily using orbit-derived densities (which will be discussed in more detail in Section 3.1.2). Newer versions now include accelerometer-derived density (see Section 3.1.2) and in-situ mass spectrometer data too.

2.2.2.3 Mass Spectrometer and Incoherent Scatter (MSIS) Models

Hedin et al. (1977a) and Hedin et al. (1977b) detailed the first Mass Spectrometer & Incoherent Scatter radar (MSIS) model, named MSIS-77. This empirical model covering the upper thermosphere modelled N_2, O, He, Ar, O_2, and H concentrations, and was based on the neutral N_2 density measurements of five satellite-based mass spectrometers (including the OGO 6 data also used in J77), and four ground-based incoherent scatter radars. The next two versions of the model (MSIS-83 of Hedin (1983) and MSIS-86 of Hedin (1987)) added more of these data sources, new sounding rocket data, atomic nitrogen profiles and the lower thermosphere, as well as improving the mathematical descriptions of geomagnetic and seasonal variations. MSISE-90 of Hedin (1991) then extended the lower boundary from $\sim$85 km to ground level to include the middle and lower atmosphere.

The Naval Research Laboratory Mass Spectrometer & Incoherent Scatter radar model (NRLMSISE-00) detailed by Picone et al. (2002) was then released, featuring major upgrades over MSISE-90. NRLMSISE-00 has become one of the more widely used empirical thermospheric models. This version added drag-derived densities from the period 1960 to around 1974 (similarly to the J77 model), and added anomalous oxygen profiles to account for O^+ ions and hot atomic oxygen, both of which were shown to impact satellite drag estimation above 500 km. An example output of the atmospheric constituents (O, N_2, O_2, He, Ar, H and anomalous oxygen) within NRLMSISE-00 is given in Figure 2.9. Mass density and neutral temperature are also outputs and have been shown in Figure 2.2

A new version, NRLMSIS 2.0 has recently been released, with the improvements described fully by Emmert et al. (2021). New data has been added into the model, notably with new orbit-derived density data covering the period 1986-2005 from 400 to 575 km taken from the study by Emmert (2015b). There are plans to add the long-term secular decrease in thermospheric density due to carbon dioxide emissions in a future release.

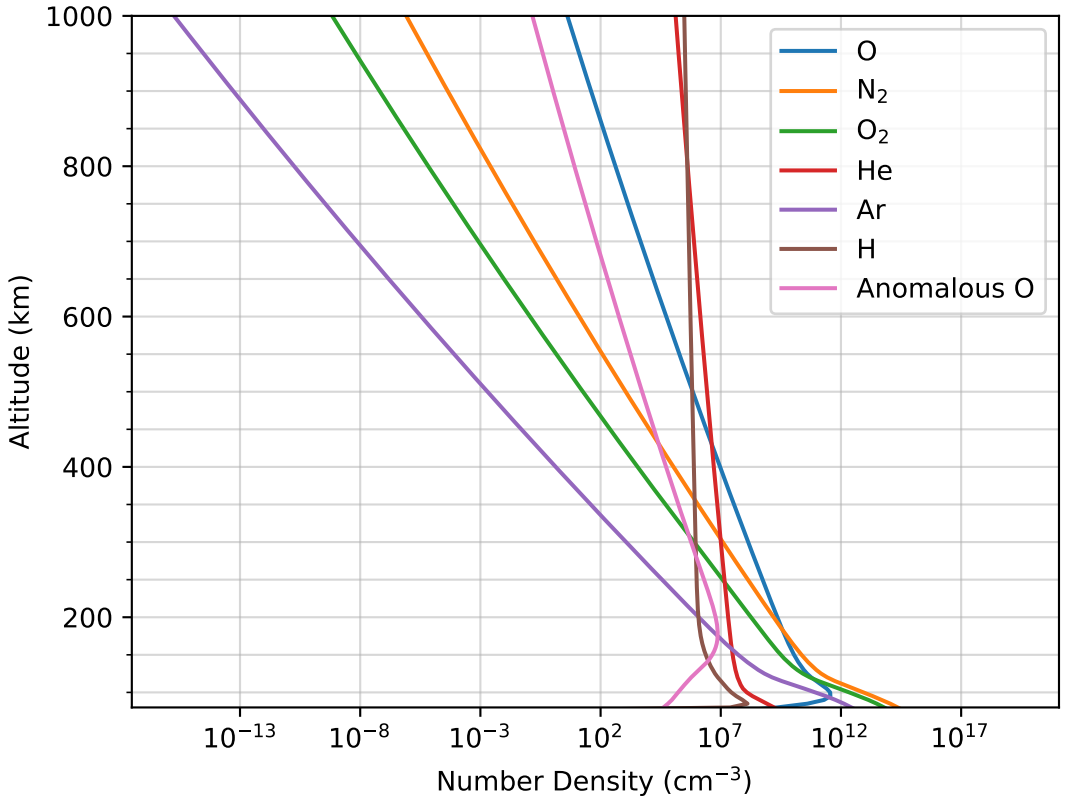

FIGURE 2.9: NRLMSISE-00 constituent number density profiles from 70 to 1000 km. This example is for midnight on 1st January 2000 at 50.9° latitude and -1.4° longitude (Southampton, UK) with historic F10.7 and Ap values

2.2.2.4 Global Average Mass Density Model (GAMDM)

Emmert and Picone (2010) described the first Global Average Mass Density Model (GAMDM), an empirical density model based on the densities derived from the orbital data of 5000 objects in the Two Line Element (TLE) catalogue[3] over the period 1967 to 2007. Unlike other empirical models which give the density as a function of latitude and longitude, GAMDM inherently gives the global average atmospheric density so only altitude is required as a positional input. The day of the year is also the only temporal input, so the model returns daily-mean atmospheric densities.

A new version, GAMDM2.0, is described by Emmert et al. (2014), which includes improved temporal smoothing of solar and geomagnetic activity. The same period of data is used (1967 - 2007), but a secular trend is added to account for the decreasing densities caused by increasing ground-level CO_2 concentration. This trend is modulated by geomagnetic activity (via Kp) only and not solar activity.

[3]TLEs are discussed in Section 2.6

2.2.3 General Circulation Models

Most General Circulation Models (GCMs) divide the atmosphere into cells, simulating the underlying chemistry, physics and dynamics within each cell along with the heat, chemical and bulk fluxes between each of its neighbouring cells. The simplest and earliest versions of this type of model were 1 dimensional, with cells defined in altitude only. Boundary conditions are imposed at the lowest and highest altitudes to best describe the expected surroundings. Three dimensional GCMs are more common nowadays, adding latitude and longitude to the grid which allows for modelling of global variations in temperature, density and composition, as well as winds and seasonal variations.

To simplify calculations, the vertical component of cells is often calculated in discrete pressure levels of hydrostatic equilibrium. As a result, these levels vary in altitude with both time and location. When working directly with altitudes, for example with satellite orbits, interpolation of the data is required between the pressure levels.

Due to the complexity of GCMs, their run-times are much longer than those of empirical models and are dependent upon both the length of time step and the size of cells. While finer cell size leads to higher resolution, it also increases run-time. Phenomena that act on scales smaller than the cells, for example gravity waves, have to be parameterized and applied to the cells separately.

2.2.3.1 NCAR Thermospheric General Circulation Models (TGCMs)

The National Center for Atmospheric Research (NCAR) released a series of Thermospheric General Circulation Models (TGCMs) which have had further parts of the upper atmosphere added with each new model. The first was the Thermosphere General Circulation Model (TGCM), described by Dickinson et al. (1981). The ionosphere was then added in the coupled Thermosphere-Ionosphere General Circulation Model (TI-GCM) covering 97 to 700 km altitude, and described by Roble et al. (1988). TI-GCM was used to find the impacts a doubling of CO_2 concentration would have in the upper atmosphere for the first time, as detailed by Roble and Dickinson (1989), Rishbeth (1990), and Rishbeth and Roble (1992). The Thermosphere - Ionosphere - Electrodynamic General Circulation Model (TIE-GCM) described by Richmond et al. (1992) added to TI-GCM by including electrodynamical effects. The most recent of the TGCMs, the Thermosphere - Ionosphere - Mesosphere - Electrodynamic GCM (TIME-GCM) of Roble and Ridley (1994) reduced the model's lower boundary from 97 to 30 km to include the mesosphere and upper stratosphere.

2.2.3.2 CESM and WACCM-X

The Community Earth System Model (CESM) is an NCAR model described by Hurrell et al. (2013). It acts as a coupler, passing fluxes and variables between geophysical models, with each individual component focusing on a different part of the Earth system. The main systems and their default models are:

- The atmosphere with the Community Atmosphere Model (CAM)
- The land with the Community Land Model (CLM)
- Rivers with the River Transport Model (RTM)
- Oceans with the Parallel Ocean Program (POP)
- Sea-ice with the sea-ice component (CICE)
- Land-ice with an extension of the Glimmer ice sheet model (CISM)

Each of these can be replaced with other models which focus on specific areas of interest within the system. Alternatively, stub components can be used which satisfy the coupler and interface requirements by introducing boundary conditions and not modelling the system.

While CAM is the default atmospheric model within CESM, it only models the troposphere and part of the stratosphere. The Whole Atmosphere Community Climate Model (WACCM), detailed by Marsh et al. (2013), added modelling of the entire stratosphere and mesosphere, reaching up to around 140 km altitude. The thermosphere and ionosphere was then added in the Whole Atmosphere Community Climate Model eXtended (WACCM-X), raising the maximum altitude up to around 600 km (Liu et al. (2010)). Each of these models is built upon the last, adding to the chemistry and physical modelling of the lower sections of the atmosphere.

WACCM-X tracks around 50 major atmospheric constituents, with their concentrations changing through over 220 possible simulated chemical reactions. By default, WACCM-X has a resolution of 1.9° latitude by 2.5° longitude, with 81 pressure levels from ground level to 2.5×10^{-9} hPa, with each pressure level in the upper atmosphere separated by half the scale height. The upper boundary of WACCM-X is in the part of the thermosphere where atomic oxygen is dominant, rather than the helium or hydrogen dominated part (see Figure 2.9 which shows how these regions dominate at different altitudes for a specific example scenario).

WACCM-X 2.0 has been released concurrently with CESM2, with the two models detailed by Danabasoglu et al. (2020) and Liu et al. (2018) respectively. WACCM-X 2.0 contains improvements to the momentum and energy equation solvers within the

thermosphere, improvements to the solving of ionospheric dynamics, and much more. The work done in this thesis used WACCM-X version 1.2.2 as WACCM-X 2.0 was not available at the start of the project.

2.3 Representative Concentration Pathways (RCPs)

Modelling anthropogenic carbon dioxide emission and atmospheric concentrations into the future is extremely challenging. It requires, for example, assumptions about how emissions will be tackled on global and regional scales, the technological advancements that may happen in the future, how economics will change land use and emissions targets, and much more. To try to tackle this issue of future modelling, the Intergovernmental Panel on Climate Change (IPCC) released Representative Concentration Pathways (RCPs) as part of its fifth Assessment Report (AR5) (IPCC (2014)). Each pathway gives the emissions and concentrations for each greenhouse gas from present through to the year 2100, along with other parameters useful for modelling. They are not meant to be predictions of the future, but rather possible scenarios for what could happen in the future. As such there are no related likelihoods within AR5 for an individual scenario emerging. The RCPs also define a limited number of scenarios allowing for easier comparison across different climate change studies. There are four key RCPs, namely RCP2.6, RCP4.5, RCP6.0, and RCP8.5. The number at the end of each refers to the radiation forcing in W/m^2 in the year 2100. The carbon dioxide concentrations of each RCP are shown in Figure 2.10, along with the historic values during the Space Age.

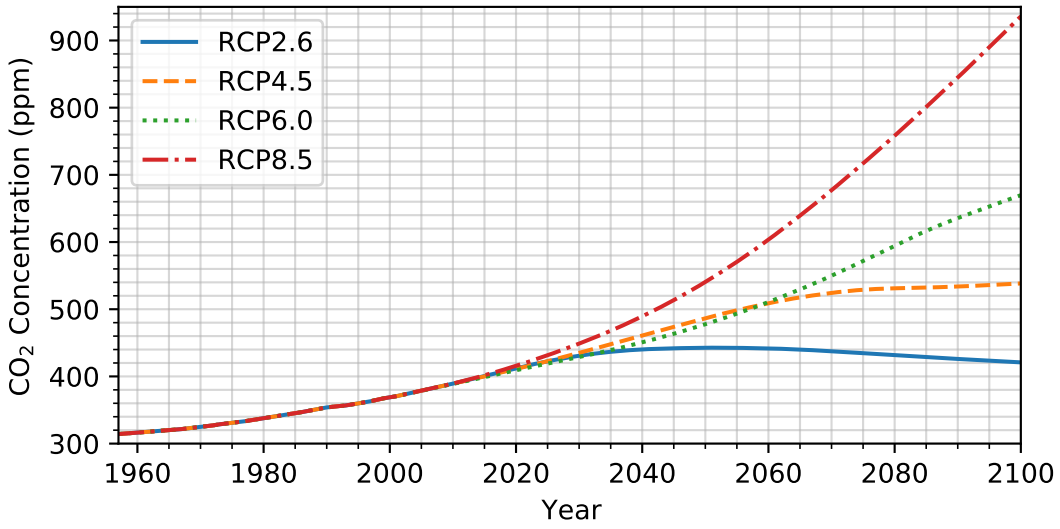

FIGURE 2.10: Future carbon dioxide concentration pathways from the RCPs of the IPCC's fifth assessment report (IPCC (2014)), appended to the historic observed ground-level carbon dioxide concentrations since the launch of Sputnik in 1957.

Alongside the RCPs, AR5 also contained the beginnings of the Shared Socioeconomic Pathways (SSPs) which tried to address and group some of the assumptions about emissions which were discussed earlier. Similarly to the RCPs, these also included greenhouse gas concentration pathways through to the year 2100, albeit with differing profiles to reflect the timings of key policy decisions and technologies. The SSPs are being expanded upon within the IPCC's sixth Assessment Report (AR6, due to be released after the 26th UN Climate Change Conference of the Parties (COP26). There are five key SSPs, namely SSP1-1.9, SSP1-2.6, SSP2-4.5, SSP3-7.0, and SSP5-8.5. While the latter number in each name refers to the radiation forcing in W/m^2 in the year 2100, the first number specifically defines a socioeconomic narrative used within the SSP. At the time of writing AR6 has not been published, so the RCPs will be used throughout this thesis.

2.4 Space Debris

Satellites play an important role in modern society, with wide ranging missions from communications to Earth observation, from scientific exploration to human spaceflight. Since the launch of Sputnik on 4th October 1957, the space environment has become increasingly populated by these satellites, along with the leftovers from their missions. Rocket bodies from their launches and fragments from in-orbit break-ups also reside within the space environment, making up the space debris population. The United Nations Committee on the Peaceful Uses of Outer Space (UNCOPUOS) defines space debris in their Space Debris Mitigation Guidelines (United Nations Office For Outer Space Affairs (2010)) as

> "... all man-made objects, including fragments and elements thereof, in Earth orbit or re-entering the atmosphere, that are non-functional."

As these pieces of space debris are non-functional, they possess no collision avoidance capability and present a risk of colliding with not only functional satellites, but other pieces of space debris, creating more debris in the process. To try to reduce this risk, the Inter-Agency Space Debris Coordination Committee (IADC) developed space debris mitigation guidelines that spacecraft operators should follow to reduce the generation of new debris. One commonly cited guideline is the "25-year rule", setting a time within which a satellite should leave the environment after mission completion, either by direct re-entry or by entering an orbit with a lifetime of less than 25 years. This guideline only holds in the highly populated Low Earth Orbit (LEO) region, which encompasses all orbits with perigees below 2000 km altitude. In the other protected region, Geostationary Earth Orbit (GEO) at 35,786 km altitude, satellites are required to move at least 300 km above the GEO ring to a graveyard orbit, so as not to present a collision risk to operating GEO satellites in the future.

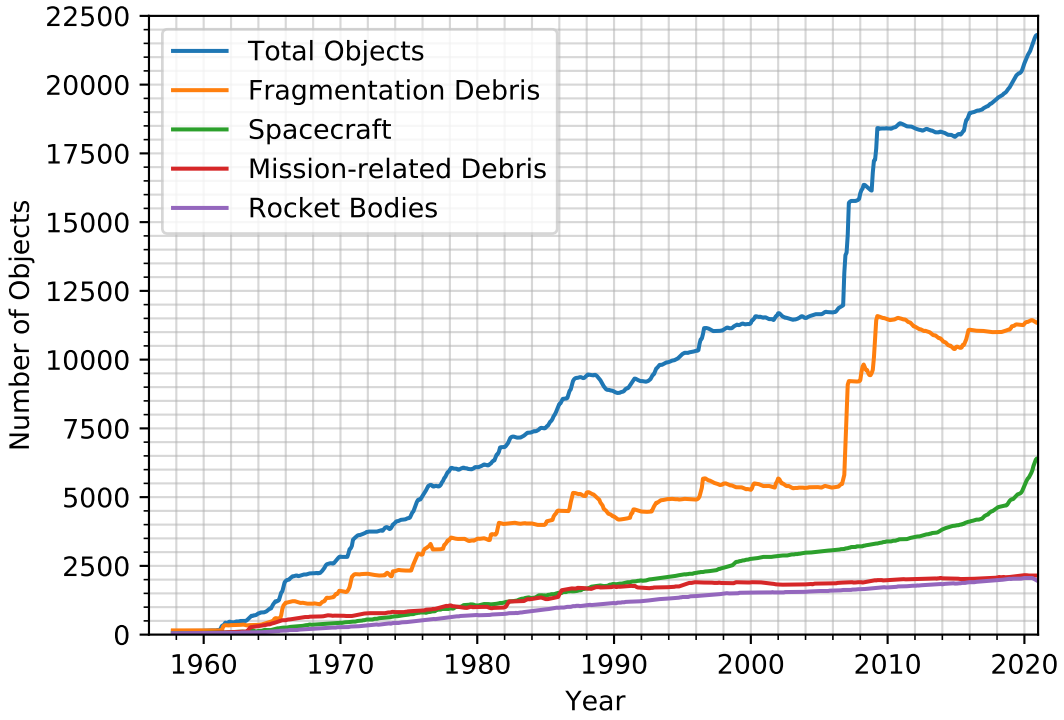

FIGURE 2.11: Monthly number of cataloged objects in Earth orbit as of 5th January 2021, as updated yearly in the Orbital Debris Quarterly News (Anz-Meador (2021)).

Historically, objects larger than roughly 10 cm in size can be tracked (depending upon altitude) and catalogued, with the total number and breakdown shown in Figure 2.11. Within this figure it can be seen how both the number of spacecraft and fragmentation debris increases over time. However sudden step changes can be seen, with particularly large increases in 2007 and 2009. The 2007 increase is a result of a Chinese anti-satellite test against the Fengyun-1C satellite at 865 km altitude, while the 2009 increase was the result of a catastrophic collision between the inactive Kosmos-2251 satellite and the active Iridium 33 satellite at an altitude of 789 km.

As a piece of space debris travels through the thin atmosphere, it experiences atmospheric drag, lowering the altitude it reaches (the apogee) on each successive orbit, as illustrated in Figure 2.12. This circularizes the orbit over time and the debris spends an increasing proportion of its orbit in a more dense part of the atmosphere, increasing the proportion of the orbit the debris experiences substantial atmospheric drag. As the orbit circularizes, the perigee also starts lowering, making the debris travel through a slightly more dense part of the atmosphere, increasing the atmospheric drag and accelerating the lowering of the orbit. This process repeats until the debris burns up in Earth's lower atmosphere[4], removing it from orbit.

[4] "Re-entering Earth's atmosphere" is the commonly used term for when an orbiting object is at such a low altitude (around 75 km) that it burns up in the thicker part of the atmosphere. It is avoided here as objects in LEO already reside within the thermosphere and feel the impacts of the atmosphere over their entire lifetime, for example through surface ablation and atmospheric drag.

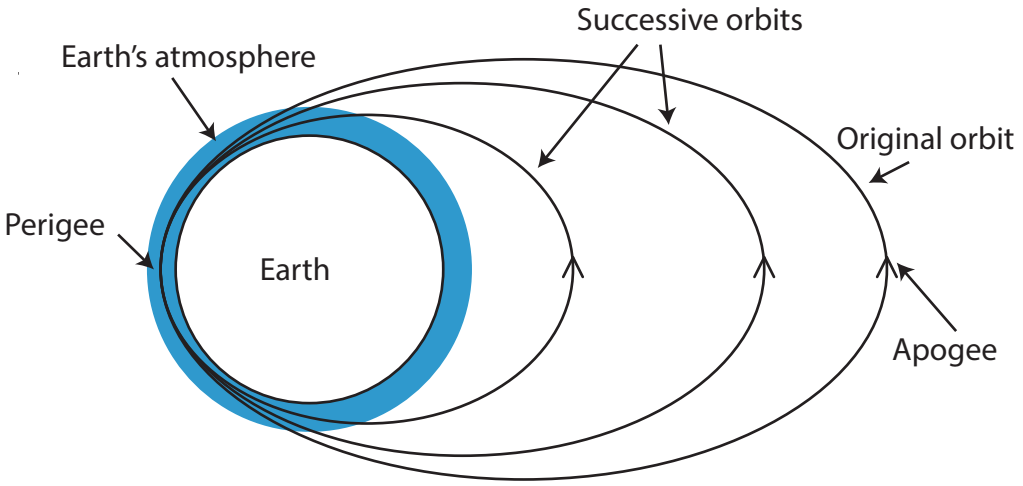

FIGURE 2.12: Illustration of an orbit circularizing due to atmospheric drag. Scale exaggerated to highlight the lowering of apogee on successive orbits while there is little change in the perigee's altitude.

Active satellites also have to account for atmospheric drag in LEO, carrying fuel and performing periodic orbit-maintenance burns to sustain their target orbit. However, atmospheric drag also provides a method for meeting the 25-year rule at a satellite's end-of-life. If a final burn can be performed to lower a satellite's altitude to a point where atmospheric drag can remove it from the environment within 25 years, the guideline will be met. Satellite operators that aim to remove their satellite within 25 years have to plan well in advance, whether by designing the mission for operation in a lower orbit, or ensuring enough fuel will remain at the end of mission to perform the orbit lowering burn. However, with satellites often taking a decade or more to get from concept and design to build and launch, before even performing their multi-year missions, a long-term change in atmospheric density may need to be taken into account when calculating required propellant mass.

A more recent development in the space environment is the launch of constellations of satellites, with each constellation aiming to provide global internet coverage via a network of LEO satellites. Two major operators with satellites in orbit at the time of writing are SpaceX's Starlink network ($\sim$1,800 launched of a planned $\sim$12,000-42,000 at $\sim$550 km) and OneWeb ($\sim$350 launched of a planned 650 at $\sim$1200 km). More constellations are planned too, with some examples being Amazon's Kuiper, Inmarsat's Orchestra, and Boeing's unnamed constellation. This has lead to a step change in the number of objects being launched into LEO, as shown in Figure 2.13, and an increasingly congested environment which presents new challenges to spacecraft operators.

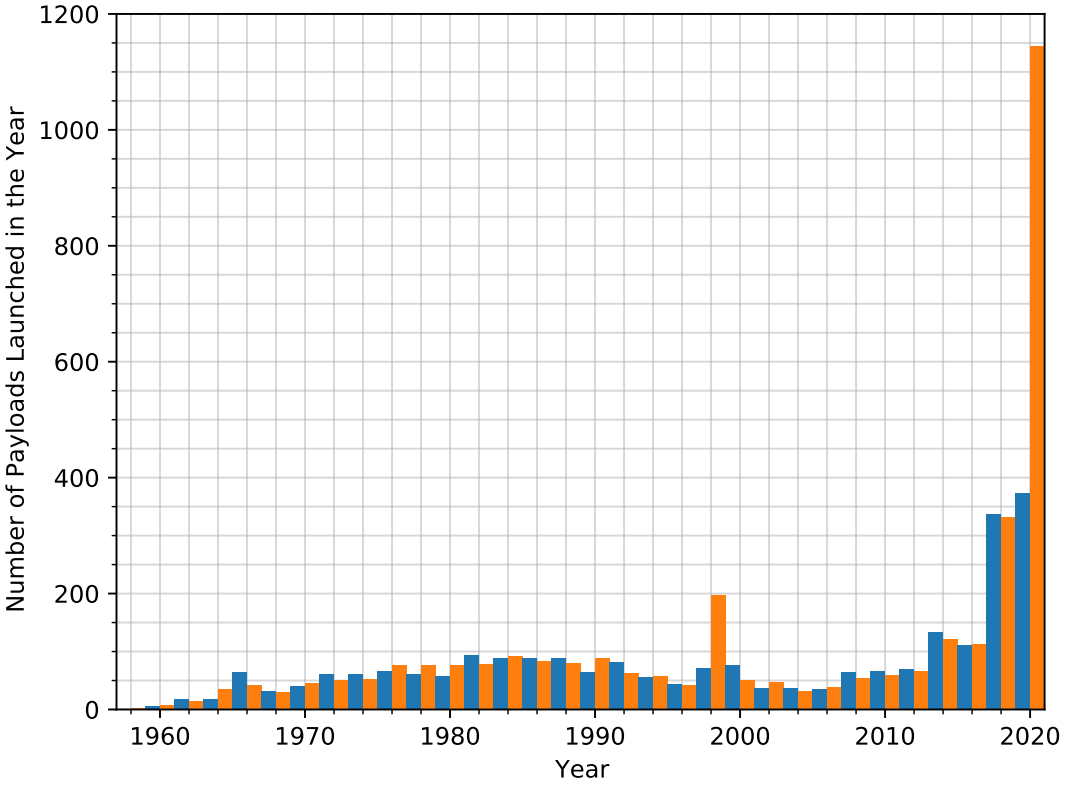

FIGURE 2.13: Yearly launch traffic into LEO (200 < perigee < 2000 km) using data from CelesTrak (2021). Alternating colours used to aid in assessing individual years.

2.5 Orbital Mechanics

This section will introduce the basic concepts of orbital mechanics, including mathematically describing an orbit, and how perturbations change it from a perfect, two-body Keplerian orbit. Much greater detail can be found in books by Vallado (2013) and Montenbruck and Gill (2005).

2.5.1 Orbital Elements

An orbiting object can be described by position and velocity vectors, with orthogonal x, y, and z components in Cartesian space with the origin at the centre of the Earth (at a particular time). These are known as state vectors and define the orbit with six variables. The acceleration can then be calculated by modelling the forces acting on an object, allowing the orbit to be fully described as it evolves in time. While useful for plotting positions and quickly calculating orbital speed and altitude, state vectors do not intuitively describe an orbit's size, shape or orientation.

Orbital elements allow for a more intuitive way of describing an orbit while maintaining a six variable definition. Each element's full definition is given in Table

2.2, with semi-major axis, a, and eccentricity, e, describing an orbit's shape and size (Figure 2.14), inclination, i, right ascension of ascending node, Ω, and argument of perigee, ω, describing the orbit's orientation (Figure 2.15), and the true anomaly, θ, describing an object's position along the orbit at a given time.

TABLE 2.2: The classical orbital elements with their symbols and descriptions.

Element	Description
Semi-major axis (a)	The distance from the centre of the ellipse to the perimeter via a focal point.
Eccentricity (e)	The oblateness of the orbital ellipse.
Inclination (i)	The angle between the orbital plane and the equatorial plane when crossing from south to north.
Right Ascension of Ascending Node (Ω)	The eastward angle in the equatorial plane from vernal equinox to the ascending node (where the satellite crosses from below the equatorial plane to above).
Argument of perigee (ω)	The angle along the orbital path in the direction of motion from the ascending node to the perigee (closest point of the orbit to the Earth).
True anomaly (θ)	The angle along the orbital path from the perigee to the satellite.

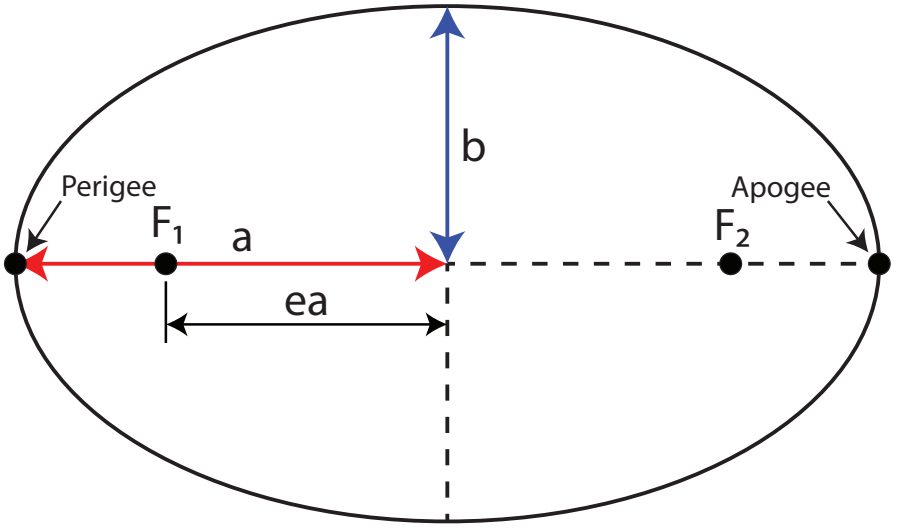

FIGURE 2.14: Geometry of an orbital ellipse showing how semi-major axis, a, and eccentricity, e, are defined. Perigee and apogee assume F_1 is the Earth. a is half the length of the major axis, while b is half the length of the minor axis. The ellipse becomes a circle when $e = 0$.

Two other ways to describe the position along an orbit are the mean anomaly (M) and eccentric anomaly (E). Mean anomaly is the angle a satellite would have travelled around a circular orbit with the same orbital period as the true orbit. Eccentric anomaly is graphically shown in Figure 2.16 and is found by considering a concentric circle with radius equal to the semi-major axis of the orbital ellipse, passing a line perpendicularly from the centre-perigee line up through the satellite to the circle to

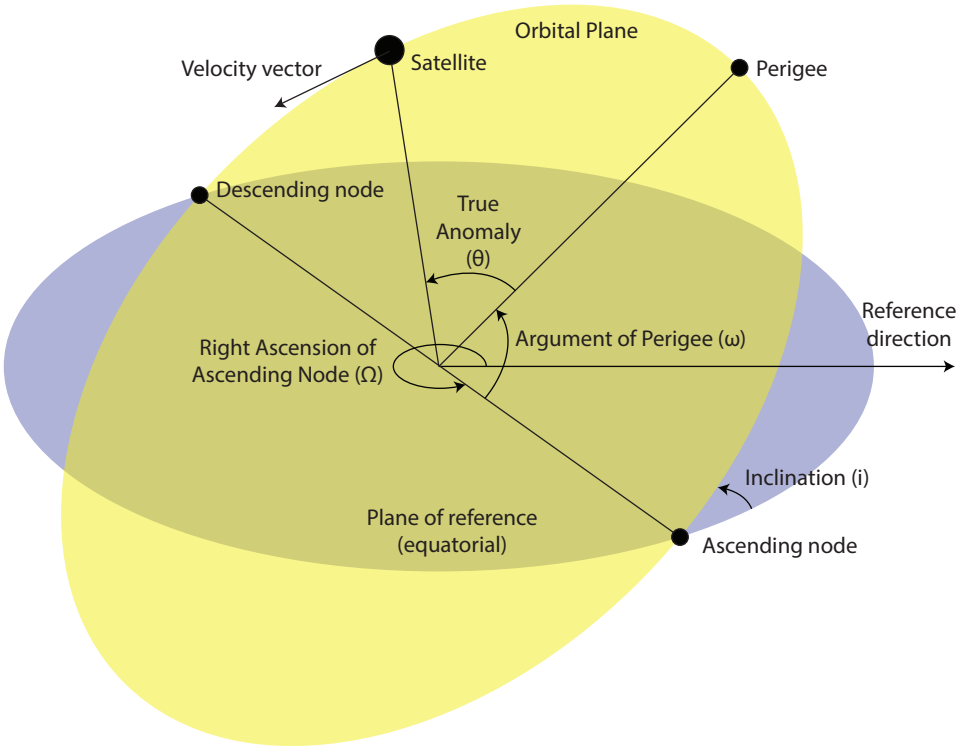

FIGURE 2.15: Orbital elements defining the orientation of an orbit (i, Ω, ω) and the position of an object along its orbit (θ).

give a new point, and then measuring the angle from the perigee to this new point on the circle.

2.5.2 Orbital Perturbations

Kepler's three laws of planetary motion describe an ideal orbit where an object orbits around a single point mass. In reality, external forces act upon the orbiting object and perturb them away from this ideal orbit. The dominant perturbing forces in LEO are caused by Earth's asymmetry, lunar and solar gravity, atmospheric drag and solar radiation pressure, with the magnitudes of each perturbation's acceleration given for an example satellite in Figure 2.17. The Earth's largest asymmetry (the J2 zonal harmonic) is the dominant perturbing force at all but the lowest altitudes. Atmospheric drag is the next most dominant, but only below around 300 to 700 km dependent upon solar activity and the object's orbit and physical characteristics.

These perturbations cause periodic variations in the orbital elements, in the short-term (within an orbit) and long-term (period on the order of multiple orbits), but also secular changes. Due to the long-term environment modelling performed within this thesis, the secular effects of the perturbations will be focused upon here, with these summarized in Table 2.3 and mathematically described in detail by Vallado (2013).

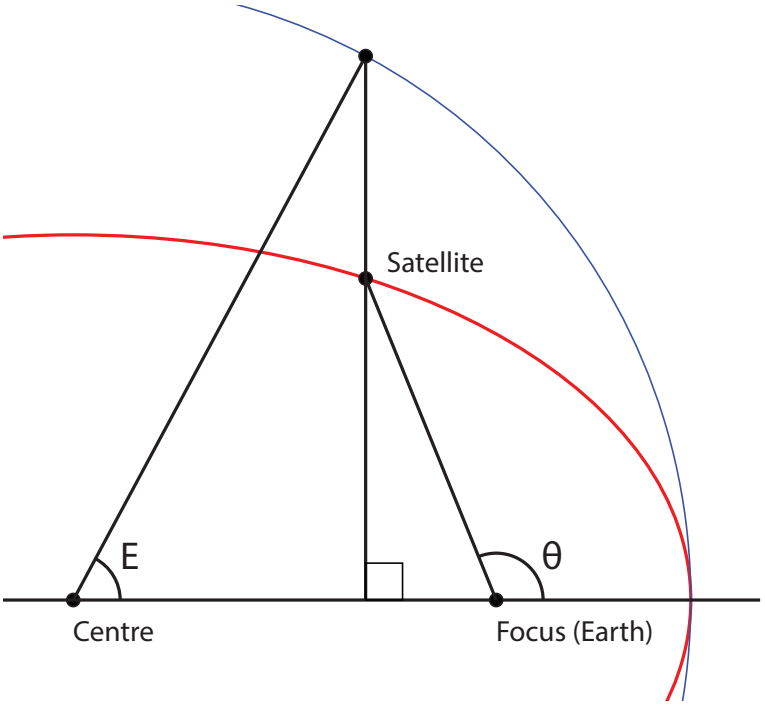

FIGURE 2.16: Graphical representation of true anomaly (θ) and eccentric anomaly (E). The red line is the orbital ellipse while the blue line is the concentric circle.

The gravitational perturbations due to J2 change the orientation of an orbit through secular changes in right ascension of ascending node, Ω, and argument of perigee, ω. In general, an object can only be removed from orbit by reducing its orbital energy and therefore reducing the size of its orbit. However, the gravitational forces due to J2 are conservative, so the orbital energy does not change and neither does the orbit's shape. However, atmospheric drag does work on an orbiting object, removing orbital energy and reducing the size of the orbit. Solar radiation pressure also does work on an orbiting object, reducing the orbital energy when travelling towards the Sun and increasing the orbital energy when travelling away, introducing periodic effects. Over an orbit these balance out so there is no secular change in semi-major axis. This balance is disrupted when part of the orbit is eclipsed, introducing a secular change in semi-major axis as detailed by McMahon (2011).

TABLE 2.3: Secular trends in orbital elements due to perturbations in low Earth orbit.

	Secular change in orbital element?					
Perturbation	a	e	i	Ω	ω	θ
Earth asymmetry	×	×	×	✓	✓	✓
Moon	×	×	×	✓	✓	×
Sun	×	×	×	✓	✓	×
Solar radiation pressure	✓*	✓	×	×	×	×
Atmospheric drag	✓	✓	×	×	×	×

* secular change only for orbits which experience eclipses.

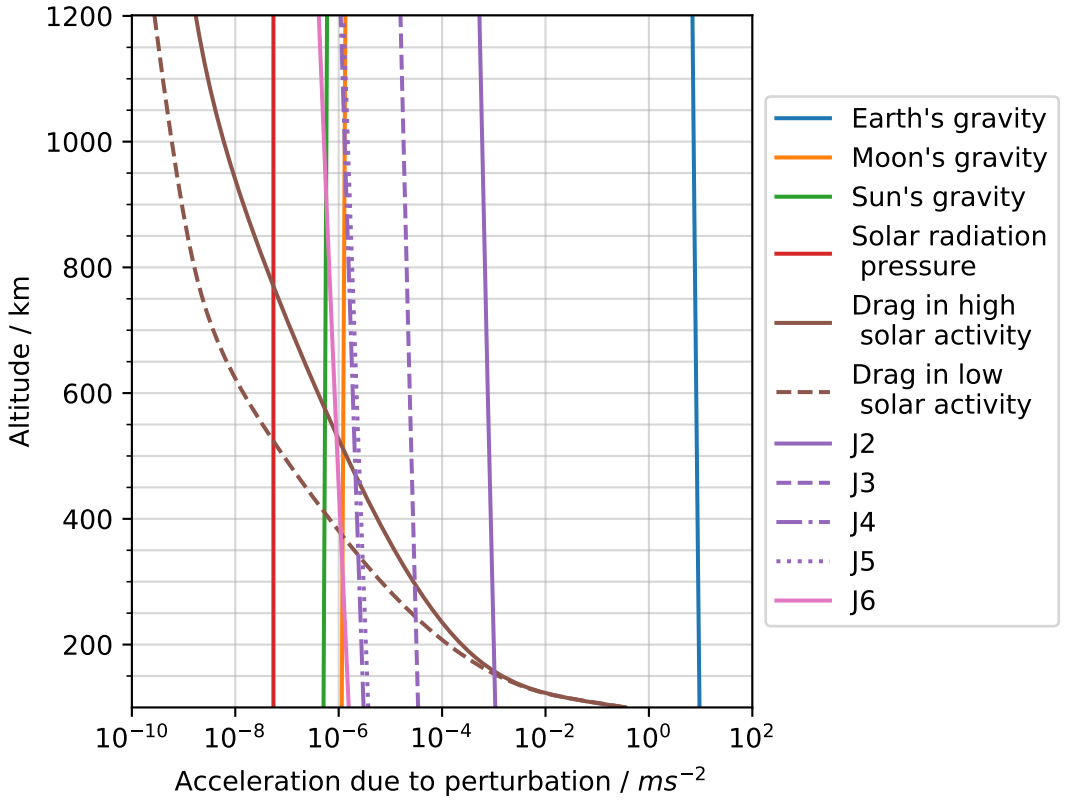

FIGURE 2.17: Magnitude of the acceleration due to each perturbing force in low Earth orbit. Example satellite is at 45 degrees longitude and latitude, with an area to mass ratio of 0.01 m^2kg^{-1}, coefficient of drag of 2.2, a reflection coefficient of 1.2. Low solar activity has F10.7 = 70 sfu, while high solar activity has F10.7 = 200 sfu. Earth's gravity refers to the main contribution by treating the Earth as a point mass, while J2 through to J6 refers to the zonal harmonics of gravity caused by Earth's asymmetry.

2.5.3 Atmospheric Drag

Objects orbiting through the thin thermosphere collide with the atmosphere's constituent molecules and atoms, transferring momentum from the particles to the orbiting object. This imparts a force upon the object known as atmospheric drag. In its simplest vector form, the acceleration due to this force, $\bar{a}_{drag}$ can be expressed as

$$\bar{a}_{drag} = -\frac{1}{2} C_D \frac{A}{m} \rho |\bar{v} - \bar{v_a}|^2 \hat{v} \tag{2.2}$$

where C_D is the drag coefficient, A is the cross-sectional area presenting itself in the air-relative direction, $\bar{v}$ is the satellite's velocity vector with its associated unit vector $\hat{v}$. The velocity of the Earth's atmosphere (due to wind and rotation) is given by $\bar{v_a}$, m is the mass of the object, and the atmospheric density local to the object is given by ρ.

As atmospheric density decreases with altitude, the acceleration due to drag is largest at perigee. The orbiting object has less energy to reach as high an apogee as during its previous orbit, reducing the semi-major axis and eccentricity as the orbital shape tends towards that of a circle [5]. As it does, the length of time the object spends in the denser part of the atmosphere increases, increasing the total amount of atmospheric drag and lowering the semi-major axis further, reducing the object's orbital lifetime at a faster rate. This can be seen in Figure 2.18 for a passive satellite with no method on-board to maintain its orbit.

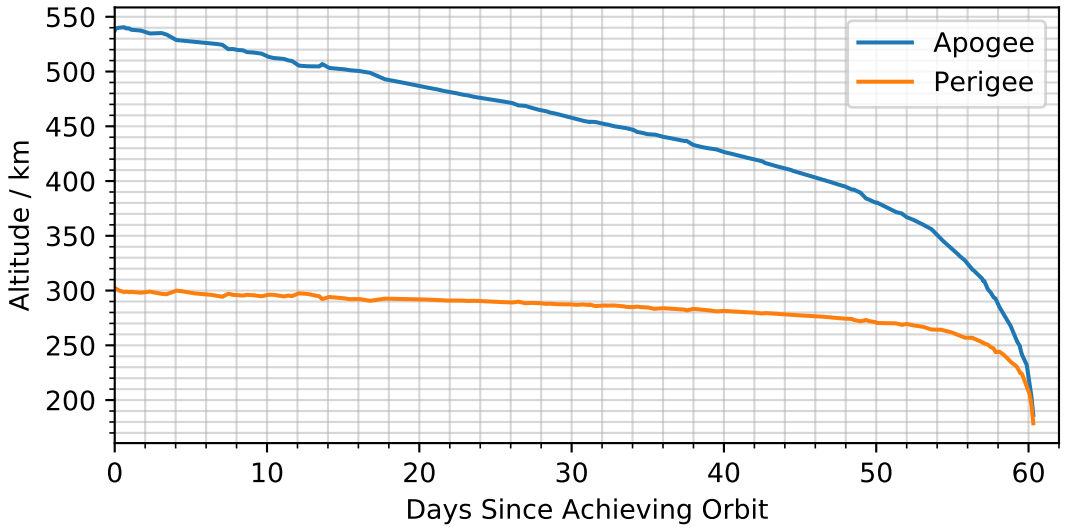

FIGURE 2.18: Evolution of the perigee and apogee altitude of Humanity Star (NORAD ID 43168) from TLE data.

King-Hele (1987) explores how the atmosphere affects a satellite's orbit in great detail. They also give a simplified equation for the lifetime of an object in a circular orbit, $L*$ in units of days, where

$$L* = \left(\frac{m}{A}\right) \frac{H}{10^{13}\rho} \tag{2.3}$$

where H is the atmospheric density scale height in km, ρ is the atmospheric density at the satellite's altitude in kgm^{-3}, and m/A is the inverse of the area-to-mass ratio given in kgm^{-2}. It is assumed $C_D = 2.2$. In Figure 2.19, this equation has been plotted for three area-to-mass ratios, and NRLMSISE-00 has been used to obtain ρ and H under low and high solar activity. Orbital lifetimes reduce by approximately an order of magnitude during high solar activity. Objects with larger area-to-mass ratios also have shorter lifetimes. This leads to the idea of drag sails being deployed at the end of missions to increase cross-sectional area and speed up reentry. Drag sails are in the early stages of in-orbit testing through missions such as InflateSail (described by Underwood et al. (2019)).

[5] This example assumes drag is applied only at the perigee as this is when the force due to atmospheric drag is at its largest. In reality, atmospheric drag applies over the entire orbit, including the apogee, albeit by a smaller amount, with the amount reducing with increasing eccentricity.

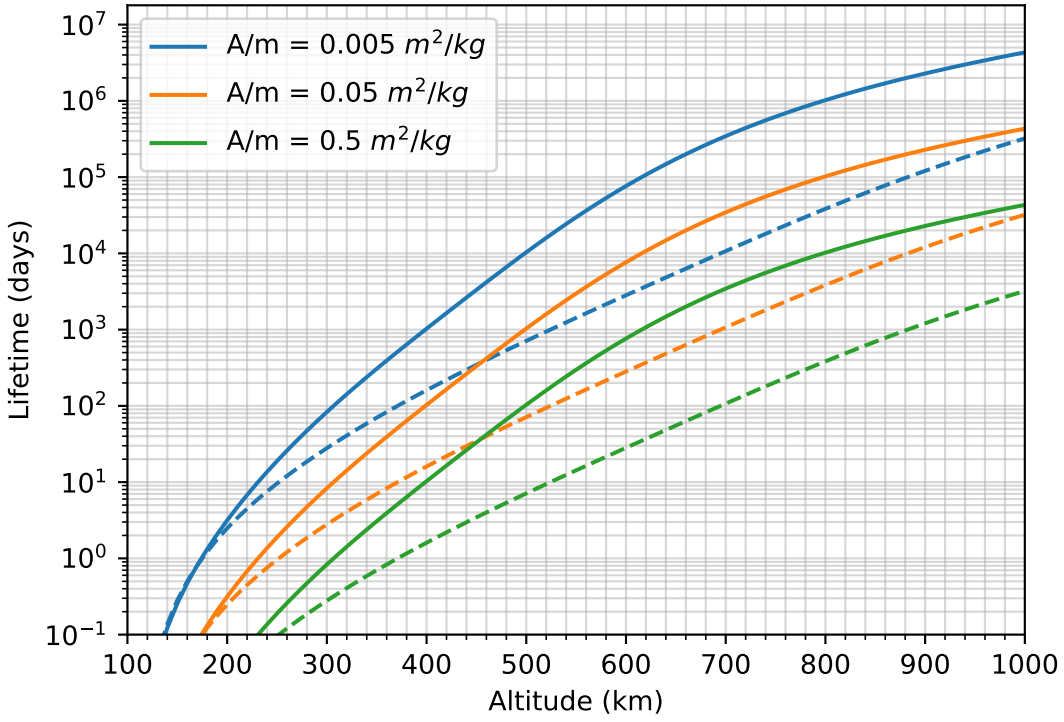

FIGURE 2.19: Orbital lifetimes versus altitude for objects in circular orbits for the specified area-to-mass ratios. Solid line denotes low solar activity (F10.7 = 70 sfu) while dashed line denotes high solar activity (F10.7 = 200 sfu). Coefficient of drag, C_D, assumed to be 2.2.

2.6 Two Line Element (TLE) Sets

North American Aerospace Defense Command (NORAD) and the Joint Space Operations Center (JSpOC) frequently release the orbital characteristics of all trackable, unclassified orbiting objects in the form of Two Line Element (TLE) sets (Vallado et al. (2006)). As these are available for all objects since Sputnik, they are an important source of information on the historical space environment and can provide a snapshot of the trackable space population. Each TLE defines the orbital characteristics at a given epoch via two lines, each of 69 characters, with each line being split up as described in Table 2.4 and 2.5. An example of a TLE is:

```
1 25544U 98067A   21277.42288701  .00003633  00000-0  74266-4 0  9995
2 25544  51.6452 162.6092 0004100  56.2525 113.7302 15.48922831305526
```

The final digit of each line is the checksum, for which letters, blanks, periods and plus signs equal 0, while minus signs equal 1, with each number of the line summed and a modulus of 10 applied.

When TLEs are created, orbital elements are converted to mean elements which remove short period orbital variations for faster propagation (Hoots and Roehrich

(1988)). This is done with the Simplified General Perturbations (SGP4) propagator, which calculates an object's position in an orbit accounting for the secular and periodic variations caused by orbital perturbations. As the Brouwer mean elements within the TLEs are specific to the SGP4 propagator (or Kozai mean elements for the original SGP propagator), they have to be processed with SGP4 to retrieve the true classical (osculating) orbital elements (Kozai (1959); Brouwer (1959)). There is also the option of using Three Line Element Sets, where the first line contains the object's name and description, and the final two lines are the standard TLE format.

TABLE 2.4: The data contained within the given positions of line 1 in a TLE. Decimal assumed in both derivatives of mean motion

Positions	Description
01-01	Line Number
03-07	NORAD satellite catalogue number
08-08	Classification (Commonly U for unclassified)
10-11	International Designator (last 2 digits of launch year)
12-14	International Designator (launch number of the year)
15-17	International Designator (piece of launch)
19-20	Epoch (last 2 digits of year)
21-32	Epoch (day of year + fraction of day)
34-43	First time derivative of mean motion (orbital revolutions/day^2)
45-52	Second time derivative of mean motion (orbital revolutions/day^3)
54-61	B^* (decimal assumed) (see Equation 2.4)
63-63	Ephermeris type (Always 0 after older TLEs were standardized)
65-68	Element set number, the number of TLEs created for the object
69-69	Checksum

TABLE 2.5: The data contained within the given positions of line 2 in a TLE.

Positions	Description
01-01	Line Number
03-07	NORAD satellite catalogue number
09-16	Inclination (i) (degrees)
18-25	Right ascension of the ascending node (Ω) (degrees)
27-33	Eccentricity (e) (decimal assumed)
35-42	Argument of Perigee (ω) (degrees)
44-51	Mean Anomaly (degrees)
53-63	Mean Motion (complete orbits per day)
64-68	Orbit number at epoch (total number of revolutions)
69-69	Checksum

The B^* term in line 1 of a TLE is given by

$$B^* = \frac{\rho_0 B}{2} = \frac{\rho_0 C_D A}{2m} \tag{2.4}$$

where ρ_0 is a reference density, given in Hoots and Roehrich (1988) as $\rho_0 = 2.461^{-5}$ kg/m^2/Earth radii.

Chapter 3

Literature Review

This chapter will summarise the current state of research in the fields of thermospheric density trends and debris modelling, building upon the theory laid out in Chapter 2. The initial focus will be on explaining how density trends have been observed through orbit-derived densities, and then how density trends have been modelled. These studies are then summarized and compared against each other. The few studies which have modelled trends into the future will then be discussed. Density trends arising due to factors other than increases in carbon dioxide concentration will then be explored.

Focus will then switch to space debris modelling, with an introduction given to the evolutionary and statistical models most relevant to the thesis. This will also include the constituent models upon which the debris models are built. There will then be a brief review of some key debris modelling studies. Finally, the two research areas will be joined together by discussing the methodology and limitations of the two studies which have applied density trends within a debris modelling context.

3.1 Neutral Density Trends

Roble and Dickinson (1989) first used the TGCM model to simulate how a doubling of carbon dioxide concentration from the 1950's value of 330 ppm would lead to a 50 K cooling of the thermosphere. This led to Rishbeth (1990) simulating the impact on the embedded ionosphere, identifying that thermospheric contraction would reduce the height of the F_2 layer (the highest concentration of free-electrons and ions in the ionosphere). Both these studies were revisited using the TI-GCM model in Rishbeth and Roble (1992), finding similar results to before. The impact on the total mass density was quantified for the first time, with an expected reduction in density of 40% at heights of 100-300 km for a doubling of CO_2 concentration. Roble (1995)

re-presented the findings, noting that observations of the phenomena had yet to take place.

This section will discuss how thermospheric densities can be measured, along with how observations of the decreasing thermospheric trends in density and temperature were performed. As the historic trends have been modelled with increasingly complex general circulation models, these will also be explored. A summary of the historic trends is provided later in Figure 3.1 and Table 3.2.

3.1.1 Accelerometer-Derived Density

If an object's area-to-mass ratio, coefficient of drag, velocity and acceleration are known, then an instantaneous neutral density can be obtained via Equation 2.2.

Obtaining the instantaneous acceleration for this method can be done with on-board accelerometers. This has been performed with data from the Challenging Minisatellite Payload (CHAMP) and Gravity Recovery and Climate Experiment (GRACE) satellites and is discussed by Doornbos (2012). Only a limited set of satellites have flown accelerometers and made their data openly available. This confines accelerometer derived-densities to the specific orbits and operational periods of their parent satellite. The high time resolution of the data allows for exploration of density changes during shorter timescale events such as Joule heating or solar events, as done by Bruinsma et al. (2006). There is potential for exploring long-term trends, particularly with the standardized satellites, global coverage, and multi-decade missions of constellations, however this has yet to be done.

3.1.2 Orbit-Derived Density Trends

An alternative method for deriving atmospheric density from atmospheric drag is to measure by how much the semi-major axis of an orbit changes over time. In its most basic form and in the absence of other perturbations, this change in semi-major axis, $\dot{a}$ can be expressed as

$$\dot{a} = -\frac{2a^2 v}{\mu}\left[\frac{1}{2}C_D\frac{A}{m}\rho|\bar{v}-\bar{v_a}|^2\hat{v}\right] \tag{3.1}$$

where v is the object's speed and μ is the Earth's gravitational constant, and where Equation 2.2 for the acceleration due to drag, $\bar{a}_{drag}$ has been used within the square brackets. King-Hele (1987) explores the theory in more depth and Picone et al. (2005) discuss how to apply the theory to Two Line Element (TLE) sets.

The TLE catalogue contains orbital data from 1957 until now, with post-1967 containing a large enough number of satellites to provide good altitude coverage across LEO. This has allowed historic studies to derive density trends with up to 4.5

decades of data, including the first direct observations of the density trend after its prediction in Roble and Dickinson (1989).

Keating et al. (2000) were the first to investigate the thermospheric density trend through the use of densities derived from the TLE catalogue, making use of theory from King-Hele (1987). The rate of change of orbital period, T_P, was calculated directly from the rate of change of mean motion, $\frac{dn_M}{dt}$, provided in the TLE via

$$\frac{dT_P}{dt} = -\frac{\left(\frac{dn_M}{dt}\right) T_P}{n_M} \tag{3.2}$$

where mean motion, n_M, in radians per second is related to semi-major axis, a, and the Earth's gravitational constant, μ, by

$$n_M = \sqrt{\frac{\mu}{a^3}} \tag{3.3}$$

King-Hele then calculated the product of ballistic coefficient, δ, and atmospheric density, ρ via

$$\delta\rho = -\frac{\left(\frac{dT_P}{dt}\right)}{3}\sqrt{\frac{2e}{\pi aH}}\left[1 - 2e + \frac{5e^2}{e} - \frac{H}{8ae}\left(1 - 10e + \frac{7H}{16ae}\right)\right] \tag{3.4}$$

where H is the atmospheric scale height, a and e are the semi-major axis and eccentricity of the orbit respectively, with each obtained from the TLE, and the ballistic coefficient, δ is defined as

$$\delta = \frac{FAC_D}{m} \tag{3.5}$$

where $\frac{A}{m}$ is the area-to-mass ratio, C_D is the drag coefficient, and F accounts for the rotation rate of the Earth's atmosphere via

$$F = \left(1 - \frac{r_p}{v_p}\alpha cosi\right)^2 \tag{3.6}$$

where r_p and v_p are the satellite's altitude and speed at perigee, α is the angular velocity of the rotating atmosphere, and i is orbital inclination. This method results in no ballistic coefficient being required to calculate the density. Instead the $\delta\rho$ product is plotted against densities from a reference model, ρ_{ref}, for each satellite and a regression coefficient K obtained through least-mean-square fit, where

$$\delta\rho = K\rho_{ref} \tag{3.7}$$

The value K is then equivalent to the proportional change in density for each satellite. This method and all the other orbit-derived density studies we will discuss in this section make use of atmospheric models to obtain reference densities and scale

heights. The use of these reference models remove the known geophysical variations which would otherwise obscure the long-term trend, for example, the order of magnitude changes in neutral density due to the solar cycle. Keating et al. (2000) used the NASA Marshall Engineering Thermosphere 1999 (MET99) model as the reference model.

This early venture in obtaining trends from orbit-derived densities focused on five objects in the TLE catalogue during the solar minima of 1976, 1986, and 1996 (those between cycles 20 and 23). These objects were in eccentric orbits, with Keating et al. stating their individual average altitude ranged from 323 to 404 km, with an overall average of around 350 km. These seem in fact to be their perigees. The density trend varied for each individual satellite, so an average was taken across the five, with the 1976 to 1986 trend given as $-4.55 \pm 3.38\%$ and the 1976 to 1996 trend given as $-9.84 \pm 2.53\%$. To best compare this against other studies, a trend per decade is commonly obtained from the 1976 to 1996 value, giving $-4.9 \pm 1.3\%$ per decade at 350 km.

The small number of objects used was the largest limiting factor in the Keating et al. (2000) study. There was a wide range of trends found for individual objects, particularly within the 1976 to 1986 period where two objects appeared to experience an increasing thermospheric density trend, the largest being $+5.00\%$ over the decade. The choice of five specific objects was also not discussed in the paper, with the apparent links being their highly eccentric orbits and long lifetimes. This would allow atmospheric drag to be the major perturbing force in only a small section of the orbit around the perigee, so as to give a more accurate representation of the density near the perigee altitude.

Picone et al. (2005) introduced a new method for deriving densities, by integrating between two TLEs for the same object with the use of the SGP4 propagator. While the rate of change in semi-major axis was given earlier by Equation 3.1, mean motion, n, is a more natural variable to use with TLEs. Assuming negligible solar radiation pressure (which often holds for LEO orbits, see Section 2.5.2), Picone et al. derived the rate of change of mean mean motion, $\dot{n}_M$, as

$$\dot{n}_M = \frac{3}{2} n_M^{\frac{1}{3}} \mu^{-\frac{2}{3}} \rho \delta v^3 F \tag{3.8}$$

This equation is integrated through use of the SGP4 propagator from the time of the first TLE, t_1, to the second TLE at time t_2, as given by

$$\Delta_{1,2} n_M \cong \frac{3}{2} \mu^{-\frac{2}{3}} \int_{t_1}^{t_2} n_M^{\frac{1}{3}} \rho \delta v^3 F dt \tag{3.9}$$

where

$$\Delta_{1,2} n_M = n_{M(t_2)} - n_{M(t_1)} \tag{3.10}$$

At time $t_{1,2} = \frac{(t_1+t_2)}{2}$, the density $\rho(t_{(1,2)})$ can be obtaining by rearranging to

$$\rho(t_{(1,2)}) \equiv \frac{\frac{2}{3}\Delta_{1,2} n_M \mu^{\frac{2}{3}}}{\int_{t_1}^{t_2} n_M^{\frac{1}{3}} \delta v^3 F dt} \tag{3.11}$$

and $n_M \sim \frac{n_M(t_1)+n_M(t_2)}{2}$ was substituted in so as to simplify to

$$\rho(t_{(1,2)}) \cong \frac{\frac{2}{3}\mu^{\frac{2}{3}}\left[n_M^{-\frac{1}{3}}\right]\Delta_{1,2} n_M}{\int_{t_1}^{t_2} \delta v^3 F dt} \tag{3.12}$$

Finally to obtain the mass density, a simple forward model was used where $\rho = \lambda \rho_{ref}$, where λ was a scaling factor given by

$$\lambda = \rho_{ref} v^3 F \tag{3.13}$$

A percentage change in density per decade can be obtained via

$$trend = \frac{1}{\lambda(t_0)}\left(\frac{d\lambda}{dt}\right) \cong \frac{1}{\rho_{ave}}\frac{d\rho_{ave}}{dt} \tag{3.14}$$

where ρ_{ave} is the global average density.

Emmert et al. (2004) used this method of Picone et al. (2005), and expanded directly upon the work of Keating et al. (2000), using 27 objects (including the original study's five) over the period of 1996 to 2001. The NRLMSISE-00 model was used as the reference model. While the value at 400 km can be obtained from a figure within the paper, a printed value was given by Emmert (2015b) of $-2.8 \pm 1.0\%$ per decade at low solar activity levels.

Emmert et al. (2004) also investigated the impact solar activity had upon the density trend, binning individual λ values into eight F10.7 bins. The result was trends staying at a rate of between -2 to -3% per decade for F10.7 values greater than 90 sfu, but dropping sharply with solar activity levels below 90 sfu, reaching a value of -7% per decade at F10.7 = 75 sfu.

The five objects from Keating et al. (2000) were revisited in Emmert et al. (2004) with the differing methodology. Negative density trends were found for all objects in the 1976 to 1986 interval, where two objects had associated increases in density previously. There was also a smaller spread in trends from the objects using the new methodology. This disparity was attributed to the differing density reference model (tackled directly by Akins et al. (2003)), the method of integration of the drag equation during propagation, and a differing method for calculating the perigee which had been used to define the altitude at which the trends were measured.

Marcos et al. (2005) approached the problem by using a slightly differing method and using five objects to calculate the density trend across the 1970 to 2000 period. While the two previously discussed studies used analytical propagators, Marcos et al. used a special perturbations numerical propagator in an attempt to retrieve more accurate densities at the cost of being more computationally intensive. A trend of $-1.7 \pm 0.2\%$ per decade was obtained from the weighted average of daily ratios for observed to modelled densities for five objects. The error was calculated from the variance between the trends from these five different objects. While the impact of solar activity was accounted for within the reference model, no binning in or uncoupling from solar activity was made so this $-1.7 \pm 0.2\%$ per decade trend was implicitly averaged across all solar activity levels. Two further objects were used to allow direct comparison with Keating et al. (2000) and Emmert et al. (2004) for the 1976, 1986 and 1996 solar minima, resulting in a trend of $-4.2 \pm 1.1\%$ per decade, agreeing with Keating's value of $-4.9 \pm 1.3\%$ per decade. While NRLMSISE-00 was used as the reference model, J70 was also used to allow comparison between the use of two differing reference models. The unnormalized data were within one standard deviation of each other, so it was argued the two models were equally effective in removing other long-term geophysical variations.

Emmert et al. (2008) saw a step change in the number of objects being used. From the $\sim$18000 objects in the TLE catalogue at the time which had perigees below 600 km, 5000 were chosen which were best suited for deriving densities. This removed all objects that could manoeuvre, lay outside the period of interest (1967-2007), or had unstable ballistic coefficients (for example, due to tumbling). The method of Picone et al. (2005) was used, with NRLMSISE-00 as the reference model. GAMDM (see section 2.2.2.4) was also used to account for known geophysical density variations and reduced the solar minimum bias present in NRLMSISE-00. The trends calculated without removing solar activity dependence skewed towards the larger trends occurring during low solar activity when using NRLMSISE-00 as the reference model, giving a value of $-3.55 \pm 0.79\%$ per decade compared to the trend of $-2.68\% \pm 0.49\%$ per decade using GAMDM as the reference model. This again highlights the dependence of the trend upon the reference model used in calculation, and at least partially the difference between the overall trends found in each study.

Saunders et al. (2011) used a numerical propagator of their own design, in contrast to the analytical propagators used by all the other derived density studies except Marcos et al. (2005). Due in part to the increased computational time from the use of a numerical propagator, 41 objects were used to derive the density trend. These objects have been summarised in Appendix A and include all but one of the objects used in the Keating et al. (2000), Emmert et al. (2004) and Marcos et al. (2005) studies, and over a longer 40 year time period than any of the previous studies. NRLMSISE-00 was used as the reference model and similarly to Emmert et al. (2008), derived densities were

binned in both time (yearly) and altitude (10 km intervals between 200 and 600 km). An overall trend of $-5.4 \pm 3\%$ per decade at 400 km was obtained, but separating the individual derived densities into two solar activity bins highlighted the difference between solar minima and maxima. At 400 km, a trend of -7.2% per decade was obtained with $F10.7 < 90$, while -4.0% per decade was obtained for $F10.7 > 90$.

Emmert and Picone (2011) used the same data set of 5000 objects in the TLE catalogue from Emmert et al. (2008), along with the same methodology to derive densities. However, Emmert and Picone (2011) highlighted that the standard error analysis used in previous studies assumed independent random deviations around the mean trend, which is not the case when looking at the upper atmosphere as it is often due to an unknown climatology instead. This had led to lower reported uncertainties than the data likely suggested. To correct for this, autoregressive models were used to make future predictions and estimate uncertainties by taking into account the historical data. While the choice of monthly or yearly averages appeared to have little impact on the calculated trends, using different reference periods had a significant impact. These have been reproduced in Table 3.1, where it can be seen that calculating the trend over an extra two years (2006 and 2007) caused a significant change due to the abnormally low solar activity during this period. Emmert et al. (2008) calculated the trend over 1967-2007, obtaining a value of $-2.68 \pm 0.49\%$ per decade. Revisting this with the autoregressive model gave a slightly larger error at $-2.68 \pm 0.78\%$ per decade (where 1σ rather than the reported 2σ has been used for direct comparison). However, the 1967-2005 period was suggested as the better period to use to avoid the lower densities caused by the low solar activity of the 2005-2007 period, so a final value of $-1.94 \pm 0.68\%$ per decade was given as the overall density trend at 400 km for Emmert and Picone (2011) (again, using 1σ rather than the reported 2σ for comparison reasons).

TABLE 3.1: Density trends at 400 km in Emmert and Picone (2011) with differing reference periods used in the autoregressive model. Errors given are 2σ.

	Density Trend Estimates (% per decade)	
Reference Period	1967-2005	1967-2007
1986 - 2007	-1.94 ± 1.35	-2.68 ± 1.55
1986 - 2005	-2.02 ± 1.18	-2.90 ± 1.57
1967 - 1985	-2.25 ± 1.25	-3.34 ± 1.73
1967 - 2005	-2.07 ± 1.20	-3.01 ± 1.62

Emmert (2015b) is the latest study to calculate trends from orbit-derived densities, using similar methodology to their previous study (Emmert and Picone (2011)). Trends over the 1967-2013 period were derived, but the abnormally low solar activity levels during the solar minimum between cycles 23 and 24 (roughly 2005 to 2010) led to the results being deemed unreliable for use in isolating the trend due to CO_2. Instead, focus switched back to 1967-2005, this time using GAMDM2.1 as the reference

model, with this model's inbuilt CO_2 trend switched off. The trend with this method and model was found to be $-2.0 \pm 0.5\%$ per decade at 400 km.

The impact of geomagnetic field activity (through the Kp index) was also explored in Emmert (2015b), although results were inconclusive. The 1967-2005 trends were binned by Kp, with all values within 1 standard deviation of the overall trend ($-2.1 \pm 1.2\%$ per decade), except the low geomagnetic activity of Kp=0.7-1 with a more negative trend of ($-3.4 \pm 0.9\%$ per decade). However, extending analysis to the 1967-2013 period which saw lower Kp values obscured the dependence upon geomagnetic activity.

3.1.3 Modelled Density Trends

Qian et al. (2006) applied the chemistry and physics of TIME-GCM within a one-dimensional model, resulting in a global mean model which varied only in altitude. This model then performed a transient run from 1970 to 2000, with a varying ground-level carbon dioxide concentration. The historic CO_2 mixing ratio observations from Mauna Loa were applied at the model's lower boundary at 30 km. Solar activity levels also followed historic F10.7 observations. A second control run was performed with a CO_2 concentration fixed at the 1970 value, but solar activity followed the historic values again. A ratio between the densities of the first run and second was taken, and a linear regression in time gave the overall trend as -1.7% per decade.

To investigate the trends under low (F10.7 = 70 sfu) and high (F10.7 = 210 sfu) solar activity conditions, simulations were performed with the varying historic CO_2 values, but at fixed solar activities. This resulted in trends under low solar activity of -2.2% per decade at 350 km and -2.9% per decade at 450 km, and trends under high solar activity of -0.7% per decade at 350 km and -0.8% per decade at 450 km. Qian and Solomon (2011) revisited the data from this study, showing how the trend over all solar activity values varied with altitude between 150 and 400 km rather than only stating values at specific altitudes. Qian and Solomon (2011) also showed how neutral temperatures and densities vary with carbon dioxide concentrations up to 800 ppm. As these can be used to explore future density reductions, this is discussed later in Section 3.1.5.

Cnossen (2009) used the Coupled Middle Atmosphere and Thermosphere version 2 (CMAT2) model to simulate DOY 80 (equinox) and DOY 172 (solstice) in the years 1965 (CO_2 concentration of 320 ppm) and 1995 (360 ppm) during low solar activity (F10.7 = 80 sfu). Focusing on the Mesosphere and Lower Thermosphere (MLT), results were given between $\sim$15 km and $\sim$280 km and no global annual average was given. However, the trend within these altitudes was shown to vary between the two

modelled days, with a trend of -1.7% per decade at 280 km altitude during equinox and -3.8% per decade during solstice. The seasonal impact on density trends was also briefly examined by Emmert et al. (2008) through the day-of-year dependence of the observed trends. However, across all other studies, annual averages take precedence.

The impact of solar activity was also investigated, simulating DOY 80 and 172 with F10.7 values of 80, 100, 125, 150, 175 and 200 sfu. During equinox, the magnitude of the trend above $\sim$ 175 km was inversely proportional to solar activity, while during solstice the largest magnitude of trend was seen for medium solar activity. Geomagnetic activity was varied for the F10.7 = 80 sfu runs, using Kp values of 2+, 4o, and 6-. However this had minimal impact on the overall density trend, on the order of 0.1% per decade at 250 km.

Each trend profile presented in Cnossen (2009) showed more variability with altitude than the other model studies, as seen later in Figure 3.1. This is likely due to the single-day modelling and an acknowledged possibility of numerical instability in the CMAT2 model.

Solomon et al. (2015) used TIME-GCM to simulate the thermosphere at $2.5^\circ \times 2.5^\circ \times H/4$ resolution during 1996 (CO_2 concentration of 363 ppm) and 2008 (386 ppm). This was done for solar activity levels of F10.7 equal to 70, 135, and 200 sfu, returning trends at 400 km of -4.9, -2.6, and -1.8% per decade respectively. The model's CO_2-O quenching rate (a.k.a collisional deactivation rate), k_q was identified to have a substantial impact on the trend due to thermospheric cooling relying on this mechanism, as detailed further by Akmaev (2003). The values given above relate to the model using $k_q = \sim 1.5 \times 10^{-12}$ cm^{3}s^{-1}, but the simulations were also performed at the higher value of 3.0×10^{-12} cm^{3}s^{-1}. This caused the trends to increase in magnitude to -6.8, -3.3 and -2.1% per decade for the same solar activity levels. Feofilov et al. (2012) summarizes the historically observed k_q rates, with recent measurements varying between 0.5×10^{-12} and 6.0×10^{-12} cm^{3}s^{-1}, with modern models such as WACCM-X using $k_q = 3.0 \times 10^{-12}$ cm^{3}s^{-1} as their default value.

Solomon et al. (2018) and Solomon et al. (2019) used the same methodology and model (WACCM-X), with the first exploring trends during low solar activity (F10.7 = 70 sfu) and the latter high solar activity (F10.7 = 200 sfu). Both used a resolution of 1.9° in latitude, 2.5° in longitude and H/4 above 1 hPa. In each study, two 5-year simulations were performed, one for the period 1972-1976 and one for 2001-2005, to provide ensembles around the years 1974 (CO_2 concentration of 330 ppm) and 2003 (375 ppm) and account for interannual variability. Annual means were taken, followed by global means, and finally an average across the five years of simulation. The two results were then compared to obtain the trends over the 1974-2003 period, retrieving the results at 400 km of -3.9% per decade in Solomon et al. (2018) (F10.7 = 70 sfu) and -1.7% per decade in Solomon et al. (2019) (F10.7 = 200 sfu). Trends were plotted from

ground-level through to 400 km. While the interannual variability of density was not directly explored, this was done for temperature. Within Solomon et al. (2018), the global mean annual mean temperature varied by ±1.2 K at 400 km around the 5-year means, only ∼0.2% of the modelled ∼ 685 K temperatures at that altitude. Similarly in Solomon et al. (2019), there is a variation at 400 km of around ±2.0 K or ∼ 0.2% around the near 1200 K 5-year means.

Cnossen (2020) performed a single simulation of the period 1950 to 2015 with a transient run of WACCM-X 2.0 using historic forcings. Global means were calculated and the variation due to solar and geomagnetic activity was removed through standard multilinear regression. This was identified as being complex due to the large amplitude of the solar cycle and long-term trends in the solar and geomagnetic activity over the period of simulation. Three regression models were used, the simplest being

$$Y = A + B \times F10.7a_{81} + trend \times year \tag{3.15}$$

where Y is the variable of interest (here, density), $F10.7a_{81}$ is the 81-day centered average F10.7. The second regression model added a geomagnetic activity term to give

$$Y = A + B \times F10.7a_{81} + C \times K_p + trend \times year \tag{3.16}$$

And the final model added a term for $(F10.7a_{81})^2$ to give

$$Y = A + B \times F10.7a_{81} + C \times K_p + D \times (F10.7a_{81})^2 + trend \times year \tag{3.17}$$

Both the first and second models retrieved a historic trend in global mean neutral density of $-5.5 \pm 0.9\%$ per decade at 400 km with an R^2 of 0.86, indicating the Earth's changing magnetic field had no impact on the global mean neutral density trend. However, the third model gave a trend of $-2.8 \pm 0.6\%$ per decade with an improved fit for R^2 of 0.94. While other studies such as Emmert (2015b) had included the $(F10.7a_{81})^2$ term in their regression model, Laštovička and Jelínek (2019) highlighted that it was not standard practice despite the better fit.

3.1.4 Summary of Historic Density Trends

As observations and models of the historic density trend have evolved, giving the trend at 400 km altitude has emerged as a way of cross comparison between studies. Table 3.2 provides a summary of these trends for low, high, and all solar activity levels, along with the time period over which the trend has been calculated.

Figure 3.1 plots the modelled and observed trends with their respective altitudes, using the trend for medium solar activity where available and noting otherwise.

TABLE 3.2: Summary of the historic neutral density trends at 400 km altitude from observations and models. Blue rows are trends in low solar activity, red for high, while the others are for overall trends. "Model used" refers to the atmospheric model used to obtain reference densities in the observational studies.

Study	Type [a]	Model Used	F10.7 (sfu)	Period	Density Trend (% per decade)
Keating et al. (2000) [b]	O	MET99	∼75	1976, 1986, 1996	-4.9 ± 1.3
Emmert et al. (2004)	O	NRLMSISE-00	≤90	1996 - 2001	-3.8
Emmert et al. (2004)	O	NRLMSISE-00	All	1996 - 2001	-2.8 ± 1.0
Marcos et al. (2005)	O	NRLMSISE-00	All	1970 - 2000	-1.7 ± 0.2
Qian et al. (2006)	M	TIME-GCM (1D)	70	1970 - 2000	-2.5 [c]
Qian et al. (2006) [d]	M	TIME-GCM (1D)	All	1970 - 2000	-1.7
Qian et al. (2006)	M	TIME-GCM (1D)	210	1970 - 2000	-0.75 [c]
Emmert et al. (2008)	O	GAMDM	<75	1967 - 2007	-5.5 ± 1.4
Emmert et al. (2008)	O	GAMDM	170 to 220	1967 - 2007	-2.1 ± 0.9
Saunders et al. (2011)	O	NRLMSISE-00	<90	1970 - 2010	-7.2
Saunders et al. (2011)	O	NRLMSISE-00	All	1970 - 2010	-5.4 ± 3
Saunders et al. (2011)	O	NRLMSISE-00	>90	1970 - 2010	-4.0
Emmert and Picone (2011)	O	GAMDM	All	1967 - 2005	-1.94 ± 0.68
Emmert (2015b)	O	GAMDM2.1	60 to 75	1967 - 2005	-3.1 ± 1.6
Emmert (2015b)	O	GAMDM2.1	60 to 75	1967 - 2013	-7.2 ± 1.2
Emmert (2015b)	O	GAMDM2.1	180 to 500	1967 - 2005	-3.0 ± 0.7
Emmert (2015b)	O	GAMDM2.1	180 to 500	1967 - 2013	-3.0 ± 0.8
Solomon et al. (2015)	M	TIME-GCM	70	1996 - 2008	-4.9 or -6.8 [e]
Solomon et al. (2015)	M	TIME-GCM	200	1996 - 2008	-1.8 or -2.1 [e]
Solomon et al. (2018)	M	WACCM-X	70	1974 - 2003	-3.9
Solomon et al. (2019)	M	WACCM-X	200	1974 - 2003	-1.7
Cnossen (2020)	M	WACCM-X 2.0	All	1950 - 2015	-2.8 ± 0.6
Brown et al. (2021)	M	WACCM-X	70	1975 - 2005	-5.8

[a] M stands for Model, and O for Observation
[b] 350 km altitude
[c] Average of the 350 *km* and 450 *km* values
[d] Result was re-presented by Qian and Solomon (2011)
[e] k_q, CO_2-O collisional deactivation rate, of $\sim 1.5 \times 10^{-12} \mathrm{cm}^3\mathrm{s}^{-1}$ and $3.0 \times 10^{-12} \mathrm{cm}^3\mathrm{s}^{-1}$

Among the models that focused on ground level upwards, there is a small increasing trend in neutral density in the lower atmosphere. Above ∼40 km, all studies found decreasing neutral densities with the magnitude of the trend peaking around the homopause at ∼110 km with values of −3 to −6 % per decade, reaching −0.9 to −3.5 % per decade in the lower parts of the thermosphere (180 - 250 km). Above ∼250 km and notably through the LEO region, the negative trend increases in magnitude with altitude.

Fewer studies focus on the trends at higher altitudes. Decreasing atmospheric drag with altitude leads to other orbital perturbations and their associated uncertainties becoming more dominant, making it harder to isolate the orbit-derived density trends. Trends modelled by general circulation models are limited by their upper boundaries. These upper boundaries could be increased in altitude by adding the extremely-low density chemistry and dynamics of the helium and hydrogen dominated parts of the higher thermosphere. However, validating the modelling of this region is complicated by the limited in-situ measurements and the difficulty in obtaining orbit-derived densities.

While thermospheric densities depend upon solar activity, the density trend also relies upon solar activity, as discussed by Mlynczak et al. (2016). The studies which explored the solar activity dependence are summarised in Figure 3.2. The reported density trends are for instantaneous F10.7 values, and so independent of a solar cycle's maximum solar activity. A higher magnitude and larger spread in the trend is found during low solar activity compared to high solar activity in all studies. Emmert (2015b) discusses the mismatch between trends from observations and models at low solar activity, stating how the long-term decrease in solar activity at solar minimum, as seen in Figure 2.7, complicates resolving the long-term density decrease due to CO_2. Each of the Emmert studies using orbital data have higher resolution in F10.7 than any of the other studies, with Emmert et al. (2008) and Emmert (2015b) suggesting trends reach their smallest magnitude during medium solar activity levels. The resolution in F10.7 in the studies using general circulation models is poor, with all but Solomon et al. (2015) only using low and high solar activity levels. The density trend of Solomon et al. (2015) during medium solar activity does not reach a minimal magnitude like the Emmert observations. While only based on one study, this suggests a disagreement in the relationship of density trends to F10.7 between the orbit-derived observations and the GCM modelled trends.

3.1.5 Future Density and Temperature Trends

The first studies of density trends explored the impact a doubling of carbon dioxide concentration would have upon the thermosphere. While it is unclear in which year these doubled concentrations would be reached, they still represent exploration of

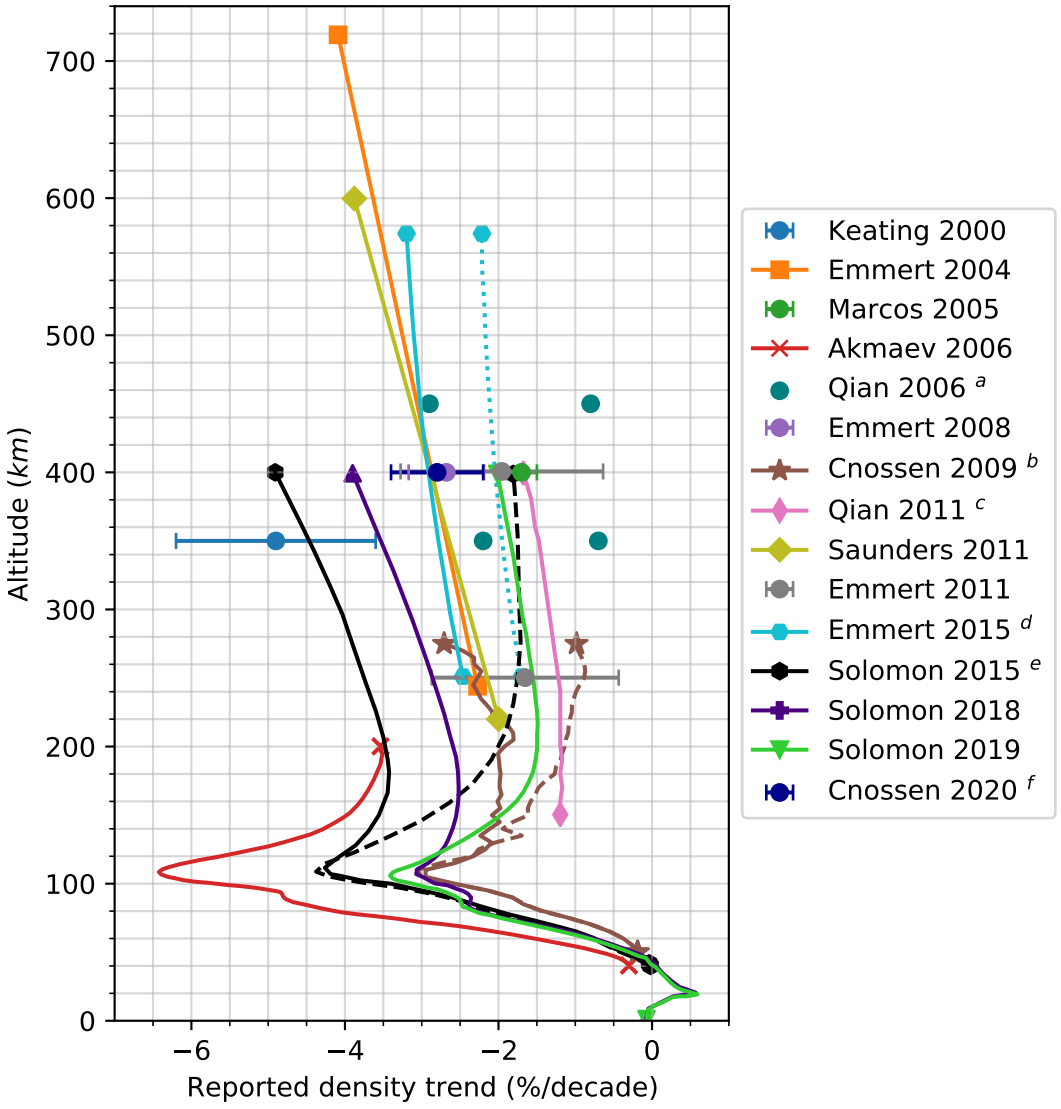

FIGURE 3.1: Summary of how reported density trends vary with altitude for overall solar activity levels (except low and high solar activity only where noted). Error bars on individual data points are provided where available. Figure updated from a similar one by Cnossen (2012).

[a] At each altitude, the more negative value is for low solar activity (F10.7 = 70 sfu), while the other is for high solar activity (F10.7 = 210 sfu). The value given at 400 km is equivalent to Marcos et al. (2005) without errors.

[b] Average of the DOY 80 and DOY 172 graphed data, with the solid line denoting low solar activity (F10.7 = 70 sfu), and dashed the high solar activity (F10.7 = 200 sfu).

[c] Qian and Solomon (2011) revisited the data from Qian et al. (2006), plotting the trend with altitude for medium solar activity levels.

[d] Dotted line denotes the trend derived over the period 1967 to 2005, while solid denotes the trend over 1967 to 2013.

[e] Dashed line denotes the high solar activity (F10.7 = 200 sfu) trend, while solid is for the low solar activity (F10.7 = 70 sfu), with both using the CO_2–O quenching rate, k_q = 1.5×10^{-12}

[f] Trend obtained from the third regression model which included an $(F10.7a_{81})^2$ term

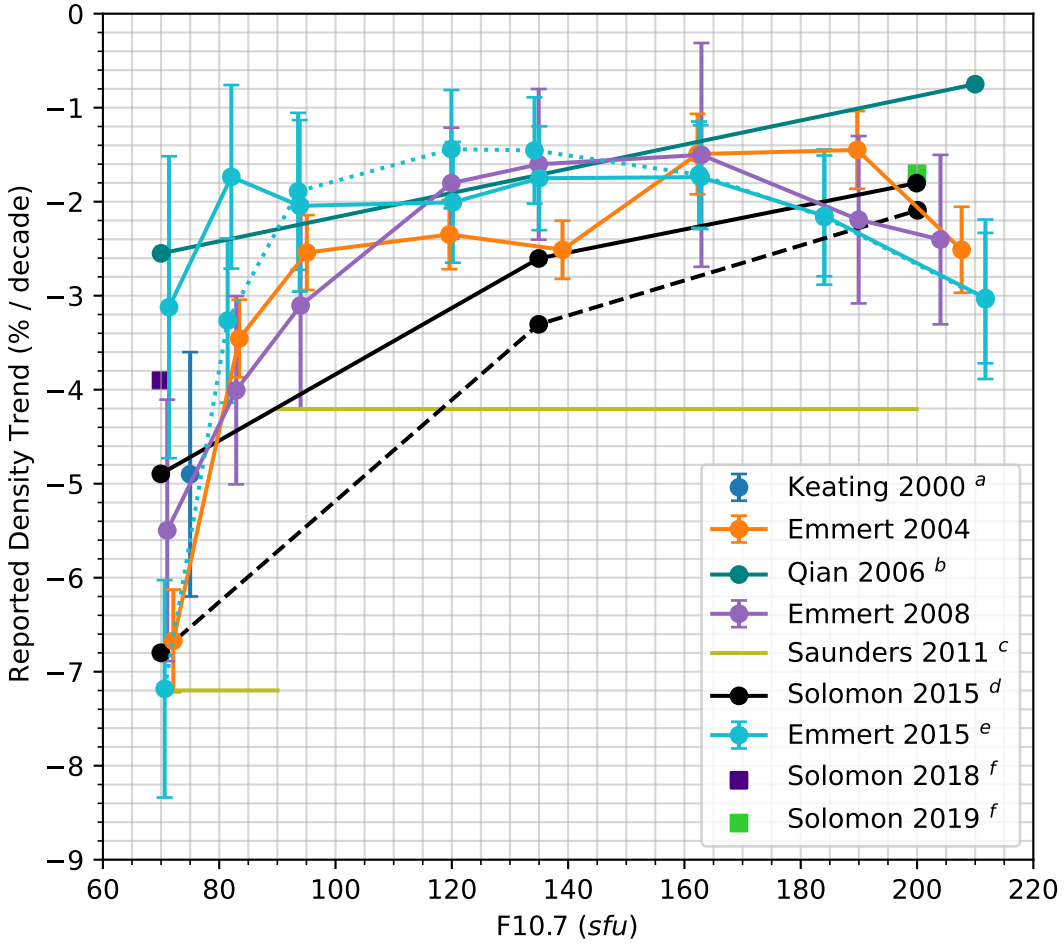

FIGURE 3.2: Summary of historical density trends at 400 km for varying solar activity levels. Error bars on individual data points are provided where available. The colours used for each study match those of Figure 3.1. Figure updated from similar in Emmert et al. (2008) and Solomon et al. (2015).
[a] Keating et al. (2000) value at 350 km only.
[b] Plotted line is mean of 350 and 450 km trends in Qian et al. (2006).
[c] Saunders et al. (2011) used large binning for F10.7, so the lines denote trends found for F10.7 < 90 and F10.7 > 90.
[d] Solomon et al. (2015) trend varied with the CO_2–O quenching rate, k_q, used in the model. The solid line denotes the default k_q of the model (1.5×10^{-12}), while dashed denotes a higher k_q (3.0×10^{-12}).
[e] Emmert (2015b) calculated the trend over different periods. The solid line denotes 1967 to 2005 and the dotted line denotes 1967 to 2013.
[f] Solomon et al. (2018) and Solomon et al. (2019) use the same methodology, but at low and high solar activity values respectively.

future scenarios. Roble and Dickinson (1989) showed that a doubling of carbon dioxide concentration from the 1950's value of 330 ppm would lead to a 50 K cooling of the thermosphere. Rishbeth and Roble (1992) explored the impact on total mass density for the first time, finding a reduction in density of 40% at heights of 100-300 km for a doubling of CO_2 concentration.

The only study to directly explore future density trends under varying CO_2 concentrations was performed by Qian and Solomon (2011). They used the same methodology as Qian et al. (2006) to find historic density trends, namely using a global mean version of TIE-GCM with a transiently varying ground-level carbon dioxide concentration. Neutral density at 400 km and with F10.7 = 150 sfu was given for carbon dioxide concentrations between 200 and 800 ppm. This is reproduced in Figure 3.3 as the neutral density relative to that modelled at 370 ppm (equivalent to the year 2000). However, this study was limited in scope, with no other solar activity levels explored, nor the density reductions tied to carbon dioxide concentrations scenarios such as the RCPs.

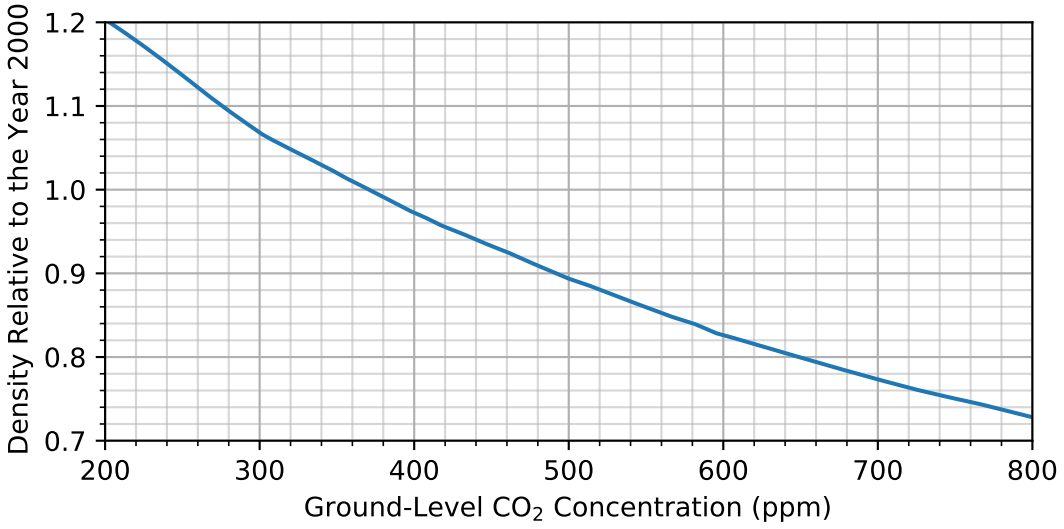

FIGURE 3.3: The historic and future globally averaged neutral density at 400 km against CO_2 concentrations of Qian and Solomon (2011). Repeated here as relative densities compared to the density seen at a CO_2 concentration of 370 ppm, equivalent to the year 2000, rather than the neutral density originally presented.

The fact that orbit-derived density trends have been derived from objects in the space environment highlights the impact the density trend is already having on objects in LEO. This will continue into the future and impact the space debris in LEO too. However the small number of studies presented in this section highlights the limited state of knowledge of future density trends.

3.1.6 Density Trends due to Other Factors

While the increase in CO_2 concentration will have the largest impact on neutral density trends in the thermosphere, changes in both the Earth's magnetic field and in ozone concentration will have much smaller, albeit substantial effects.

The Earth's magnetic field changes slowly over time, interacts with the ionosphere, changes the amount of heating via charged particles within the thermosphere, and in turn affects thermospheric densities. Cnossen (2014) explored the historic impact due to the weakening magnetic field over the period 1908 to 2008 with TIE-GCM, using the International Geomagnetic Reference Field (IGRF) for 1908 and 2008. Results were dependent upon magnetic latitude, with 10 K cooling of the neutral temperature at 300 km altitude near the northern magnetic pole, warming of 12 K at the southern magnetic pole, and reaching a minimum of 4 K warming in between the two poles. The overall warming trend was consistent with the weakening magnetic field. However the trend over a 100 year period was not substantial, and would only lead to a slight increase in thermospheric densities, whose magnitude was not stated. A separate series of similar simulations were performed, but with carbon dioxide concentrations fixed at 300 and 385 ppm for the years 1908 and 2008 respectively. These showed the magnetic field and carbon dioxide trends were independent of each other.

Cnossen and Maute (2020) explored the impact Earth's changing magnetic field will have on thermospheric densities from 2015 to 2065. TIE-GCM was used, with one simulation using the IGRF-12 for 2015, and another the magnetic field prediction for 2065 by Aubert (2015) (no carbon dioxide concentration changes). Comparing these two individual year-long simulations showed the thermospheric densities increased for all magnetic latitudes, with only small differences seen between the north and south hemispheres. The global mean neutral density over the 50 year period was seen to increase by $\sim$1% during low geomagnetic activity, and $\sim$2% during high, equivalent to a 0.2 and 0.4% increase per decade respectively, an order of magnitude smaller than the absolute value of historic carbon dioxide trends, albeit with the opposite sign.

Cnossen (2009) explored the number density trends due to changes in ozone concentration alongside the trends due to carbon dioxide (discussed in Section 3.1.3). The ozone concentrations of 1965 and 1995 were added alongside the changed carbon dioxide concentrations in additional CMAT2 runs, resulting in an additional reduction of around 0.3% per decade between 125 and 280 km. Ozone absorbs UV in the stratosphere, causing heating within the region. But with reducing ozone concentrations during the modelled period (Solomon (1999)), the amount of UV heating reduced, cooling the MLT and leading to thermospheric contraction similarly to carbon dioxide upper atmosphere cooling. However, stratospheric ozone

concentrations are recovering (Stone et al. (2018)). This may see a reversing of the trend, but this has yet to be modelled.

3.2 Space Debris Modelling

3.2.1 Particles-in-a-Box Debris Model

Talent (1992) introduced a simple, differential equation to describe debris population growth under a 'Particles-in-a-Box' (PIB) assumption. The differential equation took the form of

$$\frac{dN}{dt} = A + BN + CN^2 \tag{3.18}$$

where N is the number of objects in the environment, A is the deposition coefficient, B is the atmospheric decay coefficient, and C is the collision coefficient. The deposition coefficient accounts for objects being added into the environment through launches and non-collision fragmentations (i.e. explosions), but also accounts for objects being removed at a fixed rate by Active Debris Removal (ADR). The atmospheric decay coefficient accounts for the rate at which objects are removed from the environment by atmospheric drag. Finally, the collision coefficient accounts for both the collision frequency within the environment and the number of fragments created during collisions, i.e. the rate at which objects are added by collisions. The collision frequency can be obtained separately by following the kinetic theory of gases, giving rise to the original name of the model.

As equation 3.18 takes the form of a quadratic equation, it can be solved by the quadratic formula, resulting in

$$N_{1,2} = \frac{-B \pm \sqrt{B^2 - 4AC}}{2C} \tag{3.19}$$

where $N_{1,2}$ are the two roots of the equation. The terms within the square root, q, can be identified as

$$q = B^2 - 4AC = \text{sink terms} - \text{source terms} \tag{3.20}$$

The value of q illustrates three different, possible behaviours of the debris population:

- $q > 0$, Sinks $>$ Sources, Conditionally stable
- $q = 0$, Sinks $=$ Sources, Instability threshold
- $q < 0$, Sinks $<$ Sources, Unconditionally Unstable

The conditionally stable case is shown in Figure 3.4. When the population is less than N_1, it grows asymptotically towards N_1 as $dN/dt > 0$. When the population is greater than N_1 but less than N_2, $dN/dt < 0$ so the population decays asymptotically to N_1. Therefore as long as the total number of objects stays below N_2, the population exhibits stable behaviour. However, when the population is greater than N_2, $dN/dt > 0$ so the number of objects grows without an upper bound. In reality, the growing number of collisions would lead to increasingly small fragments with greater area-to-mass ratios, increasing their atmospheric decay rate.

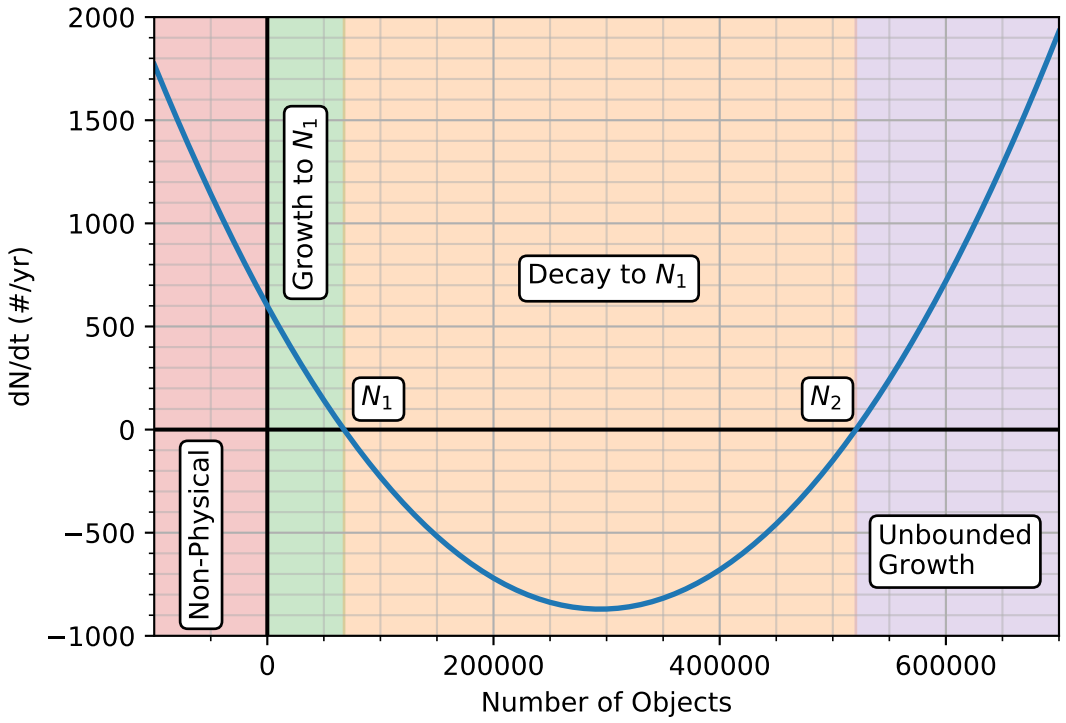

FIGURE 3.4: Illustration of stability in the Particles-in-a-Box model when the environment is conditionally stable. Reproduction of a similar figure presented by Talent (1992)

This version of the model treats every object as if they have the same characteristics. Alternatively, the environment can be split into separate species, for example by mass or altitude. Equation 3.18 would then be extended to apply to each individual species, with each species having their own value for the deposition and atmospheric decay constants, A and B. The collision coefficient, C, has to account for interactions between species. Determining each interaction's value for C becomes increasingly complex, and the simplicity of the model is lost.

The single species PIB model helps to illustrate how the debris population can evolve, how it is dependent upon the sinks and sources, and certain concepts such as a critical numbers of object above which the total number of objects will continually grow.

However, if further insight into the debris environment is required, more complex models have to be used.

3.2.2 Evolutionary Debris Models

Modelling individual objects, the evolutionary debris models can capture the full variability of objects and orbits within the space environment at the cost of being complex and computationally expensive. Examples include the University of Southampton's Debris Analysis and Monitoring Architecture to the Geosynchronous Environment (DAMAGE) developed by Lewis et al. (2001), NASA's LEO to GEO Environment Debris Model (LEGEND) by Liou et al. (2004) and ESA's Debris Environment Long Term Analysis (DELTA) model by Martin et al. (2004).

Evolutionary debris models are made up of constituent models, with each tackling a specific part of the overall problem. An illustration of these constituent models and how they interact is given in Figure 3.5.

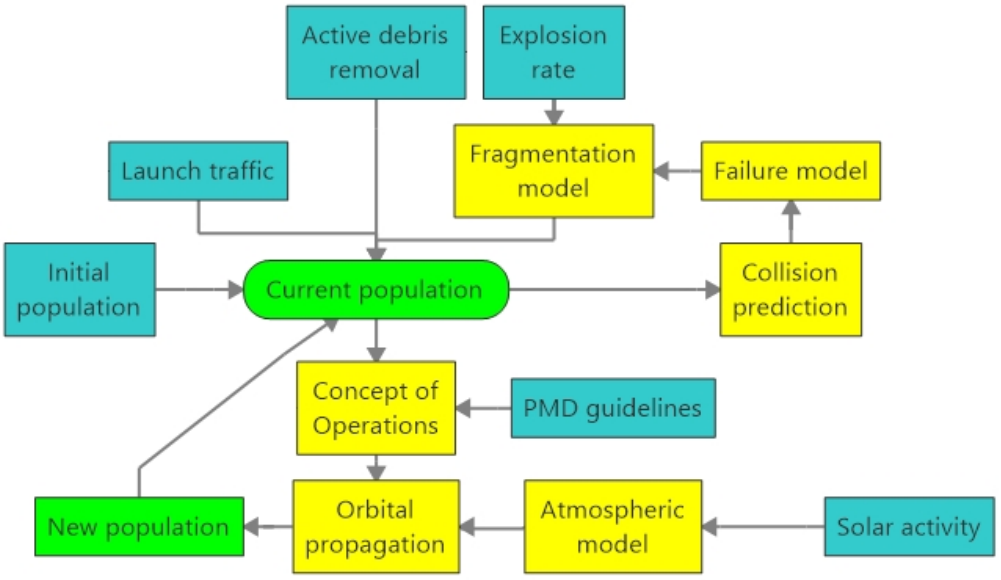

FIGURE 3.5: Conceptual map of a debris evolution model. Yellow boxes show support models, blue boxes show variable inputs, and green boxes the tracked populations.

Initial populations are used to initialise the model from a reference epoch, usually sourced from the TLE database or ESA's Database and Information System Characterising Objects in Space (DISCOS), as described by McLean et al. (2017). Launch traffic is often sourced from DISCOS too. As future launch traffic is unknown, a historical period is often repeated when predicting into the future. Without these

launches, there would not be a source of additional mass into the environment. This method of repeating traffic also provides historically realistic launch rates and orbit usage over purely random launches. However, humanity's use of space is changing, for example through the launch of mega-constellations. To reflect this when modelling scenarios involving these, specifically designed constellation launches are included in addition to the repeating historic launches (for example, in the study by Lewis et al. (2017)).

The orbits of objects within the population are propagated with an orbital propagator. One example is the Simplified General Perturbations, SGP4, propagator which was updated by Vallado and Crawford (2008). Computation speed is a major factor when doing multi-decade runs looking at many thousands of objects. Therefore empirical atmospheric models such as J77 and NRLMSISE-00 are commonly used to obtain thermospheric densities. Inclusion of the solar cycle within debris modelling is key, as the order of magnitude increase in thermospheric densities during solar maxima clears a greater number of objects from LEO than during solar minima. However, predicting future solar activity is currently impossible, but an active area of research as demonstrated by Hathaway (2015) and McIntosh et al. (2020). Therefore evolutionary models often account for the solar cycle either through the use of a sinusoidal function or repeating historic solar cycles.

Collision assessment is the next major part of debris modelling and is explored in more detail in Section 3.2.2.1. In general, the orbits of each pair of objects are assessed to confirm they can have a close approach and if this is the case, further assessed to determine if a collision has occurred. Debris from the collision is created using a fragmentation model. The NASA Standard Breakup Model described by Johnson et al. (2001) is the most commonly used and is explored in detail in Section 3.2.2.2.

Extra constituent models can be added depending upon the scenario being investigated, with some examples being Active Debris Removal (ADR) identifying and removing objects most at risk of creating a large amount of debris (see McKnight et al. (2021)), a Concept of Operations (CONOPS) to simulate mission-related orbital changes such as Post Mission Disposal (PMD), and explosions, which can be represented by a probability or by repeating historical explosions (for example, via the historical catalogue of Anz-Meador et al. (2018)).

There are numerous sources of uncertainty within these models. A very simple example can be demonstrated by assigning an object a random chance to explode in any given time step. While in one simulation, it may explode in the very first time step and cause a cascade of additional events, in another simulation it may never explode. To account for this, Monte Carlo simulations are performed, repeatedly simulating the environment. These simulations are analysed together to provide a distribution of

possible outcomes from which parameters can be retrieved such as the mean and standard deviation of the total number of objects.

3.2.2.1 Collision Probability

Calculating the probability of a collision between two orbiting objects plays a major part in debris modelling. This section will explore two different methods for calculation, firstly the "classical" approach of the asteroid collision probability algorithms which focus on sampling in space, and then the Cube approach, widely used in debris evolution models and which samples in time.

Öpik (1951) laid the groundwork for handling orbital collisions statistically by mathematically describing the case where a "test body" in an elliptical orbit would collide with a "field body". This required the orbital elements (a, e, i) as well as the radius, r, of the test body, and the corresponding values for the field body, which were denoted by a_0, e_0, i_0, and r_0. As the work focused on the probability of asteroids in eccentric orbits colliding with planets, an approximation was made early on in the calculations that the field body (i.e. the planet) is in a circular orbit with e_0 set to 0. A correction factor was added later to account for non-circular orbits.

Wetherill (1967) extended Öpik's work and addressed the correction factor by avoiding the field body's circular orbit approximation, allowing both bodies to have elliptical orbits throughout the calculation. However, a new assumption was made, namely that the true anomaly of closest approach for each orbit was uniformly distributed between 0 and 2π radians. This assumption was made to allow for Monte Carlo integration within the probability function. As an object in an eccentric orbit spends longer at its apoapsis than its periapsis, on average a close approach is more likely to occur near the apoapsis. Therefore at larger eccentricities, increasingly large errors would be introduced, requiring a correction in a similar way to the Öpik algorithm.

Greenberg (1982) further generalized the work of Wetherill (1967) by removing the assumption of uniform distribution of the true anomaly of closest approach, instead effectively integrating over the mean anomaly to account for the fact that orbital intersections were more likely in the sections of the orbit where the object spent the most time. This complicated the geometry and mathematics of the problem, but a brief overview will be given here for context. A full mathematical derivation of Greenberg (1982) is given in Appendix B, which also highlights some misprints in the original paper.

The probability was separated into two parts: (1) the probability of the orbits being close enough for a collision to be possible and, when they are close enough to collide, (2) the probability that both bodies will be close enough at the same time. Multiplying

these two parts together results in an equation for the collision rate, $P_{Greenberg}/dt$, between a field body (fixed a, e, i) and test body (fixed a_0, e_0, i_0) given a uniform distribution of right ascension of ascending nodes for both bodies, Ω and Ω_0, and their arguments of perigee, ω_0 and ω. This collision rate is described by

$$P_{Greenberg}/dt = \frac{16\tau}{(2\pi)^3} \int_0^{2\pi} \int_{\omega_0} \left(\frac{f}{sin(u-\omega)} \right) \left(\frac{\pi P_0}{4T_P} \right) d\omega_0 d(\Delta\Omega) \tag{3.21}$$

where τ is the sum of the radii of the two objects, f is a function accounting for the difference between an exact intersection of the orbits and the current geometry, u is the angle from the test body's ascending node to the intersection node of the two orbits, P_0 is the fraction of an orbit that the field object physically crosses over the test orbit (if they lined up perfectly), T_P is the orbital period of the test object, and $\Delta\Omega$, the difference in right ascension of ascending node of the two bodies.

There is a correction to the Greenberg algorithm given in Bottke and Greenberg (1993). As an inverse cosine returns a positive and a negative angle, a pair of cosines return a total of four possible pairs of solutions (+ +, - +, + -, and - -). Therefore in Greenberg (1982), a factor of 4 was included to account for values of $(u-\omega, u_0-\omega_0)$ that arise from a single set of $cos(u-\omega), cos(u_0-\omega_0)$ values, (specifically in Equation B.57). However, the relative velocity between the two objects for each possible $(u-\omega, u_0-\omega_0)$ varies, and in the Greenberg algorithm this had not been addressed. Correcting for this brought the collision probabilities closer to those calculated using other methods (as will be seen in Table 3.3). It is also worth briefly highlighting Manley et al. (1998), who followed a similar method to Greenberg with the Bottke correction, but changed reference frame and used vector maths to provide an alternative approach which produced the same results.

The Cube approach of Liou et al. (2003) is commonly used in evolutionary debris models. Whereas the previously discussed collision probability algorithms used uniformly distributed right ascension of ascending node, Ω, argument of perigee, ω, and true anomaly, θ, the Cube algorithm uses the true value of each of these. The modelled space is split into cubes, and each cube is checked to see if there are multiple objects residing within, and then the collision rate , $P_{i,j}$ between object i and object j, is given as

$$P_{i,j} = s_i s_j V_{imp} \sigma dU \tag{3.22}$$

where s_i and s_j are the spatial densities of object i and j within the cube, V_{imp} is the relative velocity between the two objects, σ is the collisional cross-sectional area, and dU is the volume of the cube. This is equivalent to the collision frequency between two particles within the kinetic theory of gas.

TABLE 3.3: Comparison of the intrinsic collision probability (10^{-18} km^{-2}yr^{-1}) between a theoretical asteroid named Astrid and the given example bodies using the Wetherill (1967) (W), Greenberg (1982) (G), Greenberg with Bottke and Greenberg (1993) correction (G+B), and Cube (Liou et al. (2003)) algorithms. Astrid's orbital elements are (a,e,i)=(2.75, 0.27, 0.28). Units of semi-major axis (a) are astronomical units, and inclination (i) is given in radians.

Object	a	e	i	W	G	G+B	Cube
1948 EA	2.26	0.61	0.32	3.10	2.49	3.20	3.23
Apollo	1.48	0.56	0.11	4.22	3.24	3.60	3.77
Adonis	1.97	0.78	0.04	4.13	3.92	4.53	4.79
1950 DA	1.70	0.51	0.21	3.90	3.13	3.76	3.65
Encke	2.21	0.85	0.22	3.49	2.91	3.43	3.64
Brorsen	3.01	0.81	0.51	0.49	0.81	0.95	1.01

To best capture the true nature of collisions within the system, Liou et al. (2003) suggested using cubes with a size of 1% or less of the average semi-major axis of objects. The algorithm benefits from computation time scaling with the number of cubes used. So computation times increase with N rather than N^2 for an N-body system.

Wetherill (1967) gave the collision probabilities between a hypothetical asteroid named Astrid, and a number of other bodies. These have since been used in following studies to allow direct comparison of calculated collision probabilities between studies, and have been reproduced in Table 3.3. While there are notable differences between the Wetherill-Öpik series of algorithms, due to the addressed issues, the difference between the Greenberg and Cube algorithms is much smaller.

3.2.2.2 Collision Fragmentation Model

The NASA standard breakup model by Johnson et al. (2001) is the most commonly used fragmentation model, with a correction published by Krisko (2011). It provides functions to calculate the number and size of fragments, along with the change in velocity, ΔV, imparted to the fragments during the collision. These functions have been fitted to the data obtained from in-orbit collisions and ground-based impact tests of Satellite Orbital Debris Characterization Impact Test (SOCIT) in 1991 and 1992. A newer impact test, DebriSat, has been performed, but has yet to be used to improve the breakup model as the cataloging of fragments is still taking place (Ausay et al. (2017)).

Collisions are separated into two groups, depending upon the relative kinetic energy of the smaller object divided by the mass of the larger object. McKnight et al. (1991) determined that if this value was greater than 40 J/g, the collision was deemed catastrophic and both objects are completely destroyed. If the value is less than 40 J/g,

the collision is non-catastrophic, where the smaller object is destroyed while damaging or disabling the larger object. The number of fragments, N, of a given characteristic length, L_c, or larger, is given by

$$N(L_c) = 0.1M^{0.75}L_c^{-1.71} \tag{3.23}$$

where L_c is given in metres, and the mass, M, is given in kg. In a catastrophic collision, M is equal to the sum of the two objects' masses. However, in the case of a non-catastrophic collision, M is equal to the mass of the smallest object multiplied by the square of the relative impact speed. This was a correction published by Krisko (2011).

Separate area-to-mass distributions are given for rocket bodies and spacecraft, with the spacecraft's area-to-mass distribution, $D_{A/m}^{S/C}$, as a function of L_c given by

$$D_{A/m}^{S/C}(\lambda_c, \chi) = \alpha^{S/C}(\lambda_c)N(\mu_1^{S/C}(\lambda_c), \chi) + (1 - \alpha^{S/C}(\lambda_c))N(\mu_2^{S/C}(\lambda_c), \sigma_2^{S/C}(\lambda_c), \chi) \tag{3.24}$$

where

$$\lambda_c = log_{10}(L_c)$$
$$\chi = log_{10}(A/m)$$

and $N(\mu, \sigma, \chi)$ is the normal distribution of form

$$N(\mu, \sigma, \chi) = \frac{1}{\sigma\sqrt{2\pi}}e^{-\frac{1}{2}\left(\frac{\chi-\mu}{\sigma}^2\right)} \tag{3.25}$$

with mean, μ, and standard deviation, σ, around the value χ, with the values used in Equation 3.24 given by

$$\alpha^{S/C} = \begin{cases} 0 & \lambda_c \leq -1.95, \\ 0.3 + 0.4(\lambda_c + 1.2) & -1.95 < \lambda_c < 0.55, \\ 1 & \text{if } \lambda_c \geq 0.55. \end{cases}$$

$$\mu_1^{S/C} = \begin{cases} -0.6 & \text{if } \lambda_c \leq -1.1, \\ -0.6 - 0.318(\lambda_c + 1.1) & \text{if } -1.1 < \lambda_c < 0, \\ -0.95 & \text{if } \lambda_c \geq 0. \end{cases}$$

$$\sigma_1^{S/C} = \begin{cases} 0.1 & \text{if } \lambda_c \leq -1.3, \\ 0.1 + 0.2(\lambda_c + 1.3) & \text{if } -1.3 < \lambda_c < -0.3, \\ 0.3 & \text{if } \lambda_c \geq -0.3. \end{cases}$$

$$\mu_2^{S/C} = \begin{cases} -1.2 & \text{if } \lambda_c \leq -0.7, \\ -1.2 - 1.333(\lambda_c + 0.7) & \text{if } -0.7 < \lambda_c < -0.1, \\ -2.0 & \text{if } \lambda_c \geq -0.1. \end{cases}$$

$$\sigma_2^{S/C} = \begin{cases} 0.5 & \text{if } \lambda_c \leq -0.5, \\ 0.5 - (\lambda_c + 0.5) & \text{if } -0.5 < \lambda_c < -0.3, \\ 0.3 & \text{if } \lambda_c \geq -0.3. \end{cases}$$

The distribution function for objects with a characteristic length less than 8 cm is given by

$$D_{A/m}^{SOC}(\lambda_c, \chi) = N(\mu^{SOC}(\lambda_c), \sigma^{SOC}(\lambda_c), \chi) \tag{3.26}$$

where

$$\mu^{SOC} = \begin{cases} -0.3 & \text{if } \lambda_c \leq -1.75, \\ -0.3 - 1.4(\lambda_c + 1.75) & \text{if } -1.75 < \lambda_c < -1.25, \\ -1.0 & \text{if } \lambda_c \geq -1.25. \end{cases}$$

$$\sigma^{SOC} = \begin{cases} 0.2 & \text{if } \lambda_c \leq -3.5, \\ 0.2 + 0.1333(\lambda_c + 3.5) & \text{if } \lambda_c > 3.5. \end{cases}$$

with a function used to bridge the gap between 8cm and 11 cm. Cross-sectional area, A_x, can be found from L_c via the relation

$$\begin{aligned} A_x &= 0.540424 L_c^2 && \text{if } L_c < 0.00167 \text{ m}, \\ A_x &= 0.556945 L_c^{2.0047077} && \text{if } L_c \geq 0.00167 \text{ m}. \end{aligned} \tag{3.27}$$

Fragments with a characteristic length between 1 mm and 1 m are created through sampling of the area-to-mass distributions from Equations 3.24 and 3.26, up until the cumulative number of fragments given by Equation 3.23 is reached. Due to the large number of small fragments in large, catastrophic collisions, fragments can be created in groups of 10, 100 or 1000, with all fragments in the group having the same area-to-mass ratio, as done by some implementations in the study by Rossi (2006). The mass of these fragments is found by dividing the cross-sectional area from Equation 3.27 by the attributed area-to-mass ratio. If the total cumulative mass of fragments between 1 mm and 1 m in size is less than the available mass of the parent body or bodies (dependent upon if the collision was catastrophic or not), the total mass is conserved by creating 2 to 8 large fragments larger than 1 m in size.

3.2.3 Statistical Debris Models

The Particles-in-a-Box debris model of Section 3.2.1 can describe multiple species of objects and how they interact. However, evaluating the coefficients which describe how the species interact is complex. Evolutionary debris models described in Section 3.2.2 model individual objects but at the cost of complexity and computational time. Statistical debris models provide a balance between the two, binning objects into separate species and modelling them similarly to an evolutionary model. The species can be binned by object characteristics such as mass, but also by orbital characteristics such as semi-major axis and eccentricity. Representative objects from each bin are then treated similarly to the evolutionary debris models through use of the same constituent models. The computation time is dependent upon the number of bins used rather than the number of objects in the population, with this proving particularly useful when modelling objects smaller than 10 cm in size or during multi-century simulations exhibiting unbound growth.

Examples of these statistical debris models are the Stochastic Analog Tool (STAT) model by Rossi et al. (1998) and its unnamed precursor by Rossi et al. (1994). Objects in these two models are binned by semi-major axis, eccentricity and mass. The mathematical equation which summarizes these models highlights the similarity with the PIB model by Talent (1992), with the change in the number of objects in bin N_I in a time step given by

$$\begin{aligned}\frac{dN_I}{dt} =&(\text{launches})_I \\ &+\sum_J [(\text{explosions})_{J\rightarrow I}] + (\text{explosions})_{I\rightarrow I} \\ &+\sum_J [(\text{propagation})_{J\rightarrow I}] - (\text{propagation})_{I\rightarrow J} \\ &+\sum_{IJ} \left[(\text{collisions})_{(IJ)\rightarrow I}\right]\end{aligned} \tag{3.28}$$

where bin I is the bin of interest and bin J refers to all other bins. Comparing directly against the Talent model of Equation 3.18, the first line relates to the deposition coefficient A, the third line to the atmospheric decay term with coefficient B, and the fourth line to the collision term with coefficient C. Whereas the multi-species version of PIB handles explosions within each species through the coefficient A, STAT handles them separately and allows fragments to migrate between bins, either through a change in mass due to the fragmentation, or a change in orbital elements caused by the explosion. This gives rise to the second line.

The use of constituent models to simulate the sources and sinks adds additional complexity to the statistical debris models over the PIB model, and also allows more variability of the environment to be captured. It also avoids the issues required in

calculating coefficients for a multi-species PIB model. However, due to STAT's date of release, it uses models fit to older data than its evolutionary debris model counterparts. For example, as the NASA SBM had not been released, fragments from collisions were generated using a formula generated by Rossi et al. (1994) which was based purely on the laboratory tests of asteroid collisions performed by Fujiwara et al. (1989). STAT also used the collision probability algorithm of Wetherill (1967), with the impact on probabilities explored in Section 3.2.2.1 and summarized in Table 3.3. This presents an opportunity in which a statistical debris model can be created using constituent models based on newer data sets and algorithms.

3.2.4 The Debris Environment

The "Kessler effect", first described by Kessler and Cour-Palais (1978), is a commonly used term in academic and popular literature about space debris. It conveys the concept that even with no further launches, once a critical spatial density of objects is exceeded, a chain reaction of collisions continues to exponentially increase the total number of space debris fragments. Rather than impacting the whole environment at once, this can happen in specific altitude shells. For example, Liou and Johnson (2006) performed a 200-year future projection of the LEO region with the LEGEND debris model, starting with the tracked population at the time and assuming no future launches. They showed that as collision fragments replaced objects removed by atmospheric drag, the total number of 10 cm and larger objects stayed approximately constant through to 2055. However post-2055, the number of collision fragments created exceeded those removed by atmospheric drag, increasing the total number of trackable objects. Sixty percent of the catastrophic collisions driving this phenomenon occurred at altitudes between 900 and 1000 km due to the higher spatial density of objects in this region. The results demonstrate that the 900-1000 km region has already reached the critical spatial density required to trigger the Kessler effect.

These findings were expanded upon in an IADC modelling study summarized by Liou et al. (2013). This made use of six different models from a range of space agencies, including DELTA, LEGEND, and DAMAGE. The study required each model to use a set of common assumptions, namely introducing launch traffic by repeating the historic 2001 to 2009 period, an 8-year mission lifetime with a 90% chance of compliance with the "25-year rule", no explosions through a 100% passivation rate, and no collision avoidance maneuvers. Using the same initial population (1st May 2009 from MASTER-2009, described by Flegel et al. (2009)) each model performed a Monte-Carlo simulation of 200 years, using their own solar activity predictions, orbital propagation algorithms and collision probability calculations. The first solar cycle used by each model had a wide range of solar maxima, ranging from an F10.7 value of 120 to 180 sfu. The maxima of later solar cycles showed much less variability between

the models, with values between 180 and 200 sfu, but reaching the maxima at different times. All models predicted a growth in the larger than 10 cm population, reaching an average increase of 30% at the end of the 200 year simulation. Again this was driven by an increase in the number of catastrophic collisions at altitudes of and 900 to 1000 km, but also at 700 to 800 km. The population below 750 km after 200 years was comparable to the initial population, with above 800 km seeing a significant increase in spatial density. Liou et al. (2013) used these results to highlight the need for a high compliance with the passivation and "25-year rule", as well as the need for active debris removal to control the rate of population growth.

Dolado-Perez et al. (2015a,b) discussed the sources of uncertainty within debris models, breaking them into two categories. The first category included constituent models, calculations and inputs which could be controlled by the modeller. These included the initial population, the atmospheric density model used and how collisions are assessed and handled. The second category included future phenomenon and events outside the modeller's control, such as launch traffic, anti-satellite tests and solar activity. Using the "Modelling the Evolution of Debris in the Earth's Environment" (MEDEE) debris model and using the same assumptions and inputs as the IADC study by Liou et al. (2013), Dolado-Perez et al. investigated the impact of solar activity on the number of trackable objects in the LEO debris environment. Scenarios for low, medium and high solar activity were simulated, using repeating solar cycles with F10.7 maxima of 150, 180 and 205 respectively. These scenarios resulted in the number of trackable objects changing by +25%, +5% and -16% at the end of the 200 year simulation period. The solar activities used by the IADC study fall into the medium to high solar activity scenarios. There is a substantial difference between the +30% on average increase in the number of trackable objects in the IADC study compared to the +5% to -16% found by Dolado-Perez et al.. The smallest increase by a model in the IADC study found only a 20% increase. The IADC study also saw a steady increase over the 200 years, while the majority of the change in each solar activity scenario of Dolado-Perez et al. (2015a) happened in the first 50 years. Despite this discrepancy, it does highlight the variability caused within a debris model just from a change in solar activity.

3.3 Density Trends Applied in Debris Modelling

Lewis et al. (2005) were the first to investigate the impact on orbital lifetimes and the debris environment with the use of the DAMAGE debris environment model. A function was fitted to the trends derived by Emmert et al. (2004) (discussed in Section 3.1.2), giving the change in density, $\Delta\rho$ (% per decade), as a function of solar activity, $F10.7$ (sfu), and altitude, h (km), where

$$\Delta\rho = -3.4 + 0.1441(F10.7 - 70) - 0.0036(h - 240) \tag{3.29}$$

with this trend assumed to hold above 800 km, where there was less data to confirm the trend. This density trend was applied onto densities from the CIRA-72 model used within DAMAGE, with the per decade change applied from an epoch of 1 January 1973.

An example of the impact on the orbital lifetime of a historic object was given. The object (mass-to-area ratio of 75 kg/m^2) began its orbit (semi-major axis 7178 km, eccentricity 0.041) on 1 January 1973. Without a trend applied, the orbital lifetime was 25 years, but with the above trend applied this extended to 26.5 years. This extension in lifetime was dependent on the start of the disposal epoch due to the following solar activity levels, however the worst case discovered was an increase of 6 years in orbital lifetime.

Investigations into the impact on the debris environment were then discussed, with the first simulations exploring the historical impact between 1 January 1973 and 1 May 2001. Comparing the model results showed only a small increase in the number of objects between 300 and 900 km when the trend was applied compared to when it was not. However, it was identified the impact would be more substantial over longer periods of time and going into the future.

A 100-year "business as usual" scenario from 1 May 2001 was simulated, repeating historic launches and explosions. Again DAMAGE simulated this period with and without the density trend applied. By May 2101, the number of objects larger than 1 cm had increased by 30.8%, and those larger than 10 cm by 9.9%, with the greatest increase in numbers seen between 2065 and 2101. Above 1200 km, there was no significant enhancement due to the lower atmospheric densities obscuring the impact of the secular density trend. The increasing number of small objects was found to be a result of an increasing number of collisions, as the number of collision fragments increased by 40%, while the number of intact objects and explosions increased by 5.2% and 8.5% respectively over the 100 year period. Furthermore, while the number of collisions increased exponentially over time in both the with and without trend scenarios, the difference between the number of collisions from 2065 onwards also increased exponentially.

Lewis et al. (2011) followed a similar methodology, fitting a function to the trend data of Saunders et al. (2011). A trend-modified density, ρ_c, was obtained of

$$\rho_c = \rho_i \left[(0.98028 - 0.00013h)^T (0.00109F10.7 + 0.88578) \right] \tag{3.30}$$

where $F10.7$ (sfu) is the solar activity level, h (km) is the altitude, ρ_i the density from CIRA-72, and T the time in decades since 1 January 1970. DAMAGE simulated a control scenario with no trend applied as a 70-year period from 1 August 2009 through to 1 August 2079. Launches repeated those of 1999 - 2009 cyclically, with no explosions occurring, and 90% compliance with the ”25-year rule”. Each scenario was repeated 100 times in a Monte Carlo simulation. A similar scenario to the control was also simulated, but with the trend applied. Finally, two more scenarios were simulated with Active Debris Removal (ADR) applied on top of the mitigation scenarios, again with and without the density trend applied. The five most massive objects between 950-1050 km were removed each year in these ADR scenarios.

In the mitigation-only scenarios, the density trend led to a 74% increase in growth rate of objects in LEO over 70 years, and a 23.5% in the total number of objects. The ADR scenarios revealed that the benefits of removing the five objects per year was lost when the density trend was applied, as the number of objects increased by 27.5% in the year 2070 when thermospheric contraction was applied. However, a final simulation was done where ten objects were removed each year, with this scenario recovering the benefits of ADR seen in the control scenario. This showed that the secular decrease in thermospheric density would decrease the effectiveness of both debris mitigation efforts and ADR.

Both density trend functions used in Lewis et al. (2005) and Lewis et al. (2011) assumed the historic density trend would remain constant when extrapolated into the future. With the functions of each study based on data from Emmert et al. (2004) (1996 - 2001 period) and Saunders et al. (2011) (1970 - 2010), a historic measurement of the carbon dioxide concentration for the start and end dates of the data can be found. Assuming a linear relationship between each of these concentrations over the historical period, these can be extrapolated out into the future linearly too. These future carbon dioxide concentrations are plotted against the RCPs in Figure 3.6 to better understand how they relate to each other. Although the results of Lewis et al. (2011) end before the RCPs, Lewis et al. (2005) reaches a similar concentration to RCP4.5 during 2100. However, the higher concentrations throughout the 100 years of RCP4.5, reaching a difference of over 40 ppm, would see a sustained larger decrease in atmospheric densities during the RCP4.5 scenario compared to Lewis et al. (2011). This is, however, a speculative scenario based on the extrapolation of historical density trends.

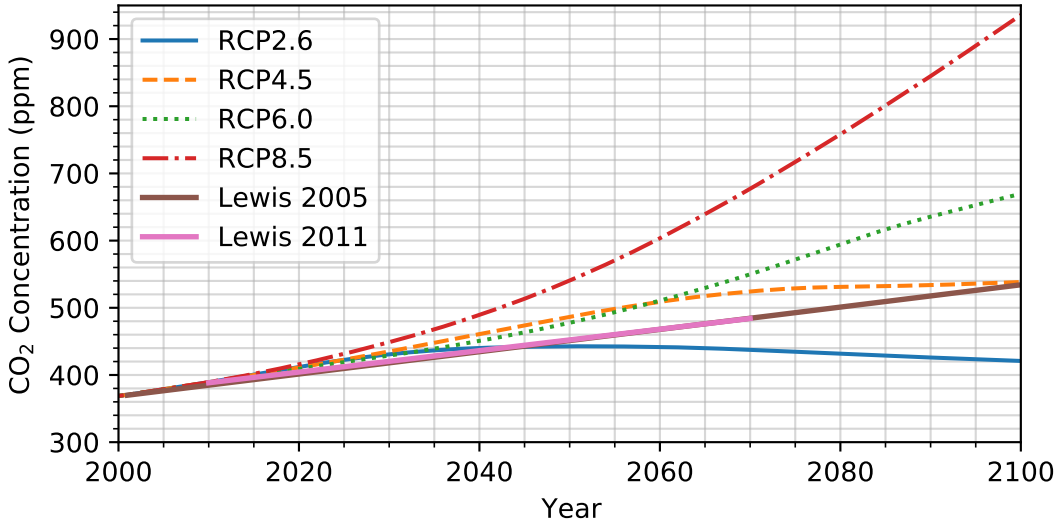

FIGURE 3.6: The assumed future carbon dioxide concentrations in the Lewis et al. (2005) and Lewis et al. (2011) debris evolution studies, derived from the density trend based on historical orbit-derived density observations. The representative concentration pathways of Figure 2.10 are included for further context.

Chapter 4

Research Aims

While historical neutral density trends in the thermosphere have been observed and modelled for two decades, very little research has been done on modelling density trends into the future. Those studies which have, also tended to focus on a limited range of solar activity and altitude. A greater understanding of the future density reductions is required to model the impact on the debris environment. Previous research in this area has been limited to the two studies of Lewis et al. (2005) and Lewis et al. (2011), with each propagating a historic trend linearly into the future as if carbon dioxide concentrations continued to increase at the same rate.

The first focus of research in this thesis was on the atmospheric densities by answering the following questions:

- By how much will upper atmospheric neutral densities reduce in the future under increasing carbon dioxide concentrations?
- How are these density reductions related to solar activity and altitude?
- Are these density reductions dependent upon latitude?

Answering these then allowed for investigation of the impact on the LEO and space debris environment. This leads to the question:

- What impact will there be on the number of objects and collisions in the LEO environment under each representative concentration pathway?

Chapter 5

Future Density Reductions

This section will focus on the modelling, verification and analysis of future density trends, part of which has been published in Brown et al. (2021). The set-up and output of WACCM-X will be explored in more detail to the introduction given in Section 2.2.3.2, with particular focus on calculating neutral densities from the output files. When first performing a simulation, WACCM-X begins with a set of initial conditions. A period of ”spin-up” is required in which WACCM-X models the atmosphere and moves away from the initial conditions to a more realistic steady-state. Therefore, Section 5.1.4 will address how the model was spun-up and the impact spin-up has on results. The global-mean annual-mean future density reductions under low solar activity conditions will then be presented, followed by those for high solar activity and under varying solar activity at a fixed future carbon dioxide concentration. As some nuance of the density reductions is lost by taking global-mean annual-means, focus will then switch to how these reductions depend on latitude. Finally the process of amalgamating the density reductions into a table of scaling factors which can be applied to empirical atmospheric models will be discussed. Finally, how neutral thermospheric densities will reduce under each of the representative concentration pathway scenarios will be explored.

5.1 WACCM-X Simulations

The simulations performed in this chapter made use of WACCM-X as part of CESM. The details of this model have been discussed in Section 2.2.3.2. CESM version 1.2.2 with WACCM-X version 1.0 was installed and used on the University of Southampton’s Iridis 4 High Performance Computing (HPC) cluster. The WACCM-X runs were made on 32 computing nodes with dual 2.6 GHz Intel Sandybridge processors, for a total of 512 CPUs.

5.1.1 Output Variables and Conversions

WACCM-X was configured to export variables as monthly averages, 3-hourly instantaneous values, and daily instantaneous values, each in their own history files in the netCDF format. Over 2500 variables from WACCM-X can be output into these history files, with the full details available in the master field list of the model. The default variables output to history files are summarised in Table 5.1, and those chosen for output for this work are summarised in Table 5.2 . While some of these variables will not be analysed within this thesis, they have been included as to enable future work which could potentially make use of them.

TABLE 5.1: The relevant default WACCM-X variables common in all output files.

Short Name	Long Name	Units	Dimension
hyam	Hybrid A Coefficient at Layer Midpoints	None	81 levels
hybm	Hybrid B Coefficient at Layer Midpoints	None	81 levels
P0	Reference Pressure	Pa	None
ap	Ap Geomagnetic Index	None	None
kp	Kp Geomagnetic Index	None	None
f107	10.7cm Solar Radio Flux (F10.7)	sfu*	None
f107a	81-day Centered Mean of F10.7	sfu*	None
sol_tsi	Total Solar Irradiance	W/m^2	None

* 1 sfu = 10^{-22} $Wm^{-2}Hz^{-1}$

TABLE 5.2: WACCM-X variables selected to be stored in monthly, daily, and 3 hourly output files. All these variables have grid dimensions $81 \times 96 \times 144$ in pressure level, latitude and longitude respectively, except PS which exists at ground level only so has a dimension of 96×144.

Short Name	Long Name	Units	Monthly	Daily	3 Hourly
PS	Surface Pressure	Pa	✓	✓	✓
Z3	Geopotential Height	m	✓	✓	✓
T	Temperature	K	✓	✓	✓
CO2	CO_2 Concentration	mol/mol	✓	✓	✓
CO	CO Concentration	mol/mol	✓	✓	✓
NO2	NO_2 Concentration	mol/mol	✓		
NO	NO Concentration	mol/mol	✓	✓	✓
O	O Concentration	mol/mol	✓	✓	✓
H20	H_2O Concentration	mol/mol	✓	✓	
QJOULE	Joule Heating	K/s	✓		
QRS_CO2NIR	CO_2 Near-IR Heating Rate	K/s	✓		
QRS_EUV	Total EUV Heating Rate	K/s	✓		
QNO	NO Cooling Rate	K/s	✓		
U	Zonal Wind	m/s	✓	✓	✓
V	Meridional Wind	m/s	✓	✓	✓

Neutral atmospheric density is calculated from the WACCM-X outputs of pressure, P, and temperature T, using the ideal gas law. P at level i, latitude ϕ and longitude λ is obtained by:

$$P(i,\phi,\lambda) = A(i)P_0 + B(i)P_s(\phi,\lambda) \tag{5.1}$$

where P_0 is the constant reference pressure, $P_s(\phi,\lambda)$ is the varying surface pressure, and $A(i)$ and $B(i)$ are the hybrid A and B coefficients at layer midpoints (named hyam and hybm in WACCM-X). Simmons and Strüfing (1981) introduced these hybrid A and B coefficients, with each controlling by how much the layers are isobaric or terrain-following respectively. This allows WACCM-X to use a continuous coordinate system which follows the terrain near ground-level, but transforms to constant pressure layers in the upper atmosphere. The neutral atmospheric density, ρ, is then obtained via the ideal gas law:

$$\rho(i,\phi,\lambda) = \frac{M(i,\phi,\lambda)P(i,\phi,\lambda)}{RT(i,\phi,\lambda)} \tag{5.2}$$

where R is the universal gas constant, M is the mean molar mass of constituents, and T is the neutral atmospheric temperature.

The hybrid A and B coefficients also define the hybrid vertical coordinates through

$$\text{Hybrid Level} = 1000(A+B) \tag{5.3}$$

where this hybrid level follows the topology of the Earth's surface near ground-level, but changes to a fixed pressure level in the upper atmosphere.

The geopotential height output from WACCM-X (named Z3 in the history files) is a diagnostic output of altitude, and accounts for the decreasing strength of gravity with altitude. It is derived in numerical atmospheric models which use pressure coordinates and assume hydrostatic balance to simplify calculations. Assuming a spherical Earth, the geopotential height, h, can be converted to a geometric altitude, z, via

$$z = \frac{hr_E}{r_E - h} \tag{5.4}$$

where r_E is the average radius of Earth. This geometric altitude is equivalent to a satellite's orbiting altitude, and will be used throughout this thesis when discussing altitudes.

5.1.2 Interpolation and Extrapolation

WACCM-X outputs data at 81 discrete pressure levels, with these levels varying in altitude, longitude and latitude, but also time as the thermosphere expands and

contracts. Therefore when investigating variables at specific altitudes, 1-D monotonic cubic interpolation is performed on the values at the two closest discrete altitudes (having obtained these altitudes via Equation 5.4) at the specific latitude and longitude.

The upper boundary of WACCM-X is at a pressure level of 4×10^{-10} hPa, with this varying in altitude from 600 km to 280 km depending upon solar activity levels and ground-level carbon dioxide concentration. One of the motivations of this work is to investigate the impact upon the LEO environment, therefore extrapolation was used to ensure there was data under all conditions up to an altitude of 500 km. A higher altitude could have been chosen to cover more of the LEO region. However, the extrapolation was based on the assumption of an atomic oxygen dominated thermosphere and at higher altitudes helium becomes dominant. Hence the conservative choice of altitude.

A range of possible functions were tested to find the one which provided the smallest sum of residual squares for NRLMSISE-00 neutral density profiles between 175 and 500 km for solar activity levels between 70 and 200 sfu. The function found to best fit the densities at points above 175 km (roughly where atomic oxygen becomes dominant) for all cases was

$$\rho(z) = az^b log(z + c) + d \tag{5.5}$$

where a, b, c and d are coefficients fit to the available modelled density above 175 km with non-linear least squares at each latitude and longitude. To validate this method, it was applied to NRLMSISE-00 for a range of solar activities and locations, using the densities between 175 and 250 km to extrapolate to higher altitudes and allow comparison against the actual model densities. Figure 5.1 shows one of these tests. The percentage difference varied slightly with solar activity and location, and the maximum overestimate reached was 3% at 500 km altitude. The absolute densities from this method were not being studied, but rather the relative difference, and as these overestimates were consistently applied, this method was kept.

As temperatures in the thermosphere tend towards the exospheric temperature with increasing altitude, it was assumed the temperature at the highest modelled altitude was the exospheric temperature, and applied to all altitudes higher than WACCM-X's upper boundary.

5.1.3 Initial Conditions and Input Data

General circulation models require a set of initial conditions from which their simulation of the atmosphere can begin. For the simulations presented in the

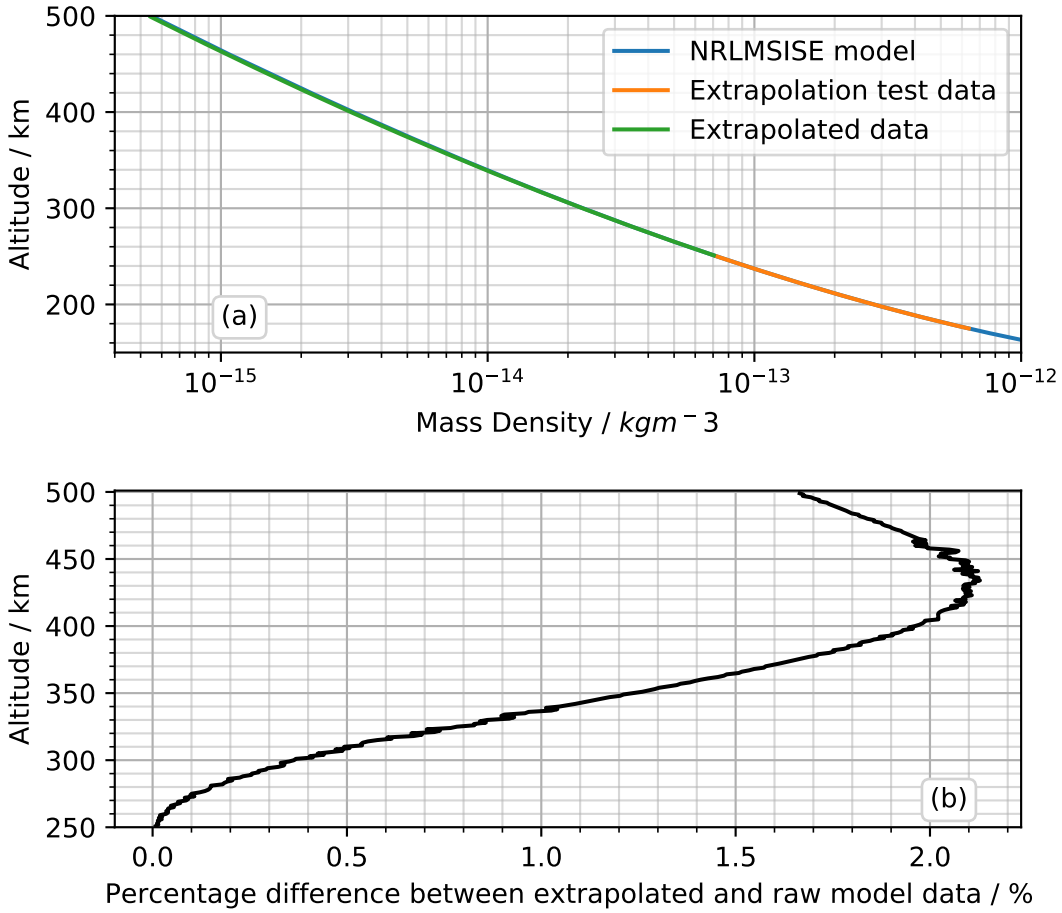

FIGURE 5.1: Density extrapolation method applied to NRLMSISE-00. Subfigure (a) shows the neutral densities output by NRLMSISE-00 in blue, the region used to calculate coefficients for Equation 5.5 in orange, and the extrapolated densities in green. As these are difficult to distinguish at this scale, Subfigure (b) gives the percentage difference between the raw NRLMSISE-00 densities and the densities calculated via extrapolation. This example is for midnight on 1st January 2000 at 50.9° latitude and -1.4° longitude (Southampton, UK) with historic F10.7 and Ap values.

following section the initial conditions for the year 2000 were used, as downloaded from the University Corporation for Atmospheric Research (2021) Subversion server. The CO_2 and CO concentrations of these initial conditions were scaled appropriately (see Section 5.1.4.1) to reflect the ground-level conditions in the RCP8.5 scenario. Some constituents, for example ozone (see study by Akmaev et al. (2006)), also vary in concentration with time due to anthropogenic effects. These have an impact on temperature trends in the middle atmosphere which would feed through to upper atmospheric densities. However, these were held constant at year 2000 levels specifically to investigate the impacts of carbon dioxide.

The FXHIST CESM component set was used to run WACCM-X, with stub and data models used for systems such as oceans (for sea surface temperatures) and land (for foliage cover), to provide data which would match WACCM-X inputs at the lower

boundary. This is detailed further by Liu et al. (2018). Default input files were used for the boundary conditions and heating sources, with two exceptions: solar activity and CO_2 emissions at the lower boundary. The solar activity was set in the solar activity file as required in each of the studies. CO_2 emissions were set using the RCP8.5 scenario.

5.1.4 Spin-Up from Initial Conditions

Atmospheric general circulation models require a period of simulation time in which the initial conditions are allowed to reach a more "realistic" steady state, referred to as 'spin-up'. Simmonds (1985) analyses how a historic general circulation model spins up, describing the spin-up period as the model forgetting the initial state, and instead beginning to reflect the nature of the model under the prescribed boundary conditions. Simmonds also states the length of spin-up is dependent upon which variables are being investigated, the complexity of the model, and the timescales of key thermodynamic and physical processes.

Solomon et al. (2018) and Solomon et al. (2019) both investigated the impact of carbon dioxide concentrations in the thermosphere using WACCM-X, and both used a spin-up time of one year under solar minimum conditions in order to allow minor constituents to equilibrate, with the latter requiring an additional three months after shifting to solar maximum conditions.

In the next section, a method used to speed up the spin-up of WACCM-X in future density reduction studies will be introduced, followed by Section 5.1.4.2 exploring how quickly WACCM-X spins-up when studying densities and temperatures in particular. The methods and results of this section led to the the spin-up time of WACCM-X within these future studies being reduced to four months, while adding confidence the model had reached a steady state.

5.1.4.1 Carbon Dioxide Concentration Scaling Method

To test the best method for optimising spin-up times, the initial files from the WACCM and WACCM-X repositories were studied. These contain the CO_2 concentration profiles for historical periods and have been plotted in Figure 5.2 and with increasing level above the lower boundary in Figure 5.3. Each profile's carbon dioxide concentration does not vary by much between ground level and the homopause, but above the homopause they quickly decrease in concentration and tend to zero. The initial files of the years 1850 and 1960 are for WACCM rather than WACCM-X and therefore have their upper boundary at a lower altitude.

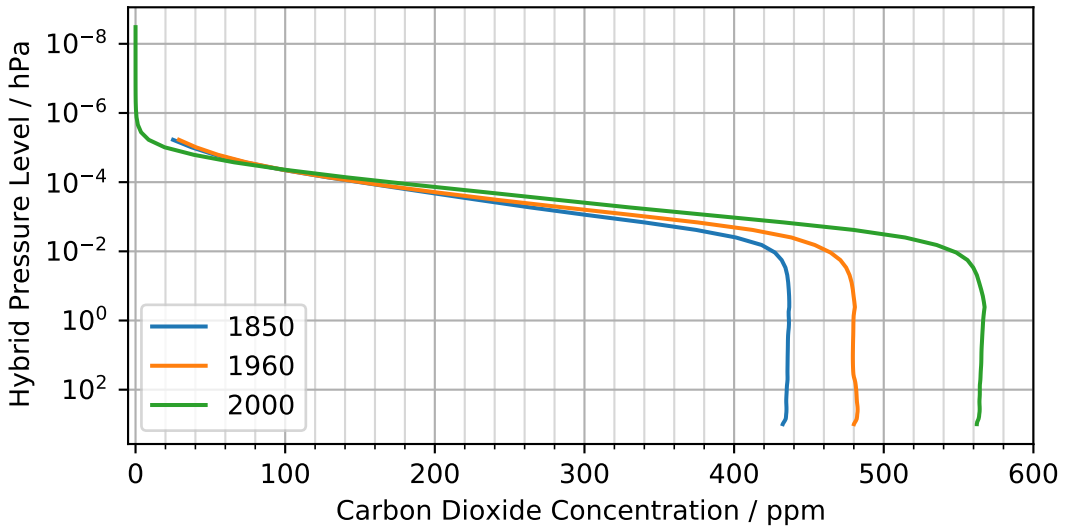

FIGURE 5.2: Carbon dioxide concentration profiles of initial files for historic years, plotted in hybrid level.

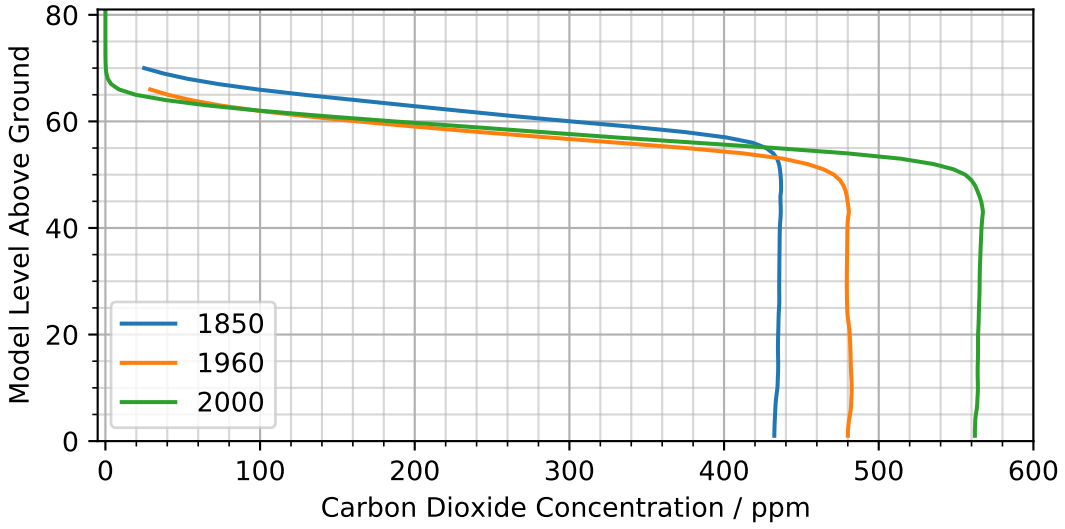

FIGURE 5.3: Carbon dioxide concentration profiles of initial files for historic years, plotted in levels above the WACCM-X lower boundary (ground level).

At altitudes above 60 km, UV radiation causes photodissociation of CO_2 into carbon monoxide (CO) and atomic oxygen (O). Carbon monoxide then reacts with atomic oxygen in the region to re-form CO_2. As a result, CO_2 and CO exist in chemical equilibrium in the lower thermosphere. The CO concentrations from the same initial files as the earlier CO_2 examples are plotted against hybrid pressure level in Figure 5.4.

To obtain the CO_2 profile in the initial files for some desired ground-level concentration, the assumption was made that the carbon dioxide concentration, x, at each modelled level, i, and grid point, ϕ and λ, could be scaled by the ratio of the

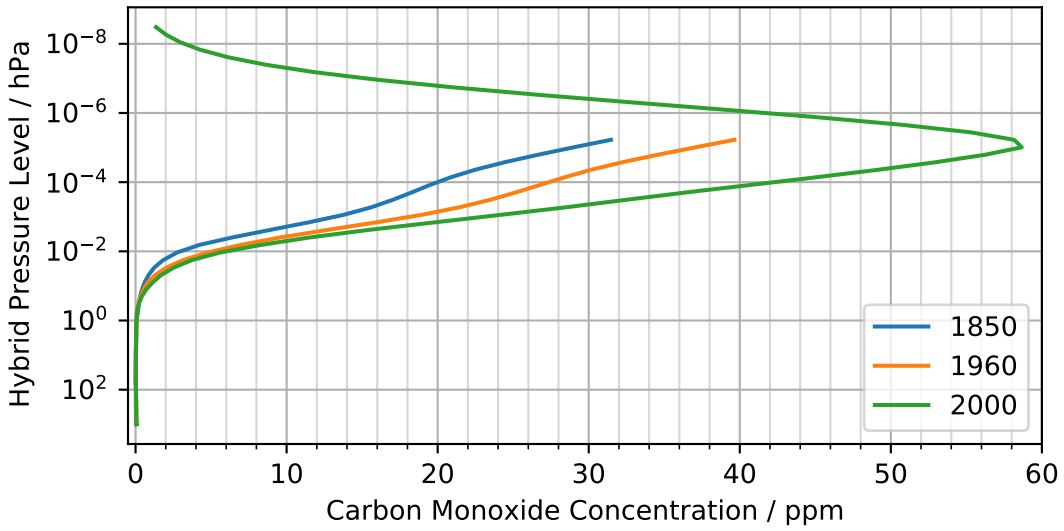

FIGURE 5.4: Carbon monoxide (CO) concentration profiles of initial files for historic years, plotted in hybrid pressure level.

desired global-mean ground-level ($i = 0$) carbon dioxide concentration to the original profile's global-mean ground-level concentration. This can be mathematically expressed as

$$n(\mathrm{CO_2})_{\mathrm{desired}}(i,\phi,\lambda) = \frac{\bar{n}(\mathrm{CO_2})_{\mathrm{desired}}(i=0)}{\bar{n}(\mathrm{CO_2})_{\mathrm{original}}(i=0)} \times n(\mathrm{CO_2})_{\mathrm{original}}(i,\phi,\lambda) \tag{5.6}$$

Due to the chemical equilibrium between CO_2 and CO, this scaling assumption was also applied similarly to the CO profile (using the relative difference of ground-level CO_2). This accounted for over 99.7% of the carbon in the thermosphere, and minor constituents containing carbon, such as methane (CH_4) were not scaled due to their more complex profiles. This CO_2 and CO scaling method was applied only to the initial concentrations in the first time step, with later time steps changing the scaled, initial concentration via chemical and dynamical processes.

5.1.4.2 Density and Temperature Spin-Up

After scaling the carbon dioxide and carbon monoxide profiles of the default initial files for the year 2000, a study was performed into the spin-up times of thermospheric density and temperature. Densities and temperatures over four cycles are shown in Figures 5.5 and 5.6 respectively with spin-up periods of 0, 120, 243, and 365 days for an example WACCM-X simulation of 1975 under low solar activity (F10.7 = 70 sfu). The global-mean temperature and density of the initial conditions start significantly below the point at which the model stabilizes. There is a rapid increase in both variables after the first modelled day, with temperature being within 10 K ($\sim$ 1%) of the values on the

same day of year in later cycles, while density is still significantly lower at 5.0×10^{-12} kgm^{-3} compared to 6.4×10^{-12} kgm^{-3}. By day 40 of this example, the densities and temperatures of the first cycle are indistinguishable from the later cycles.

Despite the substantially lower densities in the first 30 days of the no spin-up case, the annual-mean density of the first cycle is only slightly smaller at 5.12×10^{-12} kgm^{-3} compared to 5.16, 5.23, and 5.22 $\times 10^{-12}$ kgm^{-3} of cycles 2, 3 and 4 respectively. This results in a mean of annual means of $5.18 \pm 0.04 \times 10^{-12}$ kgm^{-3}. By neglecting the first 120, 243, and 365 days of data in the simulation (attributing it to the model spinning up), the mean of annual means for four cycles becomes 5.21 ± 0.02, 5.22 ± 0.03, and $5.23 \pm 0.05 \times 10^{-12}$ kgm^{-3} respectively. With similar results seen in other modelled scenarios (see Figure 5.7), this suggests spin-up time has a minimal impact on the value of interest for calculating long-term trends, namely the mean of annual-mean global-mean neutral densities and temperatures.

For each of the simulations performed within WACCM-X, a spin-up time of four months (120 days) was chosen to ensure thermospheric densities had equilibrated, while minimizing the time spent spinning-up the model and hence taking up additional computational time. While the investigations in this section suggest a shorter time than 120 days could be chosen, this value was selected to reduce uncertainty while also maintaining the same spin-up method between the different solar activity studies.

5.2 Future Density Reductions Under Low Solar Activity

This section is based on the work published in Brown et al. (2021).

Using the methodology discussed in the previous sections, WACCM-X was used to simulate the atmosphere under increasing ground-level carbon dioxide concentrations at a fixed low solar activity of F10.7 = 70 sfu. The Kp value of these runs was also fixed to a value of 0.33, which represents very low geomagnetic activity.

Ten simulations of differing ground-level carbon dioxide concentrations were performed, each of a length of 16 months (4 months of spin-up + 1 year of usable data). The concentrations used were taken from RCP8.5 at ten year intervals from 2005 to 2095 inclusive. This was partly due to a limitation with the initial condition files used which only gave values every five years from the year 2000. However, the choice of every ten years limited the number of simulations while also giving good coverage across all the RCPs as demonstrated in Figure 5.8. This choice resulted in an increasingly large difference in concentration between successive simulations. This means slightly more simulations covered the lower concentrations of RCP2.6 and 4.5

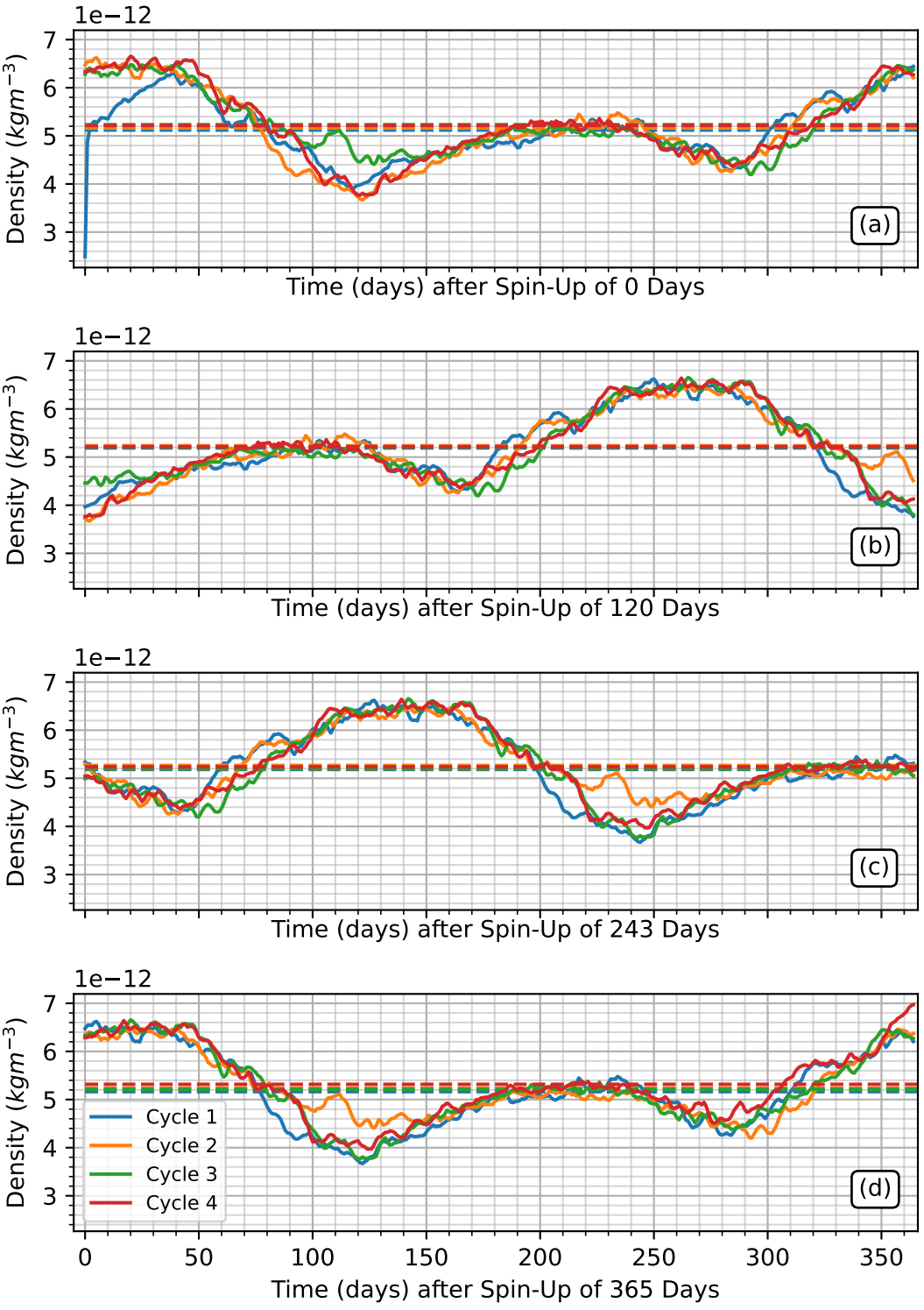

FIGURE 5.5: Daily global mean neutral density at 400 km altitude of 4 cycles, each a year long. Plots a, b, c, and d relate to a spin-up period of 0, 120, 243, and 365 days respectively, where the data in this spin-up period is removed. The end of one cycle is used as the beginning of the next. Solid lines are the daily values while the dashed lines are the annual mean for each cycle. This example is for 1975 data under low solar activity (F10.7 = 70 sfu).

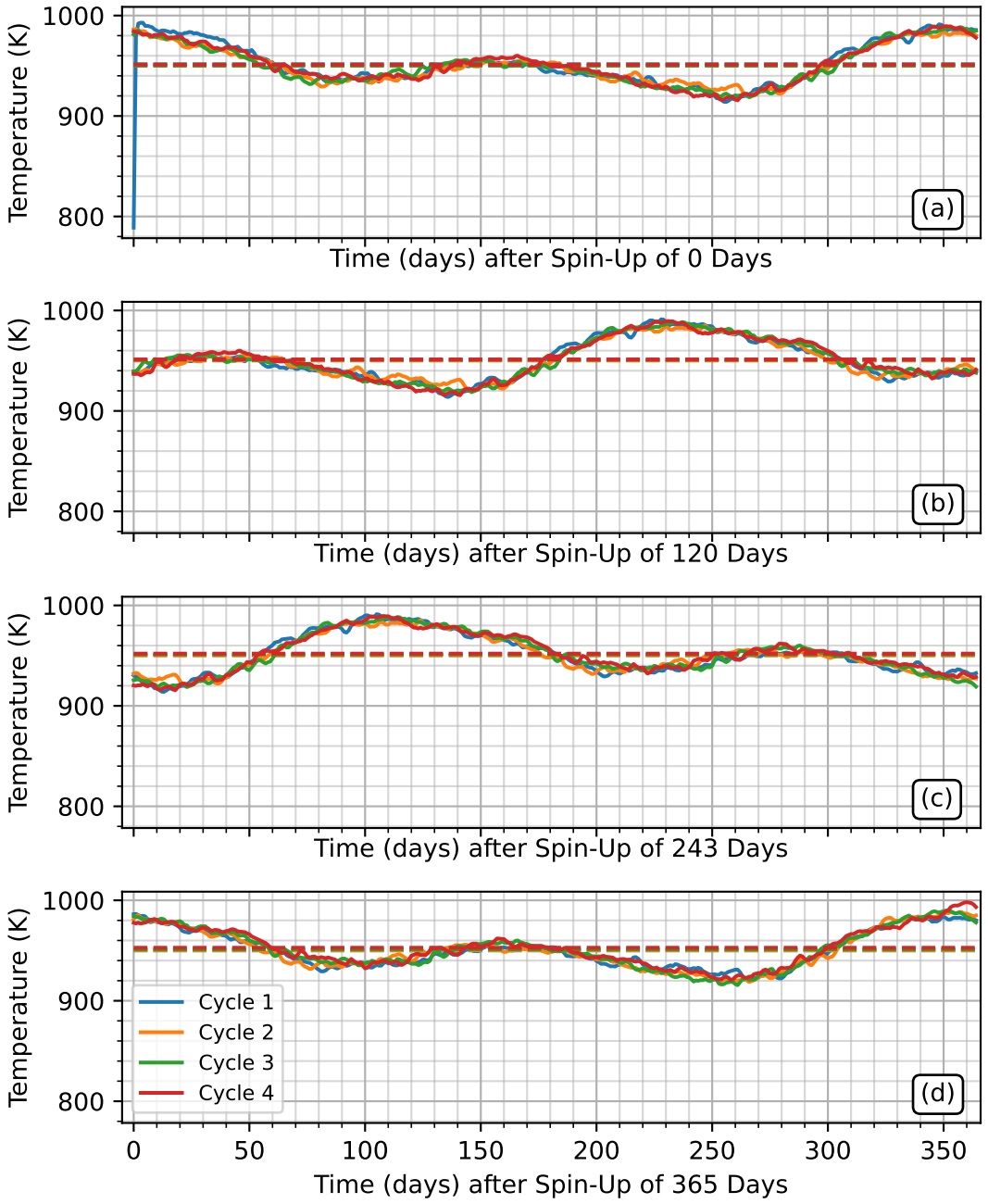

FIGURE 5.6: Daily global mean neutral temperature at 400 km altitude of 4 cycles, each a year long. Plots a, b, c, and d relate to a spin-up period of 0, 120, 243, and 365 days respectively, where the data in this spin-up period is removed. The end of one cycle is used as the beginning of the next. Solid lines are the daily values while the dashed lines are the annual mean for each cycle.. This example is for 1975 data under low solar activity (F10.7 = 70).

than would be the case if the modelled CO_2 concentrations had been uniformly spread between 368 and 890 ppm.

Alongside these ten simulations, to allow comparison against previous trend studies, a historic run using the same CO_2 scaling method was performed of the year 1975. In

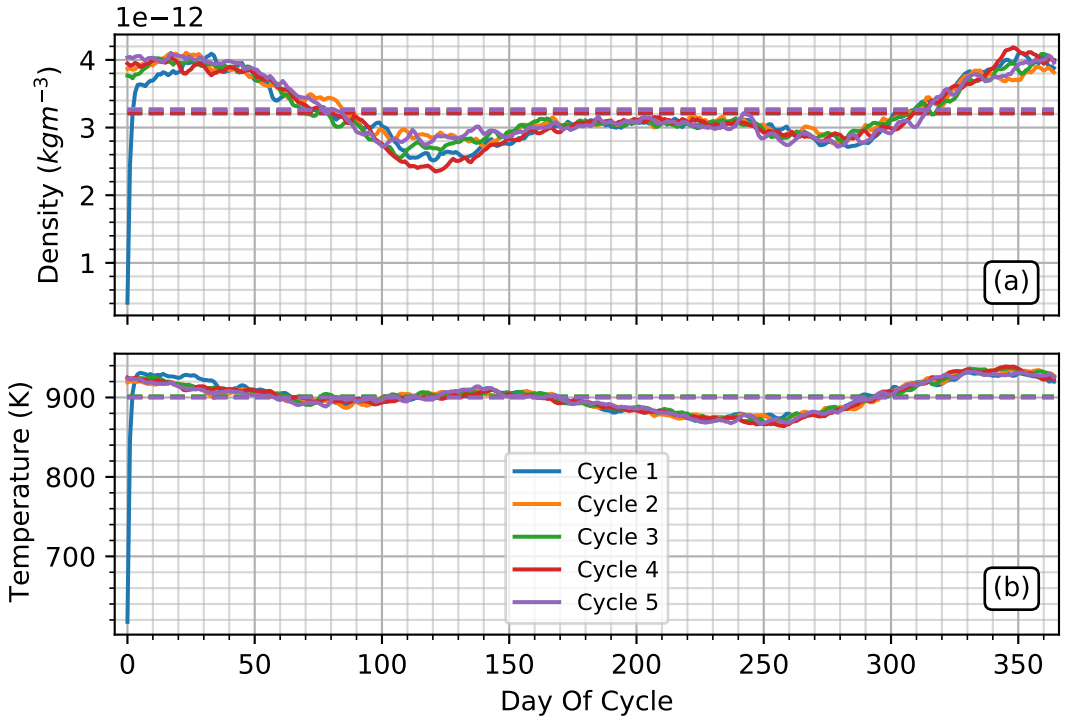

FIGURE 5.7: Impact of having no-spin up period on daily global mean neutral density, (a), and temperature, (b), at 400 km for a ground-level carbon dioxide concentration of 717 ppm (year 2075 in RCP8.5 scenario) during high solar activity (F10.7 = 200 sfu). The end of one cycle is used as the beginning of the next. Solid lines are the daily values while the dashed lines are the annual mean for the cycle.

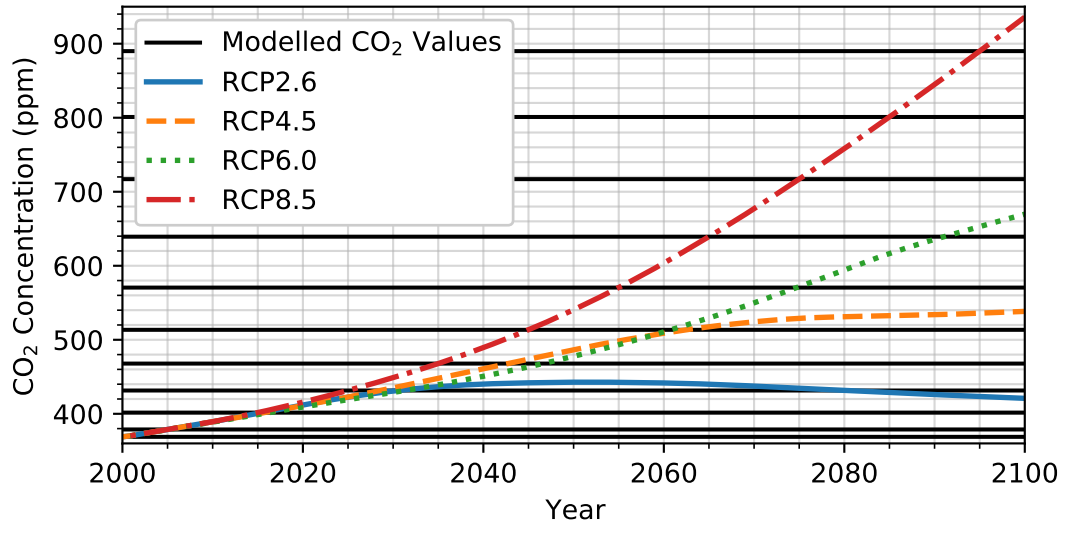

FIGURE 5.8: Carbon dioxide concentrations modelled in WACCM-X (black horizontal lines) presented with the future carbon dioxide concentration pathways from the RCPs of the IPCC's fifth assessment report (IPCC (2014)).

addition, a control simulation of the year 2000 was performed. As this would be used as a reference point for all other low solar activity simulations, after a four month

spin-up period, this model year was repeated five times using the end of one model year as the beginning of the next.

The outputs from these simulations were transformed from the model's pressure levels to geometric altitudes via the methods discussed in 5.1.1. Annual means of neutral density and temperature were then obtained for each altitude, latitude, and longitude, and finally a global mean taken by averaging over latitude (with cosine latitude weighting) and longitude to obtain global-mean annual-means.

Comparing the global-mean annual-means of the 1975 and 2005 runs gave a historic neutral density trend of -5.8% per decade at 400 km. Comparing this against the density trends from other studies summarized in Table 3.2, it lies in the middle of all the studies of low solar activities which range from -2.5 to -7.2% per decade. Furthermore, it lies within the $-5.0 \pm 1.60\%$ per decade mean and standard deviation obtained from these historic trend studies (no weighting was used to reflect the differing methods). However, its magnitude is larger than the -3.9% per decade of Solomon et al. (2018), which used the same WACCM-X model over a similar period (1974 - 2000). This may be due to the differing methodologies used, namely repeating the same model year compared to the transient run of 5 model years which Solomon et al. performed.

Cnossen et al. (2009) plotted global mean temperatures at March equinox and June solstice against carbon dioxide concentrations from 150 to 720 ppm, using different gravity wave implementations within the CMAT2 model. This provides another method of validation, as future thermospheric neutral density and temperature studies are limited in number (as discussed in Section 3.1.5). The WACCM-X data was plotted against the CMAT2 data in Figure 5.9, showing that WACCM-X is cooler than the CMAT2 model. Part of this can be attributed to the slightly differing solar activity and geomagnetic activity, namely F10.7 = 70 sfu and Kp = 0.33 in WACCM-X compared to 80 sfu and 2 respectively in the CMAT2 data. However, the neutral temperature does decrease with increasing CO_2, and at a similar rate to that of CMAT2.

The global-mean annual-mean neutral densities relative to the year 2000 for an increasing ground-level carbon dioxide concentration are plotted in Figure 5.10. Neutral densities decrease with increasing CO_2 concentrations, with the magnitude of this reduction increasing with altitude. The general result follows the previous historical studies. There is a "bump" in the data for all altitudes, between ground-level CO_2 concentrations of 430 to 550 ppm (RCP8.5 simulations of 2025, 2035 and 2045). During this "bump", the neutral density reduction appears to slow in its rate of decrease between ground-level concentrations of 430 to 470 ppm, before accelerating again between 470 and 550 ppm. No relation was found between the input data and this period. No reference was found to this period or carbon dioxide

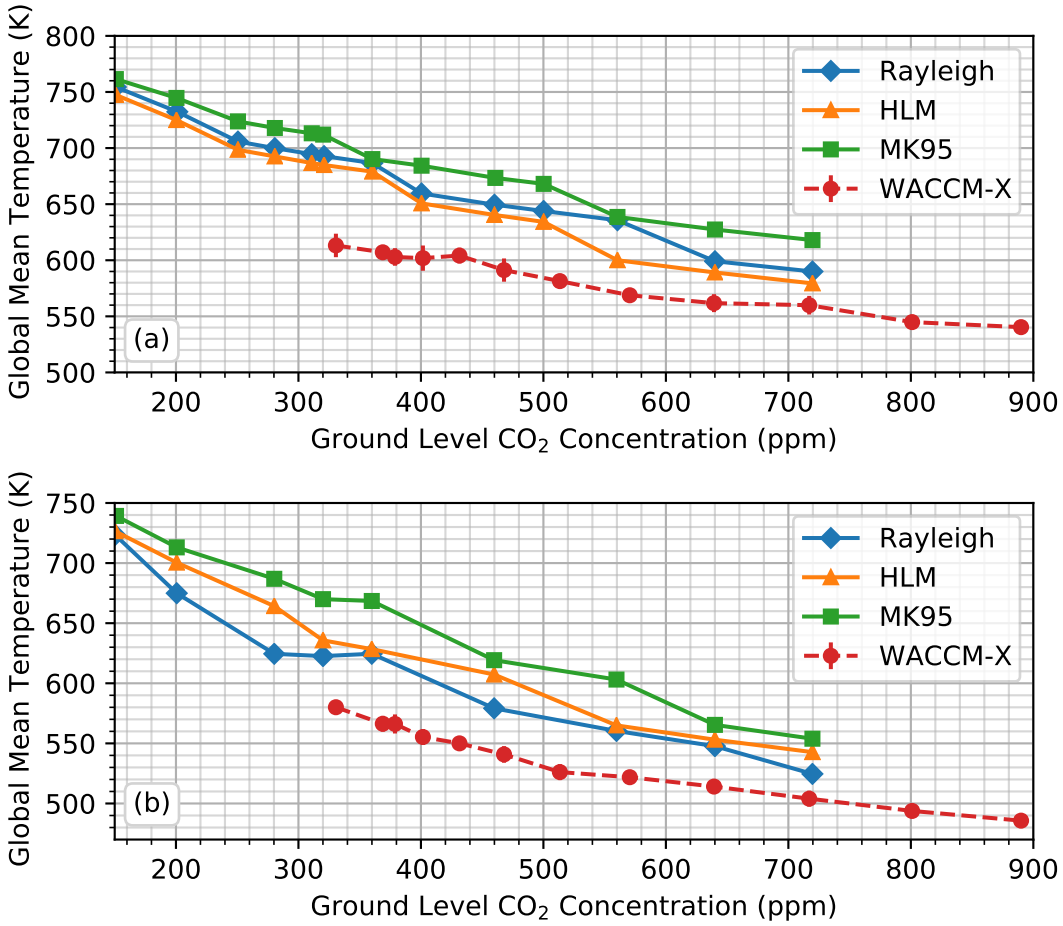

FIGURE 5.9: Global mean temperature under increasing ground-level carbon dioxide concentration at the fixed pressure level of 2.9 $\times 10^{-7}$ mbar, equivalent to around 200 km altitude. Comparison between the Rayleigh, HLM, and MK95 gravity wave implementations of CMAT2 from Cnossen et al. (2009) (solid lines), and the WACCM-X results (dashed line). CMAT2 models were run with F10.7 = 80 sfu and Kp = 2, while WACCM-X had F10.7 = 70 sfu and Kp = 0.33. Subplot (a) is for the March equinox (80^{th} day of the year) while (b) is for the June solstice (172^{nd} day of the year). WACCM-X global means and errors are from 21 days of data centered on the stated days.

concentration within WACCM-X either, suggesting this "bump" was a result of numerical modelling and not external factors. However, no explanation or physical mechanism can be found for this slowing density reduction. Furthermore this bump appeared in the high solar activity study (discussed in the next section), which performed more simulation cycles and removed the idea of errant initial conditions seeding this increase in density.

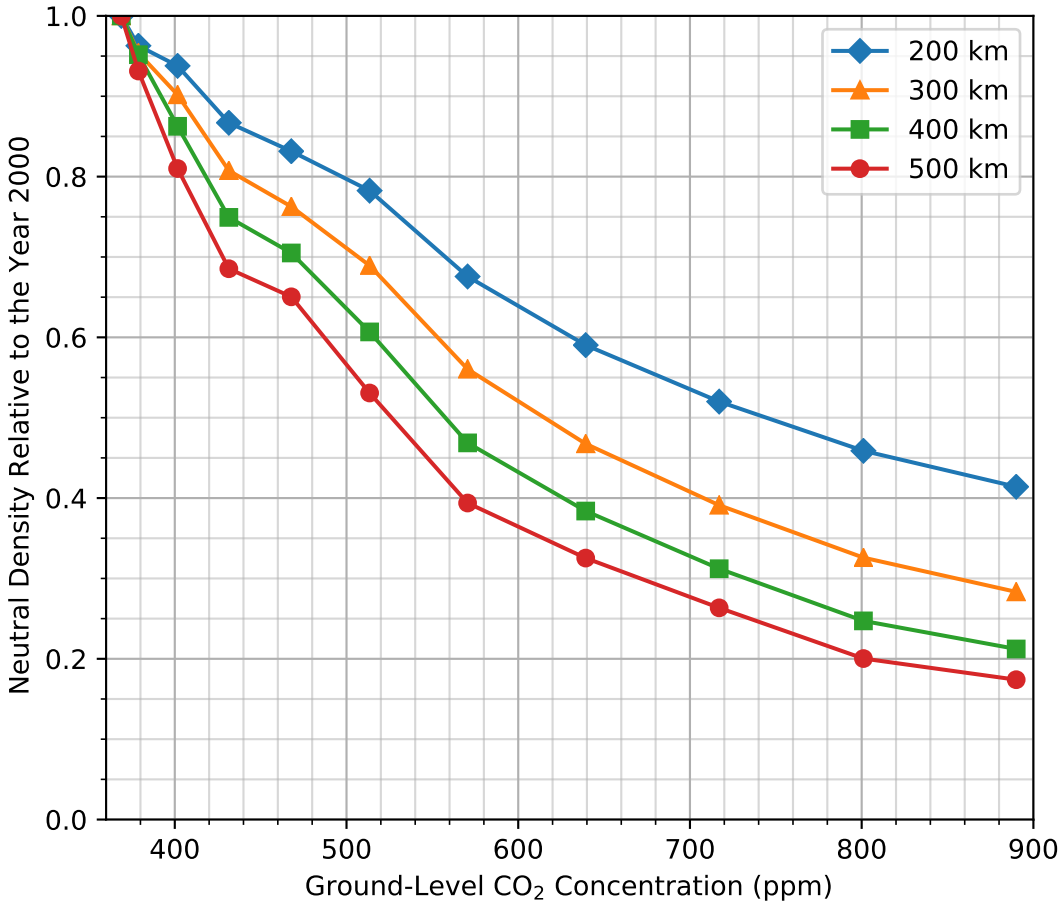

FIGURE 5.10: Neutral atmospheric density relative to the year 2000 under low solar activity (F10.7 = 70 sfu) for increasing ground-level carbon dioxide concentrations at 200, 300, 400, and 500 km altitude. No errors included as only one model year was simulated with WACCM-X for each plotted value.

5.3 Future Density Reductions Under High Solar Activity

Solar activity has an impact on neutral density trends, with trends of smaller magnitude found during high solar activity compared to low solar activity. Neutral densities also see an order of magnitude increase during high solar activity, leading to a significant increase in atmospheric drag on objects orbiting in LEO and increasing the rate of orbital decay of small debris fragments up to 1000 km. Within this context, understanding possible future density trends under high solar activity is key for modelling the LEO debris environment and planning LEO orbital operations when looking decades or more into the future.

Using a similar methodology to that of the low solar activity study (Section 5.2), WACCM-X was used to model the atmosphere under high solar activity with an F10.7 fixed at 200 sfu, and quiet geomagnetic activity with Kp of 0.33. Ground-level carbon

dioxide concentrations were set to that of 1975 and 2000 to provide a comparison against historic studies.

The historical trend under high solar activity was derived similarly to the low solar activity trend, with a result of -3.5% per decade over the 1975 to 2000 period at 400 km altitude. The magnitude of this trend is within the range of previous studies (-0.8 to -4.0% per decade as detailed in Table 3.2), but on the higher end, particularly compared to the other model studies (-0.8 to -3.0% per decade).

Nine simulations of increasing ground-level CO_2 concentrations were performed using the concentrations from RCP8.5 values from 2015 to 2095 inclusive in 10 year intervals. Due to the significant impact high solar activity trends and densities have on the debris environment, a greater understanding of the density reductions and model errors was sought than that found within the low solar activity study. The low solar activity study was performed first, and only having one cycle for each modelled CO_2 concentration did not allow errors to be calculated. Therefore each simulation under high solar activity had four months of spin-up and five year-long cycles, for a total of 64 months. The exception is the highest carbon dioxide concentration run, equivalent to 2095 under RCP8.5, where only four cycles and the four month spin-up could be completed (totalling 52 months). The year 2100 was reached during the fifth cycle, the upper time boundary of WACCM-X, limiting the amount of cycles that could be simulated.

For each cycle, a global-mean annual-mean was taken (as detailed in Section 5.2). For each ground-level CO_2 concentration, a mean and standard deviation of these cycles was calculated. The relative difference against the year 2000 for increasing ground-level CO_2 concentrations is given in Figure 5.11. The plotted uncertainties are the standard deviations over the five cycles as a percentage, with the additional percentage uncertainty from the 2000 run added to the higher CO_2 concentration runs. As each cycle starts with the same conditions as the previous cycle, these uncertainties provide an insight into the impact the initial conditions have upon the trends within WACCM-X. These high solar activity trends exhibit similar behaviour to the low solar activity results, with the trend increasing in magnitude with increasing altitude, and the cumulative nature of the multiplicative trend resulting in a curved relation. However the magnitude of density reductions are smaller than the low solar activity results, as expected from previous historical studies.

Figure 5.11 also shows a slowing neutral density reduction between 450 to 550 ppm, before recovering again. This ”bump” in the data from the RCP8.5 simulated years of 2025 to 2045 was seen in the low solar activity study at similar CO_2 concentrations. Again, no relation was found to any input data into WACCM-X or any constituent parts of CESM, nor a physical mechanism within the real thermosphere to explain the

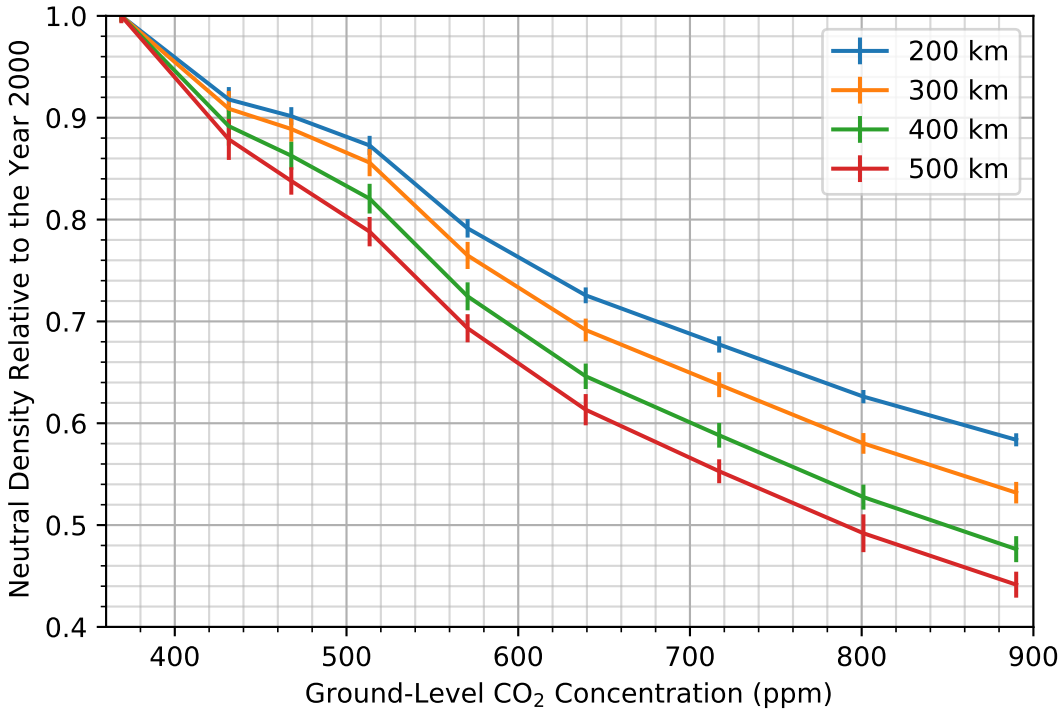

FIGURE 5.11: Neutral atmospheric density relative to the year 2000 under high solar activity (F10.7 = 200 sfu) for increasing ground-level carbon dioxide concentrations at 200, 300, 400, and 500 km altitude. Errors included are the standard deviation of the five global mean annual means.

slowing density reduction. This suggests a mechanism within the physical modelling of WACCM-X which is lost with increasing carbon dioxide concentration.

5.4 Solar Activity Dependence

After exploring density trends under low and high solar activity, the question remained of how to bridge the gap between the two. Historic studies differed on the relationship between the magnitude of trend and the solar activity level, with these summarized in Figure 3.2. Model studies have a low resolution in F10.7 (two values or less, with only Solomon et al. (2015) modelling three values), but showed a monotonically decreasing trend magnitude with increasing solar activity. However the observations of Emmert et al. (2004, 2008) and Emmert (2015b) showed a minimum in the magnitude of trend at medium solar activity, while also showing the overall tendency for a larger magnitude of trend during low solar activity compared to high solar activity. This provided the motivation to explore the solar activity dependence of the future density reductions.

As the motivation was to bridge the gap between low and high solar activity under future carbon dioxide concentrations, relative neutral density reductions were required at varying solar activity levels. This required simulating the atmosphere with the chosen future carbon dioxide concentration, as well as the atmosphere under a reference concentration (i.e. the year 2000). As a result, only one carbon dioxide concentration was simulated to limit computing times. A concentration of 639 ppm (equivalent to RCP8.5 year 2065) was chosen as a midpoint between the lowest and highest modelled carbon dioxide concentrations. It was also decided to model five solar activity levels. Each solar activity and CO_2 concentration was modelled for two model years plus spin-up, again due to limited computing time. The data for the RCP8.5 2065 simulation for an F10.7 value of 200 sfu was taken from the high solar activity study, and the low solar activity data (F10.7 = 70 sfu) extended for an extra year over that used in the previous study. New simulations were performed for the reference concentration (year 2000) and future concentration (RCP8.5 year 2065) at fixed F10.7 values of 100, 135, and 170 sfu. Geomagnetic activity was held low at a Kp value of 0.33 throughout.

The results from this study are presented in Figure 5.12 where the global-mean annual-mean neutral density in a RCP8.5 2065 scenario relative to the year 2000 has been given for varying F10.7. Again, the density reduction increases in magnitude with increasing altitude. At a fixed altitude, the largest reductions are seen under high solar activity and the smallest reductions under low solar activity. The results of Figure 5.12 show the magnitude of reduction monotonically decreasing with increasing solar activity. This matches the relation seen in previous modelling results rather than observations (with these historical studies reviewed in Figure 3.2).

5.5 Latitude Dependence

While the trends discussed in the previous sections focused on global averages, the worldwide coverage of the data sets produced by WACCM-X allows for study of the spatial dependence of trends.

Figure 5.13 plots the latitude dependence of the density reductions discussed in Sections 5.2, 5.3 and 5.4. These are the temporally averaged densities (with spin-up data removed and across multiple cycles when available), averaged across longitudes, and then divided by densities of the year 2000 reference case with matching solar activity levels.

There is more variability in the low solar activity latitude dependence than the high or varying studies. This is likely due to the fact only one year-long cycle has been simulated for each carbon dioxide concentration, compared to two cycles in the varying solar activity study and five cycles in the high solar activity study. One

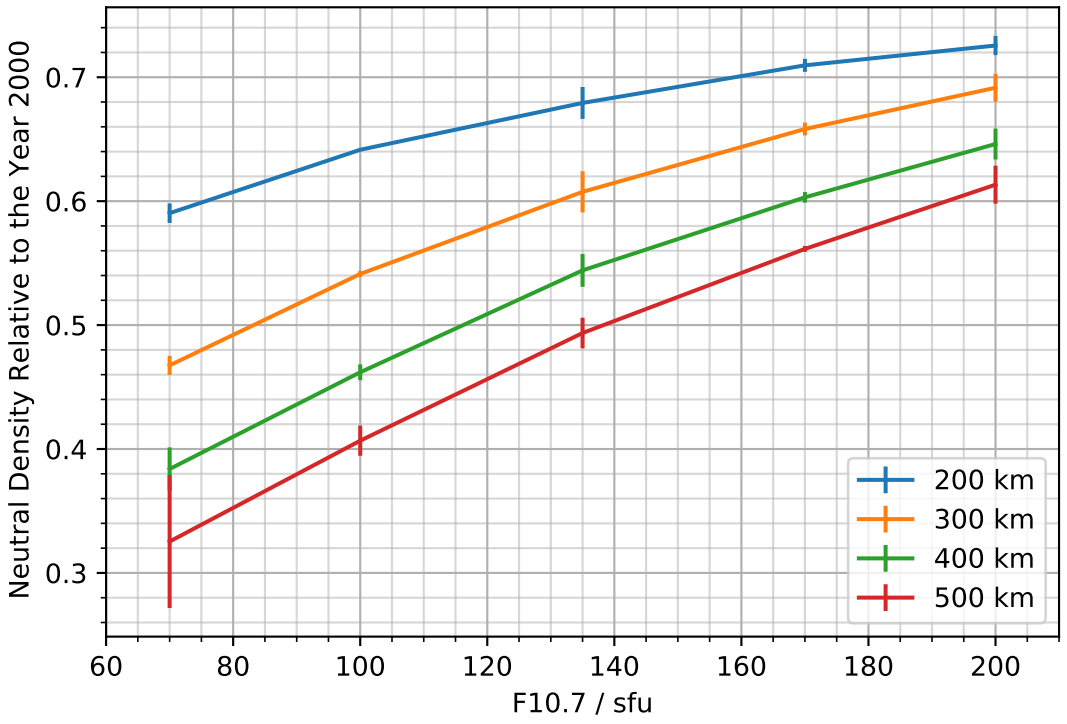

FIGURE 5.12: Neutral thermospheric densities relative to the year 2000 for a ground-level carbon dioxide concentration of 639 ppm (RCP8.5 2065) under varying solar activity and for 200, 300, 400 and 500 km altitude.

particular example of the variability is the 2025 RCP8.5 density reduction being smaller in magnitude than that of 2035 in the northern hemisphere, but larger in the southern hemisphere. This switching in hemispheres also somewhat correlates with the "bump" in data seen in the neutral density reduction at around 470 ppm of Figure 5.10. However, a similar bump was seen at similar concentrations in the high solar activity study (Figure 5.11) but the same latitude dependence is not seen in the high solar activity data of Figure 5.13, suggesting this is not the cause of the bump.

The low solar activity (F10.7 = 70 sfu) latitude dependence in the varying solar activity study used two cycles rather than one, but still shows more complex behaviour than the other solar activity levels. While more cycles would be required to be conclusive, the density reductions under low solar activity may be exhibiting this more complex behaviour as heating sources other than UV-heating play a larger role.

The latitude dependences in the high and varying solar activity studies reveal the relative neutral density decreases are largest in magnitude in regions of mid-latitude, with the northern hemisphere decreases in general being of a larger magnitude than the southern hemisphere.

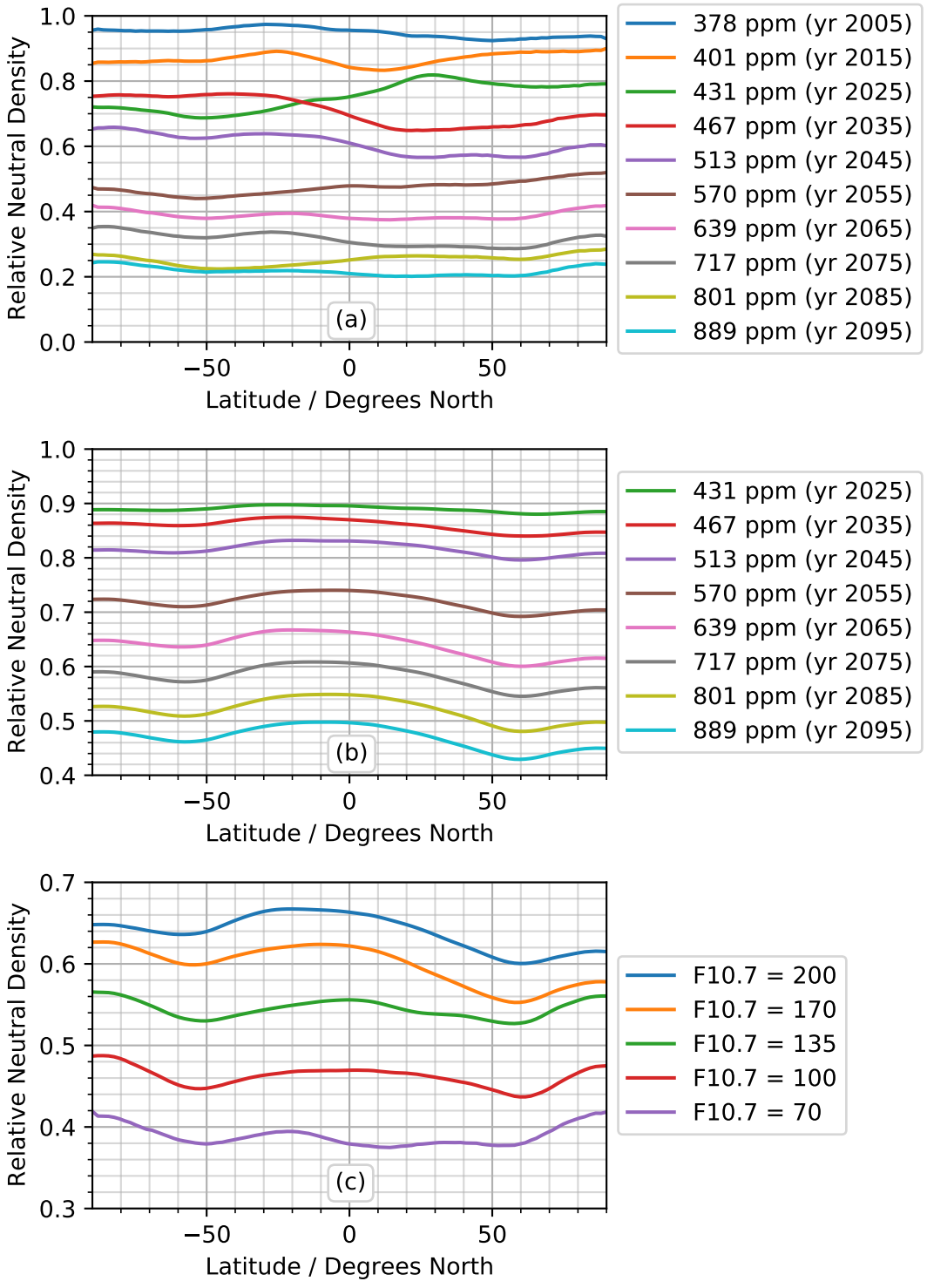

FIGURE 5.13: Latitude dependence of the neutral density decreases relative to the year 2000 of the previous studies at 400 km altitude. (a) details the low solar activity (F10.7 = 70 sfu) study, (b) the high solar activity (F10.7 = 200 sfu) study, and (c) the decreases at 639 ppm (equivalent to the year 2065 in RCP8.5) for varying solar activity levels.

5.6 Density Scaling Table for Empirical Models

The motivation behind investigating how global-mean neutral thermospheric densities will reduce into the future was to understand the impact on the space debris environment in LEO. While the data sets from WACCM-X could theoretically be put directly into a space debris evolution model, the length of time required to fully simulate the multiple decades required under multiple scenarios makes this an inefficient way of tackling the problem. Instead it was decided to use the data from the studies presented in this chapter to create a density scaling table which could be applied to the fast empirical atmospheric models already used in space debris evolution models.

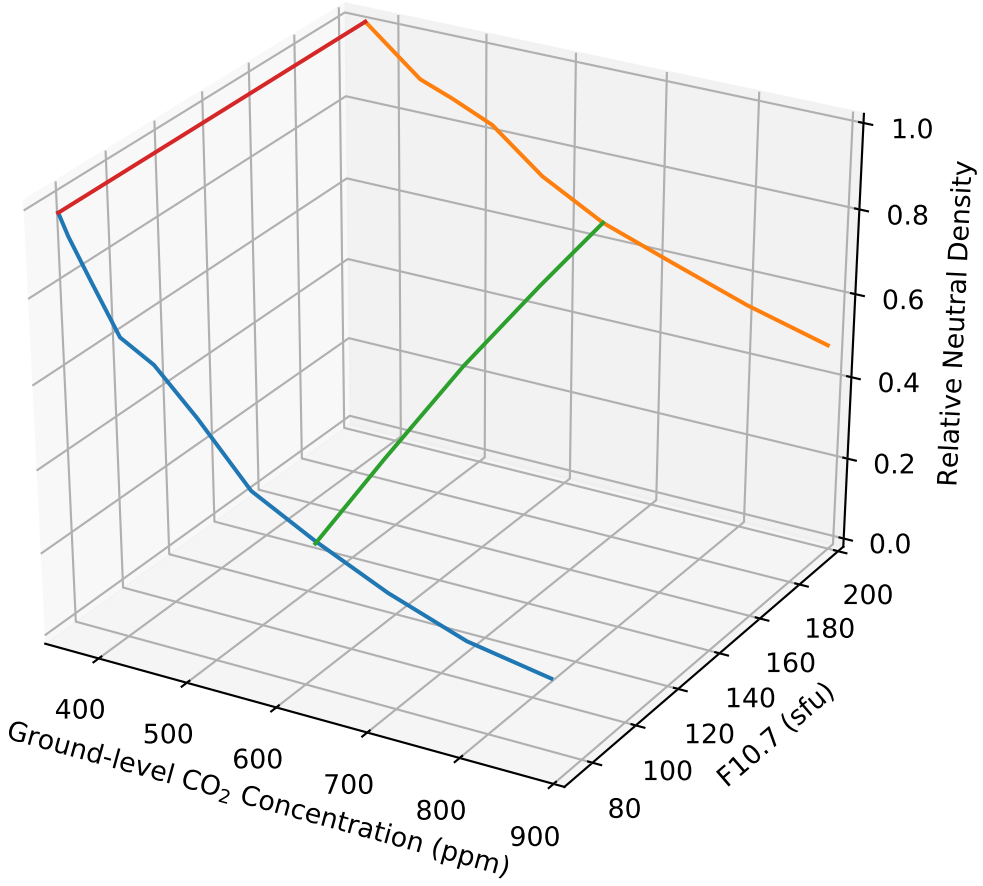

FIGURE 5.14: A three-dimensional representation of the neutral density reductions relative to the year 2000 at 400 km altitude. Combines results from Figures 5.10 (blue line), 5.11 (orange), 5.12 (green), as well as the reference line (red).

Simulations of high solar activity and low solar activity under varying CO_2 concentrations define the upper and lower boundaries in solar activity, with the varying solar activity defining the relationship between these two boundaries at a fixed CO_2 concentration. A surface which defines the density reduction for a given

ground-level CO_2 concentration and solar activity can begin to be created by combining the results at 400 km altitude from Figures 5.10, 5.11 and 5.12, as demonstrated in the three-dimensional representation of Figure 5.14. An additional reference line has been added as all density reductions have been taken relative to the year 2000. By making the assumption that the relation to solar activity scales with the increase in ground-level carbon dioxide concentration, using the upper and lower bounds from the high and low solar activity studies, a surface can be more fully defined by linearly scaling the solar activity relation exhibited in the RCP8.5 2065 simulation to the other modelled CO2 concentrations.

This surface and therefore the neutral density reductions change with altitude. Using the density reduction values calculated at other altitudes in each of the solar activity studies allows the above process to be completed for these altitudes (from 200 to 500 km). This results in a table of density reduction values which are dependent upon solar activity (via F10.7), ground-level CO_2 concentrations, and altitude. Latitude dependence could also theoretically be added as an extra dimension to this table, although it was neglected in this case as the debris model discussed in Chapter 6 only made use of globally averaged atmospheric densities in its propagation algorithm.

5.7 The Thermosphere under the Representative Concentration Pathways

The Representative Concentration Pathways (RCPs) define four scenarios for how greenhouse gases, and in particular carbon dioxide concentrations, could evolve through to 2100. They have been discussed in detail in Section 2.3 and the CO_2 concentrations are presented again in Figure 5.15.

The density scaling factors from the table discussed in Section 5.6 currently vary with ground-level carbon dioxide. This can be used along with the RCPs to define how thermospheric densities could vary into the future, with these plotted for fixed low solar activity in Figure 5.16 and for fixed high solar activity in Figure 5.17. These plots use the same y axis scale for relative neutral density to visually demonstrate the difference between each RCP scenario. In reality solar activity will vary into the future, although the nature and length of future cycles is unknown. To give a more representative example of how future density reductions could vary into the future under different solar activity levels, Figure 5.18 gives the relative neutral density reductions which would be applied to the results from an empirical atmospheric model, assuming solar activity repeats solar cycle 24 (seen in Figure 2.7).

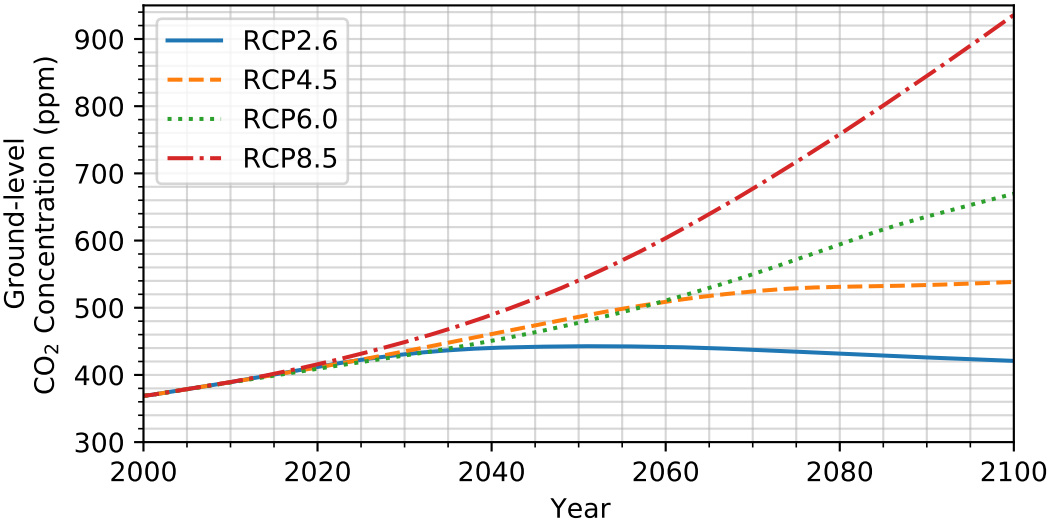

FIGURE 5.15: Future carbon dioxide concentration pathways from the Representative Concentration Pathways of the IPCC's fifth assessment report (IPCC (2014)) from the year 2000 to 2100.

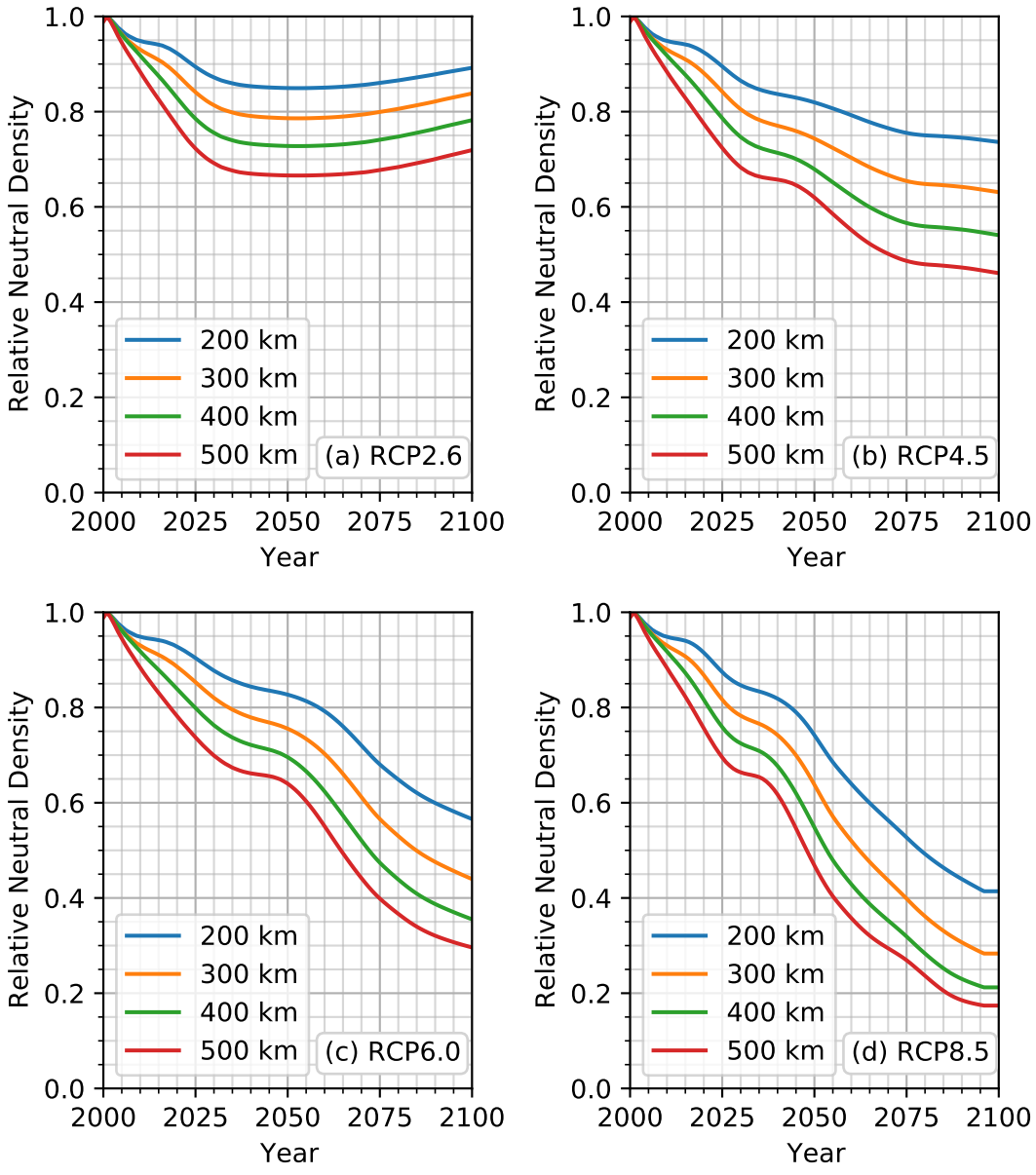

FIGURE 5.16: Global-mean neutral density reductions under each RCP scenarios and fixed low solar activity (F10.7 = 70 sfu).

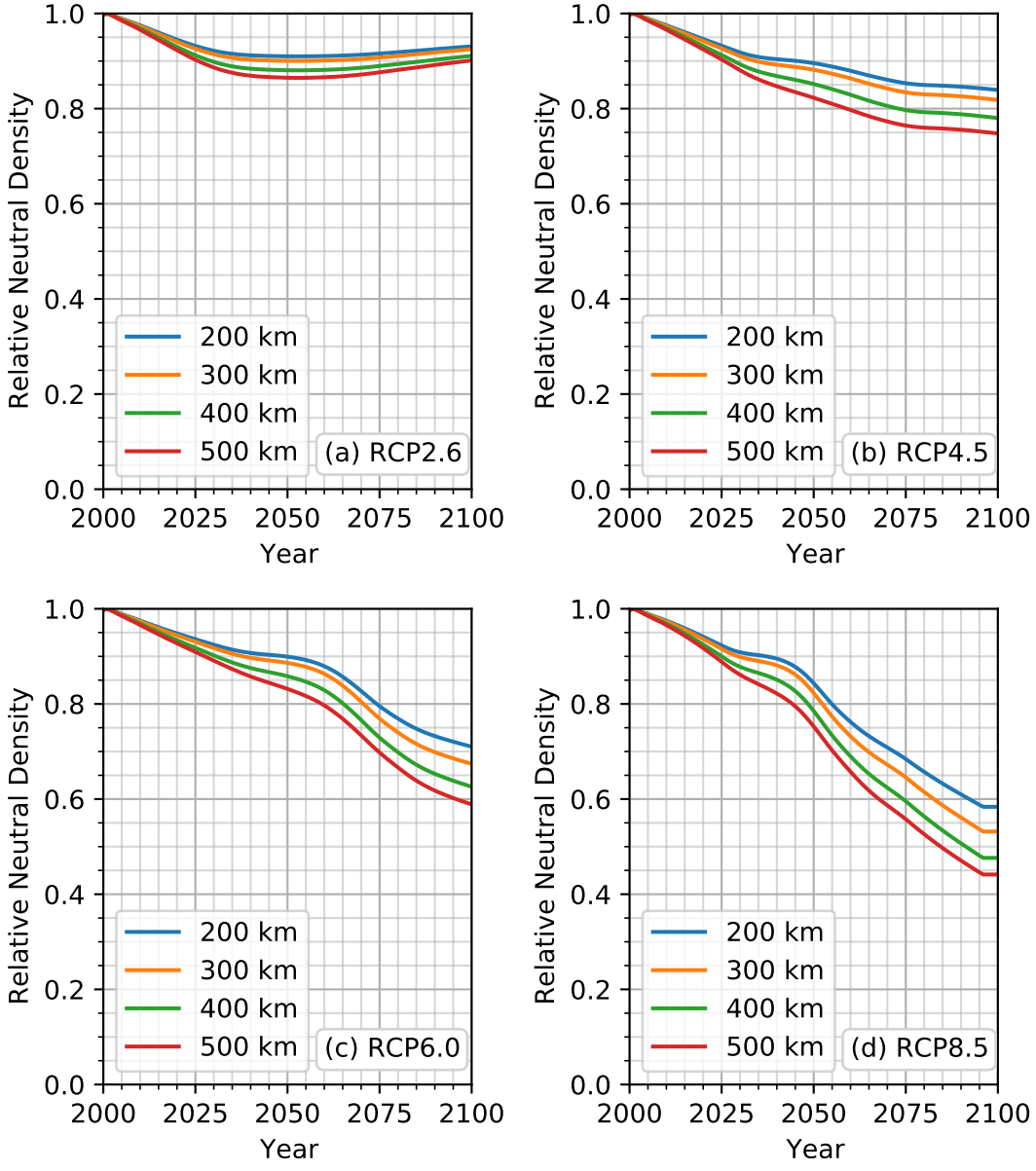

FIGURE 5.17: Global-mean neutral density reductions under each RCP scenarios and fixed high solar activity (F10.7 = 200 sfu).

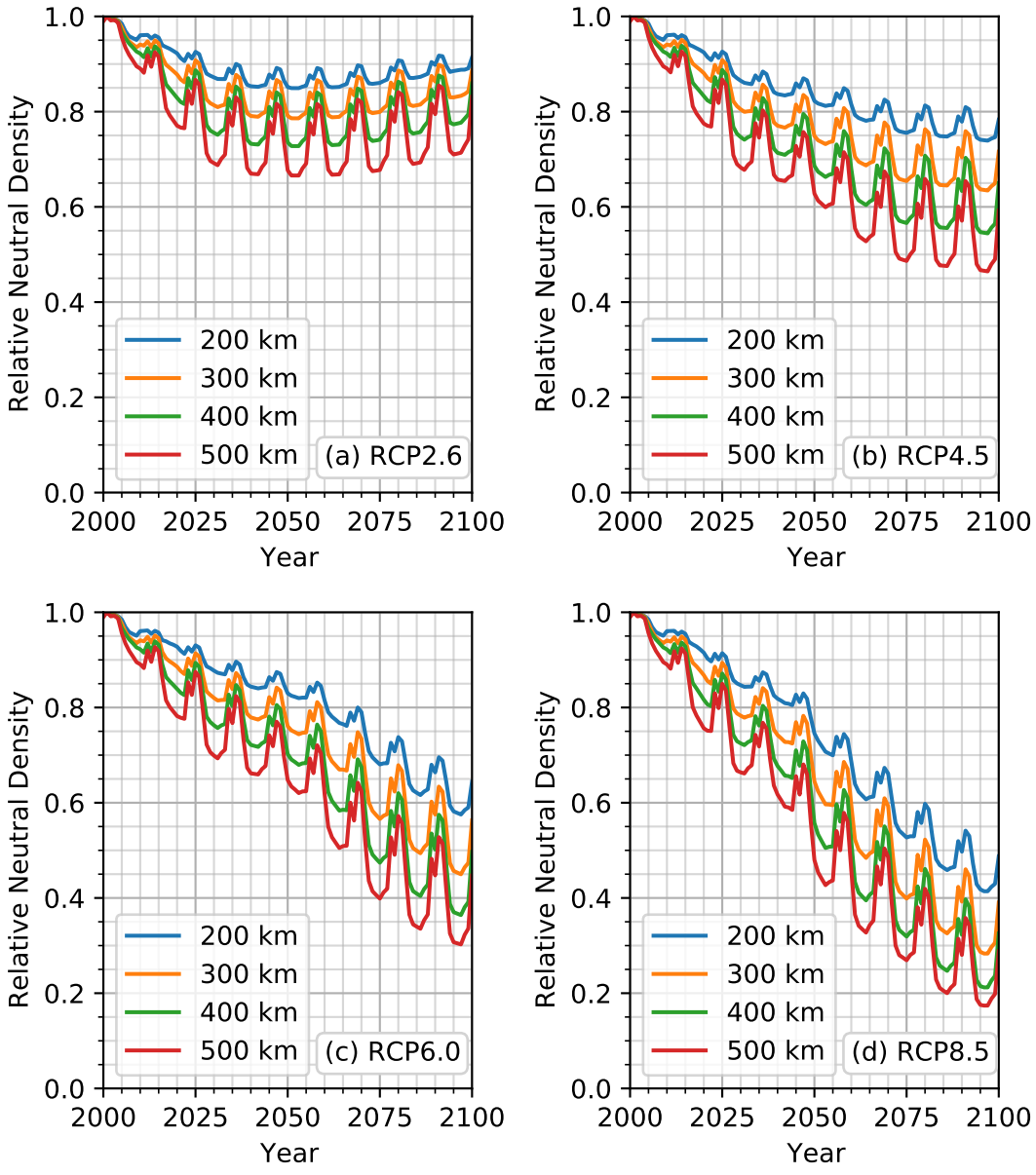

FIGURE 5.18: Global-mean neutral density reductions under each RCP scenarios with solar activity repeating solar cycle 24.

Chapter 6

Debris Environment Modelling

The reduction in thermospheric densities due to increasing carbon dioxide concentrations will also increase the orbital lifetimes of objects and space debris in low Earth orbit. The impact this has on individual objects has already been observed, with the slowing rate of decrease in the semi-major axis of objects orbiting in LEO used to derive the historical density trends. The future impact is less well understood, with the majority of debris evolution models neglecting the impact of decreasing density trends via empirical atmospheric models which do not include the trends. Lewis et al. (2005) and Lewis et al. (2011) investigated the impact on the future debris environment by extrapolating fixed historical observational trends into the future. These were both discussed in detail in Section 3.3. They both found increasingly significant impacts on the LEO debris environment the further into the future they simulated, with both the number of objects and the number of collisions increasing with time. However, both these studies linearly extrapolated a historical density trend into the future, not accounting for how the carbon dioxide concentrations could change over the modelled period.

This chapter will detail the debris evolution model which was created with the primary focus being the simulation of the debris environment including a contracting thermosphere. Each constituent model will be explored in detail, along with a summary of how they interact with each other during a simulation. Methods of validation for the key constituent models will be discussed. Finally the results from the model will be presented, showing how the debris environment changes within each RCP scenario.

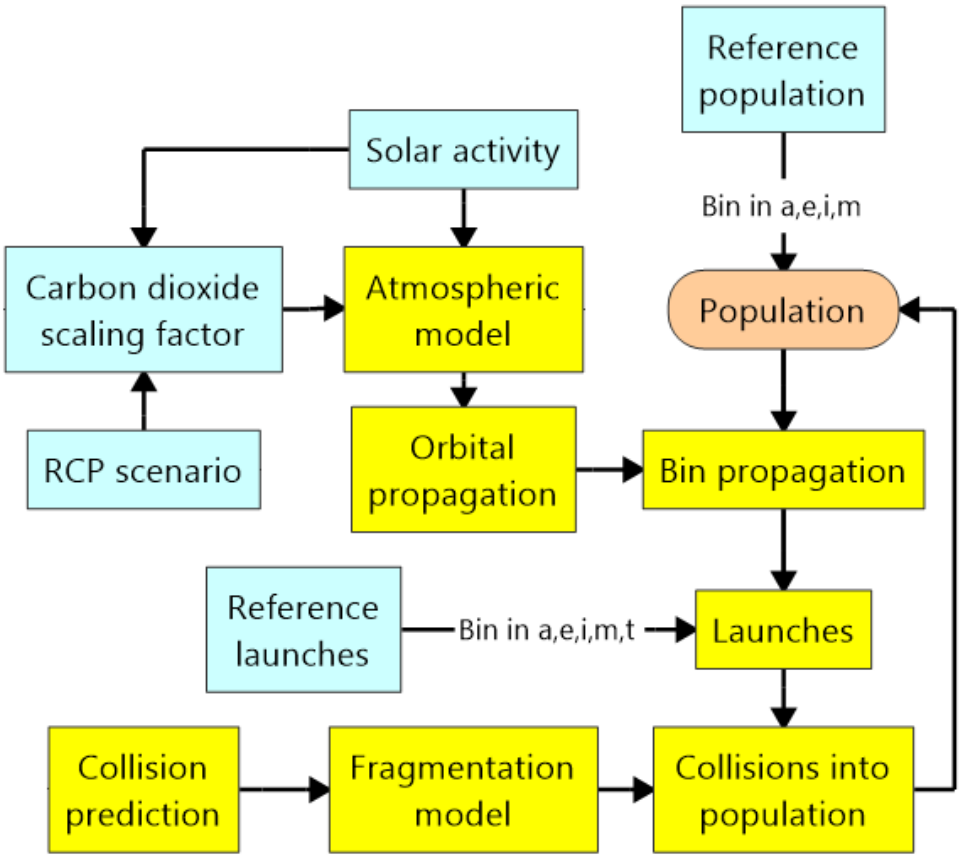

FIGURE 6.1: Conceptual map of the BRAD debris model. Blue denotes inputs, yellow the constituent models discussed in separate sections, and orange the main population which is stored at each model step for analysis.

6.1 BRAD Model Description

To investigate the impact neutral density reductions have on the debris environment, the author fully developed a new statistical debris model named the Binned Representative Atmospheric Decay (BRAD) debris model. It is summarized in Figure 6.1 and was based on the Stochastic Analog Tool (STAT) debris model of Rossi et al. (1998), which was described in Section 3.2.

6.1.1 Binning

Many space debris evolution models simulate each orbiting object individually, for example DAMAGE, LEGEND and DELTA. The debris model described in this chapter reduces the number of objects which need to be simulated by binning objects by

semi-major axis, a, eccentricity, e, inclination, i, and mass, m. Calculations are performed on a representative object at the centre of each bin instead.

The choice of both the range used for each binned variable, as well as the number and size of bins, play key roles in the characteristics of the model. Too small a range in semi-major axis and eccentricity means objects in highly eccentric orbits which cross into low Earth orbit are not captured. A balance also has to be made between the size of bins and the number of bins. Too large a bin size results in characteristics of orbiting objects being lost, for example by there being too large a range in the area-to-mass ratios derived from mass, and therefore an object having too short or long an orbital lifetime. However many smaller bins quickly increases the number of calculations which have to be performed at each time step, which at the extreme can result in the number of calculations overtaking that of modelling individual objects, effectively losing the speed benefits of binning.

TABLE 6.1: Choice of bins within the BRAD debris model

Binned variable	Minimum	Maximum	Number of bins	Bin Scaling
Semi-major axis	6678 km	7578 km	24	Linear
Eccentricity	0	0.1	8	Linear
Inclination	0	$5\pi/8$	5	Linear
Mass	10^{-2} kg	$10^{4.5}$ kg	13	Logarithmic

The choice of bins used throughout this Chapter are given in Table 6.1. These were arrived at after testing multiple combinations and finding a balance between model run-times and capturing the dynamics of the population. The choice of bins for semi-major axis and eccentricity include circular orbits from 300 to 1200 km altitude, as well as eccentric orbits up to an extreme of 440 $\times$ 1957 km. This captures objects permanently resident in the lowest LEO regions which are particularly affected by drag as well as objects with a larger semi-major axis but low perigee. However, it does neglect objects in Highly Eccentric Orbits (HEO) which cross into LEO. ESA Space Debris Office (2020) shows that less than 10% of objects with perigees below 2000 km altitude are in these HEO orbits, and they spend a short fraction of their orbit in the LEO environment. The best way to capture these objects without massively increasing the number of bins used is to use logarithmic scaling in the eccentricity variable. However, this added additional complexity, particularly in the bin propagation algorithm of Section 6.1.4. Therefore the objects in HEO objects were neglected and the BRAD model exclusively focuses on those wholly resident in the LEO environment.

To best describe the debris population with orders of magnitude difference between the smaller, untrackable fragments and the larger, trackable fragments, the mass bins follow a logarithmic scale. The largest captured mass is 31622 kg using the binning of Table 6.1. This allows for capture of all objects in the initial population (discussed in Section 6.1.2) with the ISS and traffic related to human spaceflight removed. The

relatively coarse bin choice for inclination allows for distinction of different classes of orbit, for example polar and sun-synchronous orbits from lower inclination orbits.

The orbital elements which have not been binned (right ascension of ascending node (Ω), argument of perigee (ω), and true anomaly (θ)) are assumed to be uniformly distributed.

6.1.2 Initial Population

To start the simulation, trackable objects for the desired starting date are obtained from ESA's Database and Information System Characterising Objects in Space (DISCOS), described in McLean et al. (2017). Historical simulations start from the year 1979 and use the trackable population from that year as the initial population. Anz-Meador et al. (2018) shows only a limited number of in-orbit explosions and no collisions had occurred by this date. The relatively few small, untrackable objects had been created from environment effects, such as atomic oxygen erosion and micrometeoroid impacts, and separately, the slag from solid rocket motors. However, when modelling the modern day space environment, these small fragments are large in number. While the 34,000 objects larger than 10 cm are in general trackable, there are estimated to be around 900,000 objects between 1 cm and 10 cm in size, and over 128 million objects between 1 mm and 1 cm (with these figures regularly updated at ESA (2021)).

While the majority of BRAD analysis focused on the trackable population, a method of studying the number of collisions occurring between trackable and non-trackable objects was sought. With this motivation in mind, the untracked population in the 1 cm to 10 cm size range was simulated. ESA's Meteoroid and Space Debris Terrestrial Environment Reference (MASTER) software tool, described by Flegel et al. (2009), provides spatial densities of debris and micrometeoroids between 1 μm and 100 m. These can be used to calculate the debris flux on satellites in Earth orbit. Initially the spatial densities from the MASTER model were considered to populate the untracked mass bins. However, a method could not be found to convert the altitude distribution of fragments from MASTER to the a, e, i bins used by BRAD.

Instead a scaling method was used by making the assumption that the population modelled by BRAD had a similar distribution of trackable to untrackable objects as that given in the first paragraph. Therefore the number of objects required in BRAD in the 1 cm to 10 cm range, $n_{BRAD}(1 < L_c < 10 \text{ cm})$, can be obtained by scaling the number of trackable objects in the BRAD population acquired from DISCOS, n_{DISCOS}, as given by

$$n_{BRAD}(1 < L_c < 10 \text{ cm}) = \frac{900,000}{34,000} n_{DISCOS} \tag{6.1}$$

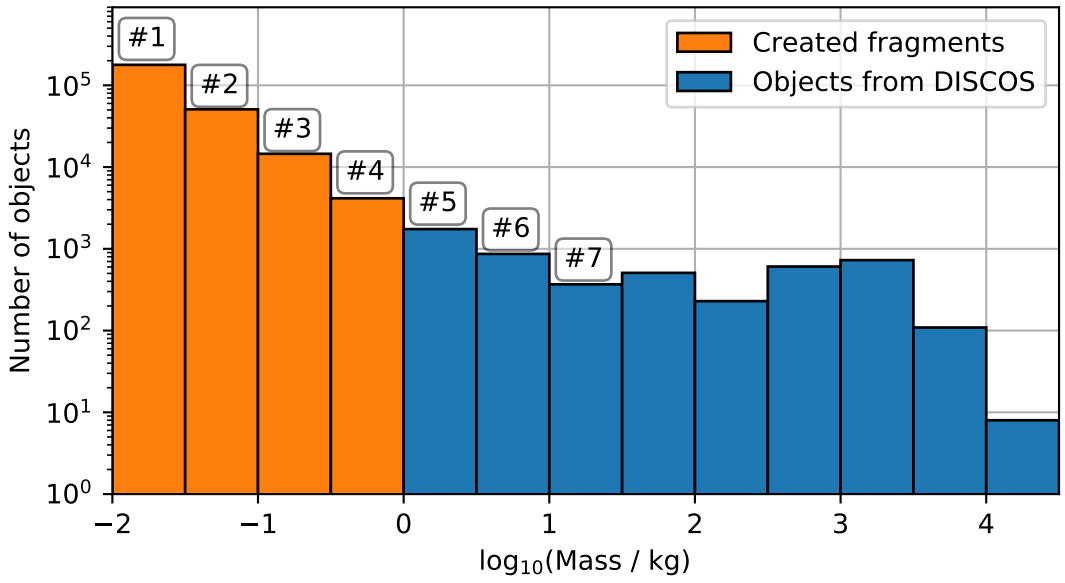

FIGURE 6.2: Total number of objects in each mass bin after the lowest mass bins are populated with untrackable fragments. The first seven mass bins are labelled to aid the description within the text.

This number of objects needs to be distributed over the bins which cover the 1 cm to 10 cm range, namely the first four, as shown in Figure 6.2. It was assumed that the ratio between the number of objects in successive mass bins would be similar over the first seven mass bins. The number of objects in mass bin 6 was found to be 3.5 times greater than bin 7, and similarly for bin 5 to bin 6. Therefore this relationship was carried into the smaller mass bins such that

$$n_{BRAD}(m = j) = 3.5 \times n_{BRAD}(m = j + 1) \tag{6.2}$$

where $n_{BRAD}(m = j)$ is the number of objects in mass bin number j. Finally, for each mass bin, this number of objects is then split over the corresponding a, e, i bins in a similar proportion to the trackable population, such that

$$n_{BRAD}(a, e, i, m = j) = n_{BRAD}(m = j) \times \frac{n_{BRAD}(a, e, i, m = 5 \text{ to } 13)}{n_{BRAD}(1 < L_c < 10 \text{ cm})} \tag{6.3}$$

6.1.3 Orbital Propagation

Orbital propagation allows objects in the BRAD population to be moved from bin to bin, as well as removed from the population via atmospheric drag. Debris models which track individual objects often account for perturbations which change the right ascension of ascending node (Ω), argument of perigee (ω), and true anomaly (θ) of

each object's orbit. Table 2.3 detailed how the perturbations due to Earth's asymmetry and third bodies change Ω, ω and θ secularly. Due to the assumption in BRAD that these orbital elements are uniformly distributed, these perturbations were neglected.

This leaves atmospheric drag and solar radiation pressure as the two perturbations which can change the binned variables of semi-major axis (a), eccentricity (e) and inclination (i). The perturbation due to solar radiation pressure is very small at all altitudes considered by BRAD (as shown in Figure 2.17), whereas atmospheric drag increases exponentially with decreasing altitude such that it is four orders of magnitude greater than the SRP perturbation at ~250 km altitude. Therefore drag is the only perturbation simulated in the BRAD model.

The method for atmospheric drag propagation follows King-Hele (1987), calculating the change in semi-major axis during each model time step for each bin's representative object. Assuming the perigee for each orbit remains constant, the eccentricity is then calculated. These changes in a and e are then passed to the bin propagation algorithm discussed in Section 6.1.4.

The rate of change in semi-major axis, $\dot{a}$, is calculated in King-Hele (1987) as

$$\dot{a} = -\frac{a^2 \rho v^3 F B}{\mu} \tag{6.4}$$

where ρ is the atmospheric density, v is the orbital velocity, μ is the Earth's standard gravitational parameter, and where B is the ballistic coefficient calculated with the coefficient of drag, C_D, and area-to-mass ratio, A/m, by

$$B = C_D \frac{A}{m} \tag{6.5}$$

and F accounts for the rotation of the atmosphere by

$$F = \left(1 - \frac{r_p}{v_p} \Lambda \omega_E cos(i)\right)^2 \tag{6.6}$$

where r_p and v_p are the radius and speed at perigee respectively, Λ is the atmospheric rotation rate, and ω_E is the Earth's angular rate. As BRAD cannot distinguish between objects' shapes, it is assumed all objects have a similar C_D which is set to the commonly used value of 2.2. This value was originally suggested by Cook (1965) and was discussed in a modern context by Moe and Moe (2005). The area-to-mass ratio, A/m, is obtained from rearranging the area to mass relation by Kessler and Cour-Palais (1978), resulting in

$$\frac{A}{m} = \frac{m^{-0.115}}{62^{0.885}} \tag{6.7}$$

Following the method set out in Rossi et al. (1998), the density used in Equation 6.4 changes to reflect the eccentricity of the orbit and the length of time spent near perigee. When $2ae \leq 50$ km, the orbit is defined as "almost-circular", so the density is assumed to be equivalent to the density at the perigee throughout the orbit. When 50 km $< 2ae \leq 2H$, the orbit is defined as "near-circular", with the average density set to

$$\rho = \rho_0 \frac{H_0}{2ae} \left(1 - exp\left(-\frac{2ae}{H_0}\right)\right) \tag{6.8}$$

where ρ_0 and H_0 are the density and atmospheric scale height at perigee. Rossi et al. also identified an elliptical case when $2ae > 2H$, although this case doesn't arise with the current bin selection of Table 6.1.

To calculate the new eccentricity, first the perigee, r_p of the original bin is calculated by

$$r_p = a(1 - e) \tag{6.9}$$

Then assuming the perigee stays constant during the propagation, the new eccentricity, e_1, is calculated by reversing Equation 6.9 and using the rate of change in semi-major axis, $\dot{a}$, from Equation 6.4 over the time step Δt, so

$$e_1 = 1 - \frac{r_p}{a + \dot{a}\Delta t} \tag{6.10}$$

Representative objects are the only things propagated at each model step, and are common between different runs. Therefore densities at each of the model's possible perigee altitudes are retrieved from NRLMSISE-00, with a global-mean taken over each model time step. These are then stored so that if BRAD performs a simulation with the same binning, time step and solar activity, the averaged densities at perigee can be retrieved rather than being recalculated, speeding up the model on repeated runs.

Finally, depending upon the RCP scenario being modelled, a density scaling factor is obtained from the scaling tables of Section 5.6 and applied to the NRLMSISE-00 density.

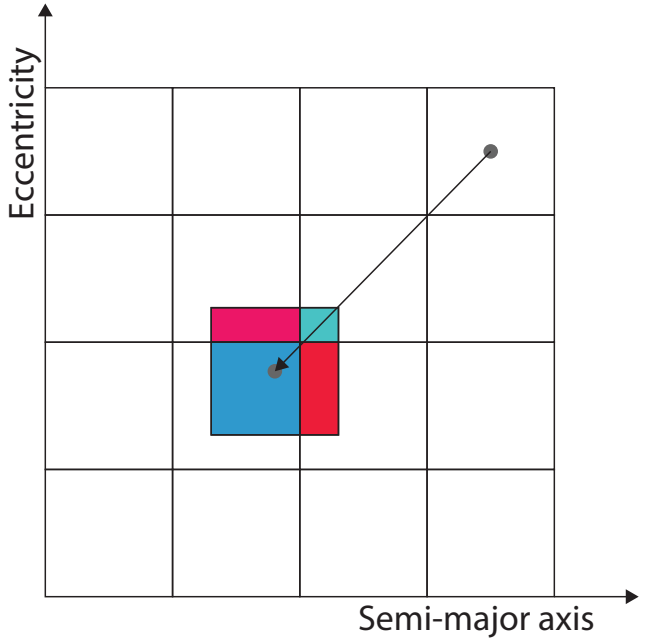

FIGURE 6.3: Visual representation of bin propagation in the BRAD debris model. The grey dot represents an object at the centre of a bin being propagated. A virtual bin is then drawn around this object. The number of objects from the original bin is then split into the original bins, with the number proportional to the size of the overlap.

6.1.4 Bin Propagation

The representative object at the centre of each (a,e,i,m) bin is propagated by the method described in Section 6.1.3, with a change in semi-major axis and eccentricity calculated at each model time step. However this propagation needs to be applied to all objects within the bin rather than just the representative object. Figure 6.3 demonstrates how this is accomplished. A virtual bin is drawn around the propagated representative object. The number of objects within the propagated bin is then split into each of the original bins, with the fraction proportional to the size of the overlap.

The orbital elements of objects at the edge of a bin would change by a different amount compared with the representative object at the centre of the bin. This would skew the bin's shape slightly compared to the illustration in Figure 6.3. Accounting for this would require propagating each corner separately and increasing the complexity of the overlap calculation. Finer bin resolution reduces the size of this error. Due to the increased complexity and the relatively small bin size in semi-major axis, the basic method of bin propagation (that shown in Figure 6.3) is maintained.

6.1.5 Launches

Future launches into space provide an additional source of uncertainty. Factors such as technological advancement, global politics and economics complicate the

prediction of how launches could change into the future. However, as the only source of additional mass into the space environment, they must be included in modelling. A common method utilised by other space debris models is to repeat a period of historical launches, with additional launches added when modelling specific scenarios such as constellation launches.

Similarly to the initial populations in Section 6.1.2, launch data was obtained from DISCOS. For historical simulations, launches follow the DISCOS data. However for future simulations, launches repeat a cycle between January 1st 2005 to December 31st 2012. This reflects a period of modern launch rates while not entering the present-day period dominated by constellations. Launches are binned in a, e, i and m, as well as the additional variable of time t which is the same size as the model time step. The number of objects launched in each time bin is shown in Figure 6.4. Then at each time step, the corresponding objects from the a, e, i and m bins are added into the main population. To prevent possible aliasing with the solar cycle, the start point of the launch cycle is randomly selected from a uniform distribution of the t bins.

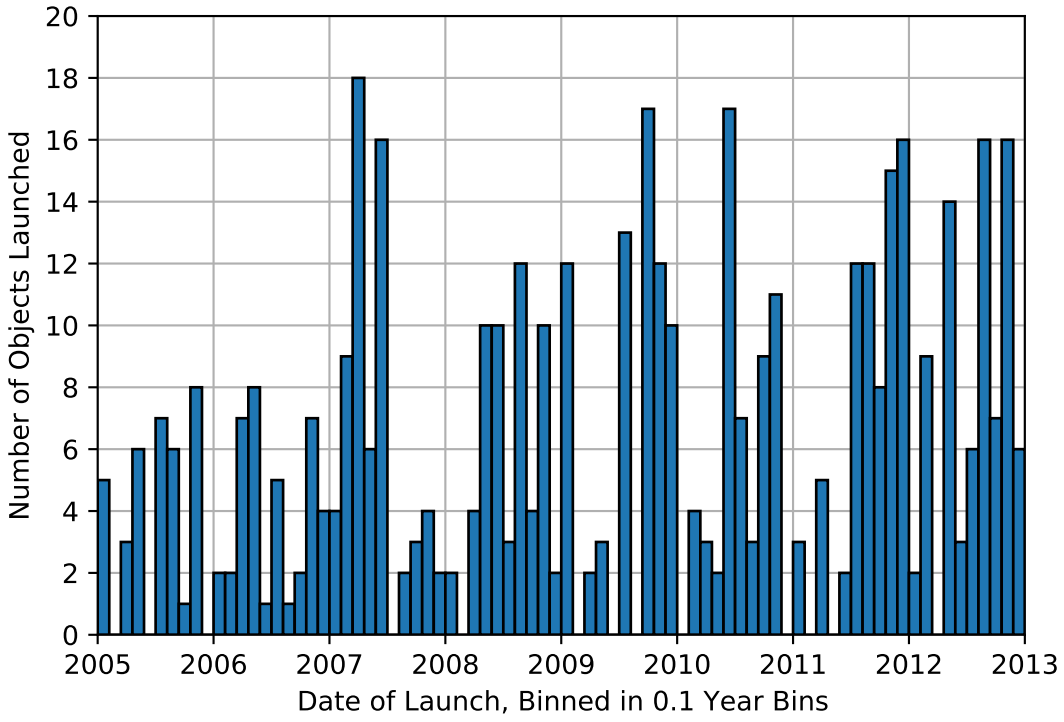

FIGURE 6.4: Number of objects launched between 2005 and 2013 binned in 0.1 year bins, with this cycle repeated when simulating future simulations.

6.1.6 Fragmentations

Explosions have not been included in the BRAD debris model. The "History of On-Orbit Satellite Fragmentations" of Anz-Meador et al. (2018) shows that explosions

have contributed a significant amount of fragments to the population. To study a "best-case scenario" where there is a 100% passivation rate (similar to the Liou et al. (2013) study), it was assumed no explosions would occur.

This leaves collisions as the only source of fragmentations within the model. The binning method used within the model limits how collisions can be identified, with only the 4 variables (a, e, i, m) associated with each bin available. While the Cube algorithm discussed in Section 3.2.2.1 is commonly used by debris evolution models, it requires knowledge of discrete objects. Therefore an algorithm which only requires the a, e, i orbital elements has to be selected. The Greenberg (1982) and Bottke and Greenberg (1993) algorithms also discussed in Section 3.2.2.1 fit this restriction.

While the Bottke algorithm is a correction to the Greenberg algorithm, the Bottke algorithm was unable to be fully implemented within BRAD. This is as the recommended corrections did not reproduce the example results given within the study (as shown in Figure 3.3). Instead the Greenberg algorithm was used as those example results could be replicated. While the Bottke correction is discussed further in Appendix B, in short, the Bottke correction used the relative velocities at four possible collision locations rather than a single one in the Greenberg algorithm. The difference between these is smaller in the low eccentricity cases of the BRAD model than the high eccentricity examples of asteroids in Table 3.3. Although the Bottke correction would be the favored option, given the inability to reproduce their results, the Greenberg algorithm was used within BRAD.

The representative object of each bin in the population could potentially collide with an object in any other bin, with a possible combination referred to from now on as a pair of bins. Greenberg (1982) presents an Intrinsic Collision Probability (ICP) for each pair of (a, e, i) orbital elements, for which BRAD uses the representative objects at the centre of each bin, through the equation

$$\mathrm{ICP} = \frac{16}{(2\pi)^3 \tau} \int_0^{2\pi} \int_{\omega_0} [f / \sin(u - \omega)] \left(\frac{2\pi\eta_0}{4 T_p U_0 T_{p0}} \right) d\omega_0 d(\Delta\Omega) \tag{6.11}$$

where τ is the combined radii of the two objects, ω and Ω are the argument of perigee and right ascension of ascending node respectively, T_p is the orbital period, and the subscript 0 is used to distinguish between similar parameters from the two orbits involved. Other variables such as f, u, η_0, and U_0 have a long series of other functions used to calculate them, and aren't reproduced here for the sake of brevity. The reader is directed to Appendix B for a full mathematical description of the algorithm.

The ICP of each pair of bins is intrinsic to the orbits of the representative objects. As these do not change between model simulations and due to the length of time required to calculate the ICP, these are calculated and stored the first time BRAD uses

a new binning selection (similarly to atmospheric densities). These are then loaded when BRAD reuses a binning selection.

To obtain the collision probability, the ICP is multiplied by the combined cross-sectional area, $\pi(r+R)^2$, where r and R are the radii of representative objects involved in the possible collision. These radii are obtained from a rearrangement of the mass to area relation by Kessler and Cour-Palais (1978) and assuming a circular cross-section, resulting in the equation

$$r = \sqrt{\left(\frac{m}{62}\right)^{0.885} / \pi} \tag{6.12}$$

where the mass m is in kilograms and the radius, r, is given in metres.

The mean number of collisions, λ, between each pair of bins is obtained by multiplying the collision probability by the number of objects in each bin and the length of the time step. This value will often be a fraction and could be used directly in the model by allowing fractions of a collision to occur. Using small fractions of a collision neglects a major characteristic of the debris environment, namely that infrequent "integer" events[1] like the Iridium 33 - Kosmos 2251 collision cause sudden, significant increases in the number of fragments. Therefore an integer number of collisions, k, is sampled from a Poisson distribution of the form

$$f(k,\lambda) = \frac{\lambda^k e^{-\lambda}}{k!} \tag{6.13}$$

When a collision has occurred within the model, fragments are created with the use of the NASA Standard Breakup Model by Johnson et al. (2001) and corrected by Krisko (2011). This fragmentation model has been commonly used in space debris evolution models since its release. The functions used to calculate area-to-mass ratios, characteristic lengths and ΔV distributions for fragments were presented in Section 3.2.2.2.

6.1.7 Fragmentation Spread Across Bins

When a collision occurs, momentum from the collision is imparted onto the fragments resulting in a change in velocity. The orbital elements of individual fragments change from those of the parent bodies, creating a debris cloud. Over time the slightly differing orbital periods, along with Earth's asymmetry and gravity of third bodies, spread the cloud out. The BRAD model's assumption of random distributed right

[1] i.e. in reality one event will suddenly occur, rather than fractions of an event over a period of time. Also, in a given time period, it is a possibility that two or more events can occur.

ascension of ascending node, argument of perigee and true anomaly fits well with this. However, the semi-major axis and eccentricities also change substantially in catastrophic collisions. This change can be implicitly seen in Gabbard plots of historic events. These plot the orbital periods of collision fragments, along with their perigee and apogee altitudes. An example is given in Figure 6.5(a), which shows the fragments created in the Russian ASAT test against Cosmos 1408 of 15th November 2021. Objects with a larger distance between their apogee and perigee exist in higher eccentricity orbits. The orbital period, T_P is directly related to semi-major axis, a, via

$$T_P = 2\pi\sqrt{\frac{a^3}{\mu}} \tag{6.14}$$

where μ is the standard gravitational parameter. Therefore the spread in orbital period also demonstrates the spread in semi-major axis. Figure 6.5(b) explicitly plots the semi-major axis and eccentricity of the same fragments from the Cosmos 1408 ASAT fragmentation. Anz-Meador et al. (2018) contains Gabbard plots for most catalogued, historic fragmentations.

To understand the distribution of fragments in semi-major axis, eccentricity and inclination, 1000 collisions using random representative objects from BRAD's modelled bins were simulated with the NASA Standard Breakup Model. For each collision and each fragment created, a ΔV was sampled from the breakup model's distribution. A direction was selected from an isotropically uniform distribution and the sampled ΔV added to the parent body's original velocity vector. The location of the collision and new velocity in Cartesian coordinates were than transformed to orbital elements, with these then sorted into the bins of the BRAD model. This is demonstrated for an example collision in Figure 6.6(a). The proportion of fragments from the collision which had entered each bin was then found by dividing the number of objects in each bin by the total number of created fragments, as shown in Figure 6.6(b). Some fragments are lost from the binned population due to their orbital elements being outside the binned ranged due to reentry or being ejected into highly eccentric orbits. This is particularly the case when the parent bodies were in bins at low or high semi-major axis or eccentricity values. The distributions from each collision are translated depending upon which bin the collision occurred in. For example in Figure 6.6(b), the collision occurred in bin 11, so the distribution is translated to be centred on bin 0.

This process is repeated for each of the 1000 collisions. A mean is taken of the proportion of fragments found in each bin from where the collision occurred. This results in the single distribution for each orbital element as given in Figure 6.7, with standard deviations included. With regards to the inclination distribution, the large bin size used for this orbital element along with the large ΔV required to change inclination resulted in the majority of fragments remaining in the bin where the

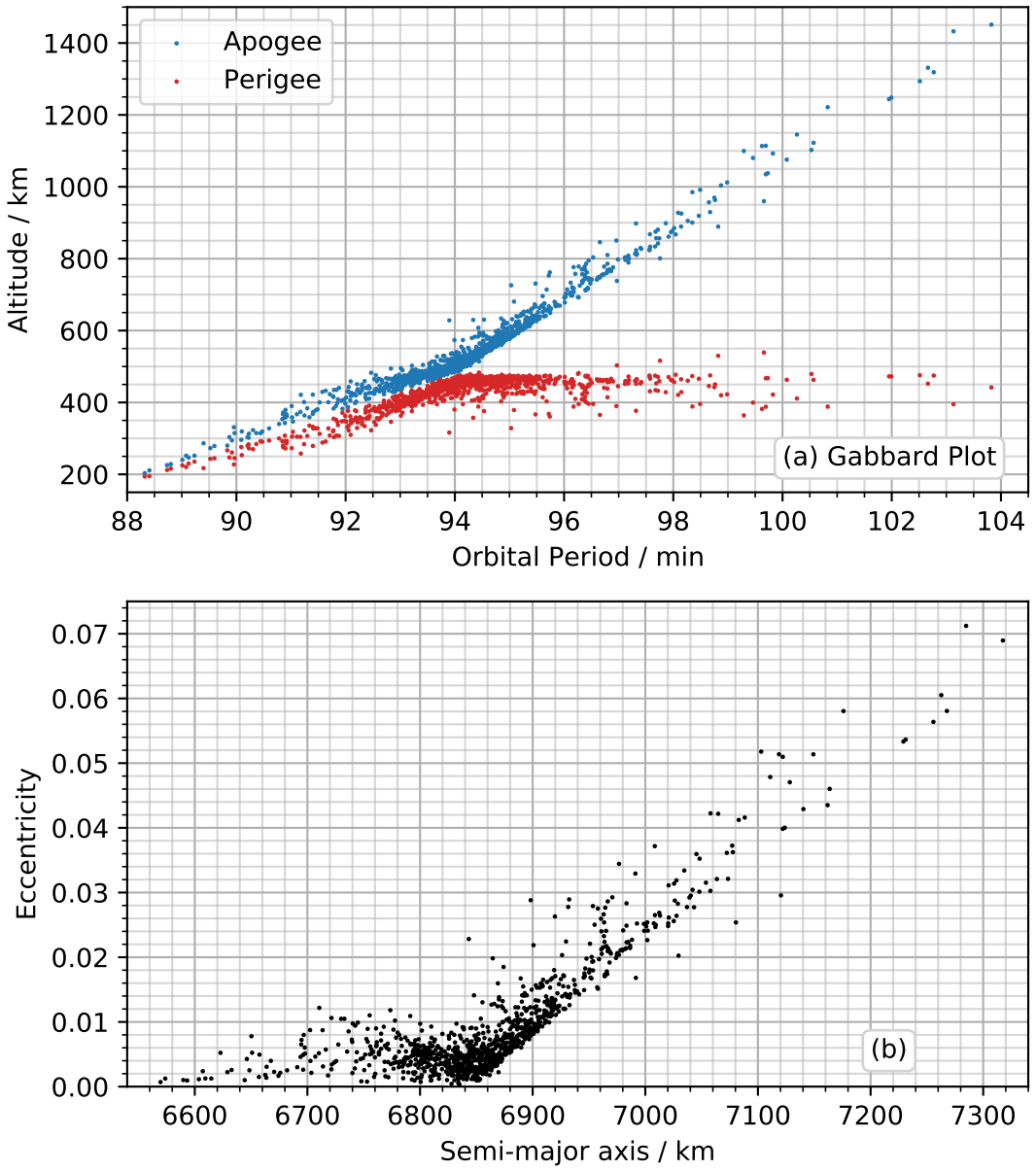

FIGURE 6.5: Subfigure (a) shows the Gabbard plot of the fragments with TLEs created by the Russian ASAT test against Cosmos 1408 as of 18th January 2022 (Event occurred on 15th November 2021). Blue dots denote the apogees of each fragment, and red the perigees. Subfigure (b) plots the semi-major axis and eccentricity of the same fragments.

collision occurred. While the semi-major axis distribution is symmetric around the bin the collision occurred in, the eccentricity distribution is skewed towards larger eccentricities. This fits with the historic observations and orbital mechanics that show it is easier for a fragment to be ejected into a higher eccentricity orbit than to have the exact delta V required to enter a more circular orbit (demonstrated in the apogee-perigee spread of Gabbard plots of historic fragmentations catalogued by Anz-Meador et al. (2018)).

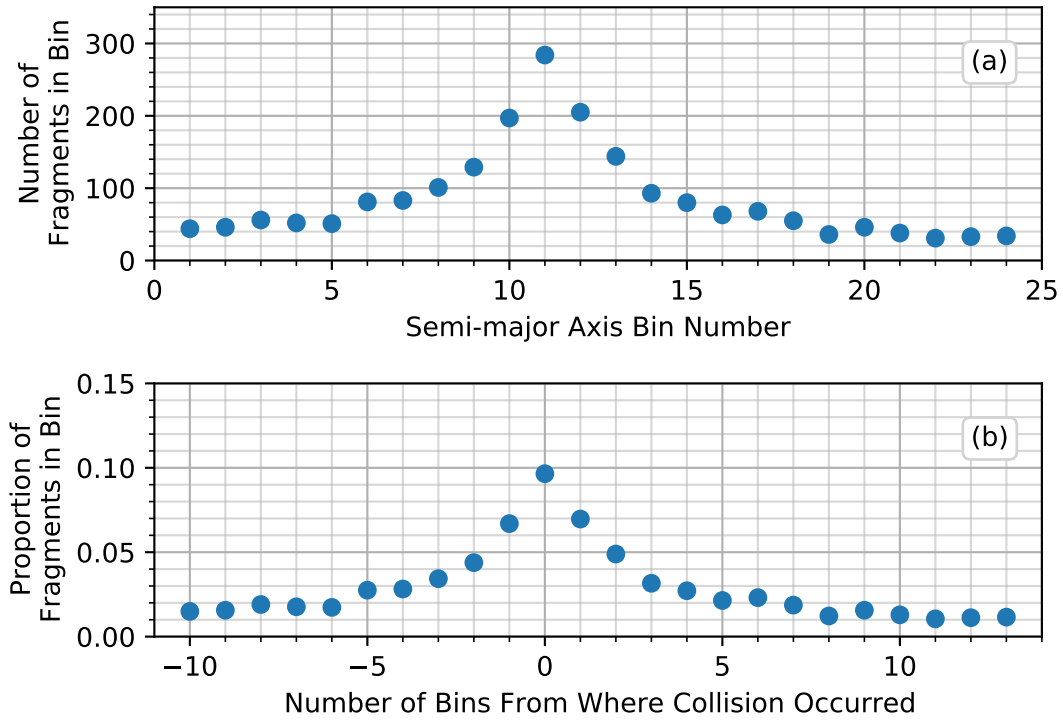

FIGURE 6.6: Demonstration of binning fragments by semi-major axis for a single collision between objects of mass 562 kg and 1778 kg at a semi-major axis of 7072 km. The collision occurs in the 11^{th} semi-major axis bin. Subfigure (a) shows the raw binning of objects, while subfigure (b) divides the number of fragments in each bin by the total number of fragments created in the collision (in this example, 2943). The bin numbers are also translated so bin 0 is where the collision occurred.

The mean distributions for semi-major axis and eccentricity of Figure 6.7 are used within the BRAD debris model to simulate collision fragments spreading between bins. Figure 6.8 demonstrates how a subset of the distribution is taken, dependent upon which bin the collision took place in. This effectively reverses the method used to obtain the distributions of Figure 6.7. This method is used in place of calculating the bin spread for each unique collision within a simulation in order to speed up the overall model.

6.1.8 BRAD Summary

The BRAD simulation process is shown in Figure 6.1 and will be summarised in this section. Bins in semi-major axis, eccentricity, inclination and mass are defined, as in Table 6.1. Atmospheric densities for all possible perigees of representative objects are then obtained from NRLMSISE-00, taking a global average and temporal average over the length of the model time step, as well as accounting for the prescribed solar cycle. These are stored and retrieved when the same binning and solar cycle are used in later

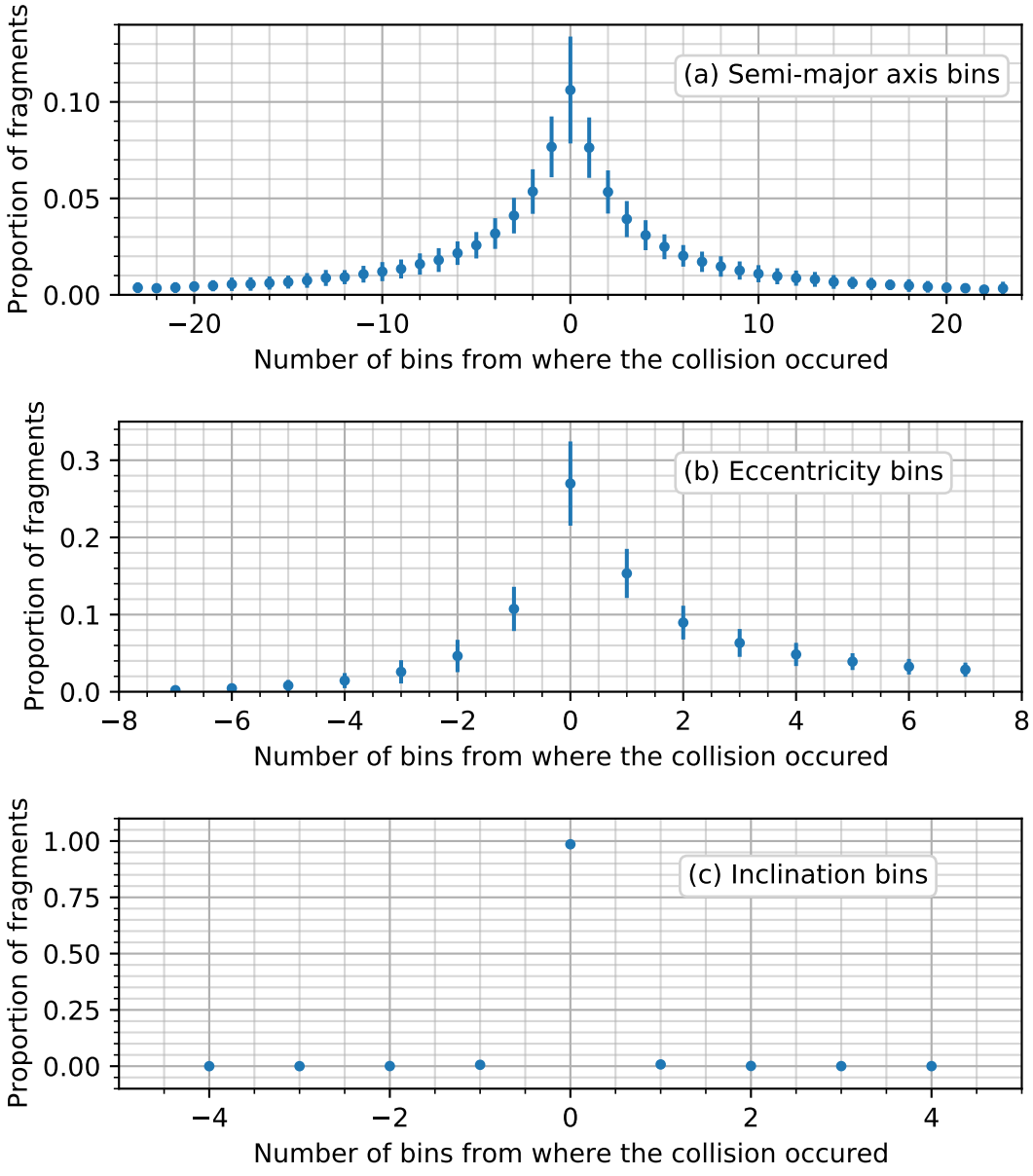

FIGURE 6.7: The proportion of fragments spreading to adjacent bins upon a collision, with the bins for (a) semi-major axis, (b) eccentricity and (c) inclination defined in Table 6.1. Results derived from 1000 collisions of random representative objects (a,e,i,m) from the bins using the NASA standard breakup model. Positive bins away from the centre denote bins with larger orbital elements.

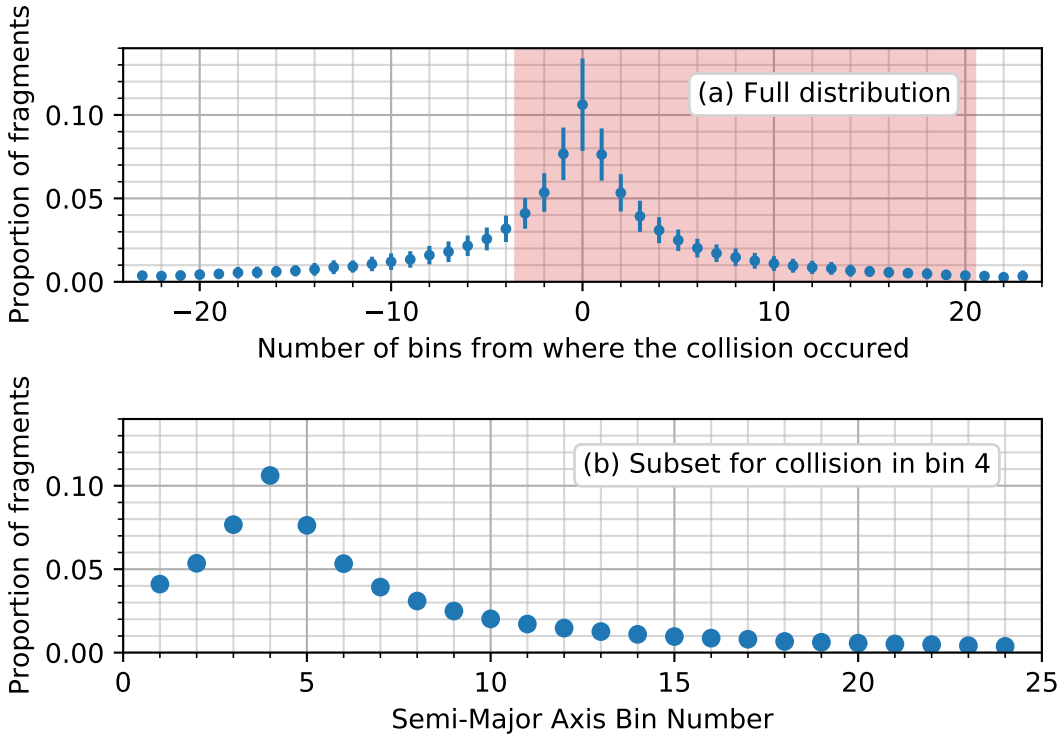

FIGURE 6.8: Demonstration of taking a subset of the possible fragmentation distribution from Figure 6.7. For this example, the collision happens in semi-major axis bin number 4. Subfigure (a) shows the full distribution, with the red highlighted region as the desired subset. Subfigure (b) then shows the transformation of the X axis to the bin numbers.

simulations. Similarly, intrinsic collision probabilities between each a, e, i pair of bins are calculated by the Greenberg algorithm, stored and retrieved for later runs.

DISCOS data are used to populate the model's bins with trackable objects. If BRAD is performing a simulation of the future, the lower mass bins are populated with sub-10 cm fragments. Launches are obtained from DISCOS and binned in a, e, i, m and t, with future simulations repeating the cycle of launches from 2005 to 2013 with a random starting point in the cycle to prevent aliasing with the solar cycle. Finally in starting up the model, the density scaling factors for the simulation's RCP scenario are loaded, to be applied to the densities from NRLMSISE-00 through the run.

BRAD then enters the main loop, first propagating objects in bins such that the effects of atmospheric drag are applied. The atmospheric densities from NRLMSISE-00 are scaled depending upon the RCP scenario being investigated. As these scaling factors only go up to 500 km altitude, any values required for higher altitudes take the value at 500 km. The launches for the current time step are then added. The intrinsic collision probability for each pair of bins is then retrieved and used to estimate the mean number of collisions by multiplying by the radii of representative objects, time step size and number of objects in each bin. This quantity is then tested against a

Poisson distribution to determine the integer number of collisions occurring. If a collision has occurred, fragments are created from the two representative objects using the NASA Standard Breakup Model, and these fragments are spread across bins to simulate the change in velocity of individual fragments.

Information on the current population, propagation, launches, collisions and fragmentations is saved for the current model step, before the loop moves into the next step. Once the desired amount of model steps has occurred, the model saves the final population along with the settings used in the model for later analysis. The process is repeated multiple times as a Monte Carlo simulation to account for the randomness arising from the collision algorithm, with the final analysis performed on the full set of runs.

6.2 BRAD Model Validation

Each component of the BRAD model was validated independently. For example ensuring the collision probability calculations of the Greenberg algorithm returned the same values as the example scenarios in Table 3.3.

Orbital lifetimes within the model depend upon both the orbital propagation calculation and the bin propagation algorithm. Therefore to test orbital lifetimes within the model, a single object was placed in the binned population and the model run with no launches. This allowed the object to propagate through the bins. However, due to the bin propagation algorithm of Section 6.1.4, fractions of the object move between bins. If the change in semi-major axis or eccentricity isn't larger than the original bin's size, then a fraction of the original number remains in the same bin. If this process repeats, than the original object may never leave the environment completely as the cumulative fraction asymptotically reaches 0. However, it was found that for a fixed solar activity, the expected lifetime was given when roughly 1% of the original object was left in the environment, with this being true for all semi-major axis and eccentricity combinations.

6.2.1 Historical Collision Validation

A detailed history of on-orbit fragmentations is available in Anz-Meador et al. (2018). From this, an overview of accidental historic collisions was summarized within Table 6.2. The majority of these were not catastrophic events, with each creating 10 trackable fragments or less. These involved fragments from historic explosions and other unknown sources colliding with spacecraft. However the Iridium 33 - Cosmos 2251 collision was catastrophic, creating a total of 2269 catalogued fragments. This

highlights the rarity of accidental collisions in the historic population, with the majority of small fragments created from explosions and ASAT tests.

TABLE 6.2: Summarised history of accidental collisions in LEO, adapted from Anz-Meador et al. (2018).

Date	Body 1	Body 2	Catastrophic?	Altitude
23/12/1991	Cosmos 1934	Cosmos 926 deb	Unknown	980 km
24/07/1996	Cerise	Ariane R/B deb	No	685 km
1997	NOAA 7	Unknown	No	∼830 km
21/04/2002	Cosmos 539	Unknown	No	∼1350 km
17/01/2005	DMSP 5B F5 R/B	CZ-4 launch deb	Unknown	885 km
10/11/2007	UARS	Unknown	No	353 - 483 km
10/02/2009	Iridium 33	Cosmos 2251	Yes	789 km

The BRAD debris model was used to simulate the historic period of 01-01-1979 to 31-12-2009. The initial population and launches were obtained from DISCOS. The simulation used historic solar activity values so began with the high solar activity seen at the peak of solar cycle 21 (see Figure 2.7). This led to objects at the lowest altitudes quickly leaving the binned population. As the historical simulation did not include explosions, the number of objects did not recover to initial levels. A Monte Carlo simulation of 32 runs was performed under these settings to see whether the model was producing similar amounts of collisions to the historical ones of Table 6.2. Not many small fragmentation events were expected to occur as explosions were not being simulated and the initial population had not been filled with small fragments from historical fragmentations. The results from the Monte Carlo simulation are shown in Figure 6.9 and the details of all collisions to occur are detailed in Table 6.3. The small step change in the total number of objects in the year 1989 was a result of a large number of launches obtained from DISCOS. All other step changes are a result of collisions in separate BRAD simulations.

Expected characteristics of collisions in the debris environment can be extracted from these results. For example in runs 15 and 25, fragments from a collision increased the chance of later collisions in similar orbits. As expected, the larger spatial density of objects at altitudes of 800 - 900 km also leads to more collisions at these altitudes. The assumption of no explosions within BRAD led to fewer small fragments, so fewer non-catastrophic collisions occurred. Catastrophic collisions during the simulated period happened at a rate of 0.28 per run, which was deemed acceptable compared to the one historic catastrophic collision which happened in the real environment. Finally, more collisions happen later on in the simulation than near the start, similarly to the real-life environment.

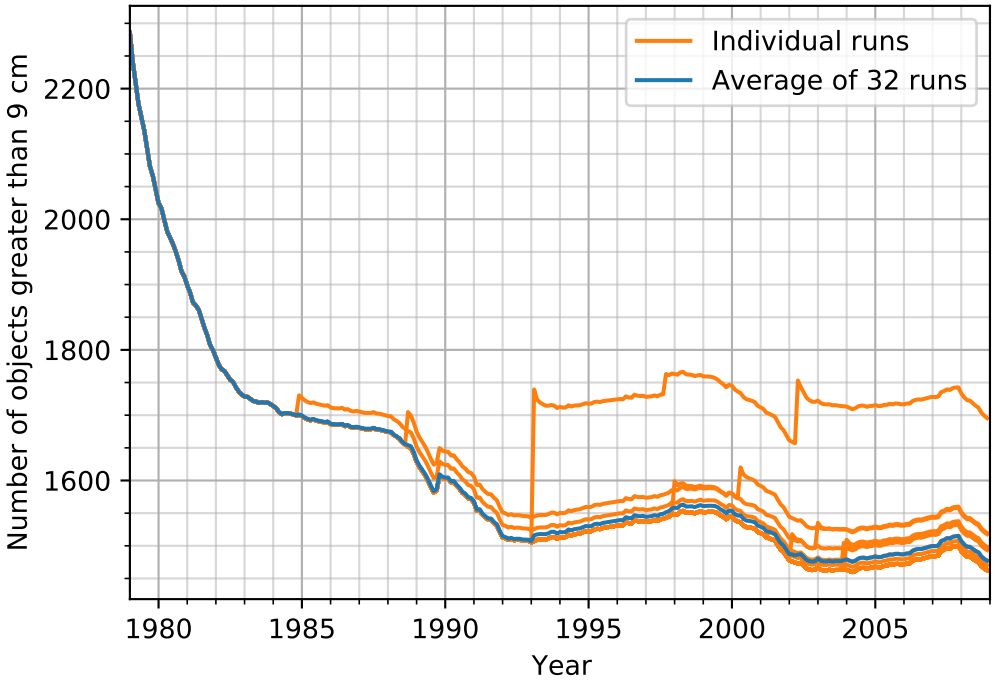

FIGURE 6.9: Number of trackable objects in historic simulation of the binned environment in BRAD. Thirty-two individual runs were performed and presented here to show the step changes caused by collisions. The mean number of collisions over the 32 runs is also included.

TABLE 6.3: Summary of collisions occurring in the 32 runs of the historical period with BRAD. The run number in which the collision occurred and the date of the event are given. Along with the mass (m), semi-major axis (a) and eccentricity (e) are also given for each representative object involved (denoted with subscript 1 and 2).

Run	Date	m_1 (kg)	m_2 (kg)	a_1 (km)	e_1	a_2 (km)	e_2
2	2003.9	1778	0.05	7259	0.00625	7259	0.00625
5	1988.7	1778	1.78	7334	0.00625	7334	0.00625
11	2001.3	562	56.2	7184	0.00625	7296	0.00625
15	1998.0	1778	1.78	7184	0.00625	7184	0.00625
15	2000.3	1778	0.178	7184	0.03125	7259	0.00625
25	1993.1	5623	1778	7259	0.00625	7297	0.00625
25	1997.7	1778	1.78	7184	0.00625	7259	0.01875
25	2002.3	5623	0.178	7222	0.00625	7297	0.03125
26	1984.9	1778	17.8	7259	0.00625	7297	0.00625
28	2002.1	1778	5.62	7259	0.00625	7297	0.00625
28	2003.0	1778	0.056	7222	0.00625	7259	0.00625
31	2004.0	1778	0.0178	7297	0.00625	7334	0.04375

6.3 Results from the BRAD Debris Model

The BRAD debris model was used to simulate the debris environment from the year 2000 through to 2100 with a time step of 0.1 years, and with solar activity conditions

repeating solar cycle 24 for this section. No debris mitigation measures were included. An initial run using no density scaling was performed to provide a control scenario. A total of 64 runs were performed in a Monte Carlo simulation from the same initial population settings, with the number of objects larger than 9 cm (i.e. bins with trackable objects) for each individual run given in Figure 6.10a. The mean and standard deviations of these runs are presented in Figure 6.10b. The impact of the solar cycle can be seen in the periodicity of 11 years. The number of objects generally increases exponentially with time (neglecting the solar cycle impact).

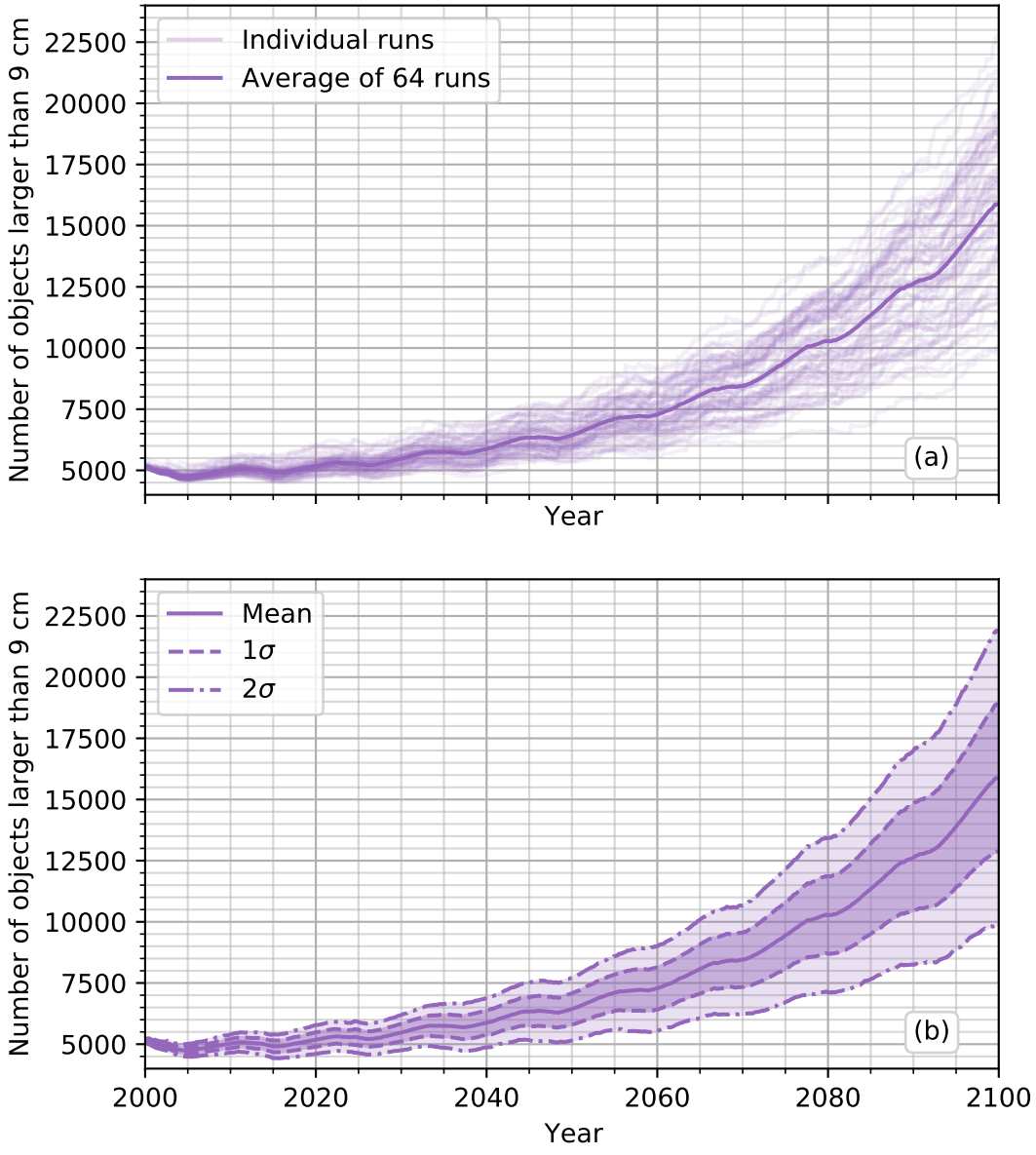

FIGURE 6.10: Monte Carlo of 64 runs simulating of the debris environment with BRAD, with no density reductions applied. This is used as the control scenario for later comparisons. Plot (a) shows the individual runs as well as the mean, while plot (b) shows the mean and standard deviations of the same runs.

The debris environment was then simulated with the same methodology as the control, but applying the thermospheric density reductions seen under each of the RCP scenarios. The results from each are presented in Figure 6.11.

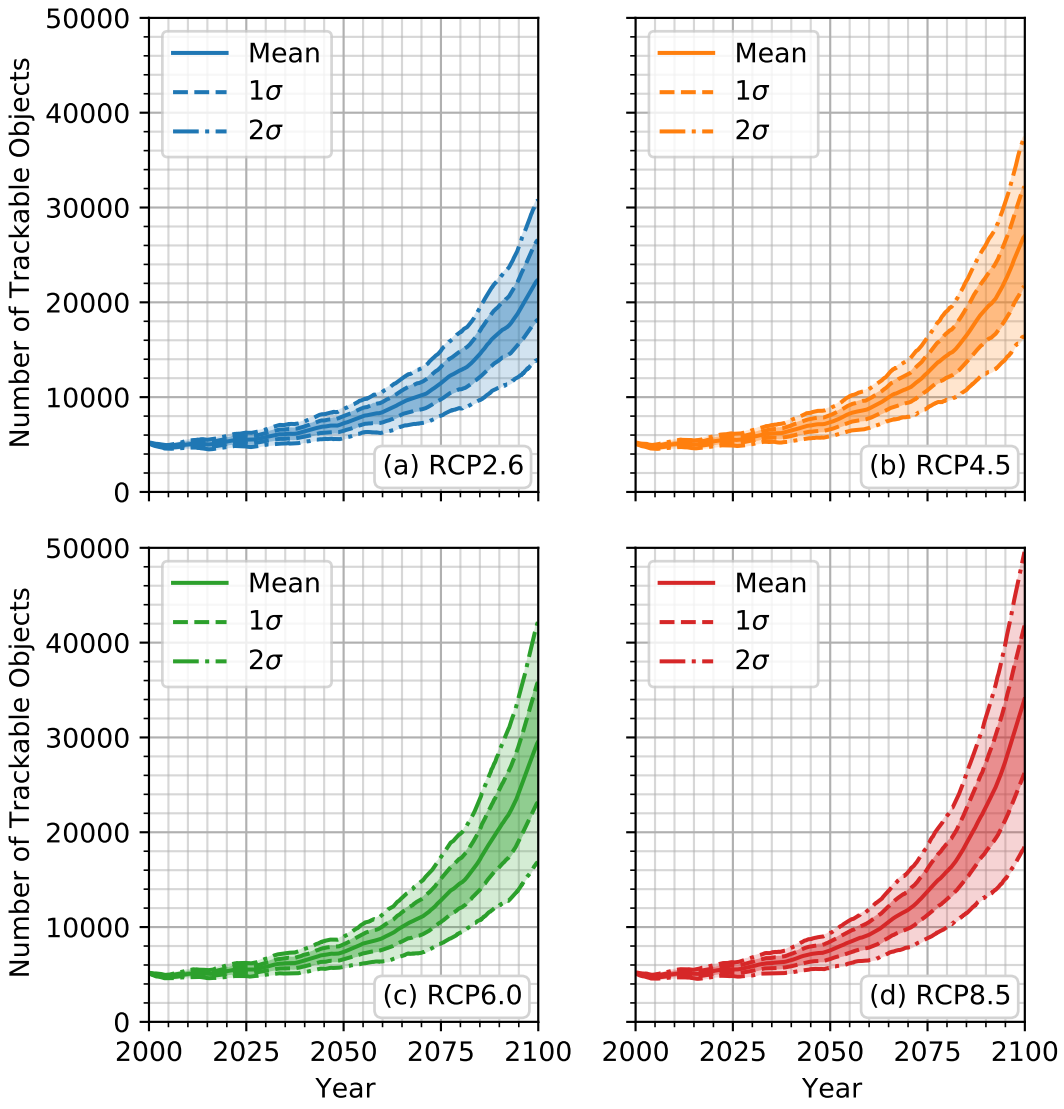

FIGURE 6.11: The number of objects in the trackable population when simulating the debris environment through to 2100 with BRAD, with a different RCP (named in graph) applied in each subplot. Means and standard deviations are given from the 64 runs performed for each RCP.

Focusing on the mean number of trackable objects, Figure 6.12 gives the number of objects in each RCP scenario compared against the control. This was obtained by dividing the mean number of trackable objects in each RCP scenario by those in the control at each model step. This method of presentation highlights the larger rate of increase in the more extreme RCP scenarios, particularly towards the end of the century. For example, RCP8.5 sees an increase of 55% over the period 2000 - 2080 and then 60% over 2080 to 2100, while RCP2.6 sees an increase of 25% and 16% over the

same periods. As these are compared to the control scenario, these increases are tied purely to the RCPs and are in addition to the rising number of objects which debris models already predict without thermospheric density reductions.

It also highlights how the debris population is correlated with the ground-level carbon dioxide concentrations of the RCPs (shown in Figure 5.15). The number of objects in the RCP4.5 and RCP6.0 track each other closely over the first 60 years before diverging, mimicking the carbon dioxide concentrations of the scenarios. In RCP2.6, the ground-level CO_2 concentrations reduce after roughly 2050, and density reductions begin to reduce in magnitude as a result. However, the number of objects and rate of increase of the number of objects continue to increase post-2050. This suggests that although only small density reductions are seen during the first half of the century, the collisions and increased number of objects during this period drive the characteristics of the last half of the century.

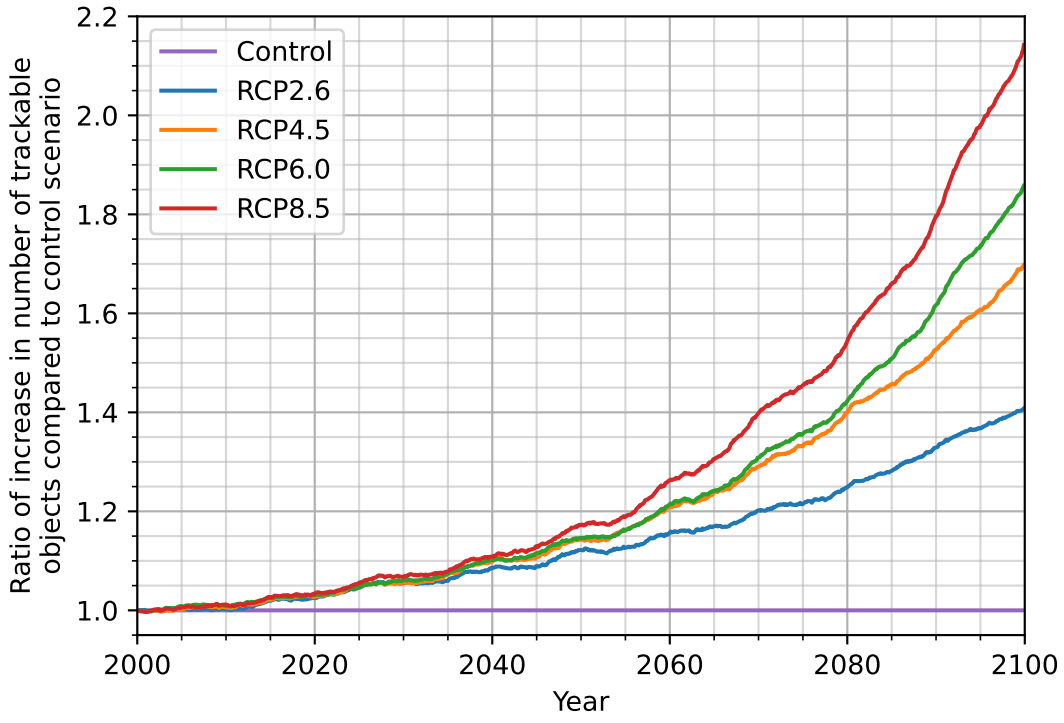

FIGURE 6.12: The ratio of the mean number of trackable objects in the debris environment when neutral densities follow each RCP scenario compared against when no thermospheric contraction is accounted for.

To explore how objects are distributed across the environment, Figure 6.13 presents the difference in the mean number of objects resident in each semi-major axis and eccentricity bin at the end of each modelled scenario (i.e. a mean across all 64 runs during the year 2100) compared to the control. A logarithm of base 10 was taken to make the differences more visible. The largest increase in the number of objects is in circular orbits at 800 km altitude in all scenarios, matching the initially high

population in this region. The reduced neutral densities cause the number of objects to increase in orbits with lower semi-major axis values, but also in orbits with higher eccentricties, where these objects have relatively low perigees. This is demonstrated by the heat map of Figure 6.13 migrating towards these values, and is most noticeable when comparing the RCP2.6 and RCP8.5 scenarios.

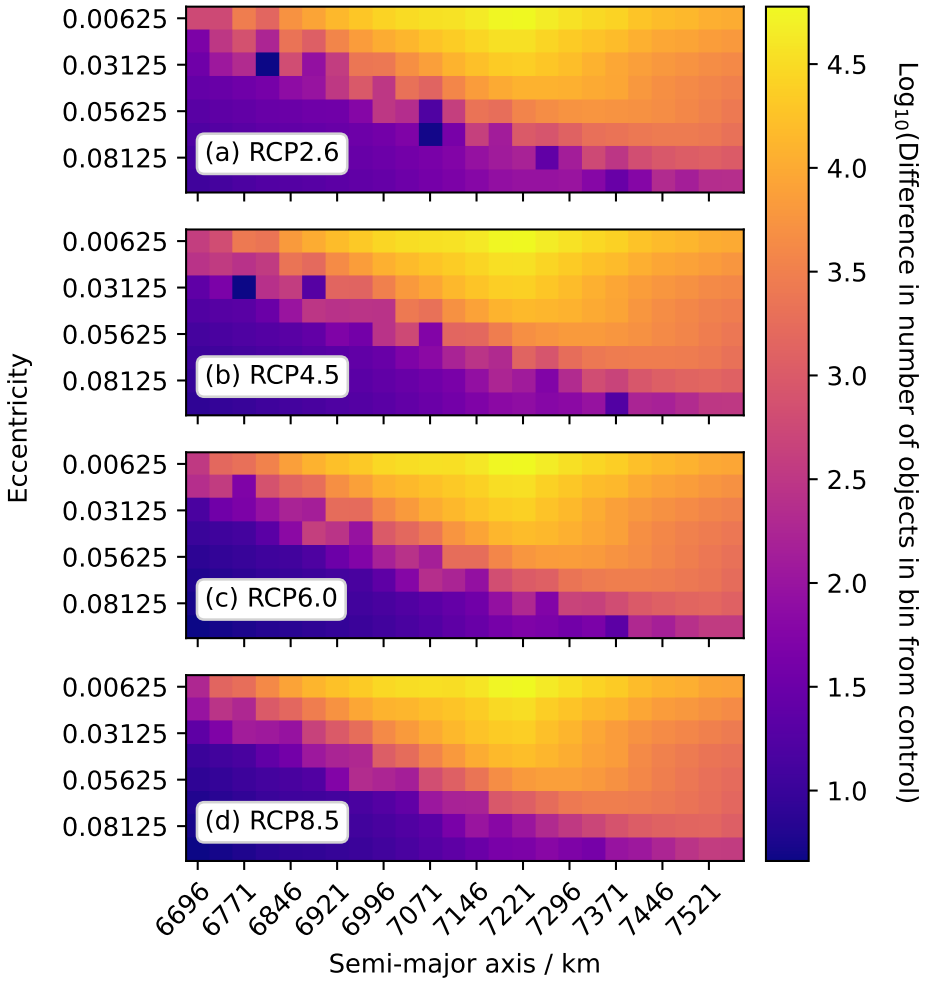

FIGURE 6.13: Heat map of the difference in the mean number of objects between the control and each RCP scenario for each semi-major axis, eccentricity bin in the year 2100. Difference given in log base 10 to aid in comparison.

Information on the collisions which occur during each run of BRAD is also stored and can be analysed. The mean number of catastrophic trackable-on-trackable collisions over time for each scenario is given in Figure 6.14. These are the events which create the largest number of fragments and are relatively rare, with the Iridium 33 - Kosmos 2251 collision being the only accidental one in the historic record. In a similar manner, the mean number of collisions involving a trackable object has been given in Figure 6.15. These were more common in the historic record and in general created a smaller number of fragments due to their often non-catastrophic nature. Both sets of graphs show similar behaviour to the number of objects, as the number and rate of collisions

increases with time and with ground-level CO_2 concentration. This demonstrates the feedback loop of the number of objects and the number of collisions. More objects in the environment increases the number of collisions, creating more fragments which in turn leads to more collisions, accelerating the rate at which the number of objects increases. The decreased atmospheric densities of each RCP scenario increase the orbital lifetime of objects, increasing the number of objects in the environment and reinforcing the collision feedback loop.

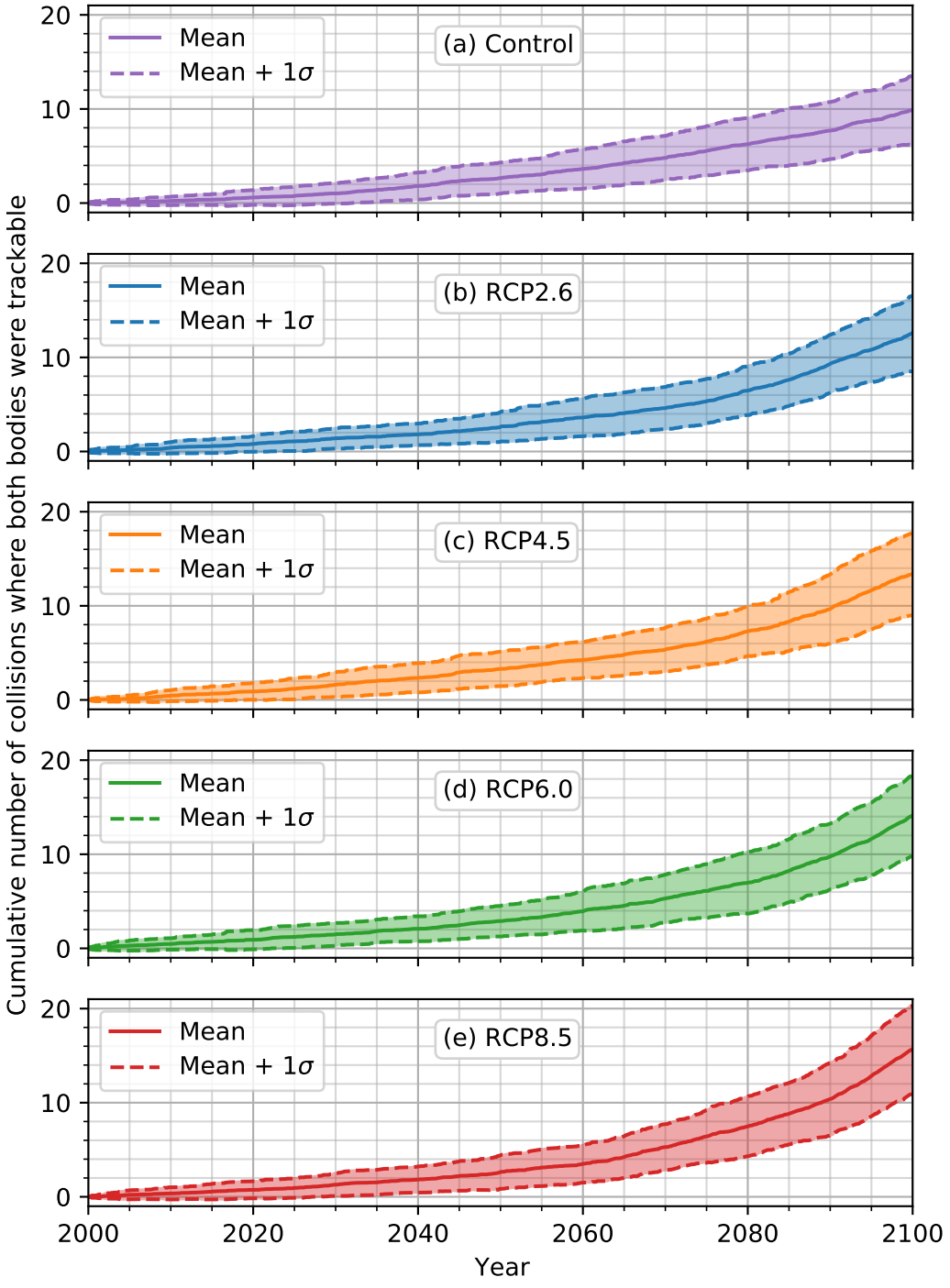

FIGURE 6.14: The mean cumulative number of collisions between two trackable parent bodies in the BRAD RCP simulations.

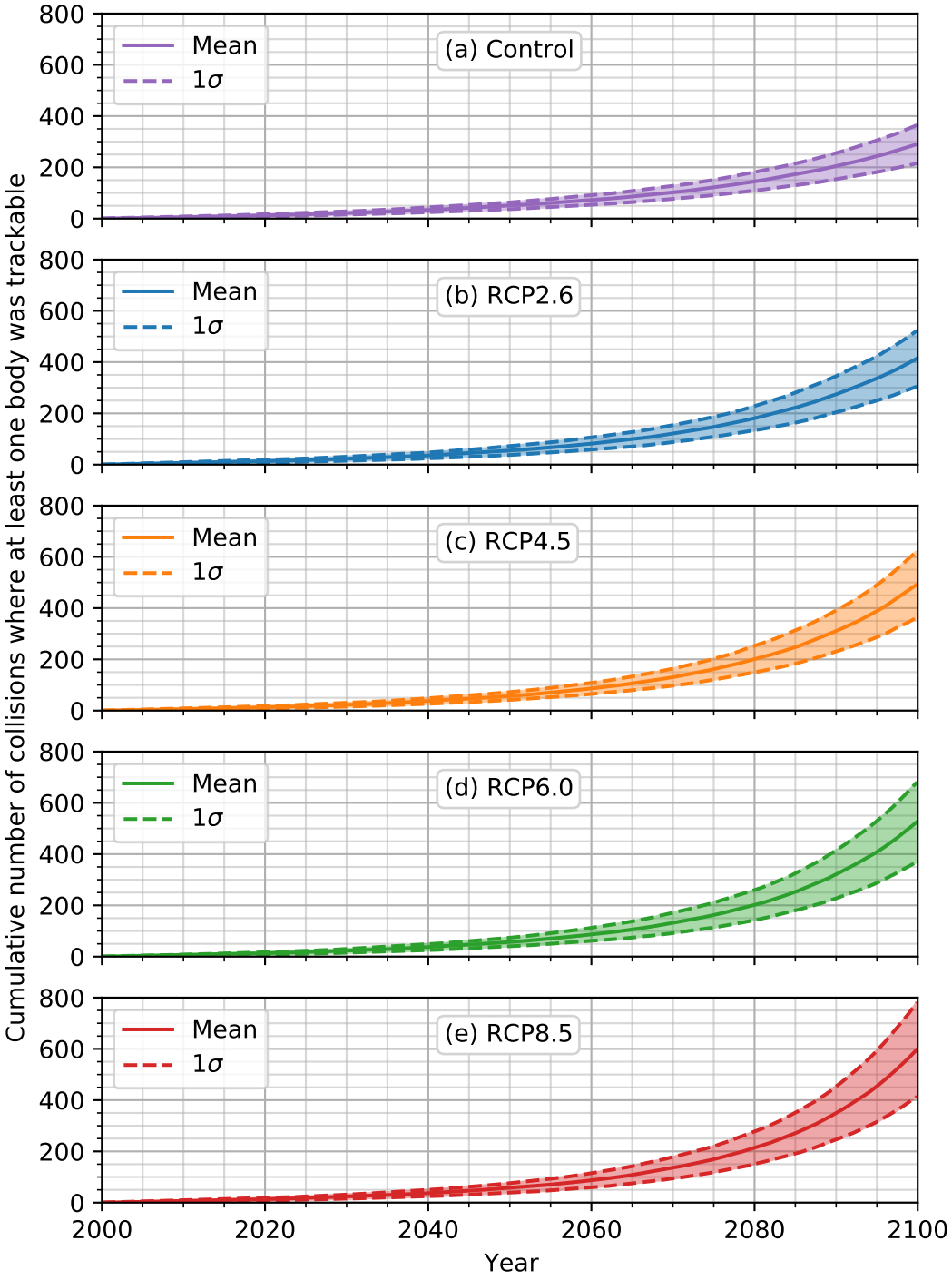

FIGURE 6.15: The mean cumulative number of collisions in the BRAD RCP simulations where at least one of the parent bodies involved was a trackable object.

Chapter 7

Discussion

This section will briefly summarise the key findings of Sections 5 and 6 and compare the results against the few previous studies which have looked at this research area. The assumptions and limitations of the methodologies will be discussed, and additional context will be given to the results. Then to round up the thesis, the research aims will be revisited and the novel contributions highlighted, followed by a summary of the research topics and questions which could be addressed in future work.

7.1 Key Findings

Chapter 5 explained how thermospheric densities continue to reduce under increasing ground-level carbon dioxide concentrations, with the effect being greater at higher altitudes. All density reductions in the chapter were given as global averages relative to the year 2000 (CO_2 concentration of 370 ppm). The reductions were modelled at F10.7 values of 70 sfu and 200 sfu, with the largest reductions seen under low solar activity (comparable with studies looking at historic periods too). Section 5.4 showed how the density reductions monotonically decrease under increasing solar activity levels when ground-level CO_2 concentrations are at 639 ppm. Combining these results allowed a density scaling table to be created which could be applied to empirical atmospheric models to allow them to account for thermospheric contraction. The scaling factors varied with altitude, solar activity and ground-level CO_2 concentrations.

Chapter 6 introduced the Binned Representative Atmospheric Decay (BRAD) space debris environment model, which makes use of the density scaling table created from the results of Chapter 5. The LEO debris environment was modelled under a control scenario with no density reductions applied, as well as under the density reductions

which would be seen in each Representative Concentration Pathway. The same initial population, launches and solar activity were used in each scenario so differences could be directly related to the density reductions. Both the number of objects and the number of collisions increased with the higher ground-level CO_2 concentrations of each RCP scenario, with the rate of increase also growing with time. This held true even in the RCP2.6 scenario where carbon dioxide concentrations and density reductions begin decreasing in magnitude after the year 2050. By the year 2100, the number of trackable objects in the population is 41%, 70%, 86% and 114% larger than in the control run for the RCP2.6, 4.5, 6.0 and 8.5 scenarios respectively. The highest spatial density in all scenarios is in a roughly 800 km circular orbit, with the number of objects decreasing as the bins move away from this in semi-major axis and eccentricity. The extra objects in the more extreme scenarios exist primarily at lower semi-major axis values due to lower atmospheric drag. The increased number of collisions can also eject objects into higher eccentricity orbits with lower perigees. These object's orbital lifetimes are longer than they otherwise would be if there were no decreasing neutral density trend. So overall, objects persist in the environment for longer and increase the risk of further collisions.

7.2 Comparison of Results Against Previous Studies

This section will directly compare the results presented in Chapters 5 and 6 against the most comparable simulations of the future. Methods for allowing easier comparisons with future studies as well as the difficulties in providing a "most likely" scenario will then be discussed.

Qian and Solomon (2011) showed how thermospheric densities would reduce under increasing ground-level CO_2 concentrations for medium solar activity (F10.7 = 150 sfu). This study was discussed in detail in Section 3.1.5. Figure 7.1 reproduces the study's results at 400 km altitude and includes the low and high solar activity results of this thesis from Sections 5.2 and 5.3. The medium solar activity results of Qian and Solomon (2011) would be expected to sit between the low and high solar activity results of this thesis but instead sit above them both for all carbon dioxide concentrations. The reason why is unclear, but may be explained partly by the different models used. Qian and Solomon used a one-dimensional, global-mean version of TIE-GCM and they do not state how carbon dioxide concentrations at the 97 km lower boundary were handled. This is above the homopause and where concentrations decrease asymptotically from the ground-level concentration towards 0 ppm (see Figure 2.3). Neither does the paper make clear how neutral densities at the lower boundary of TIE-GCM were set. As Figure 3.1 shows, there is still a significant, reducing density trend at altitudes below the 97 km lower boundary. If this isn't accounted for, neutral density trends at higher altitudes would not account for the

contraction in the atmosphere below 97 km. Therefore, the smaller density reductions of Qian and Solomon (2011) could be explained by an inaccurate carbon dioxide concentration or neutral densities at the lower boundary causing an underestimate in the thermospheric density response.

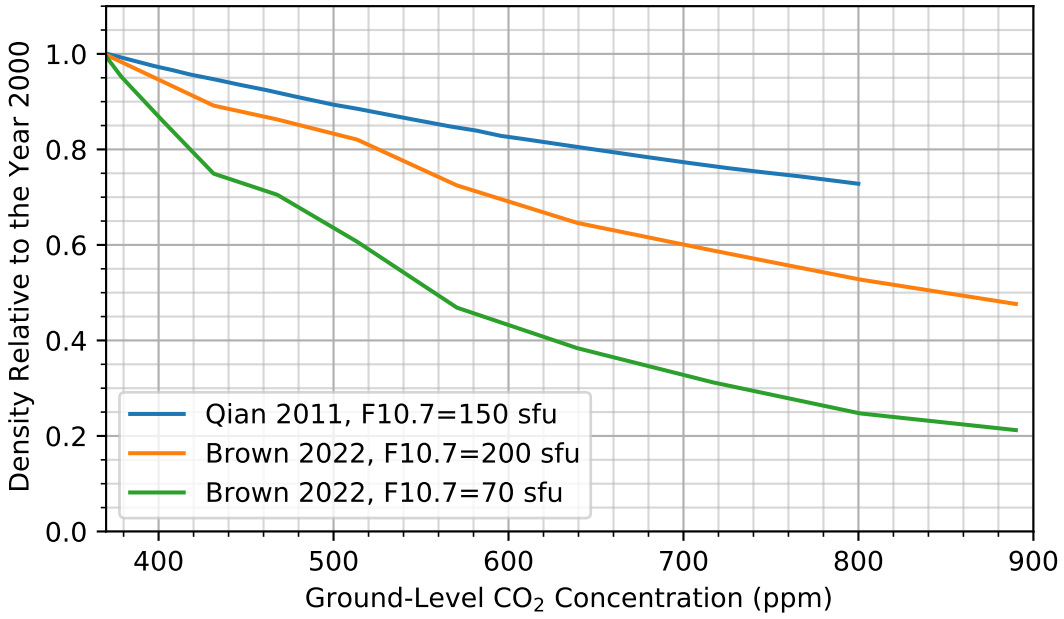

FIGURE 7.1: Comparison of density reductions at 400 km altitude from Qian and Solomon (2011) and this work. Density reductions are given relative to the year 2000 under increasing ground-level carbon dioxide concentrations.

Switching focus to the future debris environment, the literature review, presented in Chapter 3, identified that numerous studies have observed and modelled historic thermospheric density trends. Each of these studies stated there would be an impact on the debris environment. However, studies quantifying the impact have been limited to Lewis et al. (2005) and Lewis et al. (2011), with both extrapolating a historic density trend into the future and finding a substantial increase in the number of objects in the environment and number of collisions occurring.

The results of Chapter 5 represent the first in-depth study of thermospheric density reductions under increasing carbon dioxide concentrations. Tying these to the representative concentration pathways and applying them within the BRAD debris model also reflects the first time the debris environment has been modelled under different carbon dioxide emission scenarios. Atmospheric drag is the dominant mechanism for removing both inactive satellites, debris fragments and other objects from LEO. The results from Chapter 6, as well as Lewis et al. (2005) and Lewis et al. (2011), show that neglecting the effects of thermospheric contraction has a significant impact on the outputs from space debris models.

The results of Lewis et al. (2005) and Lewis et al. (2011) are explored in depth in Section 3.3. Lewis et al. (2005) used a business-as-usual scenario and found an increase of 9.9% in the number of fragments larger than 10 cm in size over the period 2001-2101 when modelling a scenario roughly between RCP2.6 and 4.5 (presented in Figure 3.6). This is less than the results from BRAD, namely increases of 41% and 70% seen under the RCP2.6 and 4.5 scenarios respectively. While Lewis et al. (2011) used a similar carbon dioxide scenario to Lewis et al. (2005), Lewis et al. (2011) also included mitigation measures and ADR scenarios in their simulations. Tracking the number of objects larger than 10 cm between the year 2009 and 2079 and taking the ratio between including and excluding thermospheric contraction, they found a 23.5% increase during the mitigation-only scenario, and a 27.5% increase in the ADR scenario. Referring to Figure 6.12, the studies reported in this thesis found an increase of 20% and 29% in the number of objects larger than 9 cm over a 70 year period in the RCP2.6 and 4.5 scenarios respectively. BRAD does not include mitigation or ADR measures within it's modelling so the total number of objects differs from Lewis et al. (2011), but the impact of thermospheric contraction on the total number falls within the expected range from BRAD.

Simulating the space debris environment into the future presents challenges as it is unknown how factors such as launch traffic, solar activity, and other factors (e.g. mitigation measures) could change over time. This uncertainty is compounded when looking multiple decades into the future. Similar challenges arise when modelling how carbon dioxide emissions could change into the future. Without close cooperation to ensure a common set of assumptions about these future scenarios, comparisons between different models is challenging.

The RCPs aid in this cross comparison by providing a common, limited set of CO_2 concentrations which can be used in modelling across multiple disciplines. However, by their nature, the RCPs provide scenarios rather than predictions of how carbon dioxide concentrations could change into the future. However, they do provide scenarios which would be useful for operational or decision-making purposes.

To add context to possible "likely" future density reductions, the commonly cited 1.5°C target of the Paris Agreement can be used as a "best-case" scenario. The IPCC says that limiting global warming to 1.5°C would allow humanity to avoid the worst climate impacts of global warming. As this target is widely used it also provides a possible upper bound to density reductions (assuming the target is met). The Emissions Gap Report by the United Nations Environment Programme (2019) states that for a 50% probability of limiting global warming to 1.5°C, the carbon budget from 2018 onward is 580 $GtCO_2$. Adding this to the 2017 globally averaged CO_2 concentration of 405.0 ppm gives a target of 480 ppm, below which ground-level warming is limited to 1.5°C (Le Quéré et al. (2018)). Under low solar activity conditions (F10.7 = 70 sfu), by referring to Figure 5.10, this 480 ppm target corresponds

to a density reduction of 32% at 400 km relative to the year 2000. Under high solar activity (F10.7 = 200 sfu), Figure 5.11 gives a value of 15% instead. While this provides a possible boundary for density reductions, it does not define a time this target could be reached or a pathway of concentrations to this boundary.

The Nationally Determined Contributions (NDCs) were investigated to define a most likely pathway for carbon dioxide concentrations over upcoming years. Each country which signed the Paris Agreement publishes an NDC every 5 years which contains their plans to reduce greenhouse gas emissions. Published plans can vary in length from 5 years to much longer term, with these plans also varying in their level of legislation. Analysis of the NDCs is annually updated in the Emissions Gap Reports (most recently by the United Nations Environment Programme (2021)). This analysis only extends out to 2030 though, and also normalizes all greenhouse gases to the warming potential of CO_2. It then presents them as a summed, total "CO_2 equivalent" parameter rather than separating out CO_2. This greatly complicates modelling the impact on the thermosphere. Therefore using the NDCs to provide a most-likely scenario would not be possible for space debris modelling, and was the reason why RCPs were used. For additional context, RCP2.6 can roughly be linked to a possible 1.5°C scenario, and RCP8.5 to a worst-case scenario of business-as-usual fossil fuel usage.

7.3 Assumptions and Limitations

This section will identify the limitations of the models and assumptions used within this thesis, how they were accounted for and their impact on the results.

7.3.1 Extrapolation to Higher Altitudes

Numerical atmospheric models have an upper boundary at which point some key physical characteristic of the environment changes or is no longer included. The upper boundary of WACCM-X is set below the point at which helium becomes the dominant species, and both hydrogen and helium are not included in the chemistry or physics of WACCM-X. The upper boundary also varies in altitude as the thermosphere expands and contracts, whether as a result of changing solar activity levels or carbon dioxide emissions. This leads to the upper boundary sometimes not being high enough in altitude to encompass the whole of the LEO environment. This phenomenon was discussed in Section 5.1.2 but it is worth revisiting with the additional context introduced from Chapter 6.

Extrapolation was limited to an altitude of 500 km as above this the model used for validation of the extrapolation across all solar activity levels, namely NRLMSISE-00,

moves towards a helium dominated regime. The altitude this occurs at also changes depending upon inputs. Using global-mean annual-means from NRLMSISE-00, Figure 7.2 shows how much each constituent contributes to the total mass density at varying altitudes under lower solar activity (F10.7 of 70 sfu). Figure 7.3 similarly shows the percentage each constituent contributes to neutral mass density, but for varying solar activity conditions at a fixed 500 km altitude. The missing helium within WACCM-X has the largest impact during low solar activity conditions

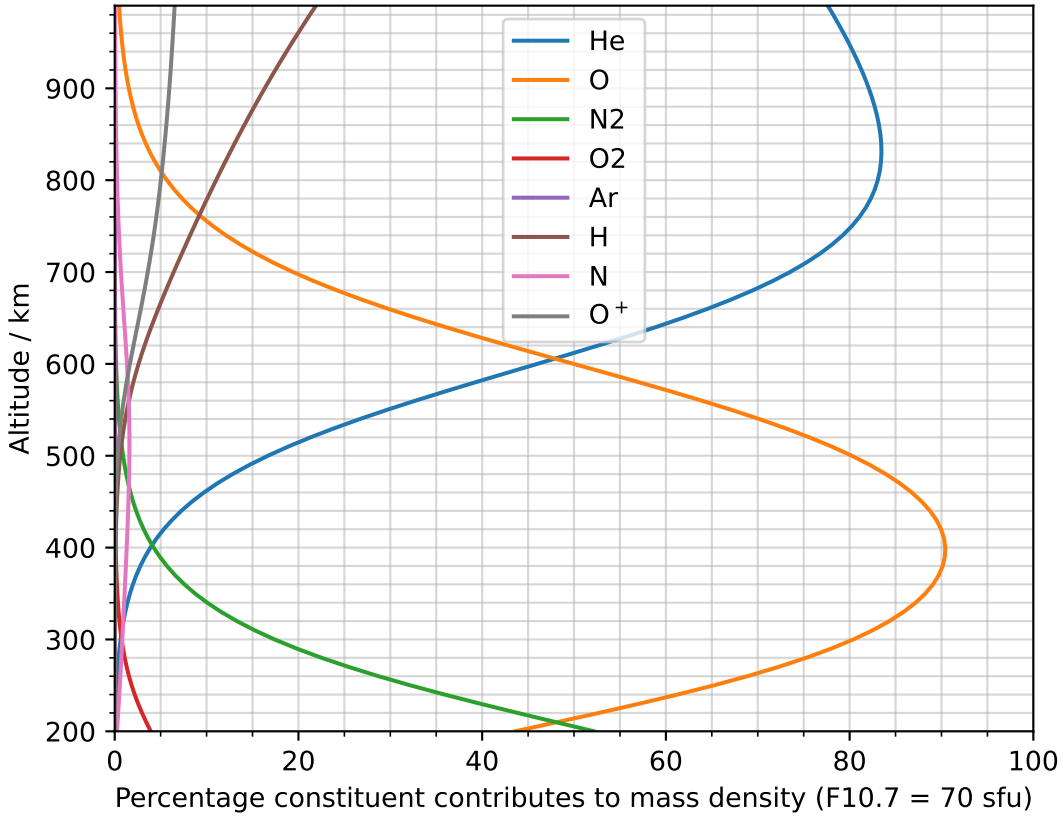

FIGURE 7.2: The proportion each constituent contributes to total mass density with varying altitude under low solar activity conditions (F10.7 of 70 sfu), calculated from a global-mean annual-mean of NRLMSISE-00 output. Anomalous oxygen from NRLMSISE-00 labelled O^+, which contributes to neutral mass density at high altitudes.

The atmosphere and therefore the neutral densities near the upper boundary of WACCM-X are dominated by atomic oxygen, which has a smaller scale height than the neglected helium. Therefore the extrapolation method of Section 5.1.2 likely overestimates the neutral density. To quantify this, the extrapolation technique has been applied to NRLMSISE-00 both including and not including helium in the calculation of neutral density. Figure 7.4 shows an example of the extrapolation for three cases, with each taken relative to the default neutral density output which includes helium, and are global-mean annual-means at F10.7 = 70 sfu, and Kp = 0.33, similar to the earlier WACCM-X simulations. The first of the cases is the default

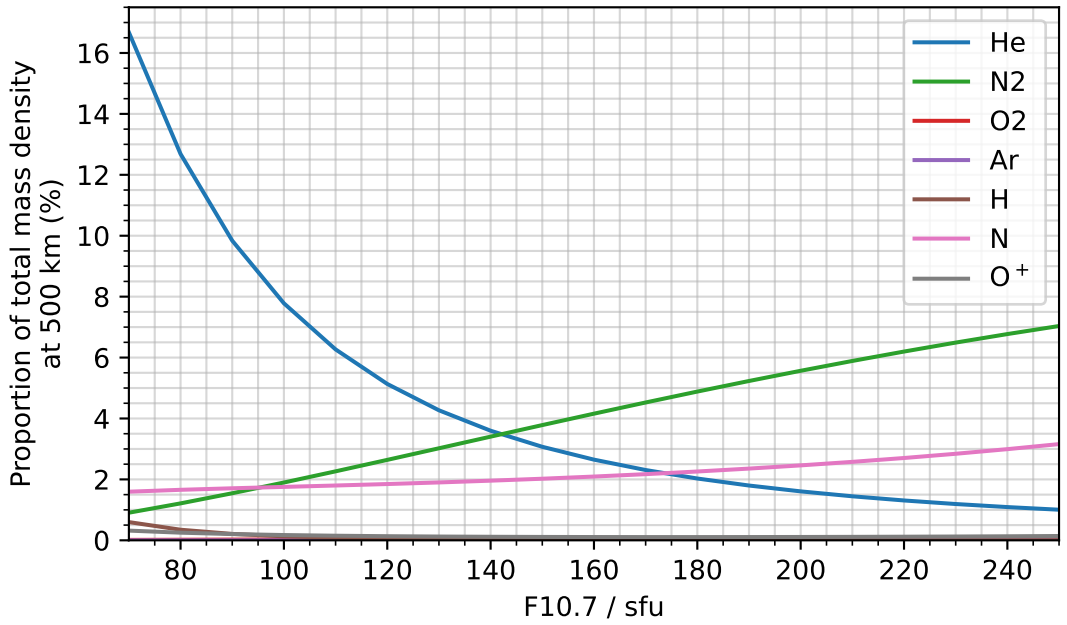

FIGURE 7.3: The percentage each constituent (excluding O) contributes to total mass density at 500 km altitude under varying solar activity conditions, calculated from a global-mean annual-mean of NRLMSISE-00 output. Anomalous oxygen from NRLMSISE-00 labelled O^+, which contributes to neutral mass density at high altitudes.

neutral density from NRLMSISE-00 up to 300 km, then extrapolated upwards. The second is the full altitude profile of neutral density minus helium and hydrogen mass densities from NRLMSISE-00, so no extrapolation was performed. The final case is the neutral density minus helium and hydrogen from NRLMSISE-00 up to 300 km, then extrapolated upwards, similar to the WACCM-X cases. Figure 7.4 demonstrates how the accuracy of the extrapolation technique reduces rapidly with altitude. The neutral density is overestimated in the 300-500 km range as expected, with the difference peaking at 9% at 500 km when helium is included in the profile being extrapolated. However, when the extrapolation technique is performed on the neutral densities neglecting helium (as a proxy for WACCM-X), the difference peaks at 4.1% as neutral densities in the part of the profile being extrapolated are already being slightly underestimated.

Figure 7.5 builds upon Figure 7.4 by looking at the same scenarios, but specifically at 500 km altitude and with varying F10.7. The extrapolation technique overestimates neutral densities at all solar activity levels, albeit at a fairly consistent rate (3 to 6%) when neglecting helium and hydrogen. Using these values as the upper and lower range of extrapolation overestimation for WACCM-X leads to an error of 3% in the stated values of Figures 5.10 and 5.11 at 500 km.

One method of potentially adding helium to WACCM-X output is to follow a

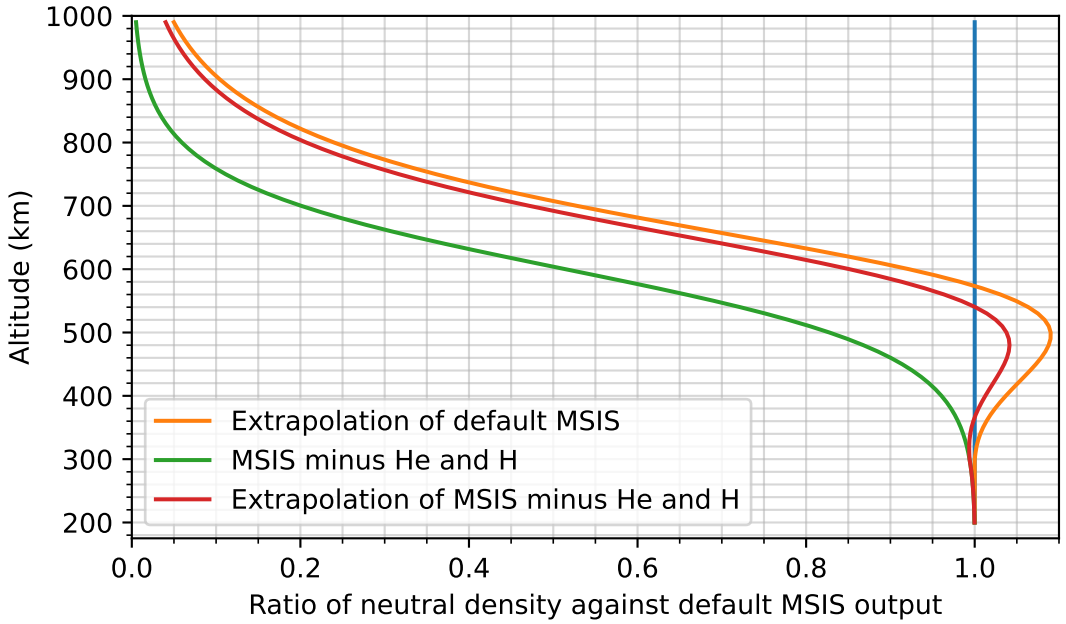

FIGURE 7.4: Extrapolation of NRLMSISE-00 neutral density from 300 km, both with and without helium and hydrogen included, and NRLMSISE-00 neutral density without helium and hydrogen (no extrapolation). Each scenario is then divided by the default neutral density. Global-mean annual-mean taken with F10.7 fixed at 70 sfu, $Kp = 0.33$.

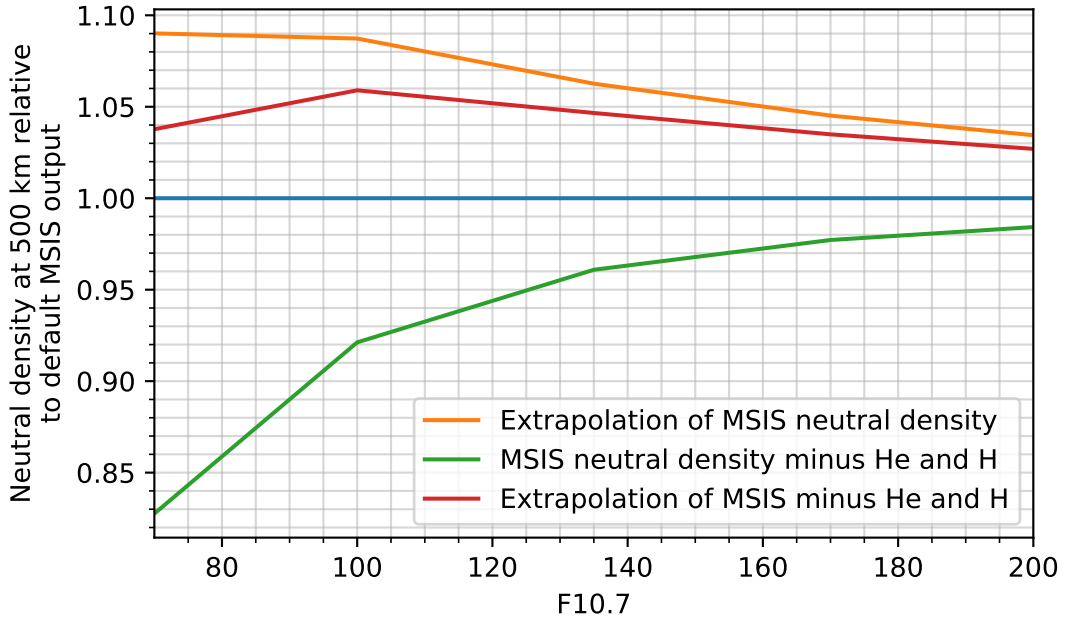

FIGURE 7.5: Extrapolation of NRLMSISE-00 neutral density from 300 km to 500 km under varying F10.7, both with and without helium and hydrogen included, and NRLMSISE-00 neutral density without helium and hydrogen (no extrapolation). Each scenario is then divided by the default neutral density. Global-mean annual-mean taken with $Kp = 0.33$.

methodology similar to the one where neutral densities are obtained from EUV airglow, with this described fully by Tuminello et al. (2022). Atomic oxygen and molecular nitrogen concentration profiles at a specific time are obtained from EUV airglow observations between around 100 and 400 km. Output from NRLMSISE-00 is then iteratively adjusted via the F10.7 input and scaled to obtain the best fit between NRLMSISE-00 predicted O and N_2 profiles and the observations. The total neutral density is then obtained from NRLMSISE-00 for the conditions which best fit the observations. This would be best accomplished on the HPC while running WACCM-X as it is computationally expensive to perform at all grid locations and times, and implementing this could be investigated in the future.

The LEO environment extends well above 500 km, with 1200 or even 2000 km used as the upper boundary by the ESA Space Debris Office (2020). Atmospheric drag is much less at these altitudes, as demonstrated in Figure 2.17. However at altitudes of around 500 - 800 km, drag still has to be considered when modelling the long-term environment, as orbital lifetimes at these altitudes are on the order of decades to centuries in length.

Density reductions have been shown to increase with altitude up to 700 km in historic studies (see Figure 3.1), and the assumption can be made that this relation could continue up to the exopause. However, in BRAD, the density reductions above 500 km are fixed to the level at the upper boundary of the calculated density trends. This likely underestimates the magnitude of the reduction. As the magnitude of the trend at higher altitudes is uncertain, fixing the trend at higher altitudes to the upper boundary was taken as the conservative approach. The magnitude of atmospheric drag also drops off rapidly above 500 km, so orbital lifetimes can extend to longer than the modelled century of Chapter 6. At higher altitudes, other orbital perturbations such as solar radiation pressure can change semi-major axis and eccentricity by a larger amount so the exact density reduction becomes less important when modelling long periods of time.

7.3.2 Impact of Kp on density reductions

Previous studies, summarised in Section 3.1.4, showed solar activity (via F10.7) has the largest impact on historic density trends. To remove the smaller impact of geomagnetic activity, the future density reductions of Chapter 5 are derived from WACCM-X simulations using a fixed, low Kp value of 0.33 throughout. The Kp value of 0.33 was chosen to help isolate the solar activity impact by reducing the impact of geomagnetic activity. It also allowed comparison with studies using a similar value of Kp, such as those by Solomon et al. (2018, 2019).

The impact of Kp on trends is explored through orbit-derived densities by Emmert (2015b), as discussed at the end of Section 3.1.2. In summary, Emmert binned observations by the 4-day average of Kp and limited results to 4-day average Kp values below 5. They found the magnitude of the historic trend decreases with increasing Kp. At Kp = 1, a trend of around -3.6 $\pm$ 0.8% per decade was found, while the trend is -1.2 $\pm$ 1.1% at Kp = 4.3.

Figure 7.6 shows the occurrence rate of 3-hourly Kp values since the year 1958 (chosen as the start of the space age, just over 5 solar cycles of data). While a value of 0.33 appears 7.6% of the time, Kp = 2.66 occurs at a similar rate (7.4%), and Kp = 1 is the most commonly occurring 3-hourly value. This raises the concern that Kp = 0.33 may not be the best value to summarise how density reductions vary with solar activity.

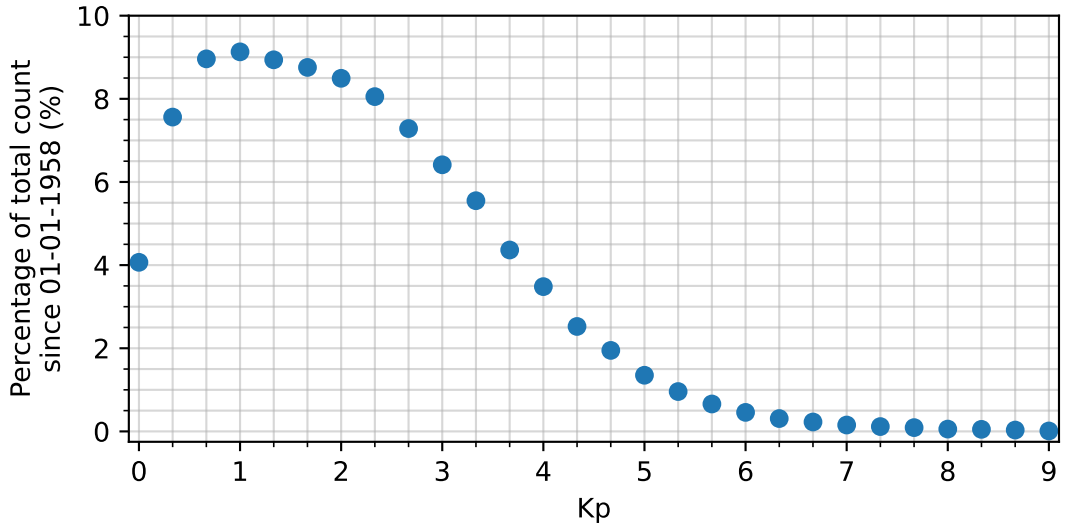

FIGURE 7.6: The percentage of occurrences of each 3-hourly Kp value since 01-01-1958. Data described and obtained from Matzka et al. (2021)

To address this concern, some additional WACCM-X runs have been performed to investigate. The results of Chapter 5 used version 1.2 of CESM and WACCM-X on the University of Southampton's Iridis 4 HPC. Iridis 4 was upgraded between those results and these Kp runs. The new Iridis 5 has a different architecture, leading to issues with model installation. The results of this section are therefore obtained from the University of Birmingham's BlueBEAR HPC with version 2.2 of CESM and version 2.0 of WACCM-X. These models are described by Danabasoglu et al. (2020) and Liu et al. (2018) respectively.

Four 15-month simulations were performed, for the years 2000 (reference), 2035, 2065, and 2095. These simulations used a similar methodology to Chapter 5, again assuming CO_2 concentrations from RCP8.5, scaling carbon dioxide and carbon monoxide as described in Section 5.1.4.1 and performing a 3-month spin-up. However, both F10.7 and Kp were allowed to vary, and the historical values from the year 2000 were used

cyclically (shown in subplots b and c of Figure 7.7). The year 2000 was chosen as the reference year as it allowed like-for-like comparison with results from Chapter 5, but also included a number of substantial geomagnetic storms. Output from WACCM-X was stored at an hourly cadence. Relative neutral densities were then obtained by taking global-means and dividing by the global-mean neutral density of the reference year 2000. These are shown in Figure 7.7. Data from periods where F10.7 is greater than 200 sfu have been removed, as solar activity effects are removed later in the analysis, and analysis was limited to the F10.7 values investigated in Chapter 5.

The effects of solar activity on the density reductions were removed with use of the scaling table described in Section 5.6. Density reductions are then binned by Kp with a lag of 2 hours from Kp onset, a mean and standard deviation of the density reductions taken within each bin, and then a ratio taken against the value for $Kp = 0.33$. This gives the relative difference in density to $Kp = 0.33$ with solar activity effects removed, and is shown in Figure 7.8. The number of occurrences of each Kp value has also been included in the figure. A relative difference of greater than one corresponds to a smaller magnitude of density reduction compared to the $Kp = 0.33$ results of Chapter 5.

It appears Kp values less than 4 appear to have little immediate impact on the magnitude of density reduction relative to $Kp = 0.33$ in WACCM-X, although the variability is large and may be hiding the effect. At Kp values greater than 4, it appears the magnitude of the density reduction decreases with increasing Kp (as the relative difference to $Kp = 0.33$ increases), but there are far fewer occurrences of these values of Kp.

Geomagnetic storms with large Kp values add substantial energy to the upper atmosphere. Models such as NRLMSISE-00 account for this by requiring geomagnetic indices up to 59 hours prior to the time of interest (although ap is used in NRLMSISE-00 rather than Kp). To investigate this, a similar investigation to the above has been performed, but binning by the mean 3-hourly Kp values over 24 and 48 hours previous to the modelled density reduction, and in bin sizes of 0.33 to match the 3-hourly Kp. Figure 7.9 shows the results for the averaged previous 24 hours, and Figure 7.10 for the previous 48 hours. Both of these show similar results to the 3-hourly Kp result, and while the increasing difference at Kp values greater than 4 appears to suggest smaller neutral density reductions, the number of occurrences makes it difficult to say if this is true.

Simulations similar to those performed with fixed Kp, but varying F10.7 could be performed in the future, but with varying Kp and fixed F10.7. This was originally considered, but limited computing time led to the above method being chosen with the hope of being able to investigate a larger number of Kp values. Previous modelling studies, summarised by Figure 3.2, used up to three values of F10.7 values.

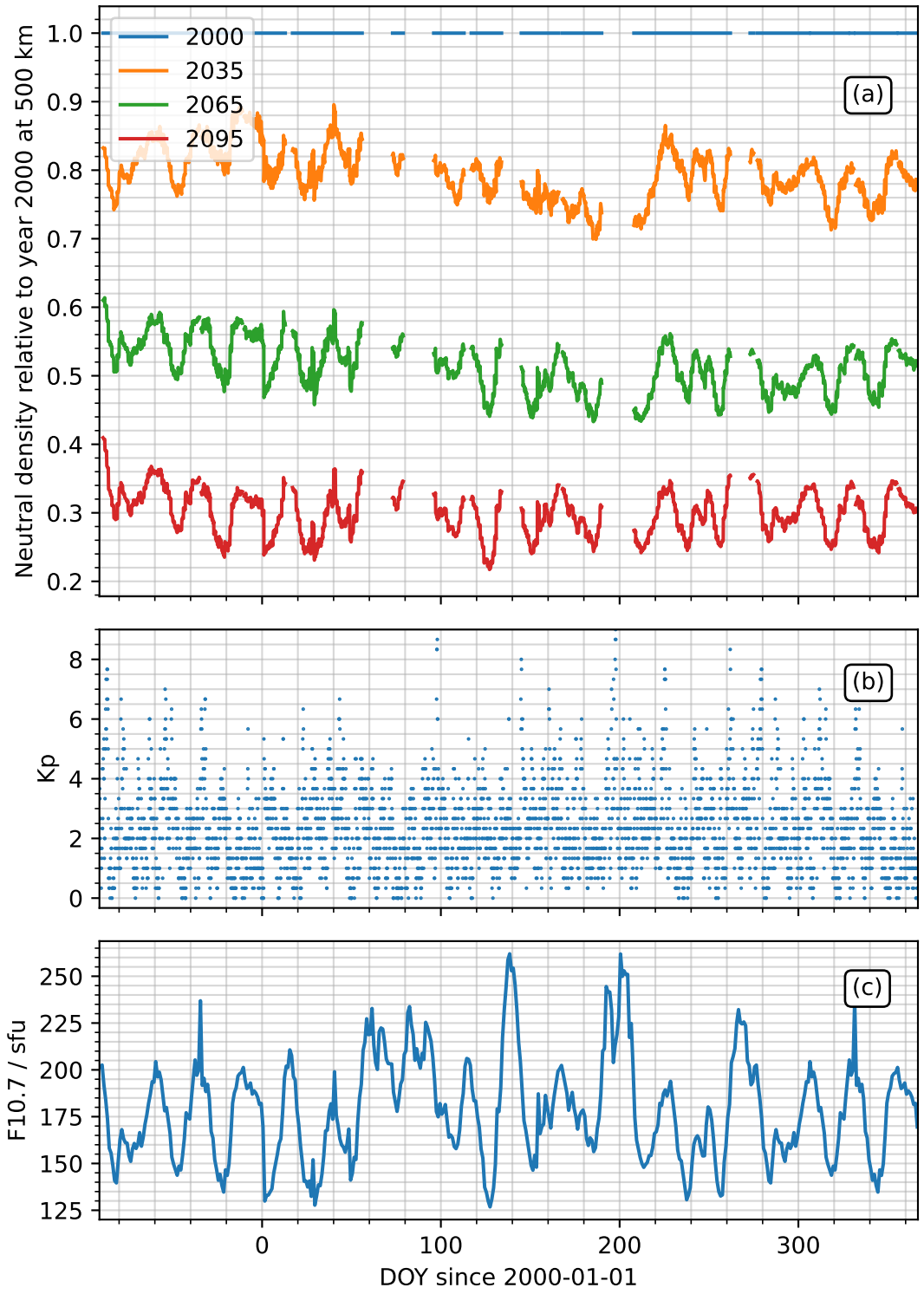

FIGURE 7.7: The neutral density relative to the year 2000 at 500 km, under varying solar activity and geomagnetic activity conditions, where the value has been removed when F10.7 is greater than 200 sfu. Subfigures (b) and (c) show the Kp and F10.7 used, namely the historical values from the year 2000. A spin-up of 91 days is used, denoted by the DOY being less than 0.

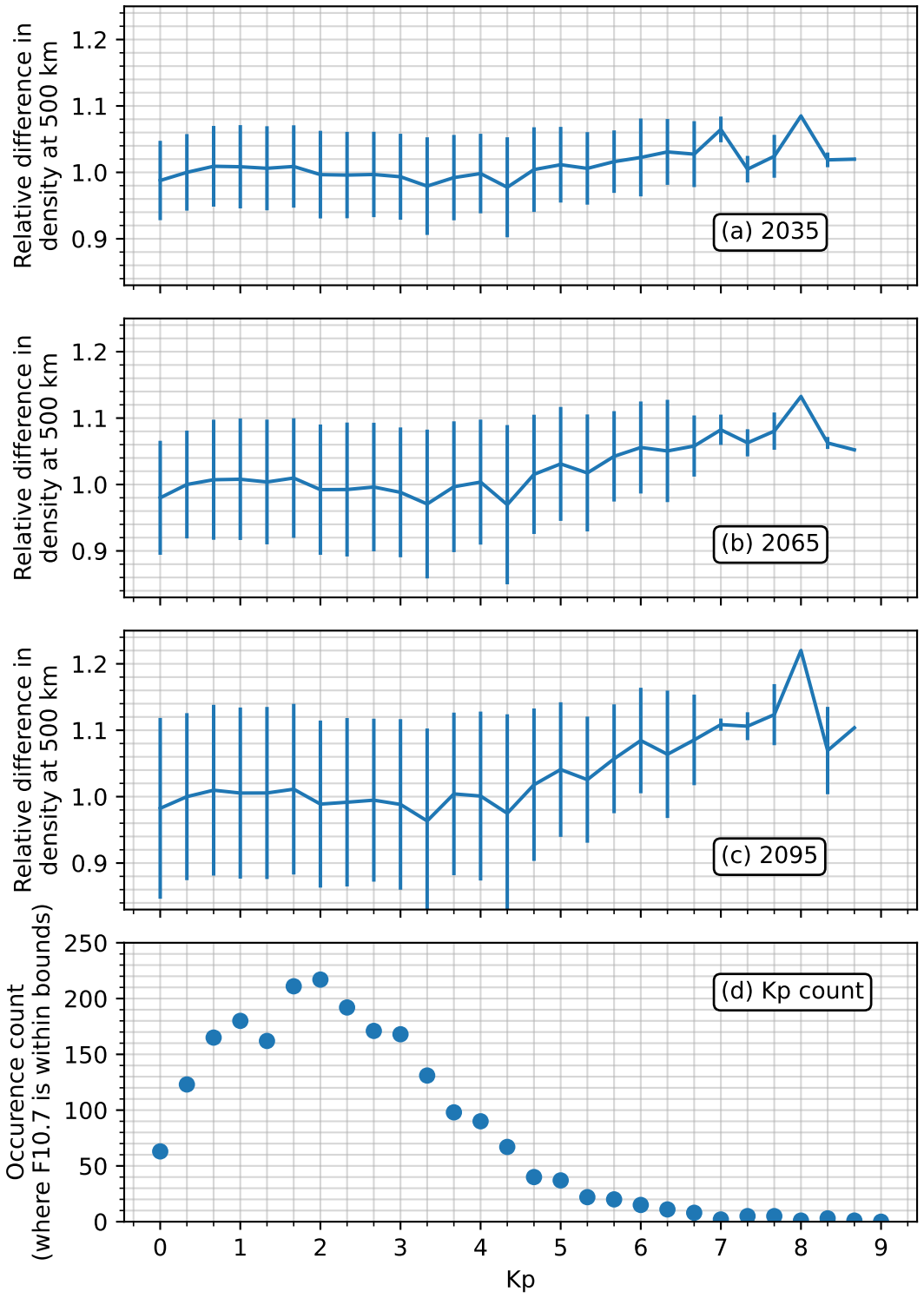

FIGURE 7.8: Relative difference in density at 500 km after solar activity effects have been removed, binned by Kp value with a 2 hour lag, and scaled to $Kp = 0.33$, for the years (a) 2035, (b) 2065, and (c) 2095. A relative difference of greater than one corresponds to a smaller magnitude of density reduction compared to the $Kp = 0.33$ results of Chapter 5. The count of each Kp value is given in (d).

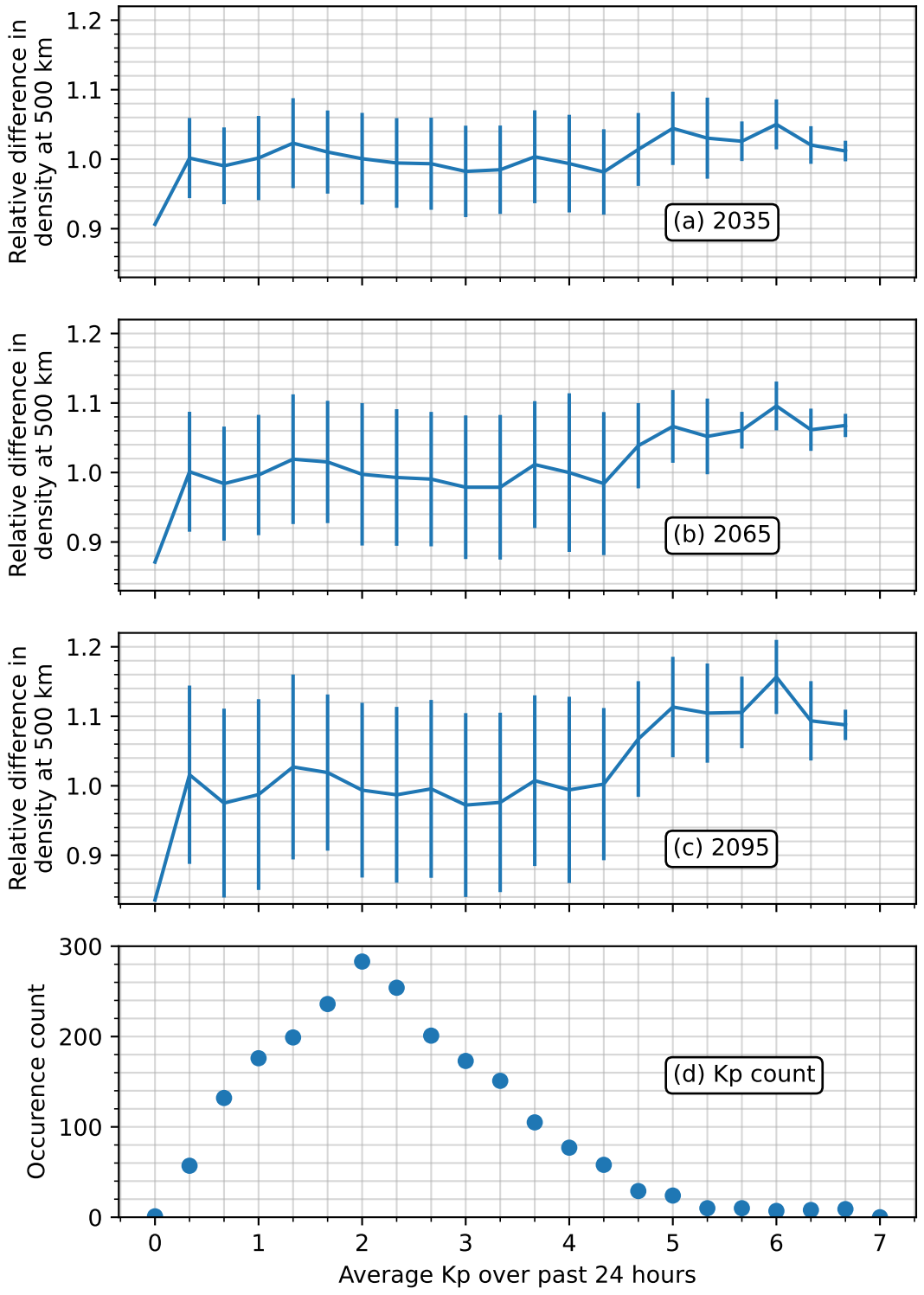

FIGURE 7.9: Relative difference in density at 500 km after solar activity effects have been removed, binned by mean Kp value over the previous 24 hours, and scaled to $Kp = 0.33$, for the years (a) 2035, (b) 2065, and (c) 2095. A relative difference of greater than one corresponds to a smaller magnitude of density reduction compared to the $Kp = 0.33$ results of Chapter 5. The count of each previous 24 hour mean Kp value is given in (d).

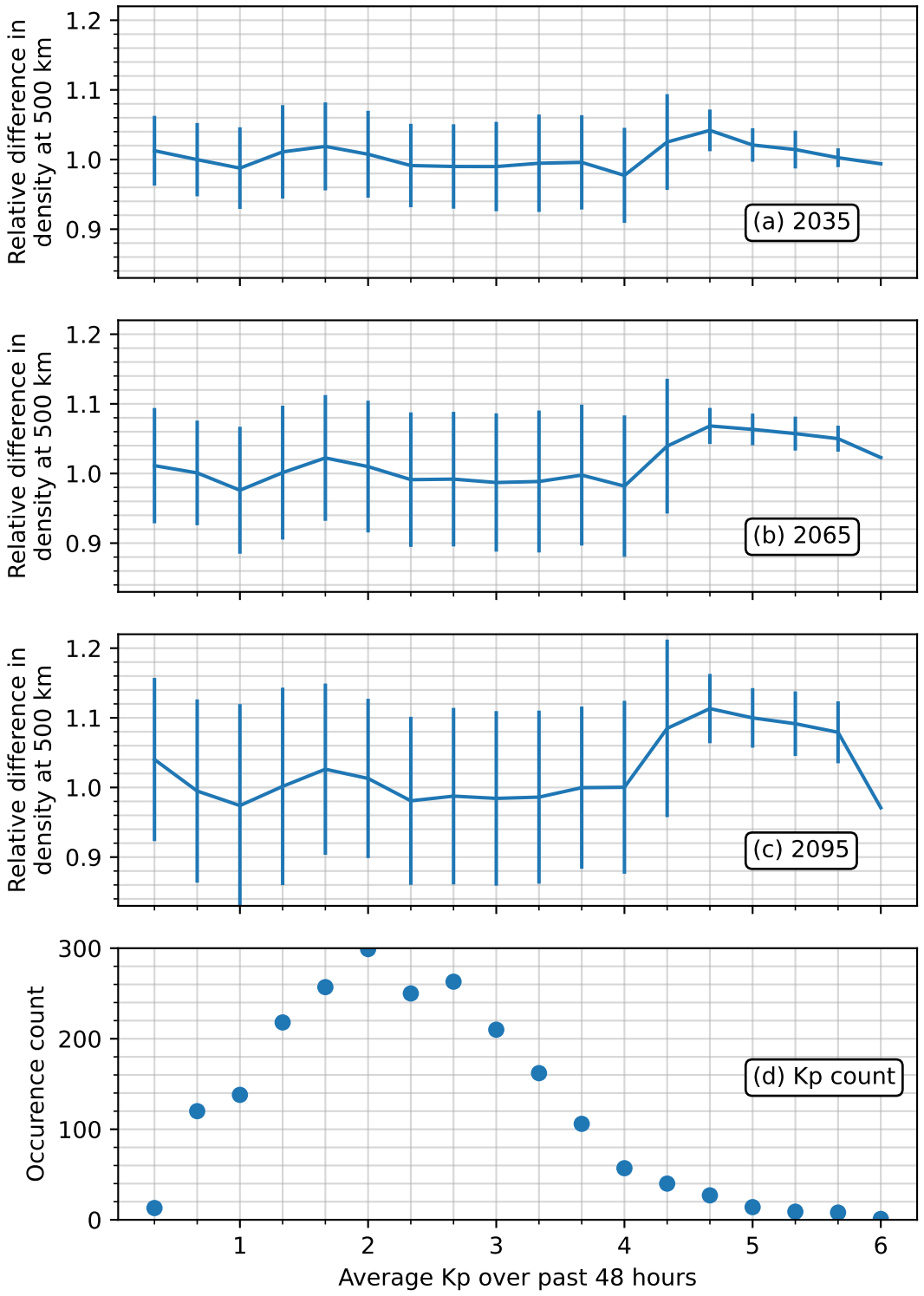

FIGURE 7.10: Relative difference in density at 500 km after solar activity effects have been removed, binned by mean Kp value over the previous 48 hours, and scaled to $Kp = 0.33$, for the years (a) 2035, (b) 2065, and (c) 2095. A relative difference of greater than one corresponds to a smaller magnitude of density reduction compared to the $Kp = 0.33$ results of Chapter 5. The count of each previous 48 hour mean Kp value is given in (d).

This limited the understanding of the trend between those values. The use of a whole year of model data with varying geomagnetic conditions was performed with the aim to resolve a larger number of Kp values. Upon reflection, a greater number of modelled years would be required to reduce the variability, at which point the previous method may be more computationally time-effective. However, particularly subfigure c of Figures 7.8, 7.9 and 7.10 Kp values less than 5, have no greater than a 16% difference from the Kp = 0.33 results between the year 2000 and 2095, equivalent to 1.6% per decade.

7.3.3 Solar Activity Extremes

The density studies of Sections 5.2 and 5.3 used F10.7 values of 70 and 200 sfu respectively. However, F10.7 is not bound to this range, with periods below 70 sfu and above 200 sfu seen during the last five cycles (plotted in Figure 2.7). These values were chosen as the boundaries in solar activity as they are commonly used in historical studies (see Table 3.2). Within the BRAD debris model, during periods of solar activity outside these bounds, the density reductions were kept fixed at the levels seen at the boundary rather than attempt to extrapolate past them.

The fraction of days that F10.7 dropped below specified solar activity levels during the last 5 solar cycles is presented in Figure 7.11. While 9.5% of days have solar activities below an F10.7 of 70 sfu, the fraction of days with lower solar activity levels quickly declines, with only 5.7% below 69 sfu, 2.6% below 68 sfu, and 0.9% below 67 sfu. The rapid drop off in occurrences below 70 sfu means simulating these lower solar activity levels would have diminishing returns. However, neutral densities are already at their lowest during low solar activity and therefore a small difference in additional density reduction at 67 sfu compared to 70 sfu would have a marginal impact on orbital lifetimes. So although the larger density reductions are seen under lower solar activities, fixing density reductions at solar activities below 70 sfu to this boundary is a good compromise.

For high solar activities, 7.4% of days in the last 5 cycles have F10.7 values larger than 200 sfu. However, a smaller proportion of days, 4.3%, have solar activities above 220 sfu, and 2.2% of days have F10.7 larger than 240 sfu. F10.7 = 200 sfu was originally chosen as the upper boundary due its use in historic studies and allowing for a more direct comparison. Reflecting upon this, a larger value would prove useful for future simulations. Although smaller density reductions are seen during high solar activity, the order of magnitude increase has a substantial impact on the debris environment so the combination of effects is of particular interest in debris environment studies. However, BRAD repeated solar cycle 24, in which only 16 days have an F10.7 value greater than 200 sfu. Therefore the impact on results is negligible in this case. The last

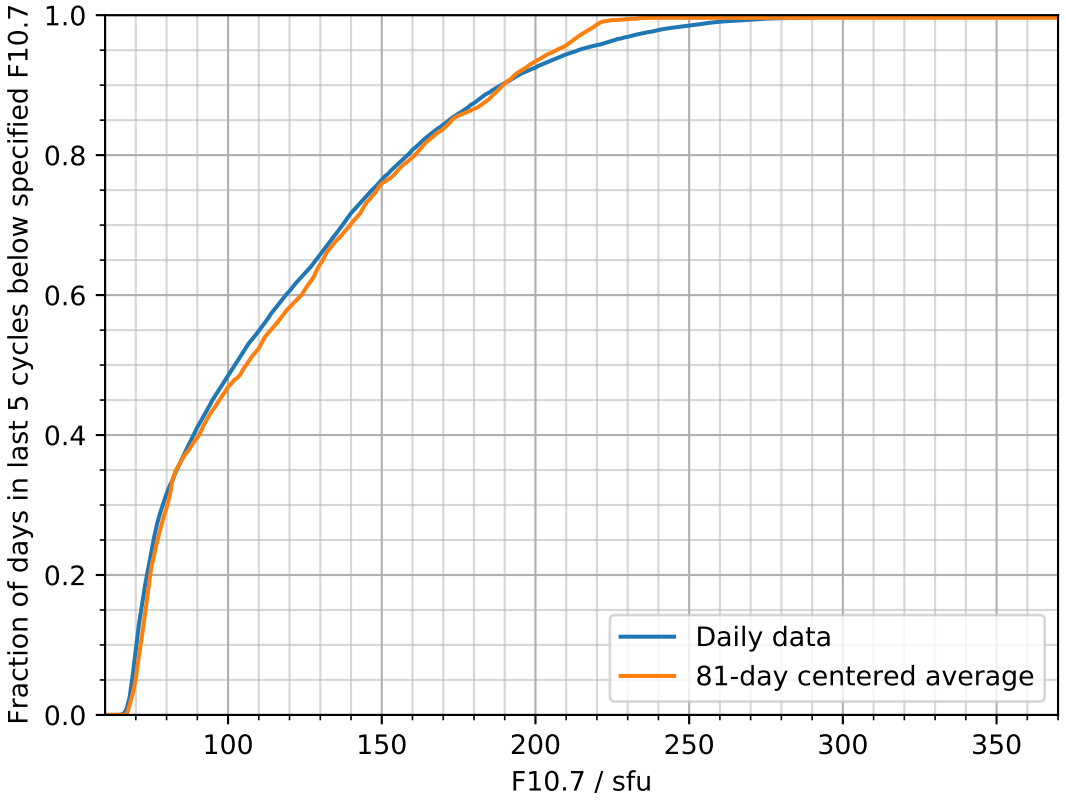

FIGURE 7.11: The fraction of days during the last 5 solar cycles which have had solar activities below each recorded F10.7 value. The solar activity data this analysis has been based on is presented in Figure 2.7.

five solar cycles have also on average been relatively high compared to the full, historic record, as summarised in Figure 2.6.

7.3.4 Applying Density Scaling to Empirical Models

Applying the density scaling table of Section 5.6 to empirical atmospheric models is a fast way to account for thermospheric contraction while maintaining the computational speed of empirical models for orbital propagation applications. However each empirical model is based upon data from different historic periods, and the density scaling table as well as results presented in this thesis give density reductions relative to the year 2000. As NRLMSISE-00 is based on thermospheric density data closest to this year, it was chosen as the empirical model of BRAD over other empirical models such as the CIRA or Jacchia models.

Updated versions of empirical models often include more up-to-date data sources, thereby implicitly including thermospheric contraction over the data period used. For example, NRLMSISE-00 used thermospheric data up to the year 1997, while the updated model version, NRLMSIS 2.0, uses thermospheric mass density data for

fitting up to the year 2005, with up to 2013 included for validation purposes (Emmert et al. (2021)).

For shorter-term modelling, for example when studying the orbit of a Cubesat launched from the ISS, using recently published empirical models will likely reduce the error caused by thermospheric contraction to a smaller size than errors from other sources (for example, solar activity prediction or estimation of C_D). Long-term modelling on the scale of multiple decades requires accounting for thermospheric contraction, as the discrepancy will grow with time. This is the case even if comparing no thermospheric contraction to the ”best-case” scenario of RCP2.6.

7.3.5 BRAD Limitations

The rationale behind creating BRAD was to quickly identify key phenomenon arising in the debris environment due to the density reductions caused by increases in carbon dioxide concentrations. To that end, the model has been successful, identifying that over 100 years even the best-case scenario of RCP2.6 has a significant impact on the debris environment compared to when density reductions are not modelled. However, as explored in Section 3.2, each type of debris model has its own limitations, and as such, BRAD's will be explored here.

While theoretically faster, the binned and statistical nature of BRAD presents problems which do not arise in the debris models which handle objects individually. An example of this is the difficulty in gauging orbital lifetimes as propagated objects are split between bins, as was explored in Section 6.2. This often leaves fractions of an object in the original bin unless the decrease in semi-major axis during the current time step is larger than the bin size. This can be addressed in part through the use of smaller bin sizes. The final choice for semi-major axis bins presented in Table 6.1 was a trade-off between run-time, having a fine enough resolution to gauge orbital lifetimes for validation purposes, and being able to discern how the debris population in different regions changed.

Two other issues arise due to binning by mass. The first arises while creating the fragments of a collision. The mass before and after collision is conserved in the SBM by design. Upon binning the fragments into the coarser BRAD bins, mass is not fully conserved. Figure 7.12 demonstrates this for 1000 simulated collisions between objects at the centres of mass bins. Overall, BRAD underestimates the summed mass of all fragments by -14.7 $\pm$ 12%. This is inherent to the choice of bins and the logarithmic scaling used in BRAD. The number of fragments from the collision is maintained during the binning procedure. Therefore the only implications are, on average, a slight overestimate in area to mass ratio of objects, and therefore slightly shorter lifetimes,

but also a compounding reduction in mass as the fragments from a previous collision are involved in further collisions.

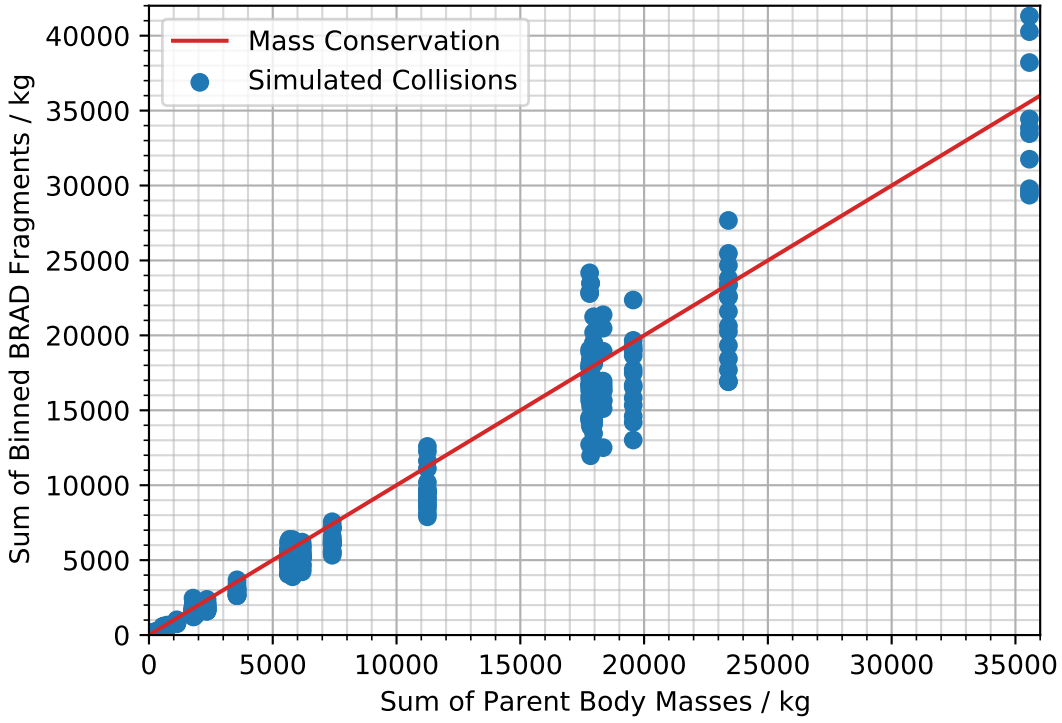

FIGURE 7.12: Breaking of mass conservation during collisions within BRAD due to binning by mass. Each point represents one of the 1000 simulated collisions between two representative objects in BRAD.

The second issue to arise due to binning by mass is the requirement for radii and cross-sectional areas in calculations such as atmospheric drag. All characteristics of objects, such as geometry and object type, are lost when binning compared to handling objects individually. This makes it impossible to simulate specific characteristics or concepts of operation within the model without introducing another population with the same a, e, i, m bins. For example, while models like NASA's SBM use different area-to-mass relations for rocket bodies and spacecraft, this would require a separate population in BRAD, doubling the total number of bins required and quadrupling the number of bin interactions. Multiple populations could be created to simulate different groups of objects which exhibit different behaviours, for example objects with drag sails deployed or actively maintaining an orbit. However, this quickly increases the total number of bin to bin pairings and threatens losing the advantages of the statistical approach, and reducing the number of Monte Carlo simulations which could be performed with the same computational resources.

Another limitation of BRAD arises because all objects are handled collectively. Individual characteristics such as orbital maintenance and collision avoidance which would be performed by active spacecraft cannot be simulated. Instead the BRAD

population represents a "dead" scenario, where all objects are treated as debris. Although the majority of trackable objects currently in the environment are debris, this active population is a substantial part which unfortunately is not modelled in BRAD. Again, this could be addressed by having a separate population for active spacecraft which interacts with the general population, but the same issues arise as previously discussed.

Noting each of these limitations with BRAD, it has still successfully modelled the LEO debris environment and demonstrated the impact carbon-dioxide related neutral density reductions have on the debris environment. The method of using a density scaling table to account for density reductions due to increasing carbon dioxide concentrations has also been demonstrated, and can be used in more debris models in the future, as will be explored further in Section 7.5

7.4 Novel Contributions and Revisiting the Research Aims

Chapter 4 laid out the research aims of the project. This section will briefly revisit these and highlight some of the novel contributions made.

Sections 5.2, 5.3 and 5.4 demonstrated how thermospheric neutral densities reduce into the future under increasing carbon dioxide concentrations. Other than the limited study of Qian and Solomon (2011), this is the first time density reductions in the future have been modeled in detail. From studies of historical density trends, it was expected that the density reductions would be dependent upon solar activity. To explore this, WACCM-X simulated low solar activity (F10.7 = 70 sfu) and high solar activity (F10.7 = 200 sfu) under varying carbon dioxide concentrations. The full solar activity impact was then simulated at F10.7 values of 100, 135, and 170 sfu. Even with only five solar activity values, this is the highest resolution modelling study of solar activity impact on density reductions. It also agreed with other model results showing the monotonically increasing density reduction with decreasing solar activity. This highlights a discrepancy between modelling results and the observations of Emmert (2015b) and Emmert et al. (2008), which saw density reductions peak at medium solar activity levels (shown in Figure 3.2). The density reductions were also shown to be dependent upon latitude, as summarized in Figure 5.13. Regions of mid-latitude saw the largest reductions, with the northern hemisphere in general being of a slightly larger magnitude than the southern hemisphere. These results were amalgamated into a simple density scaling table which can be applied to empirical atmospheric models to allow them to account for future thermospheric contraction.

Section 6 covered the debris model created to explore the impact of density reductions on the future debris environment. It also presented the results from the model, with Figure 6.12 and 6.14 showing how the number of objects and number of collisions

increase exponentially in each RCP scenario. The rates of increase are largest in the more extreme RCP scenarios. Also notably, in RCP2.6, after the middle of the century the number of objects and collisons continues to rise exponentially in comparison to the control scenario, in spite of carbon dioxide concentrations decreasing and the magnitude of the density reduction falling. These findings are the first time the ground-level concentrations have been tied into debris modelling through the RCP scenarios.

7.5 Future Work

Studies in lower parts of the atmosphere have made use of ensembles of independent models to add reliability to results, for example in the Chemistry-Climate Model Initiative (CCMI) summarized by Morgenstern et al. (2017), or in projecting ozone hole recovery as detailed by Amos et al. (2020). Currently results on future density reductions have been limited to a one-dimensional implementation of TIE-GCM (Qian and Solomon (2011)) and WACCM-X (this thesis). The computing resources and expertise required to run additional numerical thermospheric models creates the opportunity for a collaboration within the upper atmosphere modelling community to create an ensemble of models and results. A collaboration like this could also create density scaling tables similar to that discussed in Section 5.6.

The density scaling table created in this thesis has been made available and can be applied to the empirical atmospheric models within established debris models. Debris evolution models which use individual objects would allow for a more detailed study of the impacts on the debris environment. One area which requires further research is the creation of large constellations of satellites within the space environment. By design, the constellations offering global internet coverage operate in LEO, for example with SpaceX planning to launch 12,000 to 42,000 satellites at around 550 km. These satellites will be operating at the altitudes most impacted by density reductions. They also represent a large injection of mass into the LEO environment, and even if only a small percentage of satellites fail, this equates to a substantial increase in the amount of large, uncontrolled objects. The collision probability algorithm used within BRAD cannot model the structure within the orbital shells of a constellation. Debris evolutionary models have the advantage of being able to do so, and therefore including density reductions within their studies would be the next step in this area of research.

Separately, Joule heating and other space weather events cause short-term density changes, for example as observed by Sutton et al. (2009) with data from the CHAMP satellite. A short-term density change impacts orbital propagation on the order of hours to days, and would in turn affect the close-approach analysis used by satellite

operators for collision avoidance. The models and tools used in studying long term density reductions could also be used to study these shorter-term density changes and help in combining thermospheric density forecasting with short-term orbital propagation.

Chapter 8

Conclusions

The majority of atmospheric climate change research has focused on the ground-level troposphere. However the atmosphere is a connected system, with ground-level carbon dioxide emissions rising up through the atmosphere to higher levels, causing climate change impacts throughout the whole atmosphere. In the thermosphere, previous studies have observed and modelled neutral density reductions over historical periods. The observations effectively used the increasing orbital lifetimes of the objects travelling through the thermosphere to derive these density trends, highlighting the impact carbon dioxide emissions have already had on the LEO environment.

This thesis aimed to address two major questions arising from these previous studies. Firstly, how the neutral density reductions in the thermosphere could vary into the future. Secondly, what impact would these neutral density reductions have on the future debris environment in LEO.

WACCM-X was used to model the thermosphere under increasing ground-level carbon dioxide concentrations. The magnitude of the reductions in global-mean annual-mean neutral densities at 200 to 500 km altitude were shown to increase with increasing carbon dioxide concentrations, increasing altitude, and decreasing solar activity levels. Thermospheric neutral density reductions were given relative to the year 2000. The Paris Agreement target of 1.5°C corresponds to a CO_2 concentration of 480 ppm, under which neutral densities at 400 km altitude can be expected to fall by an amount between 15% for high solar activity (F10.7 = 200 sfu) and 32% for low (F10.7 = 70 sfu). Concentrations up to an extreme of 890 ppm were modelled, with this corresponding to neutral density reductions at 400 km of 52% and 79%.

Density reductions were linked to Representative Concentration Pathways (RCPs) and included in the new Binned Representative Atmospheric Decay (BRAD) debris model to explore the impact on the LEO debris environment. It was shown that both the

number of objects and the number of collisions increases exponentially as carbon dioxide concentrations increase. This is the case even when comparing a control scenario with no density reductions included against the best case scenario of RCP2.6. In RCP2.6 the carbon dioxide concentration peaks in the middle of the century and then decreases, however the impact on the debris environment is persistent, with the number of objects and the rate of collisions continuing to rise.

The results of this thesis have highlighted the importance of including neutral density reductions in long-term debris modelling of the LEO environment. There is inherent uncertainty in predicting the future environment, for example, through what carbon dioxide concentrations or space launch traffic could be. Even under the best case scenario modelled of RCP2.6, neglecting the impact on the environment from neutral thermospheric density reductions has been shown to have a substantial impact on century-long modelling of the LEO debris environment. Carbon dioxide emissions make the space debris problem exponentially worse, and nearly all space debris models currently do not include this in their modelling. This has implications for the long-term sustainability of the environment, as current licensing and guidelines miss a substantial component of the overall problem. The increasing number of objects also presents an increased risk to space missions travelling to higher orbits or even other planets and moons, as they travel through LEO in the early stages of their mission.

Discussion about the impacts of carbon dioxide emissions often focus on the ground-level impacts on humanity and the Earth environment. The studies in this thesis have shown the impacts extend high above us and into the space environment. Earth observation satellites which are used to research climate change will be placed at higher risk from debris collisions due to carbon dioxide emissions, highlighting the interconnectedness of the environment and humanity's interaction with it.

Appendix A

Summary of Objects in Orbit-Derived Density Trend Studies

Section 3.1.2 details the studies which use TLE data of objects in orbit to derive density trends. Table A.1 summarizes the objects and periods of data used in the Keating et al. (2000), Emmert et al. (2004), Marcos et al. (2005) and Saunders et al. (2011). Presenting them in this format highlights the common objects between studies and the different periods used in each study. Although Emmert et al. (2008), Emmert and Picone (2011) and Emmert (2015b) derived density trends from orbital data and included those in Table A.1, they used over 5000 individual objects. Therefore they have been omitted from this summary.

TABLE A.1: Summary of objects used in the derived density studies using a limited set of orbiting objects.

NORAD ID	Name / Description	Keating et al. (2000)	Emmert et al. (2004)	Marcos et al. (2005)	Saunders et al. (2011)
00060	Explorer 8	1976, 1986, 1996	1966-2001	1970-2000	1970-2010
00063	Tiros 2		1966-2001		1970-2010
00165	Delta 1 R/B		1966-2001		1970-2010
00229	Delta 1 R/B		1966-2001		1970-2002
00614	Hitchhiker 1	1976, 1986, 1996	1966-2001	1976, 1986, 1996	1970-2010
00750	Elektron 1 Debris		1966-2001		1970-2010
01335	SL-8 Debris				1970-2010
01370	SL-8 Debris		1966-2001		1970-2004
01616	Atlas D R/B			1970-2000	1970-2010
01685	Titan 3C Transtage Debris				1970-2010
01808	Thor Agena B Debris		1966-2001		1970-2002
01843	Cosmos-100		1971-2000		1970-2002
01857	Titan 3C Transtage Debris				1970-2010
01981	Titan 3C Transtage Debris				1970-2010
02016	Diapason D-1A		1966-2001		1970-2010
02129	Thor Altair R/B		1967-2001		1970-2002
02150	OV3-1			1970-2000	
02153	Thor Agena B Debris		1968-2001		1970-2010
02389	OV3-3	1976, 1986, 1996	1967-2001	1970-2000	1970-2010
02611	OV1-10		1969-2000		1970-2002
02622	OV1-9 R/B		1971-2001		1970-2010
02643	Delta 1 R/B(2)	1976, 1986, 1996			1970-2010

NORAD ID	Name / Description	Keating et al. (2000)	Emmert et al. (2004)	Marcos et al. (2005)	Saunders et al. (2011)
03019	SL-11 R/B		1968-2000		1970-2002
03038	SL-8 Debris				1970-2010
03462	Titan 3C Transtage Debris				1970-2010
03523	Cosmos 249 Debris		1969-2000		1970-2001
03524	Cosmos 249 Debris		1969-2000		1970-2001
03553	Cosmos 252 Debris		1969-2001		1970-2004
03608	Cosmos 249 Debris				1970-2010
03717	Cosmos 252 Debris		1975-2000		1970-2001
03835	Meteor 1-1				1970-2010
04053	Delta 1 Debris				1970-2010
04119	Meteor 1-2		1970-2001		1970-2002
04221	Azur		1970-2001	1970-2000	1970-2010
04330	Ohsumi	1976, 1986, 1996	1970-2001	1976, 1986, 1996	1970-2003
04726	Cosmos 375 Debris		1971-2000		1970-2001
04849	Meteor 1-7		1971-2001		1971-2005
04940	Cosmos 375 Debris		1971-2000		1970-2001
05977	Delta 1 R/B(2)				1970-2010
05998	Titan 3C Transtage Debris				1970-1999
06073	Cosmos 482 Descent Craft		1972-2001		1972-2010
14756	Titan 3C Transtage Debris				1973-2010

Appendix B

Greenberg Collision Probability

This appendix reproduces the equations of the collision probability algorithm created by Greenberg (1982). Additional derivations will be given to aid in reproducing the algorithm, as well as corrections to typographical errors in the original paper. Bottke and Greenberg (1993) also produced corrections to assumptions to the Greenberg algorithm, and these will be noted at the locations they arise. However, they will not be implemented here as the results could not be reproduced.

To help distinguish between the two orbits when presenting the algorithm, they are named the test orbit and field orbit. In general, the choice of which orbit is which does not matter, although singularities sometimes arise but that is addressed an the end of this appendix. Variables related to the field orbit are denoted with subscript 0, for example its classical orbital elements are a_0, e_0, i_0, Ω_0, ω_0 and θ_0 while the test orbit has no subscript, so a, e, i, Ω, ω and θ. Orbital elements were summarized in Table 2.2. The right ascensions of ascending node (Ω and Ω_0) and arguments of perigee (ω and ω_0) are assumed to be uniformly distributed between 0 and 2π. The true anomalies, θ and θ_0, are calculated for each possible close approach within the algorithm. Therefore only a_0, e_0, i_0 and a, e, i are required to calculate the intrinsic collision probability (which is independent of the objects in the orbit) between the two orbits.

The closest approach between the two orbits happens near a mutual node, as shown in Figure B.1. There is a second mutual node on the opposite side of the planet too. The positions of the mutual nodes measured from the ascending node on each orbit are u and u_0. Relationships for these can be found with spherical trigonometry, where the spherical cosine rule gives

$$\cos u = \cos u_0 \cos \Delta\Omega + \sin u_0 \sin \Delta\Omega \cos i_0 \tag{B.1}$$

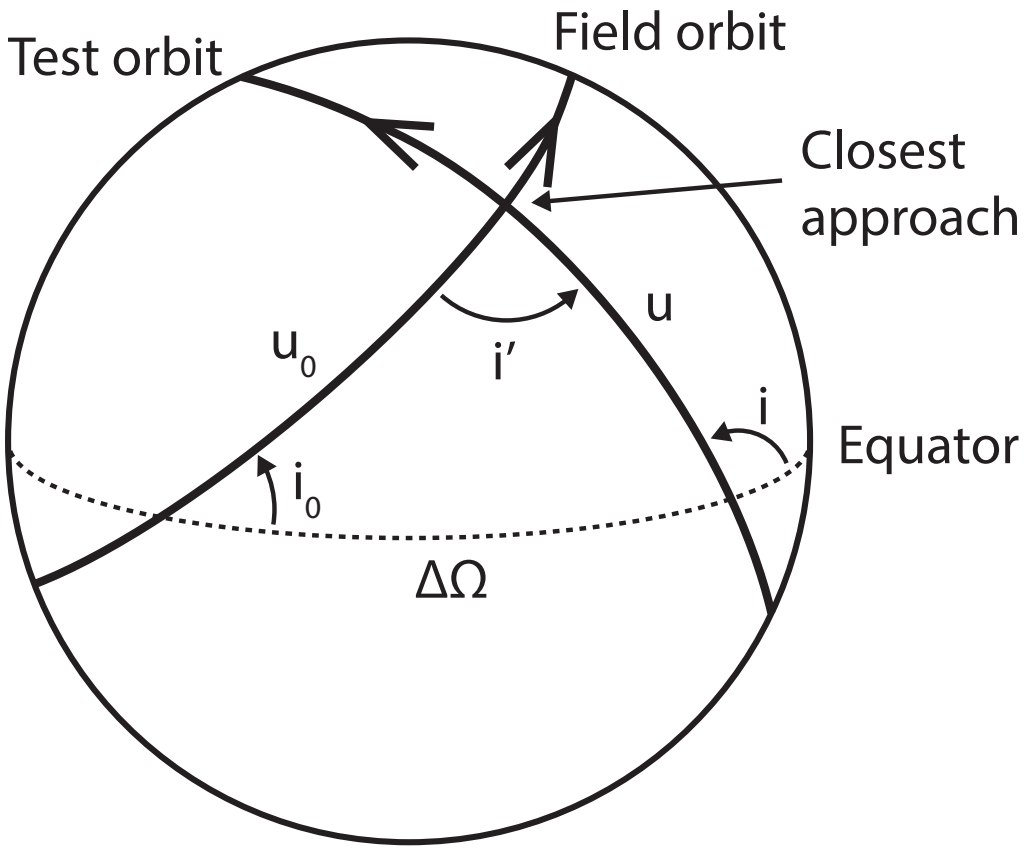

FIGURE B.1: Greenberg test and field orbits

where $\Delta\Omega$ is the difference between the right ascension of ascending nodes. The spherical sine rule gives

$$\frac{\sin i_o}{\sin u} = \frac{\sin(\pi - i)}{\sin u_0} = \frac{\sin i}{\sin u_0} \tag{B.2}$$

which can be rearranged to find

$$\sin u = \frac{\sin u_0 \sin i_0}{\sin i} \tag{B.3}$$

The mutual inclination i' can also be obtained by the spherical cosine rule such that

$$\cos i' = \cos i \cos i_0 + \sin i \sin i_0 \cos \Delta\Omega \tag{B.4}$$

where i' is positive if the selected mutual node is the ascending node of the test object on the orbit of the field object, as shown in Figure B.1, and negative otherwise.

Another equation for u_0 is given as Equation B.10 in Greenberg (1982), but the derivation of this begins with the spherical cosine rule

$$\cos u_0 = \cos u \cos \Delta\Omega + \sin u \sin \Delta\Omega \cos(\pi - i) \tag{B.5}$$

Noting $\cos(\pi - i) = -\cos i$, substituting in $\cos u$ from B.1 and $\sin u$ from B.3 gives

$$\cos u_0 = (\cos u_0 \cos \Delta\Omega + \sin u_0 \sin \Delta\Omega \cos i_0) \cos \Delta\Omega - -\sin \Delta\Omega \left(\frac{\sin i_0 \sin u_0}{\sin i} \right) \cos i \tag{B.6}$$

Then noting $tan(\theta) = \frac{sin(\theta)}{cos(\theta)}$, multiplying out and dividing through by $cos(u_0)$ gives

$$1 = \cos^2 \Delta\Omega + \tan u_0 \sin \Delta\Omega \cos \Delta\Omega \cos i_0 - \tan u_0 \sin \Delta\Omega \sin i_0 \cot i \tag{B.7}$$

which is rearranged to

$$\tan u_0 (\sin \Delta\Omega \sin i_0 \cot i - \sin \Delta\Omega \cos \Delta\Omega \cos i_0) = cos^2 \Delta\Omega - 1 \tag{B.8}$$

Noting $\cos^2 \theta - 1 = -\sin^2 \theta$ and rearranging for $\tan u_0$

$$\tan u_0 = \frac{-\sin^2 \Delta\Omega}{\sin \Delta\Omega \sin i_0 \cot i - \sin \Delta\Omega \cos \Delta\Omega \cos i_0} \tag{B.9}$$

and finally taking the inverse tangent to obtain the relationship given in Greenberg (1982), namely

$$u_0 = \arctan \left(\frac{-\sin \Delta\Omega}{\sin i_0 \cot i - \cos \Delta\Omega \cos i_0} \right) \tag{B.10}$$

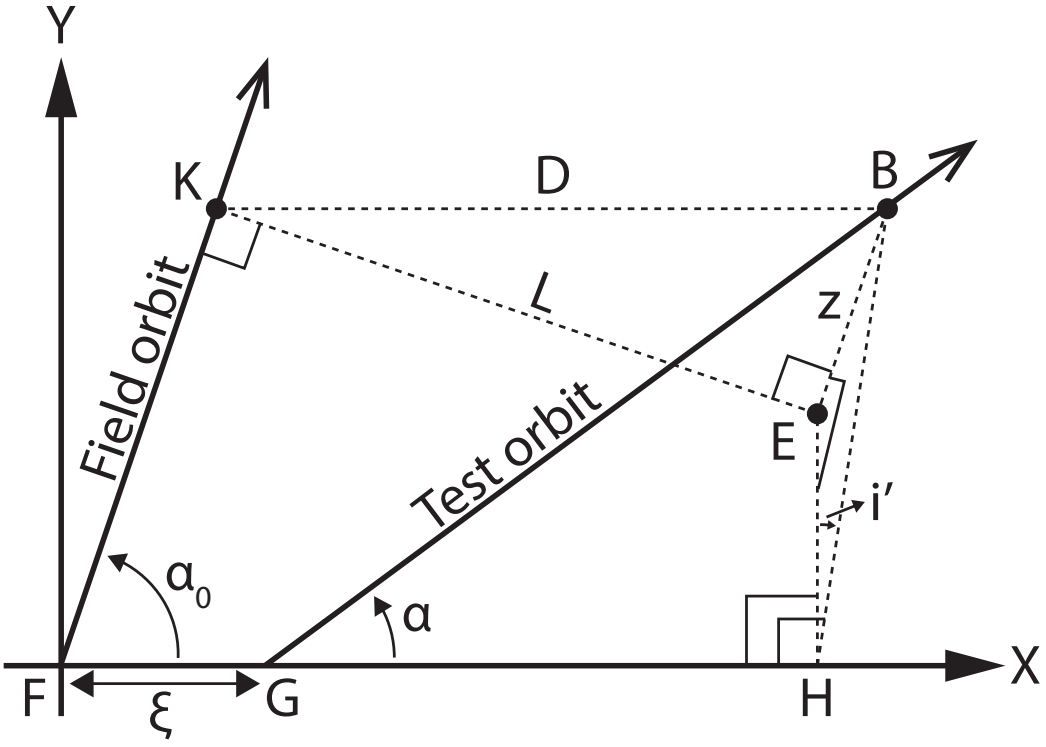

FIGURE B.2: Greenberg coordinate system. Test orbit comes out of page. Angles BEH and GHB are right angles. Negative X points towards the primary body, namely the Earth in the space debris case.

Figure B.2 presents the geometry of the problem near the mutual node and under the assumption that it is close enough that the orbits can be assumed to be straight lines. The coordinate system has its origin where the field orbit crosses the line of mutual nodes. the X axis is out along line of nodes, so the negative X direction points towards the primary body. The XY plane is the plane of the field orbit, so the test orbit comes out of the page in the Z axis, with point B on the test orbit being a distance z above the point E which resides on the XY plane. α & α_0 are the angle the orbits make with the X axis.

Treating α as flight path angle (the angle from the local horizontal), then

$$\tan\alpha = \frac{e\sin(u-\omega)}{1+e\cos(u-\omega)} \tag{B.11}$$

and using the Pythagorean identity gives,

$$\tan\alpha = \frac{e\sqrt{(1-\cos^2(u-\omega))}}{1+e\cos(u-\omega)} \tag{B.12}$$

Where the correction to Greenberg's derivation is highlighted. $\cot\alpha$ is given in the original derivation rather than the $\tan\alpha$ above. To aid in comparison with the Greenberg derivation, $\cot\alpha$ will used be used in this derivation, so that,

$$\cot\alpha = \frac{1+e\cos(u-\omega)}{e\sqrt{(1-\cos^2(u-\omega))}} \tag{B.13}$$

Equation B.13 also has a similar equation for α_0 as a function of e_0, u_0, ω_0, namely

$$\cot\alpha_0 = \frac{1+e_0\cos(u_0-\omega_0)}{e_0\sqrt{(1-\cos^2(u_0-\omega_0))}} \tag{B.14}$$

r and r_0 are set as the radial distance of an orbiting object from the primary body at a given true anomaly for the test and field body respectively. Then with the difference in distance as $\xi = r - r_0$, where $r = \frac{a(1-e^2)}{1+e\cos\theta}$ and $\theta = u - \omega$ (with similar for r_0), then

$$\xi = \frac{a(1-e^2)}{1+e\cos(u-\omega)} - \frac{a_0(1-e_0^2)}{1+e_0\cos(u_0-\omega_0)} \tag{B.15}$$

The next major target for derivation is the value D for which this distance between the field and test orbit reaches a minimum, named D_{min}. This begins with the simple Pythagorean theorem of

$$D = \sqrt{(L^2+Z^2)} \tag{B.16}$$

where L is the labeled distance in the XY plane of Figure B.2 and Z is the distance out of the page along the Z axis.

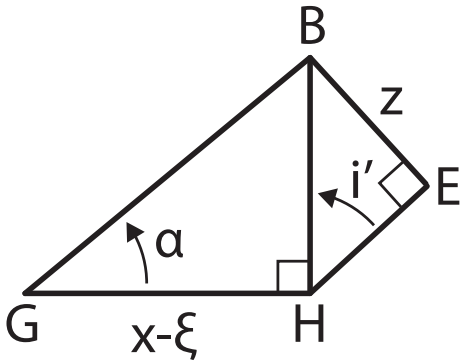

FIGURE B.3: Select triangles adapted from Figure B.2 used in the calculation of z for Equation B.17.

Some additional relations which will be useful in the derivation can be found by simple trigonometry within Figure B.2. To aid in the derivation, a few specific triangles have been redrawn in Figure B.3, giving rise to the right-angled triangle relations $\sin i' = \frac{Z}{[BH]}$, $\tan \alpha = \frac{[BH]}{(x-\xi)}$. These can be rearranged to give

$$Z = (X - \xi) \tan \alpha \sin i' \tag{B.17}$$

Different relations can be obtained from the BEH triangle in Figure B.3. The right-angled triangle relations give $\sin i' = \frac{Z}{[BH]}$, $\cos i' = \frac{[EH]}{[BH]}$, $\tan i' = \frac{\sin i'}{\cos i'} = \frac{Z}{[BH]} \frac{[BH]}{[EH]}$, then $[EH] = Z \cot i'$.

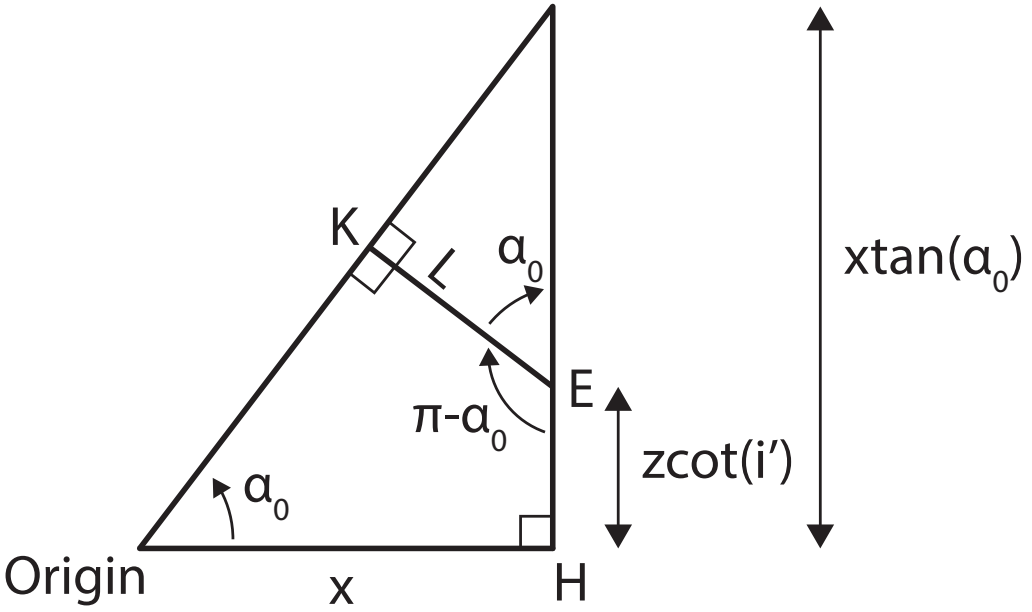

FIGURE B.4: Select triangles adapted from Figure B.2 used in the calculation of L for Equation B.29.

Figure B.4 contains a different set of triangles from Figure B.2. From the top triangle,

$$\cos\alpha_0 = \frac{L}{X\frac{\sin\alpha_0}{\cos\alpha_0} - Z\cot i'} \tag{B.18}$$

Which rearranging gives

$$L = (X - Z\cot i'\cot\alpha_0)\sin\alpha_0 \tag{B.19}$$

Coefficient substitutions of $ts \equiv \tan\alpha\sin i'$, $ts^2 \equiv (ts)^2$, and $tcc \equiv \tan\alpha\cot\alpha_0\cos i'$ are made into equations B.19 and B.17. This gives

$$Z = (X - \xi)ts \tag{B.20}$$

and

$$L = (X - (X - \xi)\tan\alpha\sin i'\cot\alpha\cot i')\sin\alpha_0 = (X - (X - \xi)tcc)\sin\alpha_0 \tag{B.21}$$

Equations B.20 and B.21 are substituted into Equation B.16 to give

$$D = \sqrt{(X - Xtcc + \xi tcc)^2\sin^2\alpha_0 + (X - \xi)^2 ts^2} \tag{B.22}$$

With the aim of finding D_{min}, this is differentiated with respect to X so

$$\frac{dD}{dX} = \frac{tcc^2\sin^2\alpha_0(X - \xi) + tcc\sin^2\alpha_0(\xi - 2X) - \xi ts^2 + X(\sin^2\alpha_0 + ts^2)}{\sqrt{\sin^2\alpha_0(X - tcc(X - \xi))^2 + ts^2(X - \xi)^2}} \tag{B.23}$$

And setting $\frac{dD}{dX} = 0$ so

$$\frac{dD}{dX} = 0 = tcc^2\sin^2\alpha_0(X - \xi) + tcc\sin^2\alpha_0(\xi - 2X) - \xi ts^2 + X(\sin^2\alpha_0 + ts^2) \tag{B.24}$$

Rearranging leads to

$$\xi ts^2 + tcc^2\sin^2\alpha_0\xi - tcc\sin^2\alpha_0\xi = (tcc^2\sin^2\alpha_0 - 2tcc\sin^2\alpha_0 + \sin^2\alpha_0 + ts^2)X \tag{B.25}$$

then

$$X = \frac{\xi ts^2 + tcc^2\sin^2\alpha_0\xi - tcc\sin^2\alpha_0\xi}{(tcc^2\sin^2\alpha_0 - 2tcc\sin^2\alpha_0 + \sin^2\alpha_0 + ts^2)} \tag{B.26}$$

Pulling ξ out of the brackets gives

$$X = \xi\frac{ts^2 + tcc^2\sin^2\alpha_0 - tcc\sin^2\alpha_0}{(tcc^2\sin^2\alpha_0 - 2tcc\sin^2\alpha_0 + \sin^2\alpha_0 + ts^2)} \tag{B.27}$$

Then noting

$$\begin{aligned}(1-tcc)^2\sin^2\alpha_0 + ts^2 &= (1-2tcc+tcc^2)\sin^2\alpha_0 + ts^2 \\ &= tcc^2\sin^2\alpha_0 - 2tcc\sin^2\alpha_0 + \sin^2\alpha_0 + ts^2\end{aligned} \tag{B.28}$$

results in

$$X = \xi\frac{ts^2 - tcc(1-tcc)\sin^2\alpha_0}{(1-tcc)^2\sin^2\alpha_0 + ts^2} \tag{B.29}$$

Where this X is the value of X (position on the test orbit) which minimizes D

Then

$$Z = \left(\xi\frac{ts^2 - tcc(1-tcc)\sin^2\alpha_0}{(1-tcc)^2\sin^2\alpha_0 + ts^2} - \xi\right)ts \tag{B.30}$$

$$Z = ts\left(\frac{\xi ts^2 - \xi tcc(1-tcc)\sin^2\alpha_0 - \xi(1-tcc)^2\sin^2\alpha_0 - \xi ts^2}{(1-tcc)^2\sin^2\alpha_0 + ts^2}\right) \tag{B.31}$$

$$Z = ts\left(\frac{-\xi tcc(1-tcc)\sin^2\alpha_0 - \xi(1-tcc)^2\sin^2\alpha_0}{(1-tcc)^2\sin^2\alpha_0 + ts^2}\right) \tag{B.32}$$

using $[tcc(1-tcc) + (1-tcc)^2] = tcc - tcc^2 + 1 - 2tcc - tcc^2 = (1-tcc)$, this is simplified down to

$$Z = \xi\frac{(tcc-1)\sin^2\alpha_0 ts}{[(1-tcc)^2\sin^2\alpha_0 + ts^2]} \tag{B.33}$$

Where the highlighted ξ doesn't appear in this equation in the original derivation of Greenberg (1982), but is included in later equations.

Putting X from Equation B.29 and Z from Equation B.33 into Equation B.19 gives

$$L = \left(\xi\frac{ts^2 - tcc(1-tcc)\sin^2\alpha_0}{(1-tcc)^2\sin^2\alpha_0 + ts^2} - \xi\frac{(tcc-1)\sin^2\alpha_0 ts}{[(1-tcc)^2\sin^2\alpha_0 + ts^2]}\cot\alpha_0\cot i'\right)\sin\alpha_0 \tag{B.34}$$

Focusing on rearranging the numerator of this equation (designated "top" here),

$$\begin{aligned}top &= ts^2 - tcc(1-tcc)\sin^2\alpha_0 - (tcc-1)\sin^2\alpha_0 ts\cot\alpha_0\cot i' \\ &= ts^2 - \tan\alpha\cot\alpha_0\cos i'\sin^2\alpha_0 + \tan^2\alpha\cot^2\alpha_0\cos^2 i'\sin^2\alpha_0 \\ &\quad - \tan\alpha\cot\alpha_0\cos i'\sin^2\alpha_0\tan\alpha\sin i'\cot\alpha_0\cot i' \\ &\quad + \sin^2\alpha_0\tan\alpha\sin i'\cot\alpha_0\cot i'\end{aligned} \tag{B.35}$$

which rearranging the 2nd and 4th term of the right hand side becomes,

$$\begin{aligned} top = ts^2 &- \sin^2\alpha_0 \tan\alpha \sin i' \cot\alpha_0 \cot i' + \tan^2\alpha \cot^2\alpha_0 \cos^2 i' \sin^2\alpha_0 \\ &- \tan^2\alpha \cot^2\alpha_0 \cos^2 i' \sin^2\alpha_0 \\ &+ \sin^2\alpha_0 \tan\alpha \sin i' \cot\alpha_0 \cot i' \end{aligned} \tag{B.36}$$

The 2nd and 5th terms cancel along with the 3rd and 4th, leaving the numerator equal to just ts. Therefore

$$L = \xi \frac{ts^2 \sin\alpha_0}{(1 - tcc)^2 \sin^2\alpha_0 + ts^2} \tag{B.37}$$

Where again, the highlighted ξ doesn't appear in this equation in the original derivation of Greenberg (1982), but is included in later equations.

Then from Equations B.16, B.37 & B.33, an equation for D_{min} can be created.

$$\begin{aligned} D_{min}^2 &= \left(\frac{\xi ts^2 \sin\alpha_0}{[(1 - tcc)^2 \sin^2\alpha_0 + ts^2]}\right)^2 + \left(\frac{\xi(tcc - 1)\sin^2\alpha_0 ts}{[(1 - tcc)^2 \sin^2\alpha_0 + ts^2]}\right)^2 \\ &= \frac{\xi^2 ts^2 \sin^2\alpha_0 (ts^2 + (tcc - 1)^2 \sin^2\alpha_0)}{[(1 - tcc)^2 \sin^2\alpha_0 + ts^2]^2} \end{aligned} \tag{B.38}$$

which simplifies down to

$$D_{min}^2 = \frac{\xi^2 ts^2 \sin^2\alpha_0}{[(1 - tcc)^2 \sin^2\alpha_0 + ts^2]} \tag{B.39}$$

where D_{min} is the minimum distance between 2 orbits of given u, ω, e, u_0, ω_0, e_0 and i'. Want to replace the ts, tcc & ts^2 substitutions with the original terms, so

$$\begin{aligned} D_{min}^2 &= \frac{\xi^2 \tan^2\alpha \sin^2 i' \sin^2\alpha_0}{(1 - \tan\alpha \cot\alpha_0 \cos i')^2 \sin^2\alpha_0 + \tan^2\alpha \sin^2 i'} \\ &= \frac{\xi^2 \tan^2\alpha \sin^2 i' \sin^2\alpha_0}{\sin^2\alpha_0 - 2\tan\alpha \cot\alpha_0 \cos i' \sin^2\alpha_0 + \tan^2\alpha \cot^2\alpha_0 \cos^2 i' \sin^2\alpha_0 + \tan^2\alpha \sin^2 i'} \\ &= \frac{\xi^2 \tan^2\alpha \sin^2 i' \sin^2\alpha_0}{\sin^2\alpha_0 - 2\tan\alpha \cot\alpha_0 \cos i' \sin^2\alpha_0 + \tan^2\alpha \cos^2\alpha_0 \cos^2 i' + \tan^2\alpha \sin^2 i'} \\ &= \frac{\xi^2 \sin^2 i'}{\cot^2\alpha - 2\cot\alpha \cot\alpha_0 \cos i' + \cot^2\alpha_0 \cos^2 i' + \frac{\sin^2 i'}{\sin^2\alpha_0}} \end{aligned} \tag{B.40}$$

then with the identities $\frac{1}{\sin^2\alpha_0} = 1 + \cot^2\alpha_0$ and
$\sin^2 i'(1 + \cot^2\alpha_0) = \sin^2 i' + \cot^2\alpha_0 \sin^2 i'$, this becomes

$$\begin{aligned} D_{min}^2 &= \frac{\xi^2 \sin^2 i'}{\cot^2 \alpha + \cot^2 \alpha_0 (\cos^2 i' + \sin^2 i') - 2 \cot \alpha \cot \alpha_0 \cos i' + \sin^2 i'} \\ &= \frac{\xi^2 \sin^2 i'}{\cot^2 \alpha + \cot^2 \alpha_0 - 2 \cot \alpha \cot \alpha_0 \cos i' + \sin^2 i'} \end{aligned} \tag{B.41}$$

So

$$D_{min} = \left| \frac{\xi \sin i'}{A} \right| \tag{B.42}$$

where $A \equiv (\cot^2 \alpha + \cot^2 \alpha_0 + \sin^2 i' - 2 \cot \alpha_0 \cot \alpha \cos i')^{\frac{1}{2}}$.

The symmetry of A highlights the fact the choice of field or test orbit does not initially matter, except for denotation purposes. A collision is possible if D_{min} is less than the combined radii of the two objects $\tau = R_0 + R$, where R_0 and R are the radii of the field and test object respectively.

In the 4-dimensional (ω, ω_0, Ω, Ω_0) space, there is some surface where $D_{min} = 0$, i.e. the orbits exactly interact. There is a finite layer both sides of this surface where $D_{min} < \tau$. The probability of a collision being possible is the volume of the finite layer divided by $(2\pi)^4$ (which is the volume of the entire 4D space).

At $D_{min} = 0$, $\xi = 0$, therefore $r = r_0$, and by Equation B.15,

$$\frac{a(1-e^2)}{1 + e\cos(u - \omega)} = \frac{a_0(1-e_0^2)}{1 + e_0 \cos(u_0 - \omega_0)} \tag{B.43}$$

$$\frac{a(1-e^2)}{a_0(1-e_0^2)} = \frac{1 + e\cos(u - \omega)}{1 + e_0 \cos(u_0 - \omega_0)} \tag{B.44}$$

with these two equations defining the $D_{min} = 0$ surface. For a given ($\Delta\Omega$, ω_0), the value of ω can be found using Equations B.1, B.10, and B.44 to find the value of u_0, u, and ω respectively. The 4D space can therefore be reduced to just 3 dimensions, namely (ω, ω_0, $\Delta\Omega$).

There is a 180° ambiguity in u & u_0 for any given $\Delta\Omega$ (this arises due to there being 2 nodes, either side of each orbit). There is also an ambiguity in ω from the arccos in Equation B.44. This means there are up to 4 possible values of ω for a given ($\Delta\Omega$, ω_0). Depending upon a & e, the arccos in Equation B.44 may give 2 or no solutions.

For a fixed field orbit, ω can be adjusted until the radial distances at a mutual node are equal. Depending upon a & e, the "radial range" of the test orbit will permit intersection at neither, one, or both nodes. Then since Kelperian orbits have 2 points at a given r, there are 0, 2, or 4 values of ω which permit intersection.

The ($\Delta\Omega$, ω_0, ω) space can be simplified further to ($\Delta\Omega$, C_0, C) where

$$\begin{aligned} C &\equiv \cos(u - \omega) \\ C_0 &\equiv \cos(u_0 - \omega_0) \end{aligned} \tag{B.45}$$

where u_0 is limited to between 0 and π radians, and u takes values from Equations B.1 and B.3. The restriction of u_0 to a single node yields a probability of a close approach within a distance of τ which is equal to half of the complete probability (due to there being 2 mutual nodes). With Equation B.45, Equation B.44 becomes

$$\frac{a(1-e^2)}{a_0(1-e_0^2)} = \frac{1+eC}{1+e_0C_0} \tag{B.46}$$

which rearranges to

$$1 + eC = (1 + e_0C_0)\frac{a(1-e^2)}{a_0(1-e_0^2)} \tag{B.47}$$

and isolating C gives

$$C = \left((1 + e_0C_0)\frac{a(1-e^2)}{a_0(1-e_0^2)} - 1 \right) \Big/ e \tag{B.48}$$

Where the highlighted $+$ is a correction to the stated $-$ in the Greenberg derivation. This equation is linear in C & C_0, and independent of $\Delta\Omega$. So on any plane of constant $\Delta\Omega$ in the ($\Delta\Omega$, C_0, C) space, the $D_{min} = 0$ locus is a straight line, as shown in Figure B.5.

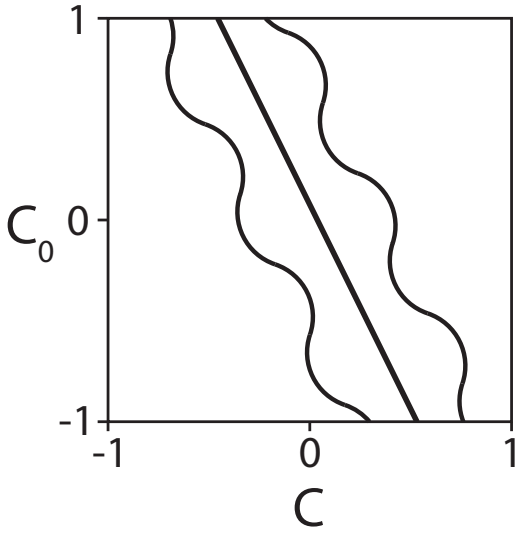

FIGURE B.5: Region enclosed by $D_{min} < \tau$ within ($\Delta\Omega$, C_0, C) space. Straight line is $D_{min} = 0$ while curved lines are $D_{min} = \tau$.

Figure B.5 also shows that there is some region around $D_{min} = 0$ in which $D_{min} < \tau$. The line defining this region is $D_{min} = \tau$. Differentiating with respect to C gives

$$\frac{\delta D_{min}}{\delta C} = \frac{\delta \tau}{\delta C} \tag{B.49}$$

which to first order in τ gives

$$\left.\frac{\delta D_{min}}{\delta C}\right|_{D_{min}=0} = \frac{\tau}{\Delta C} \tag{B.50}$$

where $\Delta\tau$ was set to τ when choosing $D_{min} = 0$. The half-width parallel to the C axis in Figure B.5 is given by

$$\Delta C = \tau \Big/ \left(\frac{\delta D_{min}}{\delta C}\right)\Big|_{D_{min}=0} \tag{B.51}$$

Substituting Equations B.15 and B.45 into Equation B.42 gives

$$D_{min} = \left(\frac{a(1-e^2)}{1+eC} - \frac{a_0(1-e_0^2)}{1+e_0c_0}\right) \sin i' \Big/ A \tag{B.52}$$

And differentiating with respect to C gives

$$\left.\frac{\delta D_{min}}{\delta C}\right|_{D_{min}=0} = -\frac{a(1-e^2)e}{(1+eC)^2} \sin i' \Big/ A \tag{B.53}$$

where an extra term from differentiating A tends to 0 at $D_{min} = 0$, so can be neglected.

Equations B.13, B.14 and B.48 are used to remove C from B.53, then B.53 can be substituted into B.51.

$$\Delta C = \tau f(C_0, \Delta\Omega) \tag{B.54}$$

where

$$f(C_0, \Delta\Omega) = 1 \Big/ \left(\left.\frac{\delta D_{min}}{\delta C}\right|_{D_{min}=0}\right) \tag{B.55}$$

where the $\Delta\Omega$ dependence arises from i' in Equation B.4. The area on a constant $\Delta\Omega$ plane in which $D_{min} < \tau$ (as in Figure B.5 is given by

$$A_{(C,C_0)} = \int_{C_{0max}}^{C_{0min}} 2\tau f dC_0 \tag{B.56}$$

where the factor of 2 accounts for both sides of the $D_{min} = 0$ line. The area on the $(u - \omega, u_0 - \omega_0)$ plane is what is required, so

$$\begin{aligned} A_{(u-\omega,u_0-\omega_0)} &= \int 2\Delta(u-\omega)d(u_0-\omega_0) \\ &= \int 2(\frac{d(u-\omega)}{dC}\Delta C)d(u_0-\omega_0) \\ &= 2\int_{\omega_0}[\tau f/\sin(u-\omega)]d\omega_0 \end{aligned} \tag{B.57}$$

with the integral over the range $\omega_0 = u_0 - \arccos(C_{0_{min}}))$ to $u_0 - \arccos(C_{0_{max}}$ where arccos takes the principle value and so $0 \leq \omega_0 \leq \pi$.

Equation B.57 also sees the first correction by Bottke and Greenberg (1993) to the Greenberg algorithm. Greenberg (1982) originally included an extra factor of 4 to account for the 4 sets of values $(u - \omega, u_0 - \omega_0)$ can take for a single set of $(\cos(u - \omega), \cos(u_0 - \omega_0))$ values. This was later carried on to an equation involving relative velocity. However, the relative velocity will not be the same at all 4 points in $(u - \omega, u_0 - \omega_0)$ space so Equation B.57 has to be evaluated at all 4 points and then summed over.

For space debris applications, τ can be taken outside of the bracket as gravitational interaction at close approach can be neglected. The derivation was originally done for asteroids where this isn't the case.

The volume in $(\omega, \omega_0, \Delta\Omega)$ space in which $D_{min} < \tau$ is given by

$$V_{(\omega,\omega_0,\Delta\Omega)} = 4\tau\int_0^{2\pi}\int_{\omega_0}[f/\sin(u-\omega)]d\omega_0 d(\Delta\Omega) \tag{B.58}$$

for each set of $(u - \omega, u_0 - \omega_0)$. The extra factor of 2 is to account for the other mutual node of the two orbits.

The probability of the two orbits passing within a collision cross section of one another is given by Equation B.58 divided by the total volume of the $(\omega, \omega_0, \Delta\Omega)$ space, $(2\pi)^3$.

So far the probability calculated is that of the 2 orbits passing close enough for a collision to be possible. Now focus switches to calculating the probability both bodies are near enough at the same time for a collision to occur.

Figure B.6 presents an alternate coordinate system for use in upcoming derivations. The Z axis links the two orbits along the D_{min} line, and is positive in the direction from test orbit to field orbit. The Y axis is parallel to the field body velocity $\bar{u_0}$ at the point of closest approach. The test particle velocity $\bar{u}$ lies in XY plane at an angle of θ to the X axis. When the test body is at the origin, the field body is at $Y = \eta$ at $t = 0$. The position of the two bodies at time t on each axis is given in Table B.1.

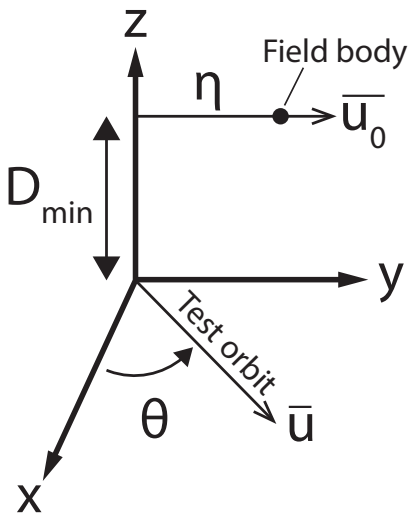

FIGURE B.6: Coordinate system defining orbits during close approach, where Z axis links the two orbits along the closest approach vector and y axis is parallel to the field body's velocity.

TABLE B.1: The position of test in field bodies in the X, Y, and Z axis at time t, using the coordinate system of Figure B.6

	Test	Field
X position	$tU\cos\theta$	0
Y position	$tU\sin\theta$	$\eta + U_0 t$
Z position	0	D_{min}

The separation, Δ, can be calculated by the Pythagorean theorem, such that.

$$\Delta^2 = (tU\cos\theta)^2 + (\eta + U_0 t - Ut\sin\theta)^2 + D_{min}^2 \tag{B.59}$$

which when differentiated with respect to time becomes

$$\frac{d(\Delta^2)}{dt} = 2t\left(U^2 cos^2\theta + (U_0 - Usin\theta)^2\right) + 2\eta(U_0 - Usin\theta) \tag{B.60}$$

Setting $\frac{d(\Delta^2)}{dt} = 0$, also setting t to the time of minimum separation t_{min}, and rearranging for t_{min} results in the time of minimum separation given by

$$t_{min} = \frac{\eta(Usin\theta - U_0)}{U^2 + U_0^2 - 2UU_0 sin\theta} \tag{B.61}$$

The relative velocity between the two bodies is given by $\bar{V}$, and the vector triangle with $\bar{U}$ and $\bar{U_0}$ is shown in Figure B.7. Noting the dot product of two vectors is given by

$$\bar{A}.\bar{B} = |\bar{A}||\bar{B}|cos\theta \tag{B.62}$$

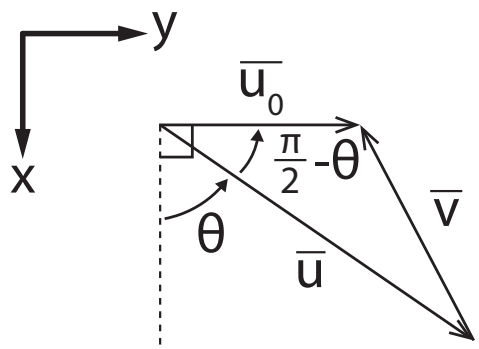

FIGURE B.7: Velocity vector triangle of the field and test orbits using the coordinate system of Figure B.6.

then $\bar{V}^2$ is equivalent to

$$\begin{aligned}\bar{V}^2 &= \bar{V} \cdot \bar{V} \\ &= (\bar{U} - \bar{U_0}) \cdot (\bar{U} - \bar{U_0}) \\ &= U^2 + U_0^2 - 2UU_0 cos\left(\frac{\pi}{2} - \theta\right) \\ &= U^2 + U_0^2 - 2UU_0 sin(\theta)\end{aligned} \tag{B.63}$$

This can be used to simplify Equation B.61 to

$$t_{min} = \eta(Usin\theta - U_0) \,/\, \bar{V}^2 \tag{B.64}$$

where dividing by $\bar{V}^2$ is a correction over multiplying by $\bar{V}^2$ in the original working by Greenberg (1982).

Squaring t_{min}, substituting it into Equation B.59 gives

$$\Delta^2 = t_{min}^2 \bar{V}^2 + 2t_{min}\eta(U_0 - Usin\theta) + \eta^2 + D_{min}^2 \tag{B.65}$$

Dividing this by η^2, substituting into the square of Equation B.64 and rearranging to find the square of the minimum separation, Δ_{min}^2, gives

$$\Delta_{min}^2 = \frac{\eta^2 U^2 \left(cos^2\theta\right)}{\bar{V}^2} + D_{min}^2 \tag{B.66}$$

For a collision to occur, $\Delta_m in$ must be less than the combined radii of objects, τ, therefore

$$\frac{\eta^2 U^2 cos^2\theta}{\bar{V}^2} + D_{min}^2 < \tau^2 \tag{B.67}$$

Rearranging for η gives

$$\eta < \left(\tau^2 - D_{min}^2\right)^{1/2} \left|\frac{V}{Ucos\theta}\right| \tag{B.68}$$

For any given D_{min}, the probability of collision is proportional to the right hand side of Equation B.68. Noting that

$$\frac{1}{\tau}\left(\tau^2 - D_{min}^2\right)^{1/2} = \left(\frac{\tau^2}{\tau^2} - \frac{D_{min}^2}{\tau^2}\right)^{1/2} = \left(1 - \left(\frac{D_{min}}{\tau}\right)^2\right)^{1/2} \tag{B.69}$$

and

$$\int_0^a \sqrt{1 - \left(\frac{x}{a}\right)^2}\, dx = \frac{\pi a}{4} \tag{B.70}$$

then

$$\frac{1}{\tau}\int_0^\tau \left[1 - \left(\frac{D_{min}}{\tau}\right)^2\right]^{\frac{1}{2}} dD_{min} = \frac{\pi}{4} \tag{B.71}$$

where this multiplied by the probability of $D_{min} = 0$ gives the average probability of collision over all values of $D_{min} < \tau$.

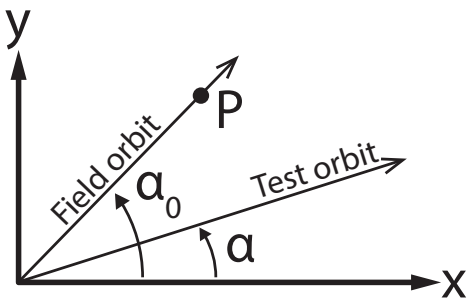

FIGURE B.8: Coordinate system with field and test orbit for a $D_{min} = 0$ close approach.

Now focus switches to finding the collision probability for $D_{min} = 0$. Figure B.8 shows the field body at time $t = 0$ is at P with the coordinates ($\eta cos\alpha_0$, $\eta sin\alpha_0$, 0) while the test body is at the origin. At the later time t, the field body is at ($\eta cos\alpha_0 + U_{0x}t$, $\eta sin\alpha_0 + U_{0y}t$, $U_{0z}t$) while the test body is at ($U_x t$, $U_y t$, $U_z t$). The square of the separation, Δ, at time t is found through the Pythagoras theorem, giving

$$\begin{aligned}\Delta^2 = &\left[\eta cos\alpha_0 + U_{0x}t - U_x t\right]^2 + \\ &\left[\eta sin\alpha_0 + U_{0y}t - U_y t\right]^2 + \\ &\left[U_{0z}t - U_z t\right]^2\end{aligned} \tag{B.72}$$

As before, from Figure B.7, $\bar{V} = \bar{U} - \bar{U_0}$, so $V_x = U_x - U_{0x}$ and similar for the y and z axes. Therefore Equation B.72 can be simplified to

$$\Delta^2 = \left[\eta cos\alpha_0 - V_x t\right]^2 + \left[\eta sin\alpha_0 - V_y t\right]^2 + \left[V_z t\right]^2 \tag{B.73}$$

Again, the time t_{min} at which Δ^2 is a minimum is required. Therefore differentiating with respect to t gives

$$\frac{d(\Delta^2)}{dt} = -2\eta V_x cos\alpha_0 - 2\eta V_y sin\alpha_0 + 2t(V_x^2 + V_y^2 + V_z^2) \tag{B.74}$$

Setting $\frac{d(\Delta^2)}{dt} = 0$ and rearranging for $t = t_{min}$ gives

$$t_{min} = \frac{\eta(V_x cos\alpha_0 + V_y sin\alpha_0)}{V^2} \tag{B.75}$$

Substituting this back into Equation B.73 and rearranging for $\frac{\Delta_{min}^2}{\eta^2}$ gives

$$\frac{\Delta_{min}^2}{\eta^2} = 1 - \left(\frac{(V_x cos\alpha_0 + V_y sin\alpha_0)^2}{V^2}\right) \tag{B.76}$$

Collisions can occur if the minimum separation D_{min} is less than the combined radii of objects, τ. So

$$\tau > \Delta_{min} = \eta\sqrt{\frac{V^2 - \left(V_x cos\alpha_0 + V_y sin\alpha_0\right)^2}{V^2}} \tag{B.77}$$

which rearranged gives

$$|\eta| < \eta_0 \equiv \tau V / \left(V^2 - \left(V_x cos\alpha_0 + V_y sin\alpha_0\right)^2\right)^{1/2} \tag{B.78}$$

The probability of collision, P_0, given $D_{min} = 0$, is the time during each orbit of the field object during which $|\eta| < \eta_0$, divided by the orbital period of the field object, T_0, which can be represented by

$$P_0 = \frac{2\eta_0}{U_0 T_0} \tag{B.79}$$

where a factor of 2 is included to account for the two points in an orbit at which a collision could occur.

The specific energy, ϵ, of an orbit is given by

$$\epsilon = \frac{V^2}{2} - \frac{\mu}{r} = -\frac{\mu}{2a} \tag{B.80}$$

Rearranging and using values for the field orbit gives

$$U_0^2 = 2\mu\left(\frac{1}{r_0} - \frac{1}{2a_0}\right) \tag{B.81}$$

Then r_0 can be obtained from the equation for orbital distance, namely

$$r_0 = \frac{a_0(1-e_0^2)}{1+e_0 cos(u_0-\omega_0)} \tag{B.82}$$

Substituting Equation B.82 into B.81 and simplifying gives

$$U_0^2 = \frac{\mu\left(1+e_0^2+2e_0 cos(u_0-\omega_0)\right)}{a_0(1-e_0^2)} \tag{B.83}$$

Then the last value for Equation B.79, namely T_0, can be obtained from Kepler's third law.

$$T_0 = 2\pi a_0^{3/2}/\sqrt{\mu} \tag{B.84}$$

Equation B.71 gives the collision probability for all values of $D_{min} < \tau$ as $\pi P_0/4$. The chance for a collision with such a probability occurs each time the test particle arrives at the point of closest approach to the field orbit, i.e. once in each test orbit period, T. Therefore the mean collision frequency is given by

$$\text{frequency}_{D_{min}<\tau} = \frac{\pi P_0}{4T} \tag{B.85}$$

but this only applies to orbits with geometries which allow $D_{min} < \tau$, so only in the volume of (ω, ω_0, $\Delta\Omega$) space which is given by Equation B.58. The overall collision frequency needs to account for the fraction of time the orbits do not pass within τ of each other, which is done by averaging over the (ω, ω_0, $\Delta\Omega$) space by dividing by $(2\pi)^3$. Doing this, and including Equation B.85 in Equation B.58 results in

$$\text{frequency} = \frac{16\tau}{(2\pi)^3}\int_0^{2\pi}\int_{\omega_0}[f/\sin(u-\omega)]\left(\frac{\pi P_0}{4T}\right)d\omega_0 d(\Delta\Omega) \tag{B.86}$$

The integration over $\Delta\Omega$ can be reduced to 0 to π by noting the problem is symmetric and therefore multiplying by 2.

The collision frequency of Equation B.86 is in fact proportional to τ^2 and therefore the collision cross-sectional area. One factor of τ is included in the P_0 of Equation B.79 through the factor of η_0 in Equation B.78. Dividing Equation B.86 by τ^2 results in the "intrinsic collision probability", P_i, named as this probability is intrinsic to the two orbits involved, but independent of the size of the objects in these orbits.

Finally, a division by zero error occurs in cases where the $D_{min} = 0$ line on the (C, C_0) plane (shown in Figure B.5) reaches $C = \pm 1$, as the denominator $sin(u-\omega)$ in Equations B.58 and B.86 will equal zero. If the $D_{min} = 0$ reaches both values of $+1$ and -1 for C, then swapping the field and test bodies avoids this problem. However, if it

only C reaches one of $+1$ or -1, calculations need to be performed along half of the D_{min} line, and then the test and field bodies switched for calculations on the other half of the D_{min} line.

References

K. A. Akins, L. M. Healy, S. L. Coffey, and J. M. Picone. Comparison of MSIS and Jacchia atmospheric density models for orbit determination and propagation. *Advances in the Astronautical Sciences*, 114:945–965, 2003.

R. A. Akmaev. Thermospheric resistance to "greenhouse cooling": Effect of the collisional excitation rate by atomic oxygen on the thermal response to CO2 forcing. *Journal of Geophysical Research: Space Physics*, 108(A7):1–13, 2003. URL https://doi.org/10.1029/2003JA009896.

R. A. Akmaev. Whole atmosphere modeling: Connecting terrestrial and space weather. *Review of Geophysics*, 2011. URL https://doi.org/10.1029/2011RG000364.

R. A. Akmaev and V. I. Fomichev. Cooling of the mesosphere and lower thermosphere due to doubling of CO_2. *Annales Geophysicae*, 16:1501–1512, 1998. URL https://doi.org/10.1007/s00585-998-1501-z.

R. A. Akmaev, V. I. Fomichev, and X. Zhu. Impact of middle-atmospheric composition changes on greenhouse cooling in the upper atmosphere. *Journal of Atmospheric and Solar-Terrestrial Physics*, 68(17):1879–1889, 2006. ISSN 13646826. .

M. Amos, P. J. Young, J. S. Hosking, J.-F. Lamarque, N. L. Abraham, H. Akiyoshi, A. T. Archibald, et al. Projecting ozone hole recovery using an ensemble of chemistry–climate models weighted by model performance and independence. *Atmospheric Chemistry and Physics*, 20(16):9961–9977, 2020. URL https://doi.org/10.5194/acp-20-9961-2020.

P. D. Anz-Meador. Monthly number of cataloged objects in Earth orbit by object type as of 5 January 2021. *Orbital debris quarterly news, Volume 25, Issue 1*, 2021.

P. D. Anz-Meador, J. Opiela, D. Shoots, and J.-C. Liou. History of on-orbit satellite fragmentations 15th edition. *National Aeronautics and Space Administration Johnson Space Center Orbital Debris Program Office*, 2018.

J. Aubert. Geomagnetic forecasts driven by thermal wind dynamics in the Earth's core. *Geophysical Journal International*, 203:1738–1751, 2015. URL https://doi.org/10.1093/gji/ggv394.

E. Ausay, A. Cornejo, A. Horn, K. Palma, T. Sato, B. Blake, F. Pistella, C. Boyle, et al. A comparison of the SOCIT and DebriSat experiments. In *Proceedings of the 7th European Conference on Space Debris*, 2017.

F. Barlier, C. Berger, J. L. Falin, G. Kockarts, and G. Thuillier. A thermospheric model based on satellite drag data. *Annales Geophysicae*, 1978. URL https://ui.adsabs.harvard.edu/abs/1978AnG....34....9B.

J. Bartels and J. Veldkamp. International data on magnetic disturbances, first quarter, 1949. *Journal of Geophysical Research*, 54(3):295–299, 1949. URL https://doi.org/10.1029/JZ054i003p00295.

J. Bartels, N. H. Heck, and H. F. Johnston. The three-hour-range index measuring geomagnetic activity. *Terrestrial Magnetism and Atmospheric Electricity*, 44(4):411–454, 1939. URL https://doi.org/10.1029/TE044i004p00411.

C. Berger, R. Biancale, M. Ill, and F. Barlier. Improvement of the empirical thermospheric model DTM: DTM94–a comparative review of various temporal variations and prospects in space geodesy applications. *Journal of Geodesy*, 72(3): 161–178, 1998. URL https://doi.org/10.1007/s001900050158.

W. F. Bottke and R. Greenberg. Asteroidal collision probabilities. *Geophysical Research Letters*, 20(10):879–881, 1993. URL https://doi.org/10.1029/92GL02713.

B. R. Bowman, T. W. Kent, F. A. Marcos, and C. Valladares. The JB2006 empirical thermospheric density model. *Journal of Atmospheric and Solar-Terrestrial Physics*, 70 (5):774–793, 2007. URL https://doi.org/10.1016/j.jastp.2007.10.002.

B. R. Bowman, W. K. Tobiska, and F. A. Marcos. A new empirical thermospheric density model JB2008 using new solar indices. *AIAA/AAS Astrodynamics Specialist Conference and Exhibit*, 2008. URL https://doi.org/10.2514/6.2006-6166.

D. Brouwer. Solution of the problem of artificial satellite theory without drag. *The Astronomical Journal*, 64:378, 1959. URL https://doi.org/10.1086/107958.

M. K. Brown, H. G. Lewis, A. J. Kavanagh, and I. Cnossen. Future decreases in thermospheric neutral density in low Earth orbit due to carbon dioxide emissions. *Journal of Geophysical Research: Atmospheres*, 126(8):1–11, 2021. URL https://doi.org/10.1029/2021JD034589.

S. L. Bruinsma. The DTM-2013 thermosphere model. *Journal of Space Weather and Space Climate*, 5:A1, 2015. URL https://doi.org/10.1051/swsc/2015001.

S. L. Bruinsma and C. Boniface. The operational and research DTM-2020 thermosphere models. *Journal of Space Weather and Space Climate*, 11:47–1, 2021. URL https://doi.org/10.1051/swsc/2021032.

S. L. Bruinsma, G. Thuillier, and F. Barlier. The DTM-2000 empirical thermosphere model with new data assimilation and constraints at lower boundary: accuracy and properties. *Journal of atmospheric and solar-terrestrial physics*, 65(9):1053–1070, 2003. URL https://doi.org/10.1016/S1364-6826(03)00137-8.

S. L. Bruinsma, J. M. Forbes, R. S. Nerem, and X. Zhang. Thermosphere density response to the 20–21 November 2003 solar and geomagnetic storm from CHAMP and GRACE accelerometer data. *Journal of Geophysical Research: Space Physics*, 111 (A6), 2006. URL https://doi.org/10.1029/2005JA011284.

S. L. Bruinsma, N. Sánchez-Ortiz, E. Olmedo, and N. Guijarro. Evaluation of the DTM-2009 thermosphere model for benchmarking purposes. *Journal of Space Weather and Space Climate*, 2:A04, 2012. URL https://doi.org/10.1051/swsc/2012005.

CelesTrak. Celestrak website, 2021. URL https://celestrak.com/. Accessed 8th October, 2021.

I. Cnossen. *Modelling of long-term trends in the middle and upper atmosphere*. PhD thesis, University of Leicester, 2009. URL https://hdl.handle.net/2381/4533.

I. Cnossen. Climate change in the upper atmosphere. In G. Liu, editor, *Greenhouse Gases: Emission, Measurement, and Management*, pages 315–336. InTech, 2012. ISBN 978-953-51-0323-3. URL https://doi.org/10.5772/32565.

I. Cnossen. The importance of geomagnetic field changes versus rising CO_2 levels for long-term change in the upper atmosphere. *Journal of Space Weather and Space Climate*, 4, 2014. URL https://doi.org/10.1051/swsc/2014016.

I Cnossen. Analysis and attribution of climate change in the upper atmosphere from 1950 to 2015 simulated by WACCM-X. *Journal of Geophysical Research: Space Physics*, 125:e2020JA028623, 2020. URL https://doi.org/10.1029/2020JA028623.

I. Cnossen and A. Maute. Simulated trends in ionosphere-thermosphere climate due to predicted main magnetic field changes from 2015 to 2065. *Journal of Geophysical Research: Space Physics*, 125:e2019JA027738, 2020. URL https://doi.org/10.1029/2019JA027738.

I. Cnossen, M. J. Harris, N. F. Arnold, and E. Yiğit. Modelled effect of changes in the CO_2 concentration on the middle and upper atmosphere: Sensitivity to gravity wave parameterization. *Journal of Atmospheric and Solar-Terrestrial Physics*, 71(13): 1484–1496, 2009. URL https://doi.org/10.1016/j.jastp.2008.09.014.

G. E. Cook. Satellite drag coefficients. *Planetary and Space Science*, 13(10):929–946, 1965. URL https://doi.org/10.1016/0032-0633(65)90150-9.

G. Danabasoglu, J.-F. Lamarque, J. Bacmeister, D. A. Bailey, A. K. DuVivier, J. Edwards, et al. The Community Earth System Model version 2 (CESM2). *Journal of Advances in Modeling Earth Systems*, 12, 2020. URL https://doi.org/10.1029/2019MS001916.

R. E. Dickinson, E. C. Ridley, and R. G. Roble. A three-dimensional general circulation model of the thermosphere. *Journal of Geophysical Research*, 86(A3):1499–1512, 1981. URL https://doi.org/10.1029/JA086iA03p01499.

W. Dieminger, G. K. Hartmann, and R. Leitinger. Geomagnetic activity indices. In *The upper atmosphere*. Springer, 1996. URL https://doi.org/10.1007/978-3-642-78717-1_26.

J. C. Dolado-Perez, C. Pardini, and L. Anselmo. Review of uncertainty sources affecting the long-term predictions of space debris evolutionary models. *Acta Astronautica*, 113:51–65, 2015a. URL https://doi.org/10.1016/j.actaastro.2015.03.033.

J. C. Dolado-Perez, B. Revelin, and R. Di Costanzo. Sensitivity analysis of the long-term evolution of space debris population in LEO. *Journal of Space Safety Engineering*, 2(1):12–22, 2015b. URL https://doi.org/10.1016/S2468-8967(16)30035-0.

E. Doornbos. *Thermospheric density and wind determination from satellite dynamics*. Springer Science & Business Media, 2012. ISBN 978-3-642-25129-0. URL https://doi.org/10.1007/978-3-642-25129-0.

T. Dudok de Wit and S. Bruinsma. Determination of the most pertinent EUV proxy for use in thermosphere modeling. *Geophysical research letters*, 38(19), 2011. URL https://doi.org/10.1029/2011GL049028.

J. T. Emmert. Thermospheric mass density: A review. *Advances in Space Research*, 56(5): 773–824, 2015a. URL https://doi.org/10.1016/j.asr.2015.05.038.

J. T. Emmert. Altitude and solar activity dependence of 1967–2005 thermospheric density trends derived from orbital drag. *Journal of Geophysical Research: Space Physics*, 120:2940–2950, 2015b. URL https://doi.org/10.1002/2015JA021047.

J. T. Emmert and J. M. Picone. Climatology of globally averaged thermospheric mass density. *Journal of Geophysical Research: Space Physics*, 115(A9), 2010. URL https://doi.org/10.1029/2010JA015298.

J. T. Emmert and J. M. Picone. Statistical uncertainty of 1967-2005 thermospheric density trends derived from orbital drag. *Journal of Geophysical Research: Space Physics*, 116, 2011. URL https://doi.org/10.1029/2010JA016382.

J. T. Emmert, J. M. Picone, J. L. Lean, and S. H. Knowles. Global change in the thermosphere: Compelling evidence of a secular decrease in density. *Journal of Geophysical Research: Space Physics*, 109, 2004. URL https://doi.org/10.1029/2003JA010176.

J. T. Emmert, J. M. Picone, and R. R. Meier. Thermospheric global average density trends, 1967-2007, derived from orbits of 5000 near-Earth objects. *Geophysical Research Letters*, 35, 2008. URL https://doi.org/10.1029/2007GL032809.

J. T. Emmert, S. E. McDonald, D. P. Drob, R. R. Meier, J. L. Lean, and J. M. Picone. Attribution of interminima changes in the global thermosphere and ionosphere. *Journal of Geophysical Research: Space Physics*, 119:6657–6688, 2014. URL https://doi.org/10.1002/2013JA019484.

J. T. Emmert, D. P. Drob, J. M. Picone, D. E. Siskind, M. Jones Jr., M. G. Mlynczak, et al. NRLMSIS 2.0: A whole-atmosphere empirical model of temperature and neutral species densities. *Earth and Space Science*, 7:e2020EA001321, 2021. URL https://doi.org/10.1029/2020EA001321.

ESA. Space debris by the numbers. 2021. URL https://www.esa.int/Safety_Security/Space_Debris/Space_debris_by_the_numbers. Accessed 6th December, 2021.

ESA Space Debris Office. Annual Space Environment Report. 2020.

D. M. Etheridge, L. P. Steele, R. L. Langenfelds, R. J. Francey, J. M. Barnola, and V. I. Morgan. Historical CO_2 Records from the Law Dome DE08, DE08-2, and DSS Ice Cores (1006 A.D.-1978 A.D). *Carbon Dioxide Information Analysis Center (CDIAC); Oak Ridge National Laboratory (ORNL), Oak Ridge, TN (United States)*, 1998. URL https://doi.org/10.3334/CDIAC/ATG.011.

A. G. Feofilov, A. A. Kutepov, C. Y. She, A. K. Smith, W. D. Pesnell, and R. A. Goldberg. $CO_2(v_2)$-O quenching rate coefficient derived from coincidental SABER/TIMED and Fort Collins lidar observations of the mesosphere and lower thermosphere. *Atmospheric Chemistry and Physics*, 12:9013–9023, 2012. URL https://doi.org/10.5194/acp-12-9013-2012.

S. Flegel, J. Gelhaus, C. Wiedemann, P. Vorsmann, M. Oswald, S. Stabroth, H. Klinkrad, and H. Krag. The MASTER-2009 space debris environment model. In *Proceedings of the Fifth European Conference on Space Debris*, 2009.

P. Friedlingstein, M. O'sullivan, M. W. Jones, R. M. Andrew, J. Hauck, A. Olsen, G. P. Peters, W. Peters, J. Pongratz, S. Sitch, et al. Global carbon budget 2020. *Earth System Science Data*, 12:3269–3340, 2020. URL https://doi.org/10.5194/essd-12-3269-2020.

A. Fujiwara, P. Cerroni, D. R. Davis, E. Ryan, M. di Martino, K. Holsapple, and K. Housen. Experiments and scaling laws for catastrophic collisions. In R. P. Binzel, T. Gehrels, and M. S. Matthews, editors, *Asteroids II*, pages 240–265. University of Arizona Press, 1989. ISBN 9780816511235.

Z. Girazian and P. Withers. An empirical model of the extreme ultraviolet solar spectrum as a function of F10.7. *Journal of Geophysical Research: Space Physics*, 120: 6779–6794, 2015. URL https://doi.org/10.1002/2015JA021436.

Goddard Space Flight Center. OMNIweb. 2021. URL https://omniweb.gsfc.nasa.gov. Accessed 1st September, 2021.

R. Greenberg. Orbital interactions - A new geometrical formalism. *The Astronomical Journal*, 87(1):184–195, 1982.

D. H. Hathaway. The solar cycle. *Living Reviews in Solar Physics*, 12(4), 2015. URL https://doi.org/10.1007/lrsp-2015-4.

A. E. Hedin. A revised thermospheric model based on mass spectrometer and incoherent scatter data: MSIS-83. *Journal of Geophysical Research: Space Physics*, 88 (A12):10,170–10,188, 1983. URL https://doi.org/10.1029/JA088iA12p10170.

A. E. Hedin. MSIS-86 thermospheric model. *Journal of Geophysical Research: Space Physics*, 92(A5):4649–4662, 1987. URL https://doi.org/10.1029/JA092iA05p04649.

A. E. Hedin. Extension of the MSIS thermosphere model into the middle and lower atmosphere. *Journal of Geophysical Research: Space Physics*, 96(A2):1159–1172, 1991. URL https://doi.org/10.1029/90JA02125.

A. E. Hedin, C. A. Reber, G. P. Newton, N. W. Spencer, H. C. Brinton, H. G. Mayr, and W. E. Potter. A global thermospheric model based on mass spectrometer and incoherent scatter data MSIS, 2. Composition. *Journal of Geophysical Research*, 82(16): 2148–2156, 1977a. URL https://doi.org/10.1029/JA082i016p02148.

A. E. Hedin, J. E. Salah, J. V. Evans, C. A. Reber, G. P. Newton, N. W. Spencer, D. C. Kayser, D. Alcayde, P. Bauer, L. Cogger, and J. P. McClure. A global thermospheric model based on mass spectrometer and incoherent scatter data MSIS, 1. N_2 Density and Temperature. *Journal of Geophysical Research*, 82(16):2139–2147, 1977b. URL https://doi.org/10.1029/JA082i016p02139.

M. P. Hickey. The NASA Marshall Engineering Thermosphere Model. Technical Report NASA-CR-179359, NASA, 1988a.

M. P. Hickey. An improvement in the numerical integration procedure used in the NASA Marshall Engineering Thermosphere Model. Technical Report NASA-CR-179389, NASA, 1988b.

F. Hoots and R. Roehrich. Spacetrack Report No.3 - Models for propagation of NORAD element sets. 1988. URL https://celestrak.com/NORAD/documentation/spacetrk.pdf.

J. W. Hurrell, M. M. Holland, P. R. Gent, S. Ghan, J. E. Kay, Kushner P. J., et al. The Community Earth System Model: A framework for collaborative research. *Bulletin of the American Meteorological Society*, 94(9):1339–1360, 2013. URL https://doi.org/10.1175/BAMS-D-12-00121.1.

IPCC. *Climate Change 2014 Synthesis Report*. IPCC, 2014. ISBN 9789291691432. .

L. G. Jacchia. A variable atmospheric-density model from satellite accelerations. *Journal of Geophysical Research (1896-1977)*, 65(9):2775–2782, 1960. URL https://doi.org/10.1029/JZ065i009p02775.

L. G. Jacchia. Static diffusion models of the upper atmosphere with empirical temperature profiles. *Smithsonian Contributions to Astrophysics*, 8(9):215–257, 1965.

L. G. Jacchia. New static models of the thermosphere and exosphere with empirical temperature profiles. *Smithsonian Astrophysical Observatory Special Report No. 313*, 1970.

L. G. Jacchia. Revised static models of the thermosphere and exosphere with empirical temperature profiles. *Smithsonian Astrophysical Observatory Special Report No. 332*, 332, 1971.

L. G. Jacchia. Thermospheric temperature, density, and composition: New models. *Smithsonian Astrophysical Observatory Special Report No. 375*, 1977.

N. L. Johnson, P. H. Krisko, J.-C. Liou, and P. D. Anz-Meador. NASA's new breakup model of EVOLVE 4.0. *Advances in Space Research*, 28(9):1377–1384, 2001. URL https://doi.org/10.1016/S0273-1177(01)00423-9.

M. Kaufmann, O. A. Gusev, K. U. Grossmann, R. G. Roble, M. E. Hagan, C. Hartsough, and A. A. Kutepov. The vertical and horizontal distribution of CO_2 densities in the upper mesosphere and lower thermosphere as measured by CRISTA. *Journal of Geophysical Research: Atmospheres*, 107(D23), 2002. URL https://doi.org/10.1029/2001JD000704.

G. M. Keating, R. H. Tolson, and M. S. Bradford. Evidence of long term global decline in the Earth's thermospheric densities apparently related to anthropogenic effects. *Geophysical Research Letters*, 27(10):1523–1526, 2000. URL https://doi.org/10.1029/2000GL003771.

C. D. Keeling, S. C. Piper, R. B. Bacastow, M. Wahlen, T. P. Whorf, M. Heimann, and H. A. Meijer. *Atmospheric CO_2 and $^{13}CO_2$ Exchange with the Terrestrial Biosphere and Oceans from 1978 to 2000: Observations and Carbon Cycle Implications*, pages 83–113.

Springer New York, New York, NY, 2005. ISBN 978-0-387-27048-7. URL https://doi.org/10.1007/0-387-27048-5_5.

D. J. Kessler and B. G. Cour-Palais. Collision frequency of artificial satellites: The creation of a debris belt. *Journal of Geophysical Research*, 83(A6):2637–2646, 1978. URL https://doi.org/10.1029/JA083iA06p02637.

D. G. King-Hele. *Satellite Orbits in an Atmosphere: Theory and Applications*. Blackie, 1987. ISBN 978-0-216-92252-5.

H. Klinkrad. *Space Debris: Models and Risk Analysis*. Springer Science & Business Media, 2006. ISBN 978-3-540-25448-5. URL https://doi.org/10.1007/3-540-37674-7.

Y. Kozai. The motion of a close earth satellite. *The Astronomical Journal*, 64:367–377, 1959. URL https:doi.org/10.1086/108389.

P. Krisko. Proper implementation of the 1998 NASA breakup model. *Orbital debris quarterly news, Volume 15, Issue 4*, 2011.

J. Laštovička and Š. Jelínek. Problems in calculating long-term trends in the upper atmosphere. *Journal of Atmospheric and Solar-Terrestrial Physics*, 189:80–86, 2019. URL https://doi.org/10.1016/j.jastp.2019.04.011.

C. Le Quéré, R. M. Andrew, P. Friedlingstein, S. Sitch, J. Hauck, J. Pongratz, P. A. Pickers, J. I. Korsbakken, G. P. Peters, J. G. Canadell, et al. Global carbon budget 2018. *Earth System Science Data*, 10:2141–2194, 2018. URL https://doi.org/10.5194/essd-10-2141-2018.

H. G. Lewis, G. G. Swinerd, N. Williams, and G. Gittins. DAMAGE: A dedicated GEO debris model framework. In *Proceedings of the Third European Conference on Space Debris*, pages 373–378, 2001.

H. G. Lewis, G. G. Swinerd, C. S. Ellis, and C. E. Martin. Response of the space debris environment to greenhouse cooling. In *Proceedings of the 4th European Conference on Space Debris*, pages 243–248, 2005.

H. G. Lewis, A. Saunders, G. G. Swinerd, and R. J. Newland. Effect of thermospheric contraction on remediation of the near-Earth space debris environment. *Journal of Geophysical Research: Space Physics*, 116, 2011. URL https://doi.org/10.1029/2011JA016482.

H. G. Lewis, J. Radtke, J. Beck, B. Bastida Virgili, and H. Krag. Self-induced collision risk analysis for large constellations. In *Proceedings of the 7th European Conference on Space Debris*, 2017.

J.-C. Liou and N. L. Johnson. Risks in space from orbiting debris. *Science*, 311(5759): 340–341, 2006. URL https://doi.org/10.1126/science.1121337.

J.-C. Liou, D. J. Kessler, M. J. Matney, and G. Stansbery. A new approach to evalulate collision probabilities among asteroids, comets and Kuiper belt objects. In *Proceedings of the 34th Annual Lunar and Planetary Science Conference*, 2003.

J.-C. Liou, D. T. Hall, P. H. Krisko, and J. N. Opiela. LEGEND - A three-dimensional LEO-to-GEO debris evolutionary model. *Advances in Space Research*, 34(5):981–986, 2004. URL https://doi.org/10.1016/j.asr.2003.02.027.

J.-C. Liou, A. K. Anilkumar, B. Bastida Virgili, T. Hanada, H. Krag, H. G. Lewis, M. X. J. Raj, M. M. Rao, A. Rossi, and R. K. Sharma. Stability of the future LEO environment - An IADC comparison study. In *Proceedings of the 6th European Conference on Space Debris*, 2013.

H. L. Liu, B. T. Foster, M. E. Hagan, J. M. McInerney, A. Maute, L. Qian, A. D. Richmond, R. G. Roble, S. C. Solomon, R. R. Garcia, D. Kinnison, D. R. Marsh, A. K. Smith, J. Richter, F. Sassi, and J. Oberheide. Thermosphere extension of the Whole Atmosphere Community Climate Model. *Journal of Geophysical Research: Space Physics*, 115(A12), 2010. URL https://doi.org/10.1029/2010JA015586.

H. L. Liu, C. G. Bardeen, B. T. Foster, P. Lauritzen, J. Liu, G. Lu, D. R. Marsh, A. Maute, J. M. McInerney, N. M. Pedatella, L. Qian, A. D. Richmond, R. G. Roble, S. C. Solomon, F. M. Vitt, and W. Wang. Development and Validation of the Whole Atmosphere Community Climate Model With Thermosphere and Ionosphere Extension (WACCM-X 2.0). *Journal of Advances in Modeling Earth Systems*, 10(2): 381–402, 2018. URL https://doi.org/10.1002/2017MS001232.

S. P. Manley, F. Migliorini, and M. E. Bailey. An algorithm for determining collision probabilities between small solar system bodies. *Astronomy and Astrophysics Supplement Series*, 133(3):437–444, 1998. URL https://doi.org/10.1051/aas:1998334.

F. A. Marcos, J. O. Wise, M. J. Kendra, N. J. Grossbard, and B. R. Bowman. Detection of a long-term decrease in thermospheric neutral density. *Geophysical Research Letters*, 32(4), 2005. URL https://doi.org/10.1029/2004GL021269.

D. R. Marsh, M. J. Mills, D. E. Kinnison, J.-F. Lamarque, N. Calvo, and L. M. Polvani. Climate change from 1850 to 2005 simulated in CESM1(WACCM). *Journal of Climate*, 26(19):7372–7391, 2013. URL https://doi.org/10.1175/JCLI-D-12-00558.1.

C. E. Martin, R. Walker, and H. Klinkrad. The sensitivity of the ESA DELTA model. *Advances in Space Research*, 34(5):969–974, 2004. URL https://doi.org/10.1016/j.asr.2003.02.028.

J. Matzka, C. Stolle, Y. Yamazaki, O. Bronkalla, and A. Morschhauser. The geomagnetic kp index and derived indices of geomagnetic activity. *Space Weather*, 19(5), 2021. URL https://doi.org/10.1029/2020SW002641.

S. W. McIntosh, S. Chapman, R. J. Leamon, R. Egeland, and N. W. Watkins. Overlapping magnetic activity cycles and the sunspot number: Forecasting sunspot cycle 25 amplitude. *Solar Physics*, 295(163), 2020. URL https://doi.org/10.1007/s11207-020-01723-y.

D. McKnight, R. Witner, F. Letizia, S. Lemmens, L. Anselmo, C. Pardini, A. Rossi, C. Kunstadter, S. Kawamoto, V. Aslanov, et al. Identifying the 50 statistically-most-concerning derelict objects in LEO. *Acta Astronautica*, 181:282–291, 2021. URL https://doi.org/10.1016/j.actaastro.2021.01.021.

D. S. McKnight, R. L. Maher, and L. Nagl. Fragmentation Algorithms for Satellite Targets (FAST) empirical breakup model. Version 1, 1991.

F. McLean, S. Lemmens, Q. Funke, and V. Braun. DISCOS 3: An improved data model for ESA's database and information system characterising objects in space. In *Proceedings of the 7th European Conference on Space Debris*, 2017.

Jay W McMahon. *An analytical theory for the perturbative effect of solar radiation pressure on natural and artificial satellites*. PhD thesis, University of Colorado at Boulder, 2011.

M. G. Mlynczak, L. A. Hunt, J. M. Russell, B. T. Marshall, C. J. Mertens, and R. E. Thompson. The global infrared energy budget of the thermosphere from 1947 to 2016 and implications for solar variability. *Geophysical Research Letters*, 43(23): 11,934–11,940, 2016. URL https://doi.org/10.1002/2016GL070965.

K. Moe and M. M. Moe. Gas-surface interactions and satellite drag coefficients. *Planetary and Space Science*, 53(8):793–801, 2005. URL https://doi.org/10.1016/j.pss.2005.03.005.

O. Montenbruck and E. Gill. *Satellite Orbits: Models, Methods and Applications*. 3rd edition, 2005. ISBN 978-3-540-67280-7. URL https://doi.org/10.1007/978-3-642-58351-3.

O. Morgenstern, M. I. Hegglin, E. Rozanov, F. M. O'Connor, N. L. Abraham, H. Akiyoshi, A. T. Archibald, S. Bekki, N. Butchart, M. P. Chipperfield, et al. Review of the global models used within phase 1 of the Chemistry–Climate Model Initiative (CCMI). *Geoscientific Model Development*, 10(2):639–671, 2017. URL https://doi.org/10.5194/gmd-10-639-2017.

E. J. Öpik. Collision probabilities with the planets and the distribution of interplanetary matter. *Proceedings of the Royal Irish Academy. Section A: Mathematical and Physical Sciences*, 54:165–199, 1951.

J. K. Owens and W. W. Vaughan. NASA Marshall Engineering Thermosphere Model - Version 2.0 (MET-V 2.0). In *Proceedings of the 41st Aerospace Sciences Meeting and Exhibit*, 2003. URL https://doi.org/10.2514/6.2003-568.

J. K Owens, K. O. Niehuss, W. W. Vaughan, and M. A. Shea. NASA Marshall Engineering Thermosphere model — 1999 version (MET-99) and implications for satellite lifetime predictions. *Advances in Space Research*, 26(1):157–162, 2000. URL https://doi.org/10.1016/S0273-1177(99)01042-X.

J. M. Picone, A. E. Hedin, D. P. Drob, and A. C. Aikin. NRLMSISE-00 empirical model of the atmosphere: Statistical comparisons and scientific issues. *Journal of Geophysical Research: Space Physics*, 107(A12), 2002. URL https://doi.org/10.1029/2002JA009430.

J. M. Picone, J. T. Emmert, and J. L. Lean. Thermospheric densities derived from spacecraft orbits: Accurate processing of two-line element sets. *Journal of Geophysical Research: Space Physics*, 110(A3), 2005. URL https://doi.org/10.1029/2004JA010585.

L. Qian and S. C Solomon. Thermospheric density: An overview of temporal and spatial variations. *Space Science Reviews*, 168:147–173, 2011. URL https://doi.org/10.1007/s11214-011-9810-z.

L. Qian, R. G. Roble, S. C. Solomon, and T. J. Kane. Calculated and observed climate change in the thermosphere, and a prediction for solar cycle 24. *Geophysical Research Letters*, 33(23), 2006. URL https://doi.org/10.1029/2006GL027185.

L. Qian, A. G. Burns, S. C. Solomon, and W. Wang. Carbon dioxide trends in the mesosphere and lower thermosphere. *Journal of Geophysical Research: Space Physics*, 122(4):4474–4488, 2017. URL https://doi.org/10.1002/2016JA023825.

M. H. Rees. *Physics and Chemistry of the Upper Atmosphere*. Cambridge atmospheric and space science series. 1989. ISBN 0-511-57311-1. URL https://doi.org/10.1017/CBO9780511573118.

A. D. Richmond, E. C. Ridley, and R. G. Roble. A thermosphere/ionosphere general circulation model with coupled electrodynamics. *Geophysical Research Letters*, 19(6): 601–604, 1992. URL https://doi.org/10.1029/92GL00401.

H. Rishbeth. A greenhouse effect in the ionosphere? *Planetary and Space Science*, 38(7): 945–948, 1990. URL https://doi.org/10.1016/0032-0633(90)90061-T.

H. Rishbeth and R. G. Roble. Cooling of the upper atmosphere by enhanced greenhouse gases - modelling of thermospheric and ionospheric effects. *Planetary and Space Science*, 40(7):1011–1026, 1992. URL https://doi.org/10.1016/0032-0633(92)90141-A.

R. G. Roble. Major greenhouse cooling (yes, cooling): The upper atmosphere response to increased CO_2. *Reviews of Geophysics*, 33(S1):539–546, 1995. URL https://doi.org/10.1029/95RG00118.

R. G. Roble and R. E. Dickinson. How will changes in carbon dioxide and methane modify the mean structure of the mesosphere and thermosphere? *Geophysical Research Letters*, 16(12):1441–1444, 1989. URL https://doi.org/10.1029/GL016i012p01441.

R. G. Roble and E. C. Ridley. A thermosphere ionosphere mesosphere electrodynamics general circulation model (TIME GCM): Equinox solar cycle minimum simulations (30–500 km). *Geophysical Research Letters*, 21(6):417–420, 1994. URL https://doi.org/10.1029/93GL03391.

R. G. Roble, E. C. Ridley, and A. D. Richmond. A coupled thermosphere/ionosphere general circulation model. *Geophysical Research Letters*, 15(12):1325–1328, 1988. URL https://doi.org/10.1029/GL015i012p01325.

A. Rossi. NASA breakup model implementation comparison of results - Presentation at 24th IADC. 2006.

A. Rossi, A. Cordelli, P. Farinella, and L. Anselmo. Collisional evolution of the Earth's orbital debris cloud. *Journal of Geophysical Research: Planets*, 99(E11):23,195–23,210, 1994. URL https://doi.org/10.1029/94JE02320.

A. Rossi, A. Cordelli, P. Farinella, L. Anselmo, and C. Pardini. Modelling the evolution of the space debris population. *Planetary and Space Science*, 46(11-12):1583–1596, 1998. URL https://doi.org/10.1016/S0032-0633(98)00070-1.

A. Saunders, H. G. Lewis, and G. G. Swinerd. Further evidence of long-term thermospheric density change using a new method of satellite ballistic coefficient estimation. *Journal of Geophysical Research: Space Physics*, 116(A2), 2011. URL https://doi.org/10.1029/2010JA016358.

R. D. Sharma and R. G. Roble. Cooling mechanisms of the planetary thermospheres: The key role of O atom vibrational excitation of CO_2 and NO. *ChemPhysChem*, 3(10): 841–843, 2002. URL https://doi.org/10.1002/1439-7641(20021018)3:10<841::AID-CPHC841>3.0.CO;2-4.

SILSO World Data Center. The international sunspot number. *International Sunspot Number Monthly Bulletin and online catalogue*, 2021. URL http://www.sidc.be/silso/. Accessed 1st September, 2021.

I. Simmonds. Analysis of the 'Spinup' of a general circulation model. *Journal of Geophysical Research: Atmospheres*, 90(D3):5637–5660, 1985. URL https://doi.org/10.1029/JD090iD03p05637.

A. J. Simmons and R. Strüfing. An energy and angular momentum conserving finite-difference scheme, hybrid coordinates and medium-range weather prediction. Technical Report, 1981. URL https://www.ecmwf.int/node/12284.

S. Solomon. Stratospheric ozone depletion: A review of concepts and history. *Reviews of Geophysics*, 37(3):275–316, 1999. URL https://doi.org/10.1029/1999RG900008.

S. C. Solomon, L. Qian, and R. G. Roble. New 3-D simulations of climate change in the thermosphere. *Journal of Geophysical Research: Space Physics*, 120:2183–2193, 2015. URL https://doi.org/10.1002/2014JA020886.

S. C. Solomon, H. L. Liu, D. R. Marsh, J. M. McInerney, L. Qian, and F. M. Vitt. Whole atmosphere simulation of anthropogenic climate change. *Geophysical Research Letters*, 45:1567–1576, 2018. URL https://doi.org/10.1002/2017GL076950.

S. C. Solomon, H. L. Liu, D. R. Marsh, J. M. McInerney, L. Qian, and F. M. Vitt. Whole atmosphere climate change : Dependence on solar activity. *Journal of Geophysical Research : Space Physics*, 124:3799–3809, 2019. URL https://doi.org/10.1029/2019JA026678.

K. A. Stone, S. Solomon, and D. E. Kinnison. On the identification of ozone recovery. *Geophysical Research Letters*, 45:5158–5165, 2018. URL https://doi.org/10.1029/2018GL077955.

R. J. Suggs and R. M. Suggs. Marshall Engineering Thermosphere Model, version MET-2007. *NASA Marshall Space Flight Center*, 2017.

E. K. Sutton, J. M. Forbes, and D. J. Knipp. Rapid response of the thermosphere to variations in Joule heating. *Journal of Geophysical Research: Space Physics*, 114(A4), 2009. URL https://doi.org/10.1029/2008JA013667.

D. L. Talent. Analytic model for orbital debris environmental management. *Journal of Spacecraft and Rockets*, 29(4):508–513, 1992. URL https://doi.org/10.2514/3.25493.

K. F. Tapping. The 10.7 cm solar radio flux (F10.7). *Space weather*, 11(7):394–406, 2013. URL https://doi.org/10.1002/swe.20064.

W. K. Tobiska, S. D. Bouwer, and B. R. Bowman. The development of new solar indices for use in thermospheric density modeling. *Journal of Atmospheric and Solar-Terrestrial Physics*, 70(5):803–819, 2008. URL https://doi.org/10.1016/j.jastp.2007.11.001.

R. M. Tuminello, S. L. England, M. M. Sirk, R. R. Meier, A. W. Stephan, E. J. Korpela, T. J. Immel, S. B. Mende, and H. U. Frey. Neutral composition information in ICON EUV dayglow observations. *Journal of Geophysical Research: Space Physics*, 127(8): e2022JA030592, 2022. URL https://doi.org/10.1029/2022JA030592.

C. Underwood, A. Viquerat, M. Schenk, B. Taylor, C. Massimiani, R. Duke, B. Stewart, et al. InflateSail de-orbit flight demonstration results and follow-on drag-sail

applications. *Acta Astronautica*, 162:344–358, 2019. URL https://doi.org/10.1016/j.actaastro.2019.05.054.

United Nations Environment Programme. *Emissions Gap Report 2019*. 2019. ISBN 978-92-807-3766-0.

United Nations Environment Programme. *Emissions Gap Report 2021*. 2021. ISBN 978-92-807-3890-2.

United Nations Office For Outer Space Affairs. Space Debris Mitigation Guidelines of the Committee on the Peaceful Uses of Outer Space. *United Nations Publication*, 2010. URL http://www.unoosa.org/pdf/publications/st_space_49E.pdf.

University Corporation for Atmospheric Research. CESM Input Data. 2021. URL https://https://svn-ccsm-inputdata.cgd.ucar.edu/trunk/inputdata/atm/. Accessed 12th December, 2022.

D. A. Vallado. *Fundamentals of Astrodynamics and Applications*. Microcosm Press, 4th edition, 2013. ISBN 978-18-818-8318-0.

D. A. Vallado and P. Crawford. SGP4 orbit determination. *AIAA/AAS Astrodynamics Specialist Conference and Exhibit*, 2008. URL https://doi.org/10.2514/6.2008-6770.

D. A. Vallado, P. Crawford, R. Hujsak, and T. S. Kelso. Revisiting spacetrack report #3. In *AIAA/AAS Astrodynamics Specialist Conference and Exhibit*, 2006. URL https://doi.org/10.2514/6.2006-6753.

G. W. Wetherill. Collisions in the asteroid belt. *Journal of Geophysical Research*, 72(9): 2429–2444, 1967. URL https://doi.org/10.1029/JZ072i009p02429.